Investigation of the CO Oxidation on highly disperse Au/TiO_2 Catalysts in H_2-rich and H_2-free Atmosphere – A kinetic and mechanistic Study

Universität Ulm
Abteilung Oberflächenchemie und Katalyse

Dissertation
zur Erlangung des Doktorgrades Dr. rer. nat.
der Fakultät für Naturwissenschaften

Birgit Schumacher
(Neu-Ulm)

2005

Amtierender Dekan: Prof. Dr. Klaus-Dieter Spindler

1. Gutachter: Prof. Dr. Rolf Jürgen Behm
2. Gutachter: Prof. Dr. Werner Tillmetz
3. Gutachter: Prof. Dr. Konrad Hayek

Tag der Promotion: 7. Dezember 2005

Una palabra no dice nada
Y al mismo tiempo lo esconde todo
Igual que el viento que esconde el agua
Como las flores que esconden el lodo.

Una mirada no dice nada
Y al mismo tiempo lo dice todo
Como la lluvia sobre tu cara
O el viejo mapa de algun tesoro.

Una verdad no dice nada
Y al mismo tiempo lo esconde todo
Como una hoguera que no se apaga
Como una piedra que nace polvo.

Si un dia me faltas no seré nada
Y al mismo tiempo lo seré todo
Porque en tus ojos estan mis alas
Y esta la orilla donde me ahogo,
Porque en tus ojos estan mis alas
Y esta la orilla donde me ahogo.

Carlos Varela

TABLE OF CONTENTS

1 Introduction

The following work is concerning the investigation of the low temperature CO oxidation, catalyzed by highly disperse Au/TiO_2, in both H_2-containing and H_2-free atmosphere. This includes the characterization of the samples as well as kinetic and mechanistic investigations.

The term *catalysis* was established by Jöns Jakob Bezelius in 1836 and means *to annul* or *to untie* or *to pick up*. The participation of catalysts in chemical reactions enhances the rate by modifying the reaction path and as a consequence lowering the activation energy [1,2]. Equilibrium concentrations are not changed by catalysis and after reaction the physical and chemical properties of the catalyst are not modified. Catalysis is involved in all parts of our life. For example the catalysts 'enzymes' are essential for metabolism. The production of many chemicals in industry involve catalysis [1,2]. Without the huge amounts of ammonia, produced by the Haber-Bosch process, and the fertilizer produced from it, the drastic population growth in the last century would not have been possible [3]. Catalysis is also important in environmental chemistry, the most popular example is the three-way catalytic converter in automobiles.

Highly disperse, metal oxide supported Au catalysts were found to catalyse various oxidation and hydrogenation reactions, in particular the CO oxidation, already at low temperatures [4-7]. It was shown, that in addition to the catalyst dispersion also the procedures for catalyst preparation and conditioning and the nature of the oxide support play an important role, and it was distinguished between 'active', easily reducible supports and less active ('inert'), stable oxides [8]. One of the most active support materials is TiO_2. For instance, Au/TiO_2 catalysts were reported to be active for CO oxidation even at 90 K [9]. Highly active Au/TiO_2 catalysts (gold particle sizes ~1-10 nm) are commonly prepared by coprecipitation (CP) or by deposition-precipitation (DP), followed by calcination in air at temperatures between 200°C and 400°C [10-15]. Au/TiO_2 catalysts could be attractive for the removal of CO impurities from feed streams for polymer membrane (PEM) fuel cells [16-18]. CO oxidation in a H_2-rich atmosphere is commonly denoted as preferential CO oxidation (PROX). Due to process reasons two different temperature regions are particularly interesting for the PROX: 250-300°C (denoted as high temperature region) and 80-100°C (denoted as low temperature region) [17]. Pt- and Ru-, based catalysts have been intensively studied for used in the high temperature (see [17] and references therein, [19,20]) as well as for the low temperature

region [21-29], while highly diperse, metal oxide supported Au catalysts are highly active and selective for the CO oxidation in the low temperature region [8,16,30-33]. The term 'low temperature CO oxidation' is not commonly used for the temperature region 80-100°C, how it is defined in this thesis. In literature CO oxidation in the temperature range from -65°C [4] to 150°C [34] is denoted 'low temperature CO oxidation'. Nevertheless, with knowing the activation energy of the CO oxidation reaction and with the assumption that the reaction mechanism does not change in this temperature scale, the reported rates can be extrapolated to 80°C, the reaction temperature studied in the present work. Thus it can be deduced from literature data, that at this temperature 'good' Au/TiO_2 catalysts have TOFs (*'turn over frequencies'*) of 1-4 s^{-1} [4,35-39] in H_2-free atmosphere. The extraordinary high upper limit of 4 s^{-1} was reported (i) for a model catalyst [35] and (ii) as initial activity of a highly disperse powder catalyst [39].

The origin of the high activity of the Au/MeO_x, especially the Au/TiO_2 catalysts, is still discussed controversially. As a rough outline the different suggestions include (i) the reaction taking place at the interface of the gold particles and the metal oxide [14,40,41], (ii) the higher amount of low-coordinated, active gold atoms in small particles [42-44], (iii) a substrate induced modification of the Au-Au distances [44,45] and (iv) a quantum size effect, which correlates with the thickness of the gold clusters [36]. In detail, the reaction mechanism was studied on model catalyst and directly on the highly disperse catalysts. The purpose of studies with model catalyst is to understand in the atomic scale how the catalysts work, i.e., to identify active sites and the detection of reaction intermediates [1]. Concerning the CO oxidation catalyzed by Au/TiO_2, model studies were performed on gold single crystals and gold deposited on TiO_2 single crystals or films [46]. On a Mo(112)-(8×2)-TiO_x model catalyst the gold bilayer structure was reported to be significantly more active than the monolayer gold [47]. CO and oxygen adsorption and CO oxidation on Au(110)-(1×2) was studied intensively by Gottfried et al. [48-52]. The most significant findings were that i) physisorbed molecular oxygen has to be activated either by electron or photon impact in order to obtain chemisorbed oxygen, ii) CO adsorbs non-dissociatively and iii) CO can only be oxidized on a oxygen-precovered (chemisorbed oxygen) gold (110)-(1×2) surface. Oxygen adsorption on a different gold surface, Au(111), was studied by Mullins and co workers [53]. They found evidence for the recombination of oxygen atoms to $O_{2,ad}$, if the oxygen atoms are deposited on the surface by exposing the sample to a plasma-jet (the plasma jet had a ~40% dissociation

fraction). They reported the same for a $Au/TiO_2(110)$ model catalyst [54,55] (prepared along [56]). The adsorption of excited molecular oxygen was not excluded, but they did not present direct evidence. Furthermore, they observed significant CO oxidation, when directing a CO beam ($p_{CO}=10^{-7}$ to 10^{-6} mbar) on the model catalyst, which was precovered with O_{ad} [57,58]. Nevertheless, it has to be pointed out, that the samples were exposed to significant amounts of reactive atomic oxygen, while for powder catalysts the reaction is observed in the presence of molecular gaseous oxygen. Hence it is questionable, whether they have a realistic model for the CO oxidation catalyzed by Au/TiO_2.

The reaction mechanism of the CO oxidation on highly disperse Au/TiO_2 catalysts was studied in numerous publications [14,59-62]. CO adsorption was intensively studied by Boccuzzi and coworkers by Fourier Transform Infrared Spectroscopy (FTIR) at 90 K and room temperature. At 90 K CO adsorbs on the gold particles and on the TiO_2 support and they postulated a back spillover from the support to the gold and a key role of support oxygen vacancies in the reaction mechanism [59,60]. At room temperature they found, that CO molecules, which are adsorbed on terrace sites and on sites at the borderline of the gold particles, are active for CO oxidation and concluded a coadsorption of CO and O_2 on metallic sites [61]. They postulated two parallel reaction mechanisms at this temperature: (i) a rapid direct oxidation of CO on the gold particles and (ii) a slower oxidation reaction between adsorbed CO and lattice oxygen species of the support, which is induced by gas phase O_2 [61]. The suggestion of lattice oxygen participating in the reaction contradicts results of Maciejewski et al. [62] and of Grunwald et al. [14]. Maciejewski et al. [62] excluded a Mars-van-Krevelen mechanism and postulated a reaction between adsorbed CO and molecularly adsorbed oxygen. Grunwald et al. [14] detected CO adsorption on gold particles and concluded oxygen adsorption on TiO_2 vacancy sites from TDS experiments. Without giving experimental evidence, they suggested that the reaction takes place on the gold particles after an O_2 spill-over from the TiO_2 support to the gold particles.

Besides the reaction mechanism, the adsorption and activation of oxygen is discussed controversially. Some groups postulate O_2 adsorption and activation on the TiO_2 support (see [11,14,62,63]), mostly with the build-up of a $O_{2,ad}^-$-species. This species was detected with EPR (*'electron paramagnetic resonance'*) by Okumura et al. (as well as its stabilization by the TiO_2 support), but they excluded its participation in the reaction mechanism [64]. The

build-up of an active O_2-species on the TiO_2 support contradicts the conclusions made by Iizuka et al. [12,65]. In the first study [12] they circulated CO over Au, TiO_2 and Au/TiO_2, samples, which were precovered with oxygen, and obtained significantly higher amounts of CO_2 on the Au/TiO_2 and Au samples than on the TiO_2 samples. From this result they concluded, that during CO oxidation on Au/TiO_2 catalysts the active oxygen is adsorbed on the gold particles. Since CO oxidation is normally performed with a simultaneous introduction of gaseous CO and O_2, it is questionable, whether their experiments contribute results for these conditions. In a later study [65], they specified, that the oxidation rate is significantly higher, if O_2 is present in the gas phase. They suggested that the gas phase O_2 is directly activated on the surface of the deposited gold partilces or their perimeter, without contacting the TiO_2 support. Experimental evidence for this suggestion was not given in the publication. Theoretical studies revealed, that on defective TiO_2 surfaces, oxygen vacancies can stabilize Au atoms and small Au clusters [66,67] as well as adsorbed molecular oxygen, whose dissociation is enhanced on these vacancies [68]. Additional DFT calculations resulted in a substantial facilitation of O_2 adsorption by steps and tensile strains [69].

As mentioned above, the CO oxidation and the preferential CO oxidation in H_2 containing atmosphere was studied in this work. The temperature and selectivity dependence of the PROX on a Au/TiO_2 catalyst was studied by Choudhary et al. [31]. In that study the gold particles were deposited by grafting a gold phosphine complex onto TiO_2, i.e., they used a procedure different from the standard precipitation methods. Schubert et al. [8,33] presented first results of the PROX on a Au/TiO_2 catalyst prepared via deposition precipitation, including long-term stability, selectivity and activation energy. Kinetic and mechanistic information were not enclosed in these publications. Reaction kinetics of the CO oxidation in H_2-free atmosphere was studied in the temperature region 0 - 60°C so far (for examples see [11,31,39,40,63,70]). Hence, there is lack of information about reaction kinetics of the CO oxidation in H_2-free and H_2-rich atmosphere the temperature region of 80-100°C, interesting for PROX.

On highly disperse catalysts the reaction kinetics are usually studied at atmospheric pressure by varying the CO and O_2 partial pressures in the gas mixtures, hence no information is obtained on the dependence of reaction rates on the total pressure (p_{tot}). This dependence is of interest, since it was found e.g., that small amounts of water play a beneficial role in the

activity of the Au/TiO_2 catalysts (see beneath). Since the vapor pressure of water increases with decreasing total pressure, this may influence the rates. Additionally, the material gap, which means the study of well ordered single crystals and model catalysts on the one hand (e.g. see [46]) and highly dispersed gold catalysts on the other hand (e.g. see [5,71]) induces a pressure gap, since for keeping the surfaces of single crystals and model catalyst defined and clean, ultra high vacuum (UHV) conditions are required [1]. There are different approaches to bridge the pressure gap: From the single crystal and model catalyst side measurements at elevated pressures are performed, e.g., by adding a separate high-pressure cell to standard UHV equipment, which can be closed off from the UHV system while operated at high pressure (see, e.g., [72-77]). Coming from the opposite side, from realistic high surface area catalysts operated at atmospheric pressure, attempts to move to significantly lower operating pressures have been scarce so far. The only exception were TAP (‘*temporal analysis of products*’) reactor studies, where a molecular beam is passed at variable effective pressure through the catalyst bed, while the surrounding atmosphere is held under vacuum conditions (typically $<10^{-3}$ mbar) [78,79]. Another approach is the low pressure plug-flow micro-reactor, which was built by R. Leppelt within the experimental work of his dissertation a [80]. This low pressure plug-flow micro-reactor was used to gain information on the reaction kinetics of highly disperse Au/TiO_2 catalysts in the pressure gap.

The above mentioned approaches to bridge the pressure gap are necessary, since CO oxidation was not reported so far in the low pressure regime CO oxidation on Au/TiO_2 model catalysts for the simultaneous introduction of gaseous CO and O_2, but only with preadsorbed O_{ad} or $O_{2,ad}$ [54,57,58,81]. In contrast, for CO and O_2 partial pressures in the 1-10 mbar range CO oxidation was reported for model catalysts during simultaneous introduction of CO and O_2. For example CO oxidation was observed on model catalysts based on TiO_2 single crystals ($Au/TiO_2(110)$) [82] and TiO_2 films ($Au/TiO_2/Ru(0001)$) [83] in our group and on a $Au/TiO_2(001)/Mo(100)$ model catalyst by Valden et al. [35]. A significant influence of the different materials can not be observed, since the reaction rates were similar to those of highly disperse Au/TiO_2 catalysts, on which the CO oxidation is usually performed in the same partial pressure ranges (e.g. see [4]). Hence the question arises, whether it is only an effect of the pressure gap, that for model catalysts no oxidation of CO by gaseous O_2 was reported in the low pressure regime. To verify this assumption, reaction rates have to be determined on highly disperse Au/TiO_2 catalysts for CO and O_2 partial pressures <1-10 mbar.

A ‘hot topic’ in recent years was the beneficial role of small amounts of water for the CO oxidation on the Au/TiO_2 catalysts. It was shown for various catalytic systems, that the activity of the CO oxidation increases, if water is added to the gas mixture [84-89]. The role of the water in the reaction mechanism, however, is not yet clear. Also first modelling theoretic studies have been published investigating the CO oxidation reaction in the presence of water [90,91]. A detailed presentation of the results and their interpretation will be given in chapter 3.5.

A common problem with Au/TiO_2 catalysts is the insufficient reproducibility of their catalytic and physical properties, which may originate in insufficient reproducible conditions for preparation and conditioning of the catalysts [4-7,92]. Since this effect was also observed in this work, a comparative study on a series of four Au/TiO_2 catalysts with similar Au loadings was performed.

As mentioned at the beginning of the introduction, the objective of this work was the investigation of the CO oxidation on highly disperse Au/TiO_2 catalysts, in both H_2-rich and H_2-free atmosphere, which included the characterization of the samples as well as kinetic and mechanistic investigations. The dissertation is structured as follows: After a short experimental chapter (chapter 2), which includes a description of the equipments and the preparation of the Au/TiO_2 samples, the experimental results and their discussion are presented in chapter 3. This chapter is divided into five parts dealing with (i) catalyst characterization by TEM and XPS (chapter 3.1), (ii) the long-term stability of the (preferential) CO oxidation (chapter 3.2), (iii) the influence of CO and O_2, including reaction kinetics, CO adsorption and isotope scrambling (chapter 3.3), (iv) the reaction kinetics in the pressure gap (chapter 3.4) and (v) transient measurements (chapter 3.5). A summary of the work is given in chapter 4.

2 Experimental

2.1 Plug-flow reactor

Two different reactor units, each with a 'conventional' plug-flow micro-reactor (i.e., the reactions were performed at atmospheric pressure) were used, one connected to a GC (*'gas chromatograph'*) and the other to an IMR-MS (*'ion molecule reaction mass spectrometer'*) as detection unit. In both set-ups the micro-reactor consisted of a quartz glass tube with 0.4 cm inner diameter and 0.6 cm outer diameter. The micro-reactors were enclosed by a cylindrical tube oven and connected to the gas lines via Swagelok fittings; for temperature regulation a Ni-Ni/Cr thermocouple was fixed with a two component adhesive based on SiO_2 (Polytec, type 905, it has the same expansion coefficient as quartz glass) in a cavity at the outside of the micro-reactors. Oven temperatures were controlled with temperature controllers from Watlow Electrics (Watlow Series 982 in both set-ups). Various temperature profiles of a reactor in the IMR-MS set-up are given in fig 2-1 (a temperature profile of a reactor in the GC set-up is given in [17]). Catalyst bed and thermocouple are fixed at the reaction coordinate 0 cm. Along the catalyst bed, with a length of 5-10 mm, the temperature deviates at most 2°C. The catalyst samples were fixed with quartz wool.

The furnaces consisted of an Alumina oxide tube (ID 14.8 mm) in the GC set-up and of a steel tube (ID 14.2 mm) in the IMR-MS set-up, around which heating bands were wrapped. For isolation, fiber blankets were fixed between the tubes and the steel coating. For the determination of the influent concentrations, beneath denoted as bypass concentrations, the reactors could be disconnected from the gas streams via 4-port-valves.

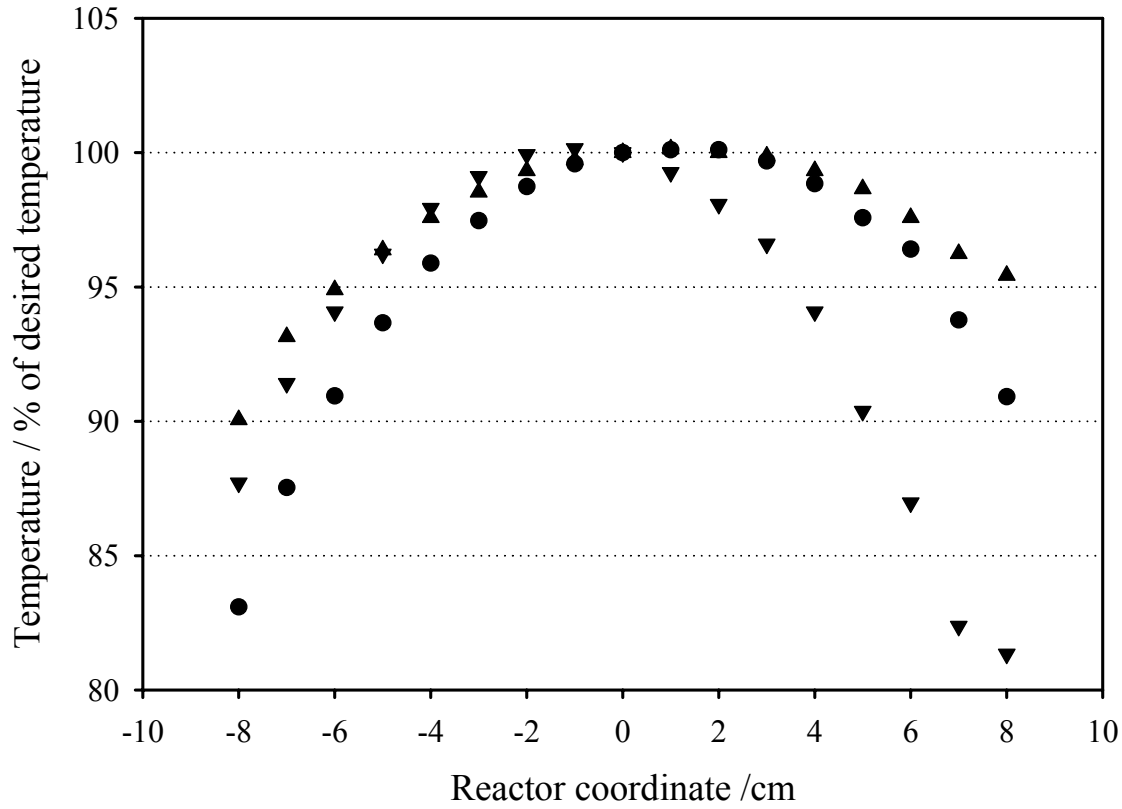

Figure 2.1: Temperature profile of a reactor in the IMR-MS set-up (ID 4 mm) at (▼) 400°C, (●) 200°C and (▲) 100°C. At the reaction coordinate x=0 cm the thermocouple and the catalyst bed are fixed. The measurements were performed in a N_2 gas stream of 40 Nml/min.

2.1.1 Basic principles and calculations

A detailed description of the basic principles of the plug-flow micro-reactor is given in [17,93]. In short, it is assumed that a volume element dV passes the reactor as a homogeneous plug (i.e., the plug has a homogeneous composition and reacts with rates corresponding to this composition) and all molecules of this volume element have similar contact times in the reactor. A mass balance of the differential volume element dV and the respective mass element dm (dV and dm correlate via the Ideal Gas Law) leads to equation (2-1), which has to be integrated along the entire catalyst bed (equation (2-2)). For differential conversions, the reactant volume flow and the reaction rate can be considered constant, hence the reaction rate can be expressed along equation (2-3).

$$dX_{reactant} = -r_{reactant} \cdot \frac{dm}{\dot{V}_{reactant,in,dm}} \qquad (2\text{-}1)$$

$$\int_0^m \frac{dm}{\dot{V}_{reactant,in,dm}} = \int_0^{X_m} \frac{dX_{reactant}}{-r_{reactant}} \qquad (2\text{-}2)$$

$$r_{reactant} = -X_m \frac{\dot{V}_{reactant,in,}}{m} \qquad (2\text{-}3)$$

$X_{reactant}$: Reactant conversion [%] in mass element

$$X_{reactant} = 100\% \cdot (c_{reactant,in} - c_{reactant,out}) \cdot c^{-1}_{reactant,in}$$

$c_{reactant,in}$: Reactant concentration at the reactor entrance

$c_{reactant,out}$: Reactant concentration at the reactor exit

$\dot{V}_{reactant,in,dm}$: Reactant volume flow at the entrance of dm

$\dot{V}_{reactant,in}$: Reactant volume flow at the entrance of catalyst bed

$r_{reactant}$: reaction rate

Since in the experiments performed here, the total gas flow ($\dot{V}_{Ges}$) and the ingoing CO concentration ($c_{CO,in}$) can be determined experimentally, the reaction rates can be calculated via equation (2-4).

$$r_{CO} = \frac{c_{CO,in} \cdot X_{CO} \cdot \dot{V}_{ges}}{m_{Au}} \qquad [\text{mole}\cdot\text{s}^{-1}\cdot\text{g}_{Au}^{-1}] \qquad (2\text{-}4)$$

Considering the dispersion D, which describes the fraction of Au atoms, located at the surface (see subsection 2.5.3), and the molar weight of Au (197 g/mole), the turn-over frequencies (TOF, reaction rate in molecules per surface Au atom and second) can be calculated (equation (2.5)). The normalization of the TOF rate to the number of available surface Au atoms [18] and therefore active sites, makes it a very useful parameter for the comparison of the catalyst performance with those reported in literature, since reaction rates given per gram catalysts (g_{cat}^{-1}) or gram gold (g_{Au}^{-1}) do not provide information on the reactivity of active sites [94].

$$r_{CO,TOF} = \frac{r_{CO} \cdot M_{Au}}{D} \qquad [\text{s}^{-1}] \qquad (2\text{-}5)$$

The *selectivity* (S) is defined by the amount of O_2 consumed for CO oxidation, divided by the total amount of consumed O_2, and calculated from the balance between CO_2 formation (CO oxidation) and O_2 consumption (equation (2-6), [20]).

$$S = \frac{\Delta O_{2,CO}}{\Delta O_{2,H_2O} + \Delta O_{2,CO}} \qquad (2\text{-}6)$$

$\Delta O_{2,CO}$: oxygen consumption for the CO oxidation

$\Delta O_{2,H_2O}$: oxygen consumption for the H_2 oxidation

It should be noted that this determination of the selectivity is only correct as long as the H_2 level is not affected by any other reactions such as the water gas shift (WGS) reaction ($CO + H_2O \leftrightarrows CO_2 + H_2$) or the methanation reaction ($CO + 3H_2 \leftrightarrows CH_4 + H_2O$). This appears justified based on previous measurements of the WGS reaction on a Au/TiO_2 catalyst under comparable conditions by Sakurai et al. [95].

Finally, a diffusion limitation of the reaction rates in the measurements described below has to be excluded. According to Weisz [96] mass and heat-flow problems do not occur, if reactions rates do not exceed the magnitude 10^{-5} mole·s^{-1}·cm^{-3}. To check whether diffusion limitation occurred in our experiments, the reaction rates have to be converted to the unit mole·s^{-1}·cm^{-3}. The average catalyst bed volume for the determination of reaction rates is 0.075 cm^3. The highest reaction rate determined for a Sachtleben catalyst (Au/TiO_2(1), for the nomenclature of the catalysts see section 2.6) was $4.5 \cdot 10^{-2}$·mole·s^{-1}·g_{Au}^{-1}. The weight of the sample was about 100 mg, the gold content 2.4 wt.-% and the catalyst was diluted with α-Al_2O_3 to a ratio catalyst : dilution = 1 : 50. With consideration of these parameters the determined reaction rate of $4.5 \cdot 10^{-2}$·mole·s^{-1}·g_{Au}^{-1} corresponds to a rate of $2.9 \cdot 10^{-6}$ mole·s^{-1}·cm^{-3}. If similar calculations are performed for the low and high loading Degussa catalysts (Au/TiO_2(3) and Au/TiO_2(8): maximal reaction rates 10^{-2} and $7 \cdot 10^{-3}$ mole·s^{-1}·g_{Au}^{-1}, gold content 3.4 and 4.5 wt.-%, dilution 1:200 and weight ~100 mg in both cases), reaction rates of $2.3 \cdot 10^{-6}$ mole·s^{-1}·cm^{-3} and $2.56 \cdot 10^{-6}$ mole·s^{-1}·cm^{-3} are obtained, respectively. In all cases the reaction rates are below the magnitude 10^{-5} mole·s^{-1}·cm^{-3}, hence diffusion limitation can be excluded.

2.1.2 Gas Chromatograph (GC) Detection

The effluent gases were analyzed with a GC from Dani (Model 86.10HT). The components were separated in two packed stainless steel columns. One column was packed with a polar polymer (Hayesep Q from Chrompack) and the other column with a mole sieve (5 Å from Chrompack). The content of the sample volume (1.5 ml) was eluted onto the polar column, where CO_2 and H_2O were separated from the less polar components CO, N_2 and O_2, which are subsequently directed on the mole sieve column via a pneumatically controlled four-way valve. The different components were synchronously eluted onto two channels, and subsequently detected in thermal conductivity detectors (modell TCD 86/40 from Dani). Since hydrogen was used as a carrier gas [97], this component could not be detected. The flux

of the carrier gas war 20 ml/min, the oven temperature 80°C and the detector temperature 95°C. For more details see [17,97].

2.1.3 Detection with Ion Molecule Reaction Mass Spectroscopy (IMR-MS)

Similar to Chemical Ionization Mass Spectroscopy (CI-MS), reaction gas ions (Kr^+ and Xe^+) are used for ionization of the analyte components in the IMR-MS (Atomika IMR-MS SP89). Contrary to CI-MS, the ionization locations of (i) the reactions gases (Kr and Xe, denoted as primary gases) and (ii) the analyze gases are separated in the IMR-MS. Components with ionization energies larger than the electron affinity of Xe^+ or Kr^+, such as N_2 and H_2, can not be ionized, which allows e.g., a quantitative detection of CO in the presence of N_2. IMR-MS has moderate ionization energies (the ionization potentials of Xe^+ ($^2P_{3/2}$) and Kr^+ ($^2P_{3/2}$) are 12.13 eV and 14.00 eV, respectively [98]), which results in a very low fragmentation probability. Hence, CO can be detected quantitatively in the presence of CO_2, without being affected by fragmentation of CO_2. The primary gases were dosed from a 1:1 gas mixture (Linde) via a leak valve (VTI), which led to a chamber pressure of 10^{-6} mbar. The analyte gas was fed into the IMR-MS via a stainless steel capillary (ID 0.2 mm) and an aperture. For a detailed description of the system see [99].

2.2 Diffuse Reflectance Infrared Transform Spectroscopy (DRIFTS)

In-situ IR measurements were performed in a DRIFTS configuration with a Magna 560 spectrometer from Nicolet, equipped with a MCT narrow band detector and a commercial in-situ reaction cell unit from Harricks (HV-DR2). This set-up allows measurements in a continuous flow of gas mixtures, equal to those in the plug-flow micro-reactors, and at elevated temperatures. For 'normal', quasi steady state, measurements (CO oxidation in H_2-rich and H_2-free atmosphere (see subsection 3.2.2) or CO adsorption in H_2-rich and H_2-free atmosphere (see subsection 3.3.2)) typically 400-600 scans (acquisition time ~4 min) at a nominal resolution of 8 cm^{-1} were added for one spectrum. For the observation of reaction transients (see subsection 3.5.1) 20 scans (acquisition time 9 s plus 3 s for data saving) at a nominal resolution of 8 cm^{-1} were added for one spectrum. The intensities were evaluated in Kubelka-Munk units, which are linearly related to the adsorbate concentration [100]. Prior to the experiments background spectra were recorded on the freshly conditioned catalyst at reaction temperature in a flow of pure nitrogen, which were used for normalization by dividing the sample spectra through the background reference. Finally, spectral contributions

of the gas phase were removed by subtracting a reference spectrum recorded over an inert carrier under similar conditions. For further details see [18].

Due to an initial change of the reflectivity after the admission of CO (color changes due to partial reduction of the TiO_2 support) the background spectra did not fit perfectly the CO adsorption spectra over the entire spectral range. Therefore, the background division had to be done separately for two different spectral regions.

2.3 The low-pressure micro-reactor

2.3.1 Set-up

As mentioned in the introduction, the only approach so far for measurements on powder catalysts with reduced pressures were TAP reactors, which on the one hand are very suitable for dynamic studies due to their high time resolution, but on the other hand are very expensive and demanding in handling. The low-pressure micro-reactor, which was constructed and built-up by Rainer Leppelt, ought to be cheaper and simpler in handling, than a TAP reactor. For the simpler handling a significantly worse time resolution was accepted. Furthermore, it ought to allow measurements in the range of the pressure gap, between 10^{-3} mbar and 10^{3} mbar and an independent adjustment of the gas flow and reactor pressure in order to enable measurements with constant contact times at various pressures. Function and calibration tests for this set-up will be presented in the dissertation of Rainer Leppelt.

The initial set-up of the reactor system (a schematic presentation of the system and a picture are given in fig. 2-2, [80]) consisted of a gas mixing unit, gas flow control, micro-reactor, pressure control, pumping stage, and the IMR-MS as gas analyzing system (see section 2.1.4). The gas-mixing unit and the available gases are described in section 2.5. Most of the gas mixture was pumped off behind the gas-mixing unit, so that between 0.01% and 10%, depending on the reactor pressure, was passed through the reactor system. The pumping speed and the pressure in the gas mixing (p_1) unit were controlled by fine dose valve V1. The minimum pressure in the gas-mixing unit was 500 mbar, since the mass flow controllers do not work reliable at lower pressures.

The gas flow was controlled with a capillary system. Five different capillaries with nominal inner diameters of 200, 100, 75, 50, and 25 µm (effective diameters: 199, 87.8, 60.2 and 49.2 µm for the first four capillaries, respectively) were available and allowed the adjustment of flows in the range of 0.5 Nµl/min to 9.26 Nml/min. For higher flow rates a stainless steel

tube with an inner diameter of 1 mm was connected. In order to receive laminar flow in the capillaries, the pressure inside them was kept >200 mbar (p_2) [101,102] with leak valve LV1. The laminar flow conditions allow a description of the gas flow by the Hagen-Poiseuille equation (equation (2.7)) and at given a flow the pressure of p_2 can be calculated along equation (2.8).

$$\frac{dV(p_0)}{dt} = \dot{V} = \frac{r_{cap}^4 \pi (p_1^2 - p_2^2)}{16 L \eta p_0} \qquad (2.7)$$

$$p_2 = \sqrt{p_1^2 - \frac{\dot{V} 16 L \eta p_0}{r_{cap}^4 \pi}} \qquad (2.8)$$

Via equation 2.8 the desired p_2 values were determined for the flows necessary to enable measurements with constant contact times (0.056 s) at various reactor pressures. Under steady state conditions the gas flow through the capillary system and the reactor are equal.

The micro-reactor consisted of a 6 mm quartz tube with an inner diameter of 4 mm. The catalyst powder was fixed inside the reactor with quartz wool. The micro-reactor is heated by a ceramic tube furnace, which can be opened to allow the simple exchange of the micro-reactor. The micro-reactor is connected via Swagelok fittings. The pressure in the reactor (p_3) is adjusted via leak valve LV2. The p_{tot} range, which was studied with this low-pressure micro-reactor set-up was between $9 \cdot 10^{-2}$-10^3 mbar. For lower total pressures, the use of the capillaries with 50 µm and 25 µm diameters would be necessary, which was not practible, since the desired flows could not be set within one day.

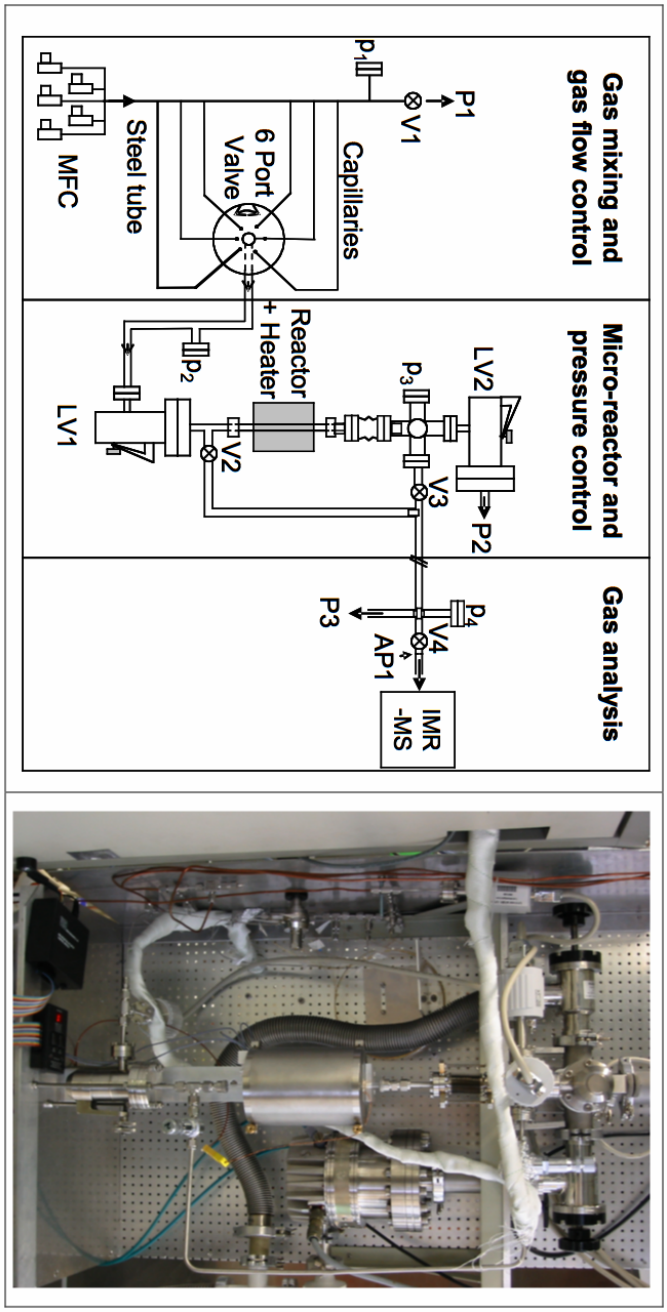

Figure 2-2: Schematic presentation (from [80]) and photo of the original low-pressure micro-reactor set-up.

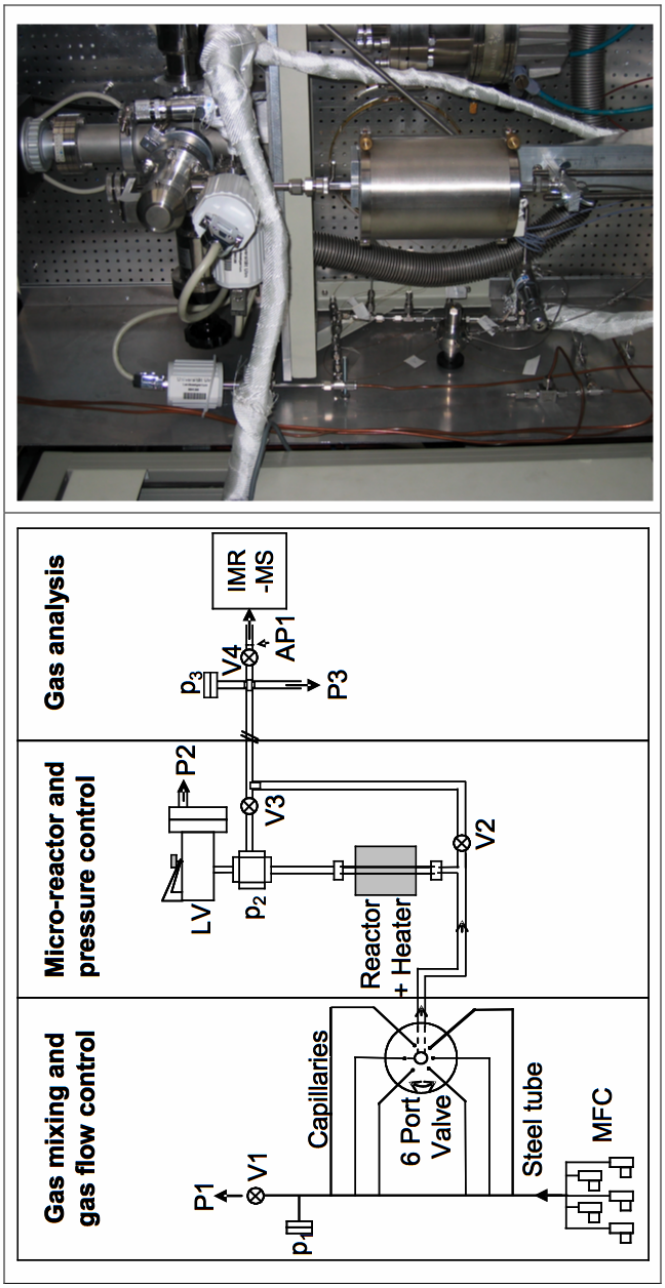

Figure 2-3: Schematic presentation and photo of the modified low-pressure micro-reactor set-up.

Since the initial set-up consisted of a big volume (139 ml) and because of the long time, that was needed for the settings of the pressures behind the capillaries (p_2) and in the reactor (p_3), the set-up was simplified (fig. 2-3). Leak valve LV1 (after the capillaries) was removed, which led to a volume reduction to 30 ml. Since after this modification the flow was not laminar any more (p_2<200 mbar), the Hagen-Poiseuille equation could not be applied. The gas flow was then calibrated via the pressure increase in the reactor at different pressure settings in the gas-mixture unit (p_1) and in the reactor (the leak valve behind the reactor was closed and the pressure increase in the reactor room was detected; the flow could be calculated for the specific settings from the initial pressure increase. Since the equipment was built by R. Leppelt, this calibration will be described in detail in his dissertation).

The reproducibility of measurements performed with the specific set-ups was as follows: With the initial set-up the maximal error was 22% and with the modified set-up 29%. Measurements performed with both set-ups were less comparable. The reaction rates deviated between 76% up to nearly one decade (538%). For both set-ups no systematic error is obvious and changes in the performance of the catalyst are not expected (the catalysts were stored in a deep freezer, see section 2.6). Therefore we used results determined with both set-ups. For a better overview it is marked in the text and the plots of chapter 3.4, which set-up was used for the respective measurement.

2.3.2 Calculation of reaction rates

In contrast to the ‘conventional’ plug-flow micro-reactor connected to the IMR-MS, where the measurements were performed at atmospheric pressure, the application of the low pressure micro-reactor did not result in exactly equal pressures for various measurements in front of the aperture to the IMR-MS. For this reason the intensities of the analyte components differed between various measurements, although the gas composition was equal. Hence, the calculation of the analyte concentrations was modified, since the ‘standard calculation’ (described in detail in [99]) assumes a constant pressure in the capillary connected to the IMR-MS.

Table 2-1: Absolute intensities of the analyte components O_2, CO and CO_2 and the CO_2/CO, CO_2/O_2 and O_2/CO ratios for two different calibration measurements (calibration gas: 1% CO_2 (4.5), 1% CO (3.7), 0.5% CH_4 (3.5), 1% O_2 (5.0), 21.5% N_2 (5.0), balance H_2 (5.0) from Westphalen). Although the absolute intensities differ significantly in the two measurements, the ratios are constant.

Absolute intensities	O_2 (in cps)	CO (in cps)	CO_2 (in cps)
Calibration 1	21188.5900	17196.9573	84628.9796
Calibration 2	15469.3964	12618.8739	63362.9820
Intensity ratios	CO_2/CO	CO_2/O_2	O_2/CO
Calibration 1	4.9212	3.9941	1.2321
Calibration 2	5.0213	4.0960	1.2259
Mean value	4.9712	4.0451	1.2290

Different pressures in front of the IMR-MS aperture lead to different absolute intensities of the analyte components. The intensity ratios of the various components, however, remain constant, if the composition of the gas is not modified (table 2-1). Hence, these constant intensity ratios were used for the determination of analyte concentrations of gases with unknown composition. For the intensity ratios the subsequent definition is made:

$$\frac{I(CO_2)}{I(O_2)} = x_i;\ \frac{I(CO_2)}{I(CO)} = y_i;\ \frac{I(O_2)}{I(CO)} = z_i$$

x, y, and z have the index ‘0’ for the calibration measurement (detection of the calibration gas, which consisted of 1% CO_2 (4.5), 1% CO (3.7), 0.5% CH_4 (3.5), 1% O_2 (5.0), 21.5% N_2 (5.0), balance H_2 (5.0)) and the index ‘1’ for the reaction measurement (unknown composition). Based on this definition, equations (2-9) to (2-11) and (2-12) to (2-14) hold true for the calibration and reaction measurements, respectively. In contrast to the calibration gas, the concentrations of O_2, CO und CO_2 are unequal during reaction measurements, why the indices ‘l’, ‘m’ and ‘n’ are established for the ratios $c(CO_2)/c(O_2)$, $c(CO_2)/c(CO)$ and $c(O_2)/c(CO)$, respectively, for these measurements.

$$I(CO_2)_0 = x_0 \cdot I(O_2)_0 \quad \text{and} \quad c(CO_2)_0 = c(O_2)_0 \tag{2-9}$$

$$I(CO_2)_0 = y_0 \cdot I(CO)_0 \quad \text{and} \quad c(CO_2)_0 = c(CO)_0 \tag{2-10}$$

$$I(O_2)_0 = z_0 \cdot I(CO)_0 \quad \text{and} \quad c(O_2)_0 = c(CO)_0 \tag{2-11}$$

$$I(CO_2)_1 = x_1 \cdot I(O_2)_1 \quad \text{and} \quad c(CO_2)_1 = l \cdot c(O_2)_1 \tag{2-12}$$

$$I(CO_2)_1 = y_1 \cdot I(CO)_1 \quad \text{and} \quad c(CO_2)_1 = m \cdot c(CO)_1 \tag{2-13}$$

$$I(O_2)_1 = z_1 \cdot I(CO)_1 \quad \text{and} \quad c(O_2)_1 = n \cdot c(CO)_1 \tag{2-14}$$

The unknown indices ‘l’, ‘m’ and ‘n’ have to be substituted by the measurable factors ‘x_i’, ‘y_i’ and ‘z_i’. This is achieved by comparing equations (2-9) and (2-12), (2-10) and (2-13), as well as (2-11) and (2-14):

$$\frac{x_0}{1} = \frac{x_1}{l} \quad \Rightarrow \quad l = \frac{x_1}{x_0}$$

$$\frac{y_0}{1} = \frac{y_1}{m} \quad \Rightarrow \quad m = \frac{y_1}{y_0}$$

$$\frac{z_0}{1} = \frac{z_1}{n} \quad \Rightarrow \quad n = \frac{z_1}{z_0}$$

The replacement of ‘l’, ‘m’ and ‘n’ in equations (2-12) to (2-14) leads to equations (2-15) to (2-17):

$$c(CO_2) = \frac{x_1}{x_0} \cdot c(O_2) \qquad (2\text{-}15)$$

$$c(CO_2) = \frac{y_1}{y_0} \cdot c(CO) \qquad (2\text{-}16)$$

$$c(O_2) = \frac{z_1}{z_0} \cdot c(CO) \qquad (2\text{-}17)$$

To solve the equation system (2-15) to (2-17), we assume that the sum of CO and CO_2 concentration is 1 % in the course of the reaction (see equation (2-18)). This hold true for the measurements presented in chapter 3.4, since in all cases 1 % of CO was introduced to the samples (for measurements with different CO concentrations a separate carbon balance has to be drawn):

$$c(CO) + c(CO_2) = 1\% \qquad (2\text{-}18)$$

After combination of equations (2-18) and (2-16), we obtain

$$c(CO_2) = \frac{y_1}{y_0 + y_1} \qquad (2\text{-}19)$$

The concentrations of O_2 ($c(O_2)$) and CO_2 ($c(CO_2)$) can be calculated with equations (2-17) and (2-15), respectively.

Conversions are caluculated from the influent analyte concentrations and the concentrations after the reaction. Reactions rates and turn over frequencies (TOF) are obtained via equations (2-4) and (2-5), respectively.

2.4 Catalyst characterization

2.4.1 X-Ray Photoelectron Spectroscopy (XPS)

XPS is a powerful technique to get information on the elemental composition of surfaces and on the oxidation state of the elements. It is one of the most frequently used techniques in catalysis and surface science [1,103]. The spectra presented in this dissertation were recorded by Dr. J. Cai with a PHI 5800 ESCA system using monochromatized Al-K_α radiation (1486 eV). The photons are absorbed by the studied samples and induce the ejection of core electrons, whose kinetic energy follows equation 2-20 [103]. The kinetic energy of the photoelectrons is detected with a hemispherical analyzer.

$$E_{kin} = h\upsilon - E_b - \varphi \qquad (2\text{-}20)$$

E_{kin}: kinetic energy of the photoelectron

E_b: binding energy of the photoelectron

φ: work function of the spectrometer

ν: frequency of the exciting irradiation

h: Planck's constant

All spectra were recorded with a power of 250 W, an angle of 45° and an aperture size of 4 mm (acceptance angle ±5°, sampled size 1 mm). The detail spectra of the elements of interest, here Au, O and Ti, were recorded with a pass energy of 11.75 eV. The scanning time differed throughout the experiments. For the characterization of the Sachtleben catalysts (Au/TiO_2(1)and Au/TiO_2(2), see section 3.1.2), the scanning times were 6.67 min, 5.00 min and 4.00 min for Au 4f, Ti 2p, O 1s, respectively, which led to poor signal-noise ratios, especially for the Au 4f peaks. For the Degussa samples the scanning times were increased to 25 min, 12.50 min and 10.00 min, respectively. The difference in quality can be seen in figs. 3.1-3 and 3.1-5. For the C 1s spectra the pass energy was enhanced from 11.75 eV for the Sachtleben catalysts to 29.35 eV for the Degussa samples, which enhanced the signal to noise ratio. The scanning times were decreased from 6.67 min to 4.03 min.

The detection depth for the Au 4f, O 1s and Ti 2p spectra can be estimated by determining the mean free path of the photoelectrons in solids via the so called 'universal curve' [1]. For the gold spectra the kinetic energy of the photoelectrons is about 1030 eV, which results in a mean free path of about 2 nm. For the O 1s and Ti 2p spectra the kinetic energies are ~960 eV and ~1030 eV, respectively, which results in a mean free path of ~1.4 nm. Since the crystals

in TiO_2 powder are oriented randomly, the mean values of the three lattice constants are used for the determination of the average amount of layers, from which photoelectrons could be detected. For anatase and rutile the mean values of the lattice constants are 0.561 and 0.404 nm [68], respectively, hence photoelectrons from two to four layers are detected, when recording the O 1s and Ti 2p detail spectra.

Shirley background subtraction [104,105] and peak fitting were performed using a public XPS peak fit program (XPSPEAK4.1 by Dr. R. Kwok). In order to exclude surface charging effects the binding energies were calibrated using the Ti $2p_{3/2}$ peak as reference (the details of the calibration of binding energies and peak areas are given in subsection 3.1.2.1). Fits of the Au 4f peaks were performed based on the following assumptions: (i) the difference between Au $4f_{7/2}$ and Au $4f_{5/2}$ was set to 3.67 eV, (ii) the integral intensity of the Au $4f_{5/2}$ is three quarters of that of the Au $4f_{7/2}$ peak, and (iii) the peak widths (FWHM) for both peaks, Au $4f_{7/2}$ and Au $4f_{5/2}$, are equal. The FWHM of Au^0 were 0.8 to 1.0 eV, those of Au^{3+} were fixed to 2.2 eV. Furthermore, the Lorenz-Gauss ratio for each Au species was kept constant. The error of the peak fits, especially of the resulting Au^{3+}/Au^0 ratios are discussed in section 3.1.2.2. For the fit of the Ti 2p peak the following assumptions were made: (i) the difference between Ti $2p_{3/2}$ and Ti $2p_{1/2}$ was set to 5.7 eV and (ii) the integral intensity of the Ti $2p_{1/2}$ is half of that of the Ti $2p_{3/2}$ peak. For the fits of the O 1s peak the FWHMs of the TiO_2 contribution were kept constant, which is justified, since all measurements were performed under the same conditions (pass energy, power, aperture size, angle).

2.4.2 X-Ray Diffraction (XRD)

With XRD catalyst properties can be studied by means of interference effects of scattered radiation [103]. Usually the diffraction of Cu K_α radiation (8.04 keV) at atoms in periodic lattices is studied. Interference maxima are detected, if the diffracted photons are in phase and constructive interference arises. XRD can be used to identify crystalline phases in catalysts and particle sizes. Particle sizes are calculated via the Scherrer equation (equation 2-21 [103]).

$$< L >= \frac{K \cdot \lambda}{\beta \cdot \cos\theta} \qquad (2\text{-}21)$$

<L>: Measure for the dimension of the particle in the direction perpendicular to the reflecting plane

λ: X-ray wavelength

β: Peak width

θ: Angle between the beam and the normal on the reflecting area

K: Constant (0.9)

The XRD spectra were recorded and evaluated by Dr. V. Plzak at the Center for Solar Energy and Hydrogen Research (ZSW) using a Siemens D5000 diffractometer.

2.4.3 Transmission Electron Microscopy (TEM)

A TEM follows a similar principle as a conventional light microscope, where the light beam is replaced by an electron beam and the optical lenses by magnetic lenses. A high energy electron beam is passed through a condenser in order to produce parallel rays, which impinge on the sample. Since the attenuation of the beam depends on density and thickness, a two-dimensional projection of the sample is formed by the transmitted electrons. The magnification of this projection is called 'bright field image' [103]. The images presented in this dissertation were recorded by Prof. Dr. F. Banhart using a Philips CM 20 microscope (200 kV).

The images were evaluated with 'Paint Shop Pro' (Jasc Software, version 5.03). For each sample at least 300 particles were evaluated. The dispersion (D), which is required for the calculation of the TOF reaction rates (see equation 2-5 in section 2.1.1), is defined by the fraction of Au atoms, which are located at the surface of the gold particles with respect to the total amount of gold atoms. If spherical particles are assumed, which is justified on the basis of the TEM images (for example see fig. 3.1-1), the dispersion can be calculated from the particles size distribution along equation 2-22.

$$D = \frac{6 \cdot v_{at}}{s_{at}} \cdot \frac{\sum n_i d_{i,part}^2}{\sum n_i d_{i,part}^3} \qquad (2\text{-}22)$$

v_{at}: Volume per Au atom

s_{at}: Surface per Au atom

n_i: Number of Au particles with diameter $d_{i,part}$

2.5 Reaction gases and mixture facilities

All facilities used for the in-situ investigation of the CO oxidation (plug-flow reactors connected to the GC or IMS-MS (see section 2.1), the DRIFTS (see section 2.2), and the low-pressure micro-reactor (see section 2.3)) were connected to gas-mixture units, which allowed measurements with different gas compositions, e.g., H_2-rich or H_2-free atmosphere. In these connections, which consisted of four independent gas lines, the gas flow was adjusted with mass flow controllers (MFCs). The gases were mixed after passing the MFCs and prior entering the reactor or, for bypass measurements, the detection system. The available gases are summarized in table 2-2. The gas mixing units connected to the GC and the DRIFTS and the one connected to the IMR-MS and the low-pressure micro-reactor, respectively, where equipped with different MFCs (different maximal flows) and that not all gases were available in all gas mixing units. For clarity, the different arrangements and the gases available for the respective MFCs are summarized in table 2-3. For further details, e.g., the calibration of the MFCs see [97,106]. The calibration of the peak areas (GC) or signal intensities and ratios (IMR-MS) was performed using a calibration gas of known composition (1% CO_2 (4.5), 1% CO (3.7), 0.5% CH_4 (3.5), 1% O_2 (5.0), 21.5% N_2 (5.0), balance H_2 (5.0)) from Westphalen.

Table 2-2: Gases available for the gas mixtures

Pure gases			Gas mixtures		
Gas	Purity	Company	Mixture	Purities	Company
H_2	5.0	Westphalen	2% CO in N_2	4.7/6.0	Westphalen
N_2	6.0	Westphalen	0.14% CO in N_2	4.7/6.0	Westphalen
O_2	5.0	Westphalen	2% CO in H_2	4.7/5.0	Westphalen
CO	4.7	Air Liquide	0.14% CO in H_2	4.7/5.0	Westphalen
			10% O_2 in N_2	5.5/5.0	Westphalen
			0.35% O_2 in N_2	5.5/5.0	Westphalen
			1.25% $^{36}O_2$ in N_2	n.n/6.0	Linde
			1.34% $C^{18}O$ in N_2	n.n/6.0	Linde

Table 2-3: Configuration of the MFCs in the different set-ups.

Configuration 1*			Configuration 2**		
MFC	max. flux	Gases	MFC	max. flux	Gases
1	20 Nml/min	10% O_2/N_2 0.35% O_2/N_2	1	30 Nml/min	2% CO/N_2
2	100 Nml/min	H_2	2	100 Nml/min	N_2 1.25% $^{36}O_2/N_2$ 1.34% $C^{18}O/N_2$
3	50 Nml/min	N_2	3	5 Nml/min	O_2
4	100 nml/min	2% CO/N_2 2% CO/H_2 0.14% CO/N_2 0.14% CO/N_2	4	30 Nml/min	H_2

* This configuration was available for the plug-flow reactor connected to the GC and the DRIFTS

** This configuration was available for the plug-flow reactor connected to the IMR-MS and the low-pressure micro-reactor

2.6 Preparation of the Au/TiO_2 catalysts

All Au/TiO_2 catalysts used for this work were prepared by Dr. V. Plzak at the Center for Solar Energy and Hydrogen Research (ZSW) via a modified 'deposition-precipitation' method: The TiO_2 powder was suspended in water at 60°C. While stirring, an aqueous solution of $HAuCl_4 \cdot 4\ H_20$ was added at the same temperature. The pH was kept constant at ~5.5 by adding 0.16 M Na_2CO_3 solution. After additional stirring for 30 minutes, the precipitate was filtered and washed carefully in order to avoid chloride contaminations, since the latter decrease the activity of the catalyst in two ways. They (i) facilitate the growth of Au particles during conditioning and [107] (ii) poison the active sites of the catalyst [107]. The filtrate was dried over night at room temperature in vacuum. Since only part of the gold deposits on the support (50-95 %), the exact gold loadings were determined via Inductively Coupled Plasma Atom Emission Spectroscopy (ICP-AES).

Two sets of catalysts were prepared: For the catalysts $Au/TiO_2(1)$, $Au/TiO_2(2)$, $Au/TiO_2(3)$ (in the following denoted as Sachtleben catalysts or Sachtleben samples) pure anatase powder from Sachtleben was used as support. Before gold deposition, this powder was annealed at 710°C ($Au/TiO_2(1)$ and $Au/TiO_2(2)$) or 670°C ($Au/TiO_2(3)$) for 30 min, which led to TiO_2 particle sizes of 25 nm (BET surface: 50 m^2/g) and 21 nm (BET surface: 65 m^2/g), respectively. Since the activity of these catalysts varied significantly (see chapter 3.2), a second set of Au/TiO_2 catalysts was prepared using Degussa P25 TiO_2 powder (~25 % rutile, rest anatase [108], BET surface 56 m^2) as support. The activity of the catalysts $Au/TiO_2(4)$,

$Au/TiO_2(5)$, $Au/TiO_2(6)$, $Au/TiO_2(7)$ and $Au/TiO_2(8)$, in the following denoted as Degussa catalysts or Degussa samples, varied significantly less than those of the Sachtleben catalysts (section 3.2). For a better overview, the specifications of all catalysts are summarized in table 2-4.

The Au/TiO_2 catalysts are extremely light sensitive. Leaving a sample at daylight for only an hour leads to a visible reduction of the catalysts, i.e., their color changes from beige to violet. For this reason the Sachtleben samples were stored in a refrigerator, covered with aluminum foil. Nevertheless, the samples became slightly violet after a few months in the refrigerator. The Degussa catalysts were stored in a deep freezer. They were still beige after more than two years in the deep freezer. Concerning the worse reproducible activity of the Sachtleben catalysts, it is noteworthy, that the anatase powder from Sachtleben was stored in a translucent plastic bottle, while the P25 powder from Degussa was stored in an opaque case.

Table 2-4: Specifications of the catalysts used in this work.

Catalyst	ZSW Charge	Support	Au loading
$Au/TiO_2(1)$	181200y	Anatase Sachtleben (annealed at 710°C, 30 min)	2.4 wt.-%
$Au/TiO_2(2)$	310102	Anatase Sachtleben (annealed at 710°C, 30 min)	2.4 wt.-%
$Au/TiO_2(3)$	190101	Anatase Sachtleben (annealed at 670°C, 30 min)	4.5 wt.-%
$Au/TiO_2(4)$	270203A	Degussa P25	3.4 wt.-%
$Au/TiO_2(5)$	270203B	Degussa P25	3.4 wt.-%
$Au/TiO_2(6)$	270203C	Degussa P25	3.0 wt.-%
$Au/TiO_2(7)$	190203B	Degussa P25	3.4 wt.-%
$Au/TiO_2(8)$	190203A	Degussa P25	5.4 wt.-%

The samples were conditioned before the measurements. Three different procedures were used: (i) conventional conditioning via calcination at 400°C in 10% O_2/N_2 for 30 minutes [4,10-12,14,15], (ii) a reductive conditioning procedure including 45 min annealing in 10% H_2 in N_2 at 200°C (before and after the reduction the samples were treated in N_2 for 30 min at 200°C), und (iii) a redox-conditioning procedure, which also included 45 min annealing in 10% H_2/N_2 at 200°C (before the reduction the samples were treated in N_2 for 30 min at 200°C), followed by calcination in 10% O_2/N_2 for 30 min at 300°C. Redox-conditioning procedures are also used in [31,39,40], though the exact processing temperatures were different. After the conditioning the samples were cooled down in N_2 to the reaction temperature (80°C).

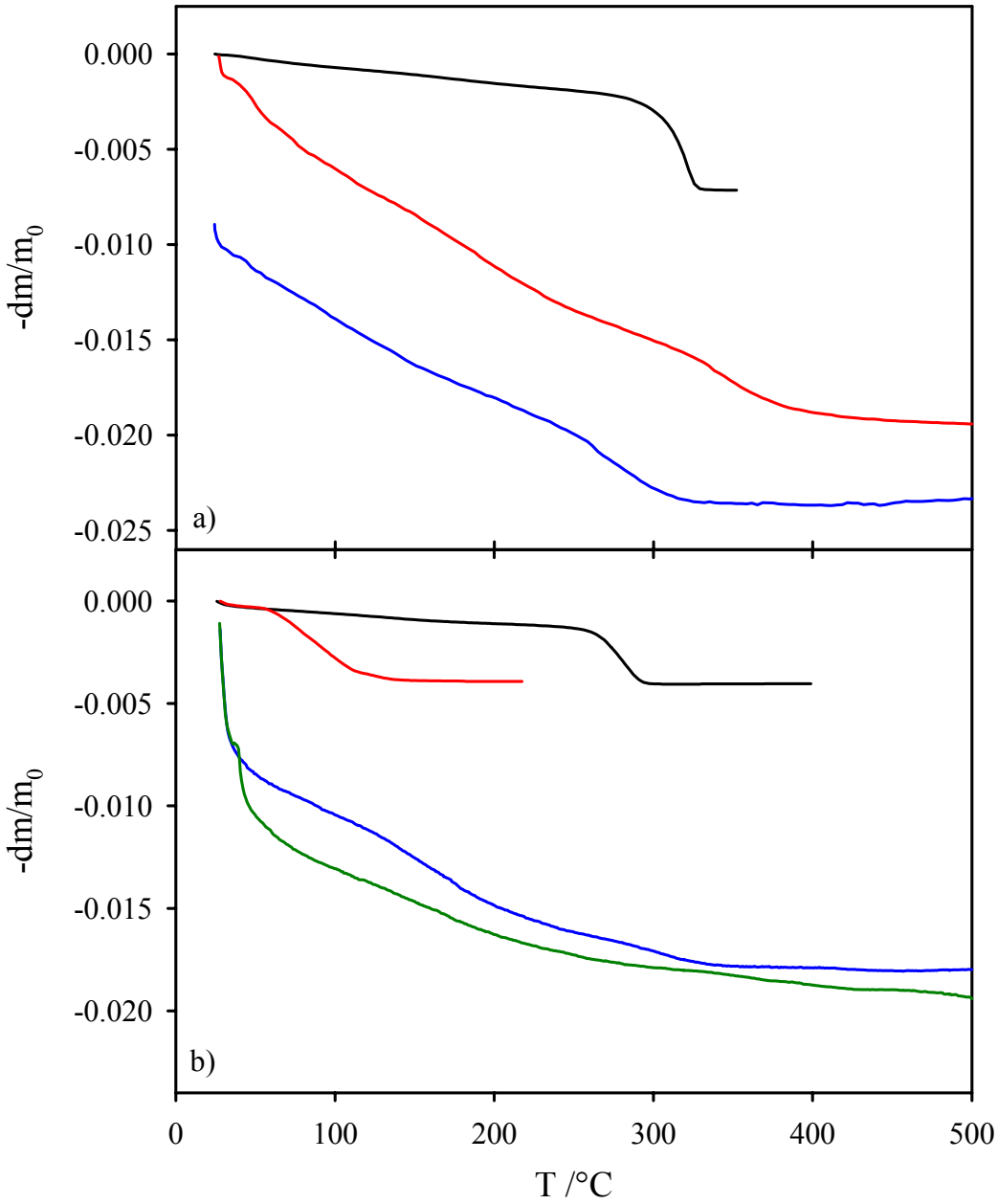

Fig. 2-4: a) TGA measurements on Au_2O_3 (black line), $Au/TiO_2(3)$ (blue line) and $Au/TiO_2(4)$ (red line) during heating in air (heating rate: 10 K/min). b) TGA measurements on Au_2O_3 in air and 10% H_2 in N_2 (black and red line, respectively) and $Au/TiO_2(2)$ also in air and 10% H_2 in N_2 (blue and green line, respectively); heating rate: 1 K/min [109].

The conditioning temperatures where chosen on the basis of TGA (*'thermo gravimetric analysis'*) measurements (fig. 2-4, performed and evaluated by Dr. V. Plzak at the Center for Solar Energy and Hydrogen Research (ZSW) on a TG-50 from Shimadzu). Fig. 2-4a shows the spectra of Au_2O_3 and the catalysts $Au/TiO_2(3)$ and $Au/TiO_2(4)$ during heating in air. The gold is reduced at about 320°C and the catalysts do not show significant changes at temperatures higher than 400°C. In H_2-rich atmosphere Au_2O_3 is reduced at around 150°C

and catalyst $Au/TiO_2(2)$ shows a significantly faster mass reduction in this gas mixture, compared to air (fig. 2-4b).

3 Results and Discussion

3.1 Catalyst Characterization

To obtain information on the physical properties of the Au/TiO_2 catalysts, they were characterized with respect to the size of the gold particles (section 3.1.1), their surface composition and the oxidation state of their components after different treatments (section 3.1.2). The gold particle size, which plays an important role in the activity of Au/TiO_2 catalysts [36], was determined by TEM, and, to a smaller extent, by XRD. XRD measurements were performed by Dr. V. Plzak at the ZSW. The surface composition and the oxidation states of the components, were investigated by XPS after the various conditioning procedures.

3.1.1 Au particle sizes

Except for the reduced samples of catalysts $Au/TiO_2(1)$ and $Au/TiO_2(2)$, all particle sizes were determined via TEM. In general the TEM images show well separated Au particles (dark spots) on the larger TiO_2 substrate particles, independent of the conditioning procedure, which is demonstrated in the TEM images of $Au/TiO_2(4)$ samples (50 nm × 50 nm), recorded after three different conditioning procedures (see fig. 3.1-1, left column). Obviously, the Au particles in the calcined sample (fig. 3.1-1a) are bigger than those in the redox-conditioned (fig. 3.1-1b) and the reductively conditioned samples (fig. 3.1-1c). This trend is reproduced by the particle size distributions of the $Au/TiO_2(4)$ catalyst evaluated from the above mentioned and similar images, which are shown in fig. 3.1-1, right column. The calcined sample (fig. 3.1-1a) exhibits a rather wide particle size distribution with a mean particle size of 3.0±0.5 nm, while the particles in the redox-conditioned and in the reductively conditioned samples have much narrower particle size distributions with mean particle sizes of 2.0±0.3 nm and 2.1±0.4 nm, respectively.

The particle size distributions of the other catalysts exhibit similar trends, the mean particle sizes are listed in table 3.1-1. In all cases the calcination procedure leads to mean particle sizes of about 3 nm, while for the redox-conditioned and for the reduced samples the particle sizes are around 2 nm. Interestingly, the increase in Au loading (samples $Au/TiO_2(3)$ and $Au/TiO_2(8)$) does not lead to a measurable increase in particle size compared to the lower loading samples, at least not within the range covered here.

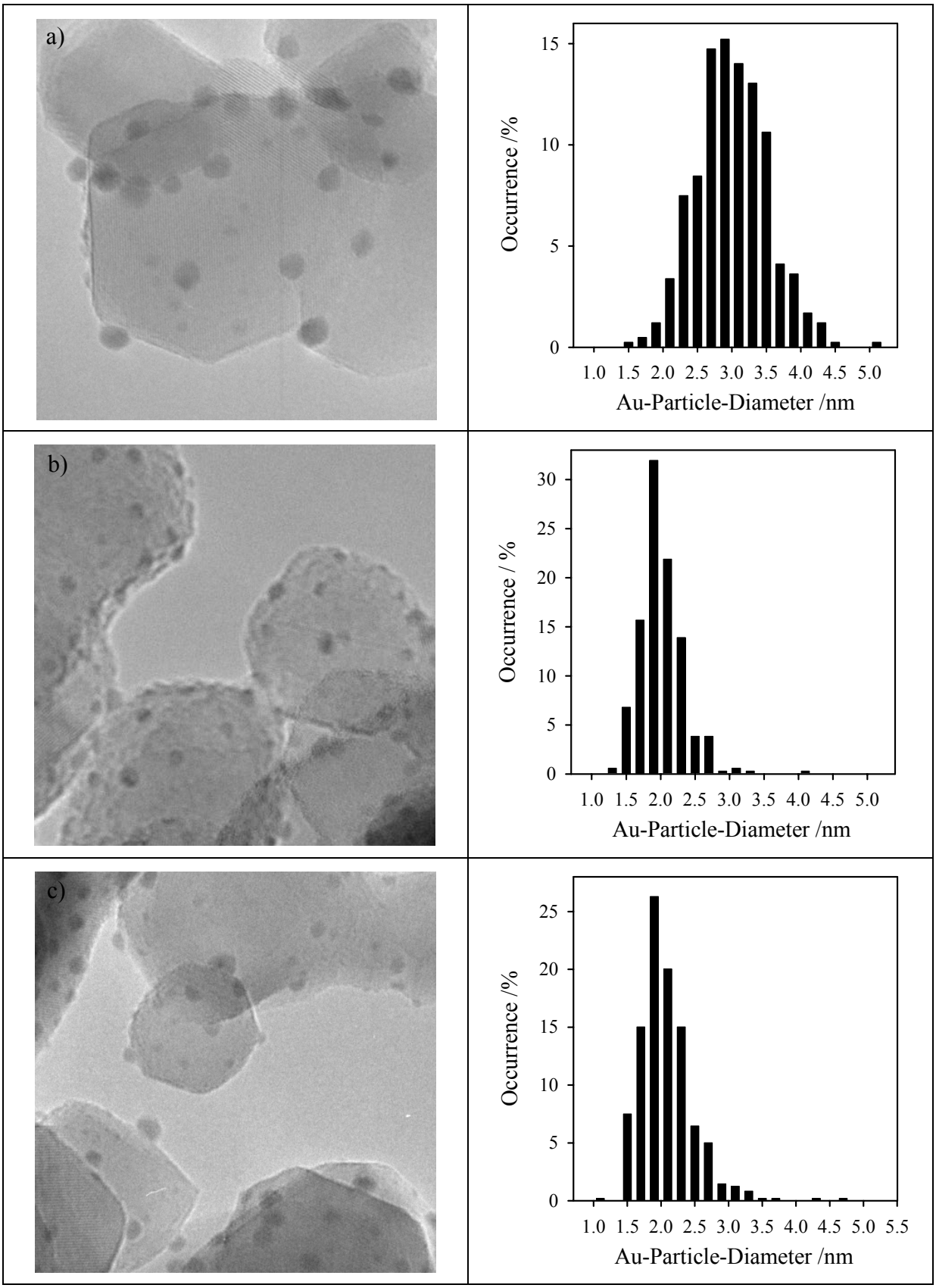

Figure 3.1-1: TEM images (left column, each picture 50nm × 50nm) and particle size distribution of catalyst Au/TiO_2(4) (right column) after a) calcination, b) redox-conditioning and c) reduction.

Table 3.1-1: Mean sizes of the gold particles after the three different conditioning procedures as determined via TEM (only for the reduced samples of $Au/TiO_2(1)$ $Au/TiO_2(2)$ particle sizes were determined via XRD by Dr. V. Plzak at the ZSW).

		Calcination	Redox-conditioning	Reductive conditioning
Sample	Metal loading (in wt.-%)	Ø (in nm)		
$Au/TiO_2(1)$	2.39	3.0±1.1	-	1.7±0.1
$Au/TiO_2(2)$	2.43	2.6±0.9	-	1.8±0.2
$Au/TiO_2(3)$	4.48	2.6±0.8	-	-
$Au/TiO_2(4)$	3.37	3.0±0.5	2.0±0.3	2.1±0.4
$Au/TiO_2(5)$	3.37	3.1±0.5	1.9±0.3	1.9±0.4
$Au/TiO_2(6)$	2.96	3.1±0.5	1.9±0.4	1.7±0.3
$Au/TiO_2(7)$	3.37	3.3±0.5	2.2±0.4	1.9±0.3
$Au/TiO_2(8)$	5.43	3.0±0.5	2.0±0.3	1.9±0.3

Previous studies of Au/TiO_2 catalysts prepared via deposition-precipitation procedures reported particle sizes ranging from 3.4 nm to 3.6 nm after 4 h of calcination at 400°C [84,110,111]. The bigger particle sizes, compared to the calcination pretreatment at 400°C here, results from the longer pretreatment periods. After calcination at 200°C for 4 h, Boccuzzi at al. reported a mean particle size of 2.4±0.9 nm for a deposition-precipitation prepared catalyst [15], and Zanella et al. determined particle sizes of 2.3±0.5 nm and 2.0±0.4 nm, respectively, for deposition-precipitation prepared catalysts using urea and NaOH as pH controlling agent [111]. Catalysts prepared via the incipient wetness method generally exhibit much larger Au particles than those prepared via deposition-precipitation [39,40,112]. For instance, a particle size of 30 nm, which is one order of magnitude larger than that of the present catalysts, was reported by Bollinger et al. for a catalyst prepared by the incipient wetness method (support material Degussa P25) after reductive conditioning at 200°C [40]. The smallest Au particles for this preparation method were reported by Ossipof et al. [112], who determined a mean particle size of 7.3 nm after drying the catalyst at 120°C. The temperature dependence of the particle size, which can be observed in the literature data, agrees well with the behavior of particle sizes determined in the present study. Apparently, the particle size is mainly controlled by the conditioning temperature, at least at the lower temperatures, while under these conditions the conditioning atmosphere is less important. It should be noted that recent results obtained for reactive annealing of planar $Au/TiO_2(110)$ model catalysts in an O_2 atmosphere (50 mbar) and in air (1 atm.) showed significant changes

in particle size for annealing temperatures of 300°C and above, while heating under UHV conditions up to 400°C did not cause significant changes in particle size [113].

The redox-conditioning procedure with an initial reduction step at 200°C, followed by a calcination step at higher temperature (300°C) has been developed in the course of the experimental work for this thesis. It was based on activity tests in a reaction atmosphere (subsection 3.2.1.2). Related procedures, though at different temperatures, have also been reported from other groups [39,40,59,112,114]. For instance, Schimpf et al. reported that redox-conditioning of a 1.7 wt. % Au loaded catalyst (preparation via deposition-precipitation, support: Degussa P25), which involves calcination at 300°C for 8 hours and reduction at 300°C for 3 hours, leads to Au particles with a mean diameter of 5.3 nm [114]. Since significant loading effects were not found in this range, the much larger particle size of these catalysts, which is more than twice as high as the particle sizes of the here presented redox-conditioned samples, is attributed to the higher reduction temperature and the longer conditioning times.

3.1.2 Surface composition and oxidation states

The surface composition and the oxidation states of the Au, Ti and O species of the unconditioned catalysts and after the different conditioning procedures was studied by XPS for two Sachtleben catalysts (Au/TiO_2(1) and Au/TiO_2(2), untreated, calcined and reduced samples) and for the Degussa catalysts (untreated and after the three conditioning procedures). Since the activity of the Sachtleben catalysts was not determined after redox-conditioning (see chapter 3.2), they were not characterized after this conditioning procedure. Detail spectra were taken from the Ti 2p, Au 4f and O 1s peaks and partly from the C 1s peak.

3.1.2.1 Peak calibration and the Ti 2p peak

The binding energies (BE) were calibrated using the Ti $2p_{3/2}$ peak in order to exclude surface charging effects. Its binding energy (BE) was set to 459.2 eV, the reported value for anatase and rutile [115]. For the Degussa catalysts the peak resulted exclusively from Ti^{4+} contributions, independent from the conditioning procedure. An example of the Ti 2p peak is given in fig. 3.1-2.

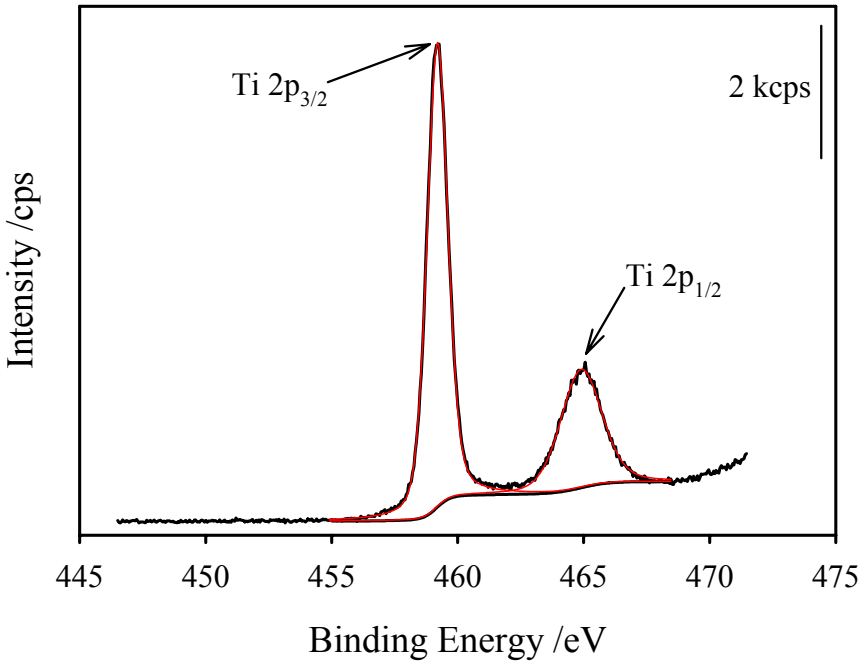

Figure 3.1-2: Ti 2p peak of catalyst Au/TiO_2(4) after calcination at 400°C. Only one contribution resulting from TiO_2 can be fitted (red lines). For calibration, the Ti $2p_{3/2}$ is shifted to 459.2 eV, the reported value of rutile and anatase [115]. The peak area is calibrated according to table 3.1-2. Pass energy: 11.75 eV, scanning time: 12.50 min.

The untreated samples of Au/TiO_2(1) and Au/TiO_2(2) contained impurities (compare figs. 3.1-2 and 3.1-3). For the two Sachtleben catalysts the space between the minimum at ~462 eV and the Shirley background is significantly bigger than for the Degussa sample and the Ti $2p_{1/2}$ peaks of the Sachtleben samples are less symmetric. Both spectra in fig. 3.1-3 allow the fitting of Ti^{3+} contributions (17 % and 8 % for catalysts Au/TiO_2(1) and Au/TiO_2(2), respectively) with binding energies of 457.1 eV for the Ti $2p_{3/2}$ peak. This binding energy is close to the value determined by Gonbeau et al. [116], who reported a binding energy (BE) of 456.6 eV for Ti^{3+} in a Ti_2O_3 sample. In that publication the Ti^{4+} BE from TiO_2 was set to 458.7 eV, hence it is shifted by 0.5 eV with respect to the BE calibration used in this work. Nevertheless, is must be mentioned that the Ti $2p_{1/2}$ peak of this contribution has FWHMs of 540 eV, which is an extraordinary high value. Therefore it can not be stated certainly, that the space between the minimum at ~462 eV and the Shirley background results from Ti^{3+}.

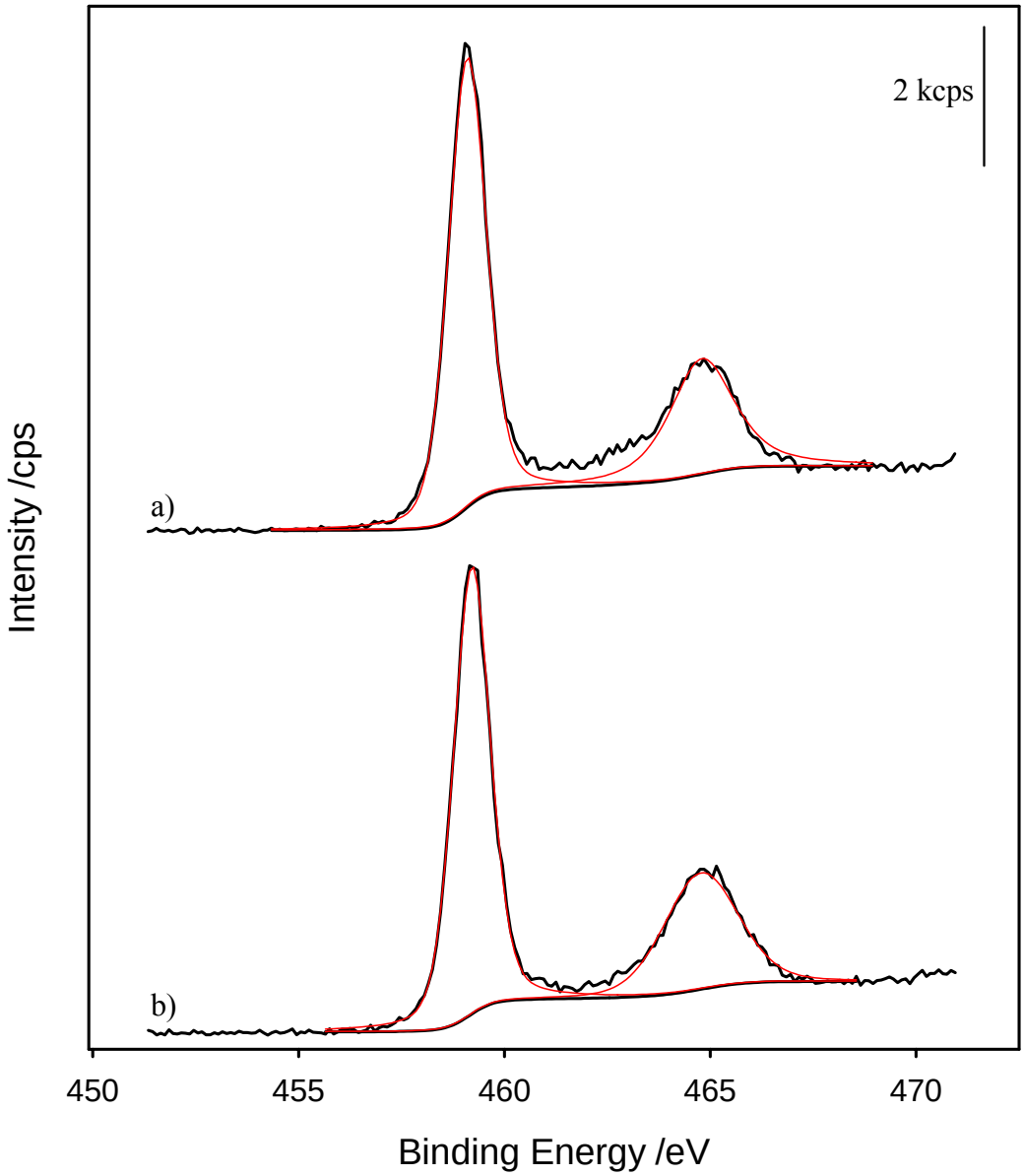

Figure 3.1-3: Ti 2p peaks with Shirley background and peak fit (red lines) of untreated samples of the catalysts a) Au/TiO_2(1) and b) Au/TiO_2(2). The peak areas are calibrated according to table 3.1-2. Pass energy: 11.75 eV, scanning time: 5.00 min

In contrast to the Degussa catalysts, the Sachtleben catalysts were not equal after preparation (fig. 3.1-3). A source of the differences in the Ti 2p peaks of the untreated Sachtleben catalysts is the storage of the TiO_2 powder: While the Degussa P25 TiO_2 powder was stored in an opaque black box, the TiO_2 powder from Sachtleben was stored in a translucent bin. It is well known, that the semiconductor TiO_2 is photoactive (see, e.g. [117-119] and references therein). By the absorption of light, an electron-hole pair is created (in the following denoted as e^- and h^+, respectively), which can undergo charge transfer reactions, here most likely with

oxygen, since air contains 21% of oxygen. Photoadsorption of O_2 can occur by hole trapping reactions [117]:

$$O^{2-}_{lattice} + h^+ \rightarrow O^-$$

$$O^- + O_2 \rightarrow O_3^-$$

Since lattice oxygen is involved in this reaction, also the electronic state of the surrounding Ti atoms changes slightly, which can cause the additional Ti 2p contribution visible in fig. 3.1-3. The light irradiation in Ulm depends on season and weather, hence the amount of photoadsorbed oxygen is different each day, which results in the different amounts of the additional Ti 2p contribution in the two Sachtleben catalysts (compare figs. 3.1-3a and b).

After the two conditioning procedures only completely oxidized TiO_2 support was detected in both Sachtleben catalysts (see fig. 3.1-4), i.e., the photoadsorption was reversed in the detected layers. But since the photoelectrons from maximal the first four layers are detected (see experimental section), it can not be excluded, that O^- species were still present in the bulk (see also subsection 3.1.2.3).

The peak areas of the Ti 2p, Au 4f and O 1s were calibrated to the peak area of the Ti 2p peak in the redox-conditioned sample of catalyst $Au/TiO_2(8)$; the calibration factors are summarized in table 3.1-2. The peak areas of the C 1s peak were not calibrated with these factors, since the Sachtleben and Degussa samples were measured with different pass energies (see experimental section).

Table 3.1-2: Calibration factors for the XPS peak areas.

Sample	Untreated	Reduction	Redox-conditioning	Calcination
$Au/TiO_2(1)$	2.14	1.66		2.68
$Au/TiO_2(2)$	2.20	3.06		2.41
$Au/TiO_2(4)$	1.22	1.38	1.87	1.34
$Au/TiO_2(5)$	1.13	1.76	2.10	1.20
$Au/TiO_2(6)$	1.01	1.47	2.22	1.20
$Au/TiO_2(7)$	1.43	1.63	1.99	2.67
$Au/TiO_2(8)$	1.01	1.77	1.00	1.22

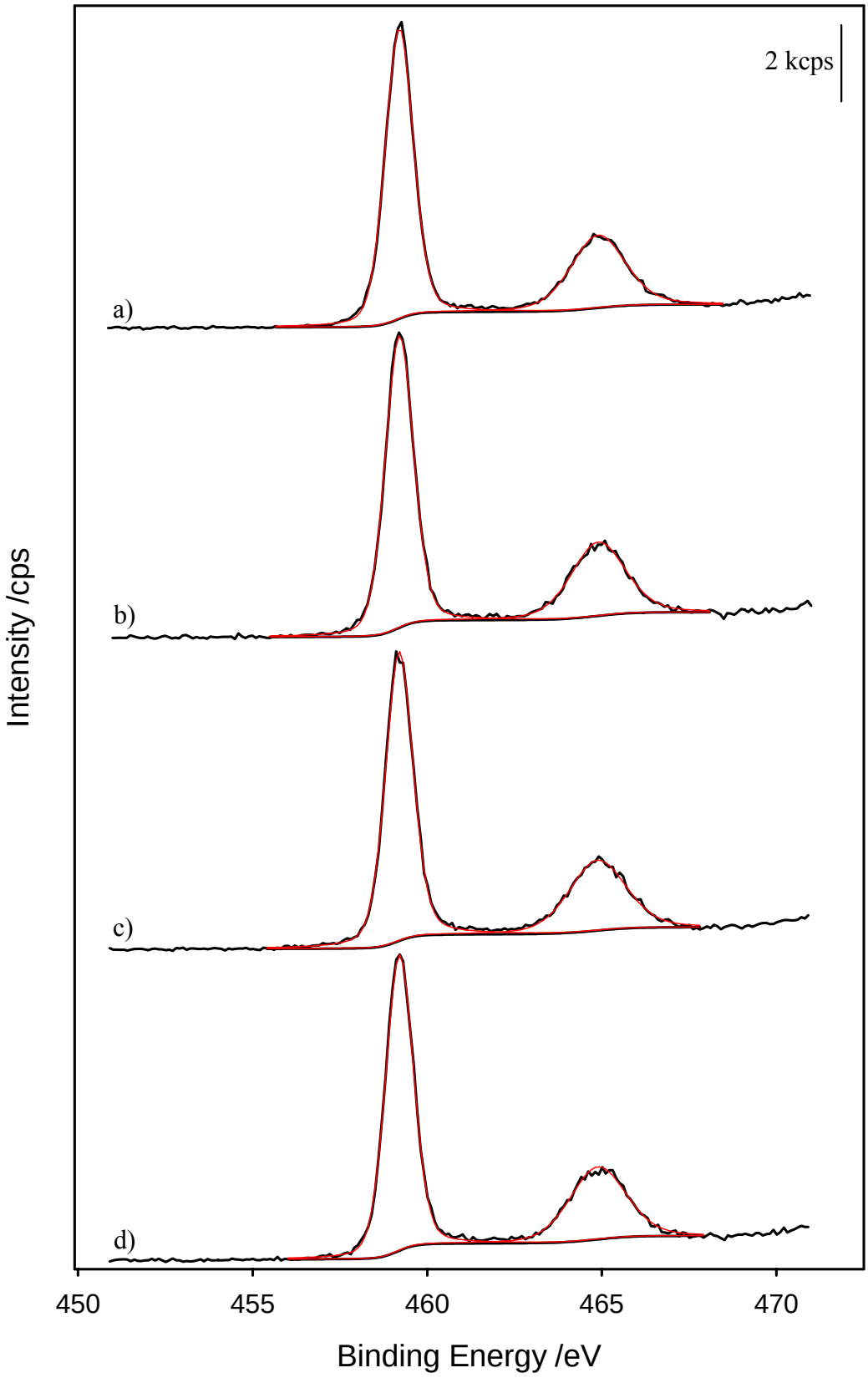

Figure 3.1-4: Ti 2p peaks, Shirley backgrounds and peak fits (red lines) of a) reduced $Au/TiO_2(1)$, b) reduced $Au/TiO_2(2)$, c) calcined $Au/TiO_2(1)$ and d) calcined $Au/TiO_2(2)$. The peak areas are calibrated according to table 3.1-2. Pass energy: 11.75 eV, scanning time: 5.00 min

3.1.2.2 The Au 4f Peak

Au 4f spectra of the Au/TiO_2 catalysts in their *unconditioned state* are presented in fig. 3.1-5. All peaks are very broad and show significantly higher binding energies compared to Au^0 (the position of Au^0 is indicated in the figure with dashed lines). The higher binding energies can be explained by more oxidized species (initial state effect) and by final state effects indicative of very small Au particles. The larger width of the Au 4f peaks reflects either a distribution of particle sizes or different oxidation states. It can not be decided which of the mentioned possibilities is the reason for the larger peak width, since the consequence of the final state effect on small particles of different sizes is unknown. The peaks of the unconditioned samples were not fitted, since they are expected to result from a sequence of peaks with continuously increasing binding energies. The positions of the main peaks vary about 1 eV. This is due to the fact, that these samples are very light sensitive and dependent on the preparation time for the measurement (fixing the samples on the carbon plate and pumping out of the transfer chamber), the samples started to be reduced at the beginning of the XPS measurements. Contrary to the other samples, the unconditioned sample of catalyst $Au/TiO_2(8)$ has a significant contribution with a binding energy of 87-88 eV (depending on the fit parameters), which is separated from the main peak. According to [120] this contribution can be assigned to Au-hydroxide, which is present on the catalysts due to the preparation procedure. Since this contribution is detected for the catalyst with the highest gold loading only, it is tentatively suggested, that Au-hydoxide is more stable, if a higher amount of Au is deposited on the support.

The Au 4f peaks of the *conditioned samples* could be deconvoluted into different contributions, since the particle sizes were ≥ 1.7 nm (see table 3.1-1) and therefore the strength of the final state effect was too low to influence the binding energy in a detectable extent. For background subtraction the Shirley method was used [104,105] and the peaks were fitted with the parameters mentioned in the experimental section. Representative fits obtained on the catalysts after the three different conditioning procedures, respectively, are shown for catalyst $Au/TiO_2(4)$ in fig. 3.1-6.

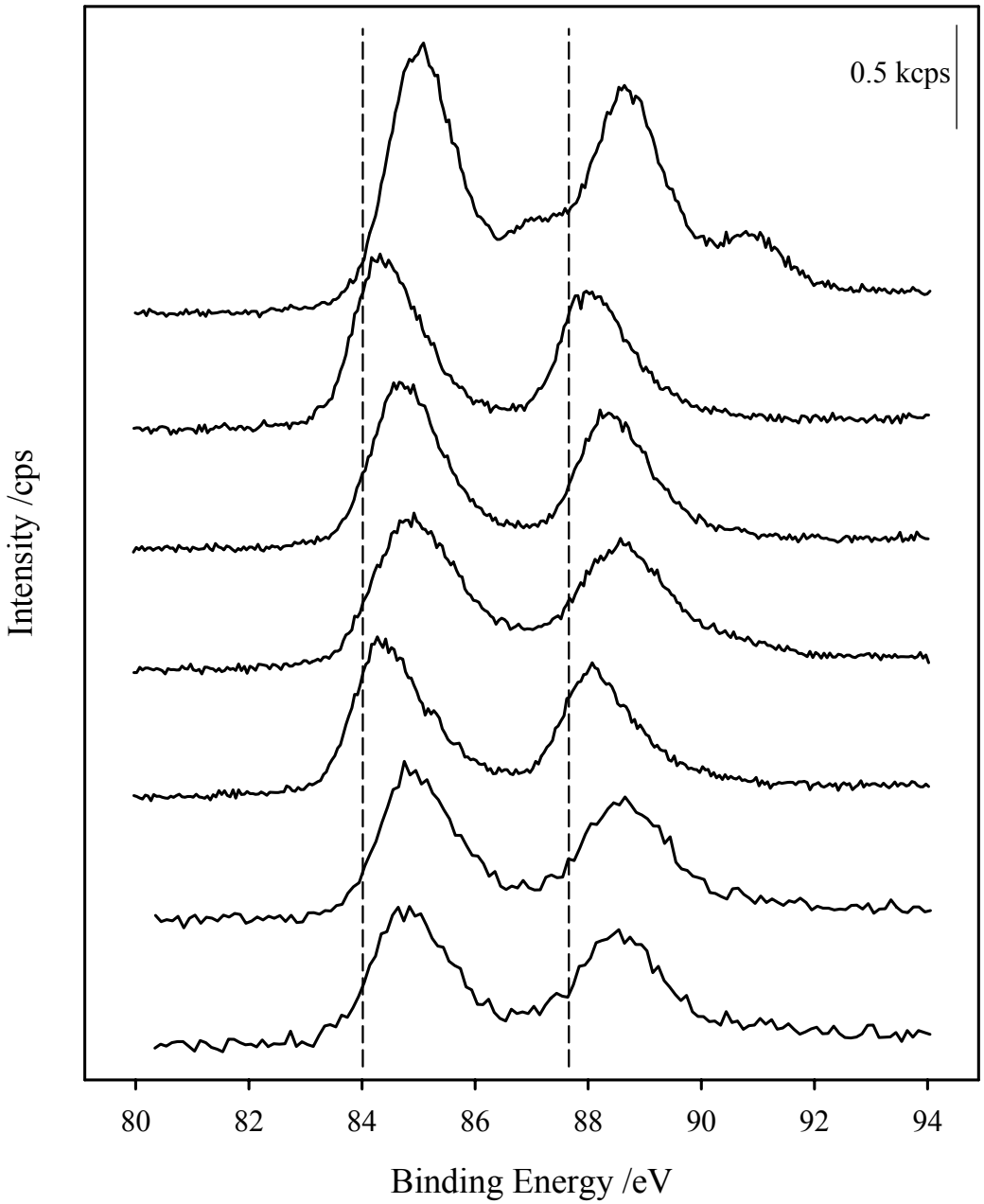

Figure 3.1-5: Au 4f peaks of the untreated catalysts. The spectra are shown from bottom to top for catalyst Au/TiO_2(1), Au/TiO_2(2), Au/TiO_2(4), Au/TiO_2(5), Au/TiO_2(6), Au/TiO_2(7) and Au/TiO_2(8). The peak areas were calibrated according to table 3.1-2. Pass energy for all samples: 11.75 eV, scanning time: for Au/TiO_2(1) and Au/TiO_2(2): 6.67 min, for the other samples: 25 min.

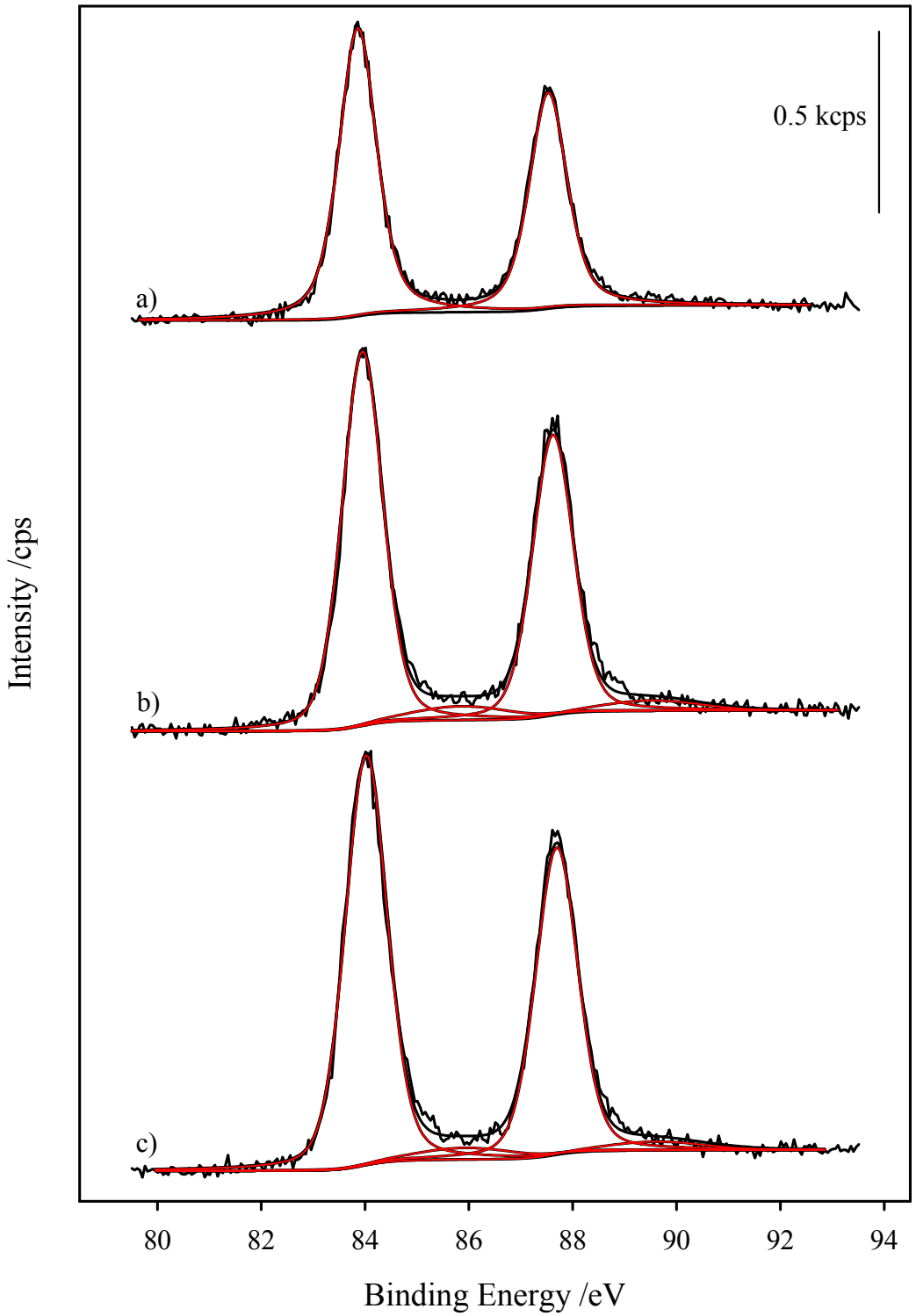

Figure 3.1-6: Au 4f peak of a a) calcined, b) redox-conditioned and c) reduced sample of catalyst $Au/Ti_2(4)$ and the fits for Au^0 and Au^{3+} (red lines). For the calcined sample only Au^0 could be fitted, the redox-conditioned and reduced samples consisted also of a contribution of Au^{3+}-species with a BE shift of 1.9 eV. The peak areas were calibrated according to table 3.1-2. Pass energy: 11.75 eV; scanning time: 25 min.

Since for the other samples the fitting was done equally, for brevity only the raw data peaks are plotted here for the calcined (fig. 3.2-7a), redox-conditioned (fig. 3.1-7b) and reduced (fig. 3.1-7c) samples and the peak positions of Au^0 and Au^{3+} (literature values) are indicated by straight and dashed lines, respectively. The Au 4f peaks including the deconvolution for each sample are shown in Appendix B-I. The calcined samples (fig. 3.1-7a) consist only of metallic Au, with BEs between 83.9 eV and 84.0 eV (see table 3.1-3), which is in good agreement with literature values for bulk Au [7,11,121,122]. Fits with an additional Au^{3+} contribution resulted in a worse modulation of the raw data peak, which justifies the assignment of Au^0 only. From fig. 3.1-7a it is obvious that for catalyst $Au/TiO_2(1)$ the Au $4f_{7/2}$ contribution is too small compared to Au $4f_{5/2}$ (the area ratio Au $4f_{7/2}$:Au $4f_{5/2}$ should be 3:4). This results from the too low scanning times for the measurements on the Sachtleben catalysts $Au/TiO_2(1)$ and $Au/TiO_2(2)$ (see experimental section), and the resulting poor signal to noise ratio. The Au 4f peaks of the redox-conditioned (see fig. 3.1-7b) and reductively (see fig. 3.1-7c) conditioned samples show metallic Au as main component and small contributions of Au^{3+} species. The latter appear at 1.9 eV higher binding energies, at values of 85.7 to 86.0 eV, independent of the conditioning procedure or gold loading. These values agree well with those reported by Holm and Storp [123], Dickenson et al. [124] and Aita et al. [120]. In contrast to the findings here, Soares et al. reported Au^{3+} contributions upon calcination up to temperatures of 450°C for a catalyst prepared via the incipient wetness method, while a similar conditioning procedure resulted in purely metallic Au particles for catalysts prepared via deposition precipitation upon calcination at temperatures of 120°C and higher [122].

The binding energies of the Au^0 and Au^{3+} signals, the Au/Ti intensity ratios (calculated from the peak areas with consideration of the sensitivity factors) and the Au^{3+}/Au^0 intensity ratios for all seven studied catalysts are listed in table 3.1-3. The differences in the Au/Ti ratios between the samples $Au/TiO_2(1)$, $Au/TiO_2(2)$ and the P25 catalysts, especially after calcination result from i) the lower gold loading of catalysts $Au/TiO_2(1)$ and $Au/TiO_2(2)$ and ii) the different scanning times for the detail spectra and the resulting poor signal to noise ratio (see experimental section and the caption of fig. 3.1-7).

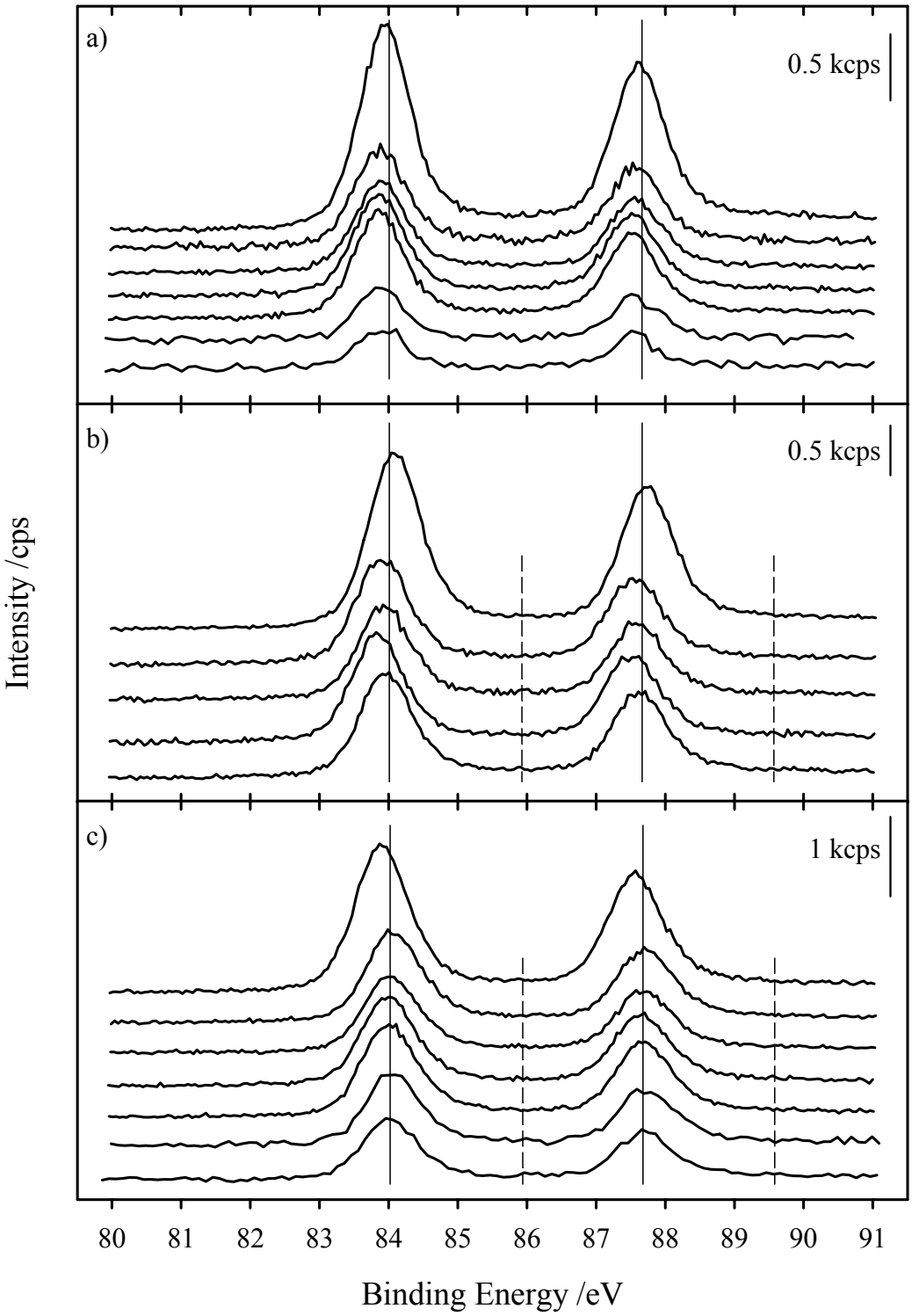

Figure 3.1-7: Au 4f peaks after a) calcination, b) redox-conditioning and c) reduction. The straight lines indicate the literature values of Au^0, the dashed lines of Au^{3+} [123]. For graphs a) and c) from bottom to top the spectra of catalysts Au/TiO_2(1), Au/TiO_2(2), Au/TiO_2(4), Au/TiO_2(5), Au/TiO_2(6), Au/TiO_2(7) and Au/TiO_2(8) are shown. For graph b) from bottom to top the spectra of catalysts Au/TiO_2(4), Au/TiO_2(5), Au/TiO_2(6), Au/TiO_2(7) and Au/TiO_2(8) are shown. The peak areas were calibrated according to table 3.1-2. The deconvolution of the peaks is shown in Appendix B-I. Pass energy for all measurements: 11.75 eV, scanning time: for Au/TiO_2(1) and Au/TiO_2(2): 6.67 min, for the other samples: 25 min.

Table 3.1-3. XPS data of the catalysts after the different conditionings: binding energies of Au $4f_{7/2}$ in different oxidation states. For the Au/Ti fraction sensitivity factors are used.

	Calcination		Redox conditioning				Reduction			
Sample	BE(Au^0) (in eV)	Au/Ti	BE(Au^0) (in eV)	BE(Au^{3+}) (in eV)	Au^{3+}/Au^0	Au/Ti	BE(Au^0) (in eV)	BE(Au^{3+}) (in eV)	Au^{3+}/Au^0	Au/Ti
Au/TiO_2(1)	83.9	0.012	-	-	-	-	84.0	85.9	0.015	0.0401
Au/TiO_2(2)	83.9	0.018	-	-	-	-	84.1	86.0	0.040	0.0509
Au/TiO_2(4)	83.9	0.043	84.0	85.9	0.078	0.059	84.0	85.9	0.058	0.066
Au/TiO_2(5)	83.9	0.043	83.8	85.7	0.069	0.060	84.0	85.9	0.063	0.064
Au/TiO_2(6)	83.9	0.038	83.9	85.8	0.074	0.053	84.0	85.9	0.050	0.054
Au/TiO_2(7)	83.9	0.042	83.9	85.8	0.088	0.061	84.1	86.0	0.075	0.066
Au/TiO_2(8)	84.0	0.083	84.1	86.0	0.051	0.094	83.9	85.8	0.052	0.103

Table 3.1-4. Comparison of Au^{3+}/Au^0 ratios of reductively conditioned catalysts Au/TiO_2(6) and Au/TiO_2(7) after fitting with various parameters.

		Au/TiO_2(6)				Au/TiO_2(7)			
		Au^0 $4f_{7/2}$	Au^0 $4f_{5/2}$	Au^{3+} $4f_{7/2}$	Au^{3+} $4f_{5/2}$	Au^0 $4f_{7/2}$	Au^0 $4f_{5/2}$	Au^{3+} $4f_{7/2}$	Au^{3+} $4f_{5/2}$
• Au^{3+} FWHM fixed • Au^0 and Au^{3+} GL ratio fixed	FWHM / eV	0.96	0.96	2.20	2.20	0.97	0.97	2.20	2.20
	GL ratio / %	26	26	0	0	26	26	0	0
	peak areas / a.u.	731.6	548.7	36.2	27.2	787.0	590.2	58.9	44.2
	Au^{3+}/Au^0-ratio	0.050				0.075			
• Au^{3+} FWHM fixed • Au^0 and Au^{3+} GL ratio not fixed	FWHM / eV	0.96	0.96	2.20	2.20	0.97	0.97	2.20	2.20
	GL ratio / %	28	23	0	0	29	23	21	0
	peak areas / a.u.	731.2	548.4	37.2	27.9	787.4	590.5	62.4	46.8
	Au^{3+}/Au^0-ratio	0.051				0.079			
• Au^{3+} FWHM not fixed • Au^0 and Au^{3+} GL ratio not fixed	FWHM / eV	0.96	0.96	2.23	2.23	0.96	0.96	3.29	3.29
	GL ratio / %	28	23	0	0	28	24	0	0
	peak areas / a.u.	730.9	548.2	33.8	28.2	770.1	577.6	81.1	60.9
	Au^{3+}/Au^0-ratio	0.046				0.105			

For all catalysts the Au/Ti ratios are smaller after calcination than after the other two conditioning procedures, which agrees well with the bigger gold particles in these catalysts. Likewise, the small intensity differences between the redox-conditioned and the reduced samples for the Degussa catalysts are consistent with the similar particle sizes determined with TEM after these conditioning procedures (see table 3.1-1). The high reproducibility of the preparation of the P25 catalysts is indicated by the constant Au/Ti ratios of the different catalyst samples for each conditioning procedure and shown beneath in the presentation of the activity measurements (section 3.2.1.2). The variation between the samples with similar Au loading (catalysts Au/TiO_2(4), Au/TiO_2(5), Au/TiO_2(6), Au/TiO_2(7)), are very small.

The Au^{3+}/Au^0 ratio (see table 3.1-3) is not as constant as the Au/Ti ratio. Here the variation between the values is two to five times as higher than in the Au/Ti ratios. Since the value of the Au^{3+}/Au^0 ratio is very sensitive on the peak-fit parameters, the information value of these peak-fits is considered. The Lorenz-Gauss (GL) ratios and the FWHM were fixed for the peak-fits of the Au^{3+} species (for the Au^0 component fixing of the FWHM was not necessary, since the values varied only in the range of 0.8 to 1.0 eV). Table 3.1-4 shows exemplary for the reductively conditioned samples of catalysts Au/TiO_2(6) and Au/TiO_2(7), how the peak areas and Au^{3+}/Au^0 ratios vary, if i) the Lorenz-Gauss-ratios and ii) the Au^{3+} FWHM are not fixed. These two examples were chosen to show, that a modification of the parameters can result in very small (Au/TiO_2(6)) or significant changes (Au/TiO_2(7)). For catalyst Au/TiO_2(6) the Au^{3+}/Au^0 ratio remains 0.05 for all three fitting procedures, while it is 40 % bigger for catalyst Au/TiO_2(7), if FWHM and GL ratio are not fixed. Furthermore, if the FWHM of Au^{3+} is not fixed, a peak width of 3.3 eV results for catalyst Au/TiO_2(7), while for the other catalysts this value spreads from 2.2 to 3.9 eV. Since there is no logical explanation, why equal species should have different peak widths in different samples, the fixing of this parameter is justified.

The standard deviations of the Au^{3+}/Au^0 ratios for the reduced and redox-conditioned catalysts for a) each sample after the different deconvolution procedures and b) the Degussa catalysts after the particular deconvolution procedures are summarized in table 3.1-5. (The Sachtleben catalysts are excluded from the second calculation, since the significantly different physical properties of these catalysts (different support and activity behavior) would falsify this consideration.) Fixed FWHM and GL ratios of the Au^{3+} species lead to a significantly

lower standard deviation, than the other two fitting procedures (table 3.1-5). Furthermore, for redox-conditioning the standard deviation of all samples except for $Au/TiO_2(6)$ is bigger than the standard deviation of all samples calculated from the fits with fixed parameters (bold in table 3.1-5). After reduction catalyst $Au/TiO_2(8)$ has a bigger value. For these two cases the Au^{3+}/Au^0 ratios of the other fitting procedures have to be considered additionally, before conclusions can be drawn.

Table 3.1-5: a) Standard deviations of the Au^{3+}/Au^0 ratios of redox-conditioned and reduced catalysts calculated from the results of the three fitting procedures. b) Standard deviation of the Au^{3+}/Au^0 ratios of the five Degussa catalysts after the particular deconvolution procedures.

		Standard deviation after	
		Redox-conditioning	Reduction
a)	$Au/TiO_2(1)$	-	0.0036
	$Au/TiO_2(2)$	-	0.0081
	$Au/TiO_2(4)$	0.0202	0.0039
	$Au/TiO_2(5)$	0.0173	0.0122
	$Au/TiO_2(6)$	0.0062	0.0023
	$Au/TiO_2(7)$	0.0350	0.0165
	$Au/TiO_2(8)$	0.0170	0.0773
b)	Degussa catalysts ($Au/TiO_2(4)$-$Au/TiO_2(8)$)		
	• Au^{3+} FWHM fixed • Au^0 and Au^{3+} GL ratio fixed	**0.0133**	**0.0193**
	• Au^{3+} FWHM fixed • Au^0 and Au^{3+} GL ratio not fixed	0.0205	0.0756
	• Au^{3+} FWHM not fixed • Au^0 and Au^{3+} GL ratio not fixed	0.0291	0.0749

After reduction the higher loading catalyst of the Degussa samples, $Au/TiO_2(8)$, has a higher relative intensity of the Au^{3+} species than the other catalysts, indicating that reduction is adversely affected by the higher Au content (table 3.1-3, for the other two fitting procedures the Au^{3+}/Au^0 ratio is even higher (0.231 and 0.235)). After redox-conditioning the Au^{3+} content is significantly lowered for catalyst $Au/TiO_2(8)$, (the values are 0.063 and 0.084 for the other two fitting procedures, respectively), which must originate in thermal decomposition during the oxidation step since the presence of oxygen should enhance the content of the Au^{3+} species. In contrast to catalyst $Au/TiO_2(8)$, a very slight reoxidation during redox-

conditioning can be observed for the lower loading catalysts. Catalyst Au/TiO_2(1) has a significantly lower Au^{3+} content than the Degussa catalysts after reductive conditioning (see also the fitted peaks in Appendix B-I).

3.1.2.3 The O 1s Peak

XPS spectra of the O 1s peak of catalyst Au/TiO_2(4) in its unconditioned state and after the three conditioning procedures are shown in fig. 3.1-8. Clearly, neither the position nor the intensity of the peaks show any significant effects imposed by the conditioning procedures. For all samples the O 1s contribution resulting from TiO_2 (red lines in fig. 3.1-8) can be fitted with a peak with constant width (FWHM 1.1 eV). The binding energies for this O 1s species, which are between 530.4 and 530.5 eV and the resulting O/Ti ratios for all catalysts in their unconditioned and conditioned states are listed in table 3.1-6. The binding energy agrees well with data on TiO_2 (rutile) from Dupin et al. [125], who reported a main O 1s peak at 530.0 eV. Taking into account that they reported a binding energy of 458.7 eV for the corresponding Ti $2p_{3/2}$ peak, which is 0.5 eV lower than the reference value used here, their data fit excellently to the results reported here. Additionally the assignment of the main O 1s contribution is supported by the O_{TiO2}/Ti ratios, which are close to 2, as expected from the stoichiometry of TiO_2 (see table 3.1-6).

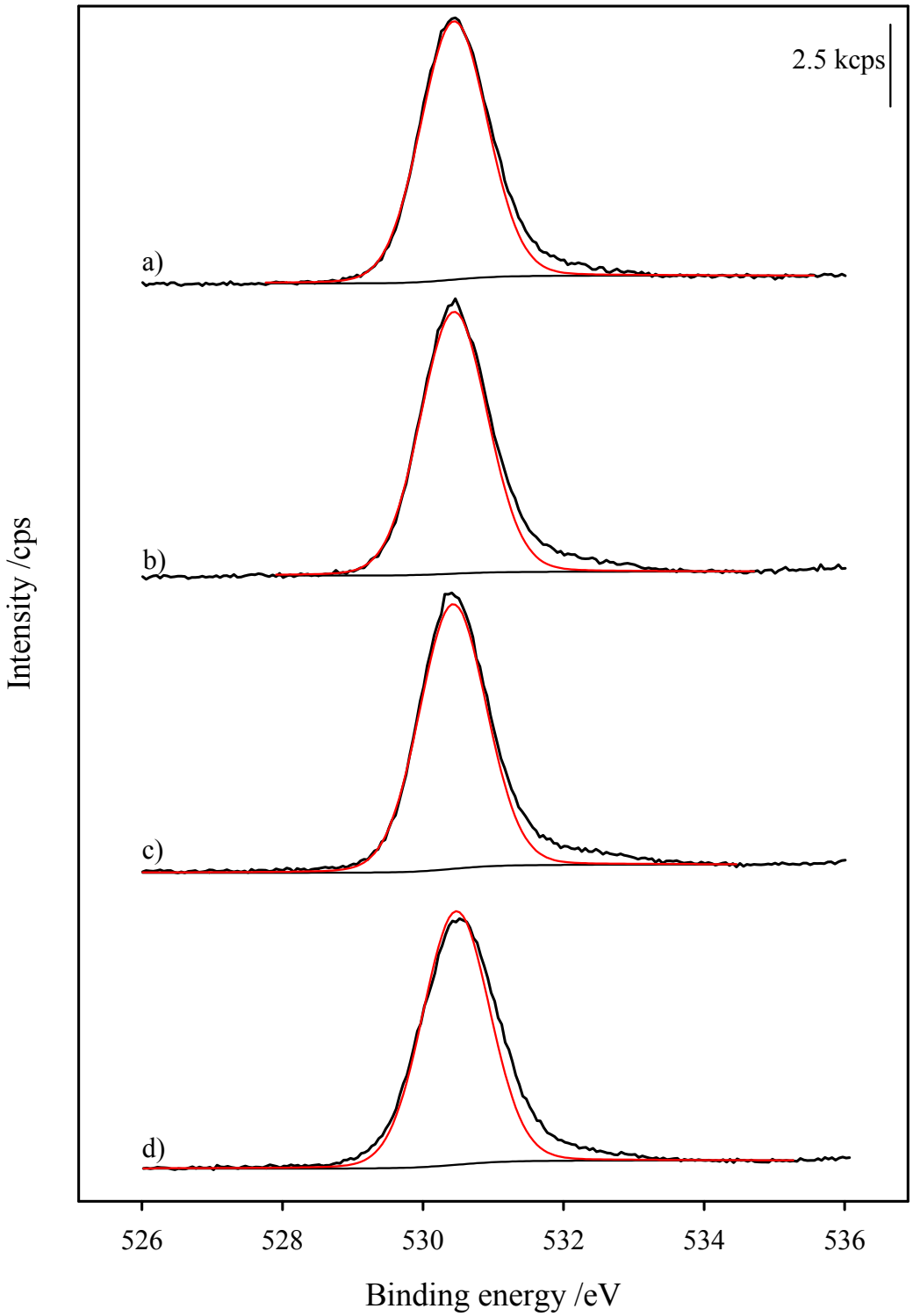

Figure 3.1-8: O 1s spectra of catalyst Au/TiO_2(4) after a) calcination, b) redox-conditioning, c) reduction and d) in untreated state. The fits for the TiO_2 contribution is given in red lines. The peak areas were calibrated according to table 3.1-2. Pass energy: 11.75 eV, scanning time: 10.00 min.

Beside the main contribution Dupin et al. detected a shoulder at a high binding energy (531.8 eV, corrected value 532.3 eV), which contributes about 13% to the total intensity. It was assigned to weakly adsorbed species or to subsurface oxygen. The subsurface oxygen has

a lower electron density than the O^{2-} ions of the crystalline network and can be described as O^- species [125]. The spectra in fig. 3.1-8 also show a shoulder at similar, higher binding energies (beneath denoted as higher binding energy shoulder). Beside Dupin et al.'s assignment of subsurface oxygen, the following sources for this shoulder have to be considered: i) O^- and O_3^- species can be formed by photoadsorption of oxygen (see subsection 3.1.2.1; the XPS experiments, especially the sample preparation could not be performed with complete absence of light), ii) surface hydroxyl groups, which were observed even after conditioning at 400°C with DRFITS; a similar behavior was reported also by Martra [126] and iii) carbonate species, which begin to form on the samples as soon as they are exposed to a CO_2 containing atmosphere, e.g., during transport through air. This carbonate contamination could be detected with XPS. The C 1s peaks of unconditioned catalysts $Au/TiO_2(1)$ and $Au/TiO_2(2)$ and a calcined sample of catalyst $Au/TiO_2(4)$ are presented in (fig. 3.1-9). In all three samples a contribution with binding energies of 289.2 to 289.4 eV appeared (plotted with red lines in fig. 3.1-9), which can be assigned to carbonates [127,128].

For the calcined, reduced and redox-conditioned samples the higher binding energy O 1s shoulder contributes 8-13% of the total peak (calculated from its peak area divided by the total peak area), except for the redox-conditioned catalyst $Au/TiO_2(5)$, whose shoulder takes 27% of the total peak. In the untreated samples this contribution occupies 11 to 22% of the total peak intensity, except for catalyst $Au/TiO_2(1)$ with 30%. In order to estimate the surface contamination with the species, which cause the higher binding energy shoulder, the detection depth of maximal four layers is laid down (see experimental section). If the simplifying assumption is made, that each layer contributes the same fraction to the O $1s_{TiO2}$ signal, for a 90%-content of the TiO_2-O 1s signal, each layer contributes 22.5%. Relating the 10% contribution of the shoulder to this value, 44.4% of the surface oxygen atoms are covered with contaminations. Hence, if the TiO_2 stoichiometry is laid down, ~30% of the surface is covered with the contaminating species. The same calculation for a 30% contribution of the higher binding energy shoulder results in a surface coverage of the contaminating species of ~80%.

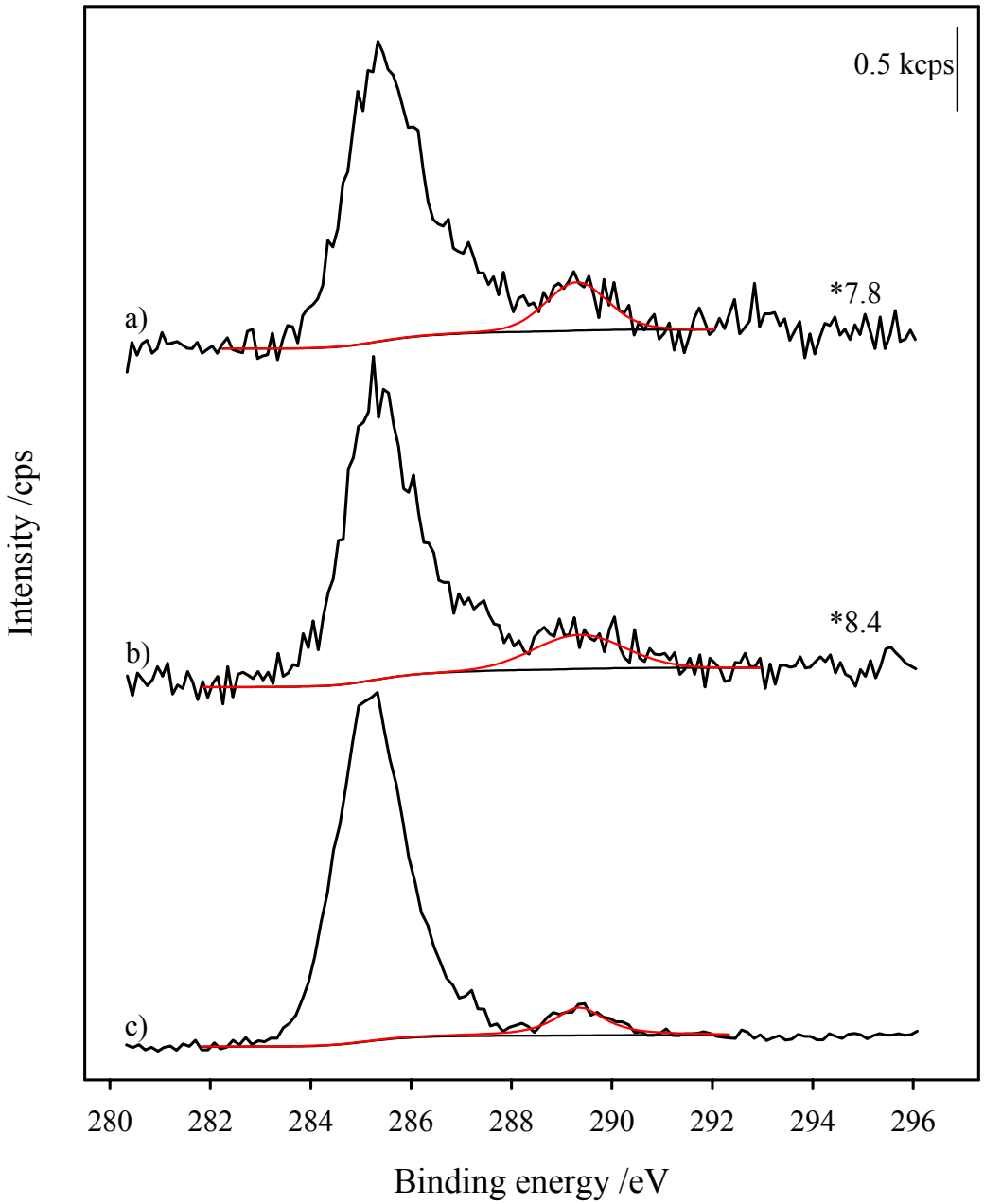

Figure 3.1-9: C 1s spectra of a) untreated catalyst Au/TiO_2(1), b) untreated catalyst Au/TiO_2(2) and c) calcined catalyst Au/TiO_2(4). The fits for the carbonate contribution is given in red lines. Pass energies: samples a) and b): 11.75 eV, sample c) 29.35 eV. Scanning times: samples a) and b): 6.68 min, sample c): 4.03 min.

The difference between the two Sachtleben catalysts is noticable: While for catalyst Au/TiO_2(1) the higher binding energy shoulder contributes 30% of the peak intensity, its fraction is only 19% for catalyst Au/TiO_2(2). This higher amount in catalyst Au/TiO_2(1) correlates with the Ti 2p peak (see fig. 3.1-3), where a higher amount of an additional contribution could be observed. It was suggested in subsection 3.1.2.1, that this contribution is caused by photoadsorption of oxygen. As mentioned above, the products of this

photoadsorption, O^- and O_3^-, can also contribute to the higher binding energy shoulder. We assume that the additional amount of the high binding energy soulder in the $Au/TiO_2(1)$ sample is caused by the higher amount of these species. This assumption is approved by the finding, that in the conditioned Sachtleben samples only Ti^{4+} from TiO_2 could be detected (see fig. 3.1-4) and the contribution of the higher binding energy shoulder in the O 1s spectra of both catalysts are similar (see table 3.1-6). As already mentioned in subsection 3.1.2.1, the absence of O^- species can not be concluded from this result, since only maximal the first four layers are detected with XPS. Hence, after conditioning the electronic structure of some Ti and O atoms in the bulk of the Sachtleben catalysts can still be modified and it can not be excluded that during reaction these 'defects' migrate to the surface [68] and influence the activity of the catalysts.

Beside Au^0 also Au^{3+}-species were present in the reduced and redox-conditioned samples (subsection 3.1.2.2). If the Au^{3+} contribution originated in Au_2O_3, a O 1s contribution at 530.2 -530.4 eV should be visible [129]. This is inside the binding energy range, where the TiO_2 contribution of the O 1s peak is located [130] (see fig. 3.1-6). Calculations of the areas of Au 4f and O 1s show, that the Au_2O_3 contribution would occupy only ~0.2 % of the O 1s peak area. Since this low amount of Au_2O_3 besides the big amount of TiO_2 can not be fitted, the presence of Au_2O_3 species can only be concluded from the Au 4f spectra.

Table 3.1-6: XPS data of the catalysts untreated and after the different conditionings: binding energies of O 1s of the TiO oxygen. For the O/Ti fractions sensitivity factores are used.

	Calcination			Redox conditioning			Reduction			Untreated		
Sample	BE [eV] O-TiO_2	O_{TiO2}/Ti	O_{tot}/Ti	BE [eV] O-TiO_2	O_{TiO2}/Ti	O_{tot}/Ti	BE [eV] O-TiO_2	O_{TiO2}/Ti	O_{tot}/Ti	BE [eV] O-TiO_2	O_{TiO2}/Ti	O_{tot}/Ti
Au/TiO_2(1)	530.4	1.94	2.14	-	-	-	530.4	2.01	2.23	530.4	1.90	2.72
Au/TiO_2(2)	530.4	2.11	2.33	-	-	-	530.4	2.09	2.37	530.4	1.94	2.39
Au/TiO_2(4)	530.4	1.96	2.13	530.4	1.99	2.21	530.4	2.01	2.32	530.5	1.93	2.17
Au/TiO_2(5)	530.5	2.01	2.20	530.5	1.98	2.70	530.5	2.05	2.24	530.4	1.79	2.30
Au/TiO_2(6)	530.5	1.97	2.14	530.4	2.01	2.25	530.5	2.04	2.35	530.4	2.00	2.28
Au/TiO_2(7)	530.4	1.98	2.19	530.4	1.96	2.23	530.4	2.05	2.23	530.4	1.99	2.25
Au/TiO_2(8)	530.4	2.00	2.23	530.4	2.04	2.23	530.5	2.00	2.28	530.4	1.94	2.38

The catalyst characterization unraveled a dependence of the physical properties on the conditioning procedure. It was shown, that the Au particle size is ~3 nm after calcination at 400°C, while after reduction at 200°C and redox-conditioning at 200°C and 300°C particles sizes of ~2 nm were observed, respectively. The increase of gold particle sizes with higher conditioning temperature goes along with smaller Au/Ti ratios detected with XPS. Higher gold loadings did not induce changes in the gold particle sizes. The XPS study of untreated and conditioned samples showed a reduction of the gold during all three conditioning procedures. While after calcination the gold is entirely reduced to metallic gold, residual Au^{3+} species could be detected after the other two conditioning procedures. In contrast to the particle sizes, the Au^{3+} content depended on the gold loading. After reductive conditioning the higher loading catalyst contained a significantly higher Au^{3+} amount. Part of the Au^{3+} is thermally decomposed during the oxidation step of the redox-conditioning. Contrary to the high loading catalyst, the Au^{3+} content was slightly enhanced by the oxidation step of the redox-conditioning in the lower loading catalysts. It could be shown, that the main fraction of detected oxygen belongs to TiO_2, while a smaller part belongs to oxygen containing impurities, which cover 30 to 80% of the surface. OH-groups, which could be detected by DRIFTS, and carbonates, whose characteristic signal appeared in the XPS spectra, could be identified as impurities. Furthermore, a contamination by O^-/O^{3-} species, which are produced by photoadsorption of oxygen, was concluded for the untreated Sachtleben samples from a correlation of Ti 2p and O 1s contributions, which do not originate in TiO_2. The reason for the photoadsorption of oxygen was the storage of the photoactive Sachtleben TiO_2 powder in a translucent box. Although these impurities could not be detected on the calcined and reductively conditioned samples, their absence in the bulk TiO_2 could not be concluded, since XPS is a surface sensitive technique. It was suggested that the photoadsorption of oxygen and the resulting non reproducible modification of the electronic properties of the TiO_2 powder were the origin for the significant differences in activity of the Sachtleben catalysts, which will be demonstrated in the following chapter. This theory is supported by the absence of the above mentioned Ti 2p-contributions in all Degussa samples and the well reproducible activity of these catalysts (see next chapter).

3.2 CO oxidation in H_2-rich and H_2-free atmosphere

As mentioned in the introduction, Au/TiO_2 catalysts are highly active for the CO oxidation [4-7], even at temperatures as low as 90K [9]. For 90K only the qualitative statement of an occurring reaction can be made without the knowledge of reaction rates, since the cited publication discusses a FTIR study, in which a CO_2 signal can be observed in the same size scale as adsorbed CO. Au/TiO_2 catalysts are active in the temperature range of 80-100°C, which could make them attractive for the clean-up of reformer gas from CO impurities in feed streams for polymer membrane (PEM) fuel cells [16,131]. For this reason reaction rates of the CO oxidation on Au/TiO_2 samples was determined in H_2-free (1 kPa CO, 1 kPa O_2, balance N_2) and H_2-rich atmosphere (1 kPa CO, 1 kPa O_2, 75 kPa H_2, balance N_2) at 80°C (section 3.2.1). The TOF rates presented in this chapter were calculated based on the particle sizes determined after conditioning (see table 3.1-1) and with the assumption that the particle sizes do not change during reaction. In H_2-rich atmosphere additionally the selectivity in respect of the CO oxidation (side reaction: H_2 oxidation) was studied (section 3.2.2). The evolution of surface species developing during reaction in the two different atmospheres, were studied by DRITFS, both on a Sachtleben ($Au/TiO_2(1)$) and a Deguassa catalyst ($Au/TiO_2(5)$). The results are presented in section 3.2.3. For clarity, the sections are divided into subsections, dealing with the results of the Sachtleben ($Au/TiO_2(1)$ to $Au/TiO_2(3)$) and Degussa catalysts ($Au/TiO_2(4)$ to $Au/TiO_2(8)$), respectively.

3.2.1 Activity measurements

3.2.1.1 Sachtleben catalysts

For this set of catalysts three different conditioning procedures were applied, i) calcination at 400°C, ii) a reductive conditioning at 200°C iii) drying at 120°C in N_2 over night. The activities of the differently conditioned samples of $Au/TiO_2(1)$ for CO oxidation in H_2-rich gas mixture (1 kPa CO, 1 kPa O_2, 75 kPa H_2, balance N_2) are plotted in fig. 3.2-1. Turnover frequencies (TOFs) were calculated from Au mass-specific rates using the average particle size. The reductively conditioned $Au/TiO_2(1)$ catalyst with Au particle sizes of about 1.7 nm shows a significantly higher rate and also higher TOF numbers than the calcined sample with particle sizes about 2.5 nm to 3 nm, contrasting the results reported in refs. [4,10,36,62], where samples with the latter particle sizes were found to be most active. Chemical effects as source of the higher reaction rates of the reduced sample appear unlikely because of the

similar composition of the reduced and calcined samples, respectively, as detected by XPS (due to table 3.1-3, the calcined sample consists only of metallic gold and 1.5% of the gold in the reduced sample is ionic, which is a much lower content than in the Degussa catalysts). Hence, the significantly higher activity of the reduced catalyst compared to the calcined sample (see fig. 3.2-1) have to originate in the much smaller particle sizes of the reduced samples (see table 3.1-1).

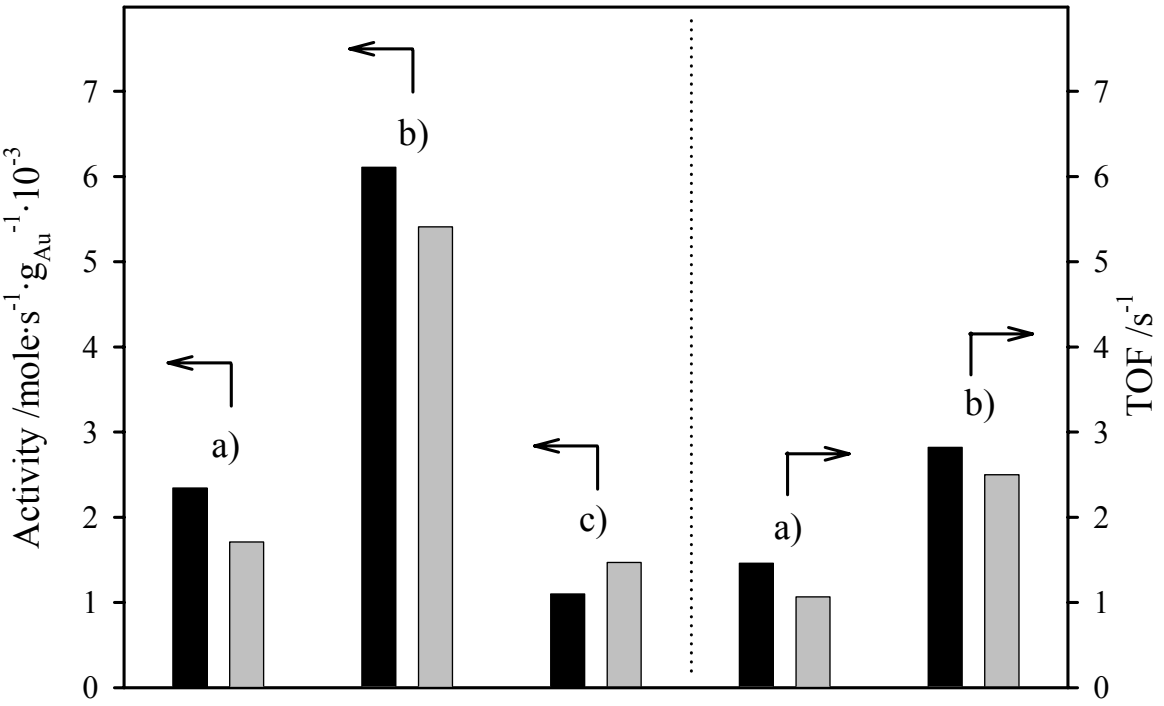

Figure 3.2-1: Rates (left axis) and TOFs (right axis) for the CO oxidation in idealized reformer gas (1 kPa CO, 1 kPa O_2, 75 kPa H_2, balance N_2) at 80°C after 17 min (black bars) and after 85 min (grey bars) on differently treated Au/TiO_2(1). a) After calcination at 400°C, b) after reductive conditioning at 200°C in H_2/N_2, c) after drying in N_2 over night at 120°C. For experimental conditions see Appendix B II.

For a comparison of the reaction rates with the activities of highly active Au catalysts reported in the literature (see, e.g. ref. [4] and values given therein), one has to correct the differences in temperature. This is done here using an average activation energy of 30 kJ/mol. Taking this correction and comparable experimental conditions (preparation via deposition precipitation, calcination at 400°C prior the CO oxidation, reaction in a plug flow reactor) into account, the activity of the calcined catalysts is comparable to the activities reported there. The activity of the reduced catalyst is at least by a factor of two higher than those values. It has to be mentioned, that the significant higher activity of the reduced samples was not observed for the Degussa catalysts (see subsection 3.2.1.2).

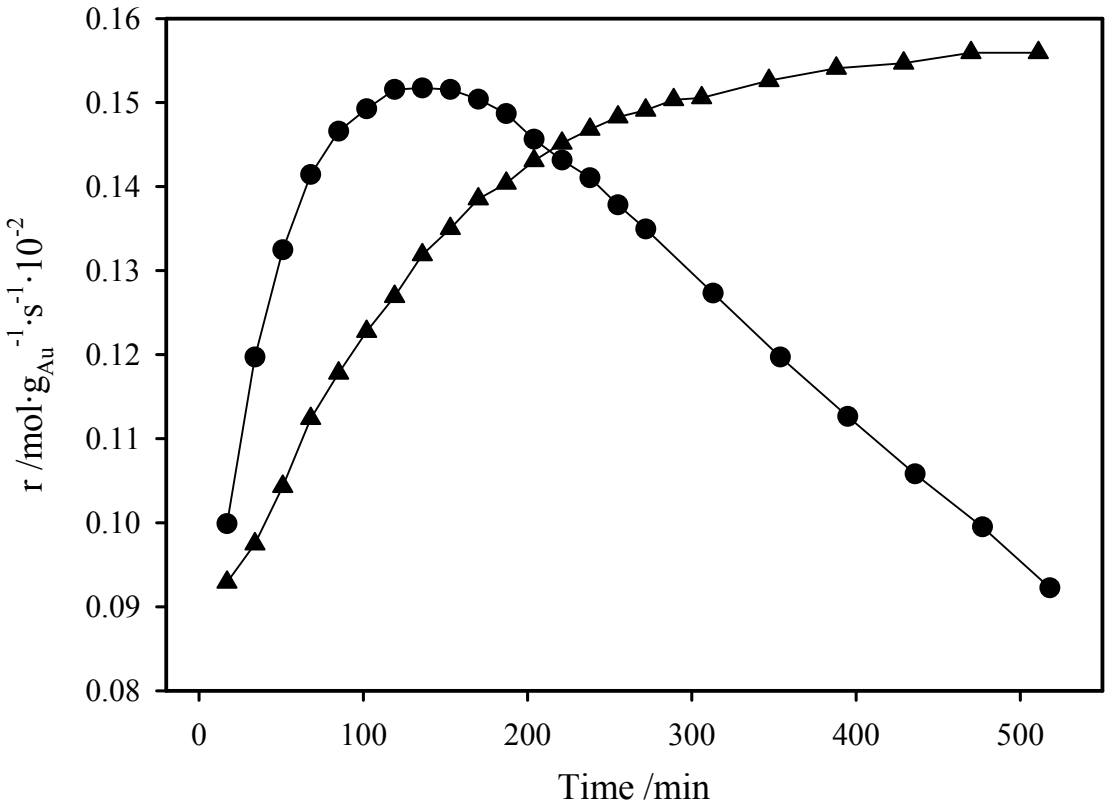

Figure 3.2-2: Activation of catalyst $Au/TiO_2(1)$ after drying at 120°C in N_2 in (●) H_2-rich (1 kPa CO, 1 kPa O_2, 75 kPa H_2, balance N_2, filled symbols) and (▲) H_2-free (1 kPa CO, 1 kPa O_2, balance N_2, empty symbol) atmosphere. Note that the reaction rates were multiplied with a factor of 100. For experimental conditions see Appendix B II.

The lowest mass specific activity after the three conditioning procedures is found for the dried catalyst (see fig. 3.2-1). Since both, TEM imaging and XRD did not resolve Au particles, only mass specific rates are available in this case. In contrast to the other samples, an increase of activity for this sample during the first 2 h on steam (1 kPa CO, 1 kPa O_2, 75 kPa H_2, balance N_2) was observed. We assume that this increase in activity goes along with a reduction of the gold by H_2 and CO. This is supported by the findings in H_2-free atmosphere (1 kPa CO, 1 kPa O_2, balance N_2). Compared to H_2-rich atmosphere, the activity after 17 min of reaction is about equal and the activation leads to about the same rates, but the activation is significantly slower (see fig 3.2-2, the first data points were recorded after 17min of reaction, why the rates are not exactly equal, since the differently fast reduction had already started). Activation by reduction of the gold species was also reported by Schröder's group, who detected increasing reaction rates when introducing a reactive atmosphere (20% O_2, 1% CO, balance He) to untreated Au/TiO_2 catalysts (prepared via deposition precipitation on Degussa P25, 0.09-0.63 wt.-% Au) in the temperature range 50-80°C [132,133]. By in-situ XAS studies they detected the reduction of Au^{3+} species, to metallic gold parallel to the increasing reaction

rates. Similar effects were also discovered by Daté et al. [84], who found that leaving a low-temperature conditioned Au/TiO_2 sample in the reactor for a few days increases the activity.

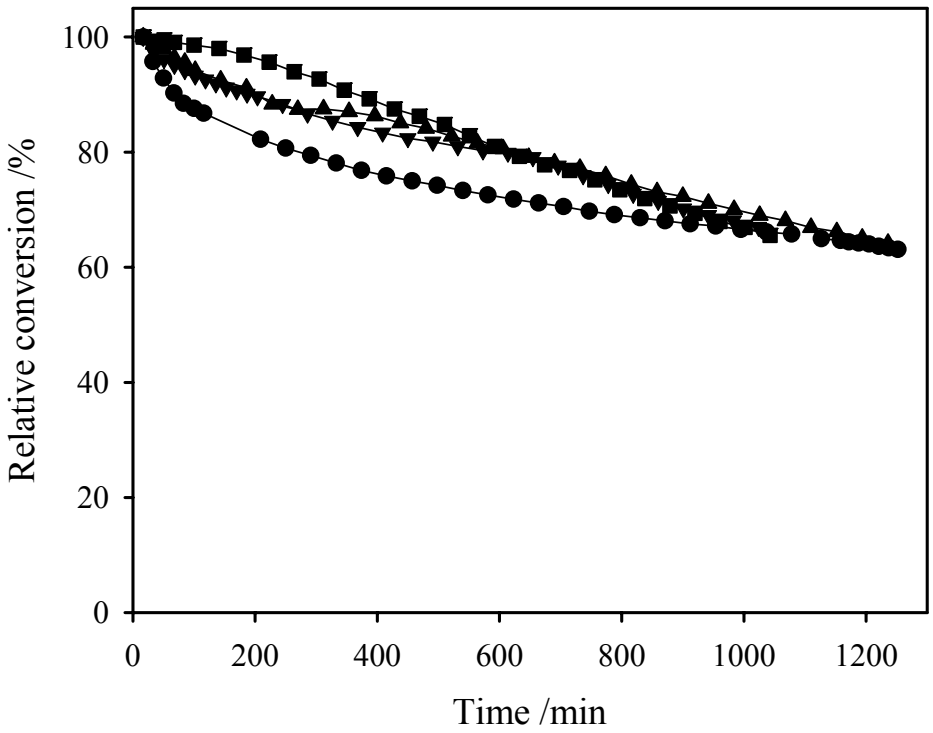

Figure 3.2-3: Relative deactivation during CO oxidation on the Sachtleben catalysts. ▼: $Au/TiO_2(1)$, H_2-free atmosphere (1 kPa CO, 1 kPa O_2, balance N_2); ▲: $Au/TiO_2(1)$, H_2-rich atmosphere (1 kPa CO, 1 kPa O_2, 75 kPa H_2, balance N_2); ■: $Au/TiO_2(2)$, H_2-rich atmosphere; ●: $Au/TiO_2(3)$, H_2-rich atmosphere (initial conversion: 41.0%). All conversions are normalized to an initial value of 100%. For experimental conditions see Appendix B II.

The long-term stability of the three Sachtleben catalysts was evaluated by following their activity over 1200 min (fig. 3.2-3). For better comparison all curves were normalized to an initial conversion of 100% independent of their absolute conversions. The general deactivation behavior is identical for all three samples. A strong decrease of the activity at the beginning of the reaction is followed by a stabilization in the later stages (1000 min). A similar behavior was observed also for other Au/MeO_x catalysts [33]. The absolute deactivation of Au/α-Fe_2O_3, Au/CeO_2 and Au/TiO_2 in this publication is comparable to the samples presented here. Au/Ni_2O_3, Au/MgO and Au/SnO_2 deactivated much stronger (maximal deactivation to 9.9% of the initial activity), Au/MnO_2 and Au/γ-Al_2O_3, had a completely different temporal activity behavior. Because of the potential application of Au/TiO_2 catalysts for the removal of CO from H_2-rich reformer gas in PEM fuel cell feed streams, the deactivation behavior was investigated in a H_2-rich atmosphere (1 kPa CO, 1 kPa O_2, 75 kPa H_2, rest N_2) for all catalyst and only for $Au/TiO_2(1)$ additionally in H_2-free

atmosphere. As evident from fig. 3.2-3 there is no significant effect of the gas composition or the catalyst preparation on the deactivation behavior.

Although the Sachtleben catalysts did not show significant differences in the deactivation behavior, the absolute activity of the Sachtleben catalysts had a poor reproducibility (fig. 3.2-4). The activity of catalyst $Au/TiO_2(2)$ is about 400% of that of catalyst $Au/TiO_2(1)$, which has the same loading. In contrast $Au/TiO_2(1)$ and $Au/TiO_2(3)$ have different gold loadings, but exhibit similar reaction rates. As demonstrated in section 3.1-2, the translucent storage of the Sachtleben TiO_2 powder resulted in irreproducible electronic properties of O and Ti. We assume that this is the reason for the strong variations of the reaction rates. Hence, the Degussa catalysts, whose activity will be discussed in the following subsection, were prepared from TiO_2 powder stored in an opaque box.

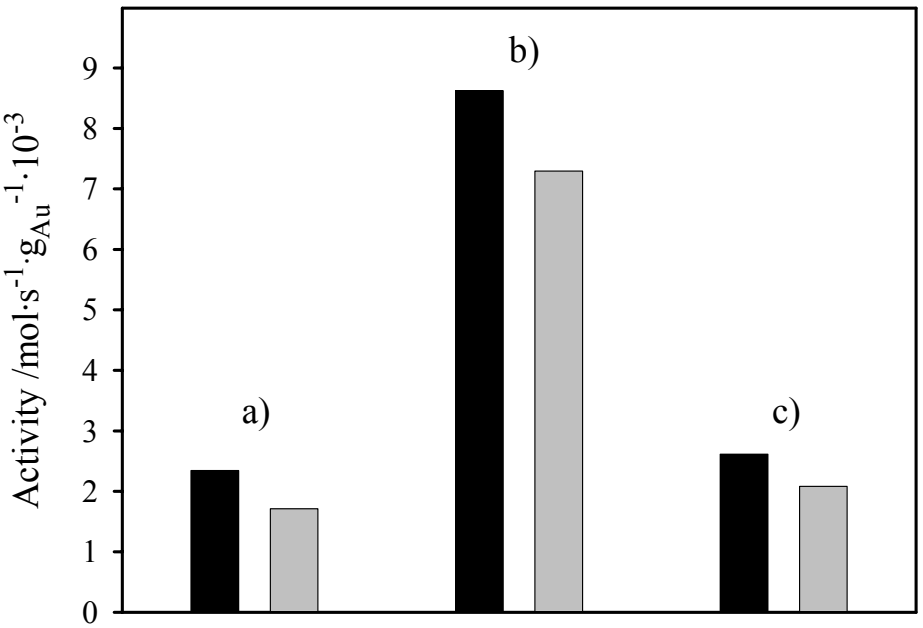

Figure 3.2-4: Activity of the Sachtleben catalysts a) $Au/TiO_2(1)$, b) $Au/TiO_2(2)$ and c) $Au/TiO_2(3)$ after calcination at 400°C in 10% O_2/N_2 for 30 min in H-rich atmosphere (1 kPa CO, 1 kPa O_2, 75 kPa H_2, rest N_2). Since $Au/TiO_2(1)$ and $Au/TiO_2(2)$ have the same gold loading (2.4 wt.-%), the poor reproducibility of the activity of the Sachtleben catalysts is obvious. For experimental conditions see Appendix B II.

3.2.1.2 Degussa catalysts

In order to test the reproducibility of the Au/TiO_2 preparation procedure, a set of Degussa catalyst was prepared with four samples with similar gold loadings and one sample with a higher loading. Similar as before, two conditioning procedures, calcination at 400°C and reduction at 200°C, were tested for both, operation in H_2-rich and H_2-free atmosphere (fig. 3.2-5).

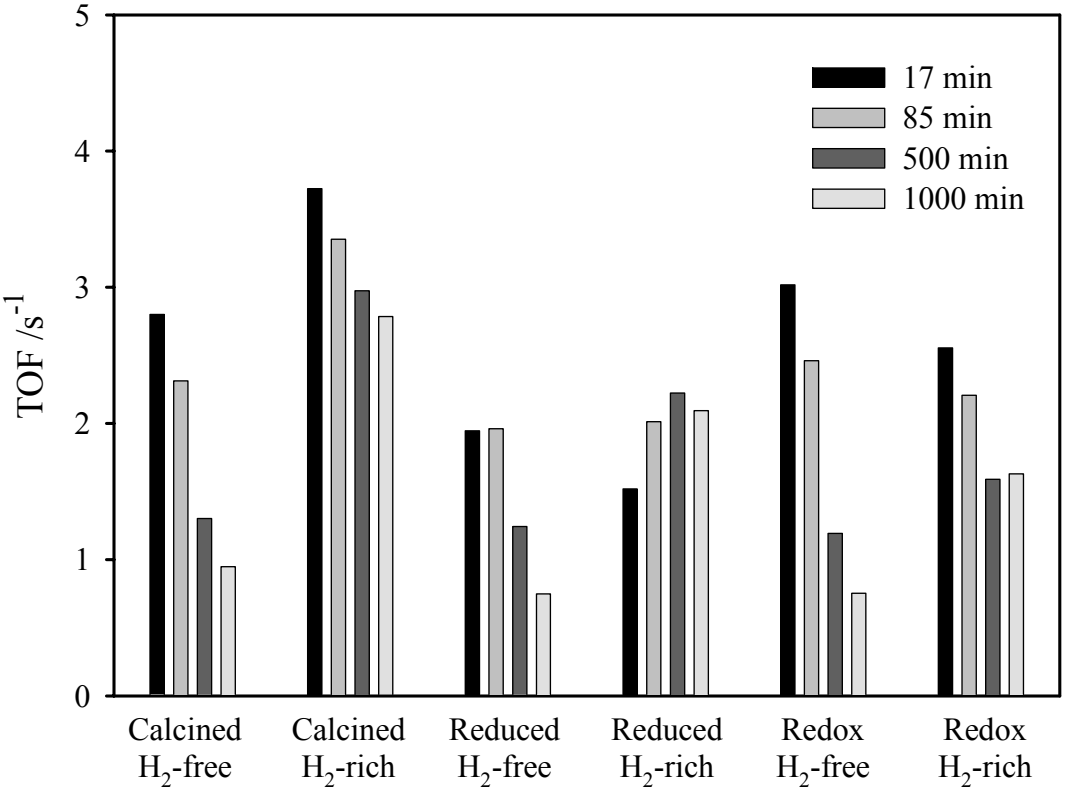

Figure 3.2-5: Reaction rates of the CO oxidation after 17, 85, 500 and 1000 min on catalyst $Au/TiO_2(4)$ after calcination (30 min at 400°C in 10% O_2/N_2), reduction (treating in N_2 for 30 min at 200°C, annealing in 10% H_2 in N_2 for 45 min at 200°C, treating in N_2 for 30 min at 200°C) and redox-conditioning (treating in N_2 for 30 min at 200°C, annealing in 10% H_2 in N_2 for 45 min at 200°C, heating in N_2 to 300°C, calcination in 10% O_2/N_2 for 30 min at 300°C). For experimental conditions see Appendix B II.

The activity of $Au/TiO_2(4)$ was worse in H_2-free atmosphere after a reductive conditioning at 200°C compared to that of the calcined sample. For this reason a redox-conditioning procedure was applied, involving reduction at 200°C and subsequent calcination at 300°C (for a detailed description see experimental section). This led to initial reaction rates in H_2-free atmosphere comparable to those obtained after calcination at 400°C. In H_2-rich atmosphere the reaction rates were worse than after the reductive conditioning. For this reason the activity of the other samples was tested by i) experiments in both atmospheres using calcined

catalysts, ii) experiments in H_2-rich atmosphere using reduced catalysts and ii) experiments in H_2-free atmosphere using redox-conditioned catalysts.

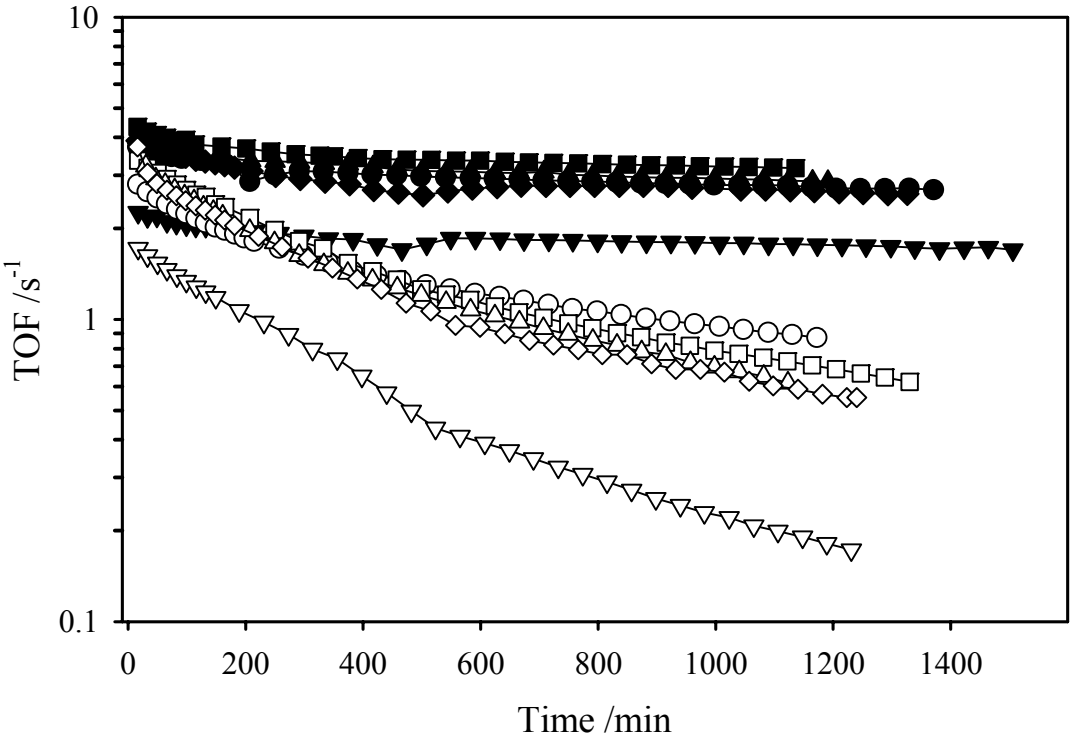

Figure 3.2-6: Long-term stability and deactivation of the Degussa catalysts (pretreatment: calcination at 400°C) during reaction in H_2-rich (1 kPa CO, 1 kPa O_2, 75 kPa H_2, balance N_2, filled symbols) and H_2-free (1 kPa CO, 1 kPa O_2, balance N_2, empty symbol) atmosphere. ○: $Au/TiO_2(4)$, □: $Au/TiO_2(5)$, △: $Au/TiO_2(6)$, ◇: $Au/TiO_2(7)$, ▽: $Au/TiO_2(8)$. For experimental conditions see Appendix B II.

The temporal evolution of the CO oxidation reaction rates on the calcined catalysts is shown in fig. 3.2-6, both for reaction in H_2-free (1 kPa CO, 1 kPa O_2, balance N_2, empty symbols) and in H_2-rich atmosphere (1 kPa CO, 1 kPa O_2, 75 kPa H_2, balance N_2, filled symbols). Clearly, deactivation is much more pronounced in H_2-free atmosphere than in H_2-rich atmosphere. After 1000 min on stream the activity in H_2-rich atmosphere has decayed to 70-80% of the initial value. In contrast, in H_2-free atmosphere it decreased to 15-35 % for samples $Au/TiO_2(4)$, $Au/TiO_2(5)$, $Au/TiO_2(6)$ and $Au/TiO_2(7)$ and even 10% for the high loading catalyst $Au/TiO_2(8)$, as can be seen in fig. 3.2-7. Both the initial activities and the deactivation behavior of the four catalysts $Au/TiO_2(4)$, $Au/TiO_2(5)$, $Au/TiO_2(6)$, $Au/TiO_2(7)$ is very similar in both reaction atmospheres, only the high loading catalyst $Au/TiO_2(8)$ shows a lower surface normalized activity than the other samples. This behavior agrees well with the findings of the Sachtleben catalysts, except for the much stronger deactivation of the present, anatase/rutile supported catalysts in a H_2-free atmosphere compared to the anatase supported

catalysts (compare figs. 3.2-3 and 3.2-7). Apparently, the addition of rutile enhances the tendency for deactivation during CO oxidation.

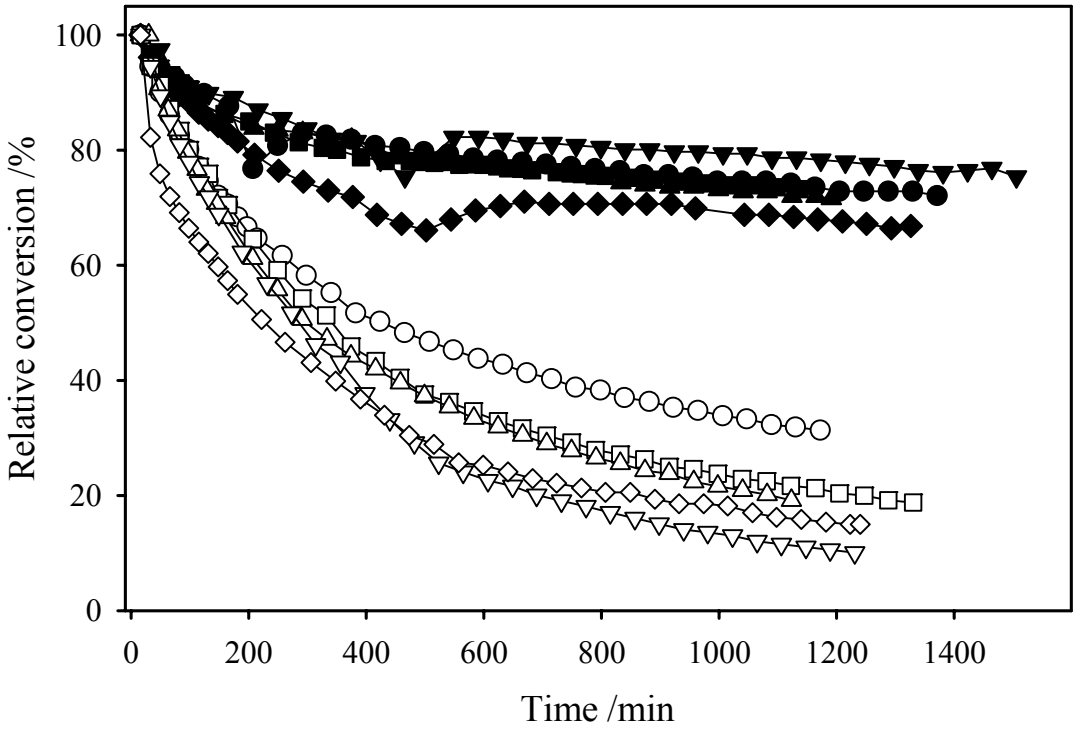

Figure 3.2-7: Relative deactivation of the Degussa catalysts (pretreatment: calcination at 400°C) during CO oxidation in H_2-rich (1 kPa CO, 1 kPa O_2, 75 kPa H_2, balance N_2, filled symbols) and H_2-free atmosphere (1 kPa CO, 1 kPa O_2, balance N_2, empty symbol). ○: Au/TiO_2(4), □: Au/TiO_2(5), △: Au/TiO_2(6), ◇: Au/TiO_2(7), ▽: Au/TiO_2(8). The curves were normalized to an initial activity of 100%. For experimental conditions see Appendix B II.

Comparing the results with the deactivation behavior in previous studies, no unique trend is found, despite of rather good agreement with several reports. Zanella et al. reported a significant deactivation during CO oxidation at 5°C in 1 % CO, 2 % O_2 , balance N_2 for catalysts which were equally prepared via deposition-precipitation using Degussa P25 as support material, if these catalysts were calcined at temperatures ≥ 200°C [111]. After 5 h on stream the activities decreased to 20-75 % of the initial values. The deactivation behavior and the reaction rates depended strongly on the calcination temperature: the higher the calcination temperature, the lower the final reaction rates and the stronger the deactivation. For catalysts prepared using NaOH for pH control and subsequent calcination at low temperatures (100-150°C) these authors found a small, initial activation (13% and from 0 to 0.01 $mole_{CO} \cdot mole_{Au}^{-1} \cdot s^{-1}$ after calcination at 150°C and 100°C, respectively) of the catalyst, followed by a slow deactivation to the initial activities. Park et al. reported a slight deactivation of 4 to 30% during 5 h on stream in 1 % CO, 5 % O_2, balance N_2, at a reaction

temperature of 50°C for catalysts prepared via deposition precipitation and calcined at different temperatures for 5 h [86]. Similar to the findings of Zanella et al. the mass related reaction rates were higher after lower calcination temperatures. Konova et al. found a deactivation of about 50 % of the initial activity during 1000 min of CO oxidation at room temperature in 0.06 - 0.24 vol.-% CO in air for catalysts prepared via deposition-precipitation and subsequent calcination in air at 120°C for 1 h [134]. On the other hand, Arri et al. did not observe any deactivation of a Au/TiO_2 catalysts prepared via laser vaporization, upon CO oxidation at 160°C in 2 % CO, 2 % O_2, balance He during 70 h on stream [135]. Equally, Mallick et al. did not see any deactivation during 200 min in 10 % CO, 10 % O_2, balance He at different reaction temperatures for a catalyst prepared via deposition precipitation on Degussa P25 [136]. It should be noted, however, that in the two latter studies high amounts of catalyst were used, resulting in conversions of ≥ 80 %, and it can not be excluded that the observed stability is an artifact caused by the presence of 'unused' catalyst.

The (initial) reaction rates in fig. 3.2-6 are comparable with those of 'good' catalysts reported in the literature. Extrapolating the published TOF numbers to a reaction temperature of 80°C with the activation energies given in the publications, one obtains values in the range of 1.0 s^{-1} to 3.5 s^{-1} (note that the small differences in partial pressures where not corrected) [4,37-39]. For a model catalyst even a TOF of 4 s^{-1} at 80°C was published [35], while in our group they were in the range of 0.1 to 0.6 s^{-1} [82,83].

The decreasing, active site normalized, activity of the Au/TiO_2 catalyst with higher Au content (catalyst $Au/TiO_2(8)$) in both atmospheres compared to that of the other samples can be compared with findings by Zanella et al. [111]. They observed about similar TOF based activities for a 3.1 wt% Au containing catalyst (prepared via deposition precipitation, pH control with NaOH) and a 7.6 wt.-% Au containing catalyst (prepared by deposition precipitation, pH control with urea), 0.095 s^{-1} and 0.08 s^{-1}, respectively, interpolating to a similar particle size of 3 nm for both catalysts from their fitted size-dependence of the rates. It should be noted that in the above examples not only the Au content, but also the preparation procedure was changed slightly, while in the present case only the Au content is varied. Since despite of the higher loading in sample $Au/TiO_2(8)$ the mean Au particle size is similar to that of the other samples, and also the BET surface areas are similar, the main difference between the higher and lower loading catalysts in the present series is the average support area

available per Au particle. Therefore we speculate that the size of the substrate zone around each Au particle plays an important role for the activity of the catalyst [132,137].

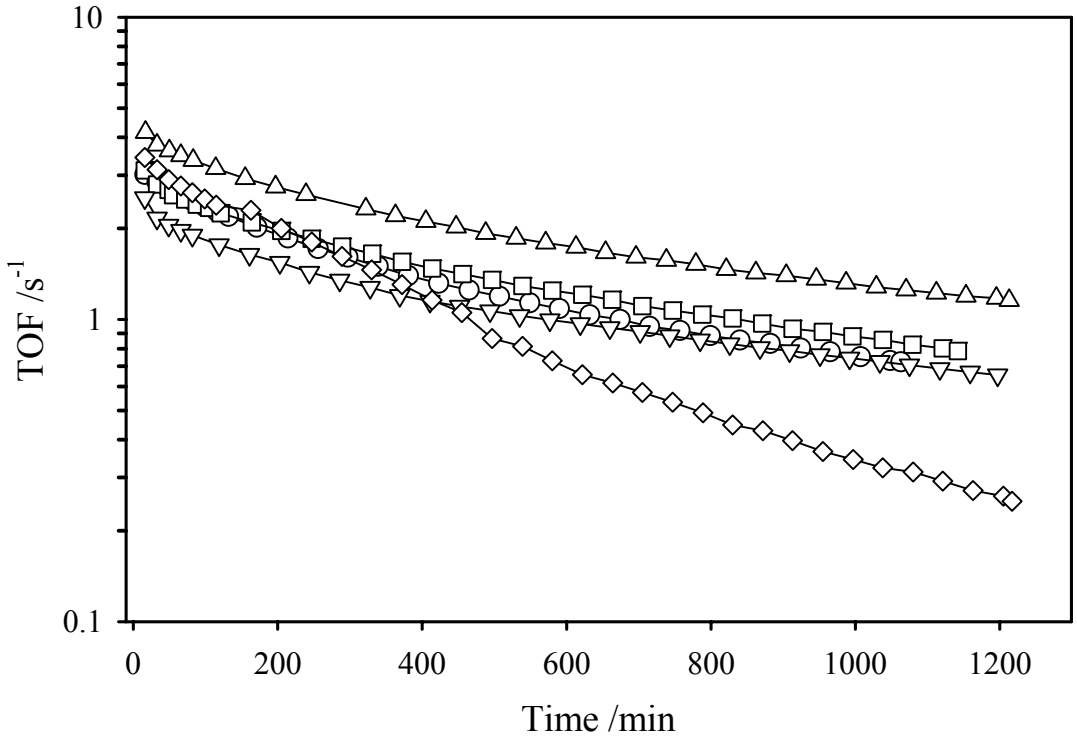

Figure 3.2-8: Long-term stability and deactivation of the Degussa catalysts (pretreatment: redox-conditioning at 200°C and 300°C) during reaction in H_2-free atmosphere (1 kPa CO, 1 kPa O_2, balance N_2). ○: Au/TiO_2(4), □: Au/TiO_2(5), △: Au/TiO_2(6), ◇: Au/TiO_2(7), ▽: Au/TiO_2(8). For experimental conditions see Appendix B II.

The reaction rates for CO oxidation on the redox-conditioned catalyst in H_2-free atmosphere and of the reductively pretreated catalyst in H_2-rich atmosphere are shown in figs. 3.2-8 and 3.2-9, respectively. Similar to the calcined samples a pronounced deactivation can be observed for the redox-conditioned samples in H_2-free atmosphere. Within 1000 min reaction time the activity of catalysts Au/TiO_2(4), Au/TiO_2(5), Au/TiO_2(6) and Au/TiO_2(8) decreased to 25 %-35 % of the initial values, that of catalyst Au/TiO_2(7) to 10 %. Hence, while the initial activities are comparable to those of the calcined catalysts, the reproducibility is significantly worse in this case than after calcination. The deactivation (not the initial activity) of sample Au/TiO_2(7) deviates considerably from that of the other samples. Also the loading effect is not as pronounced as for the calcined catalysts, the activity of the high loading sample Au/TiO_2(8) is only little less than that of the other lower loading catalysts. While there is no satisfactory explanation in the moment for the strong deactivation of catalyst Au/TiO_2(7) (the gold particle sizes were equal), it should be noted that this catalyst had the highest Au^{3+} amount after redox-conditioning (see table 3.1-3).

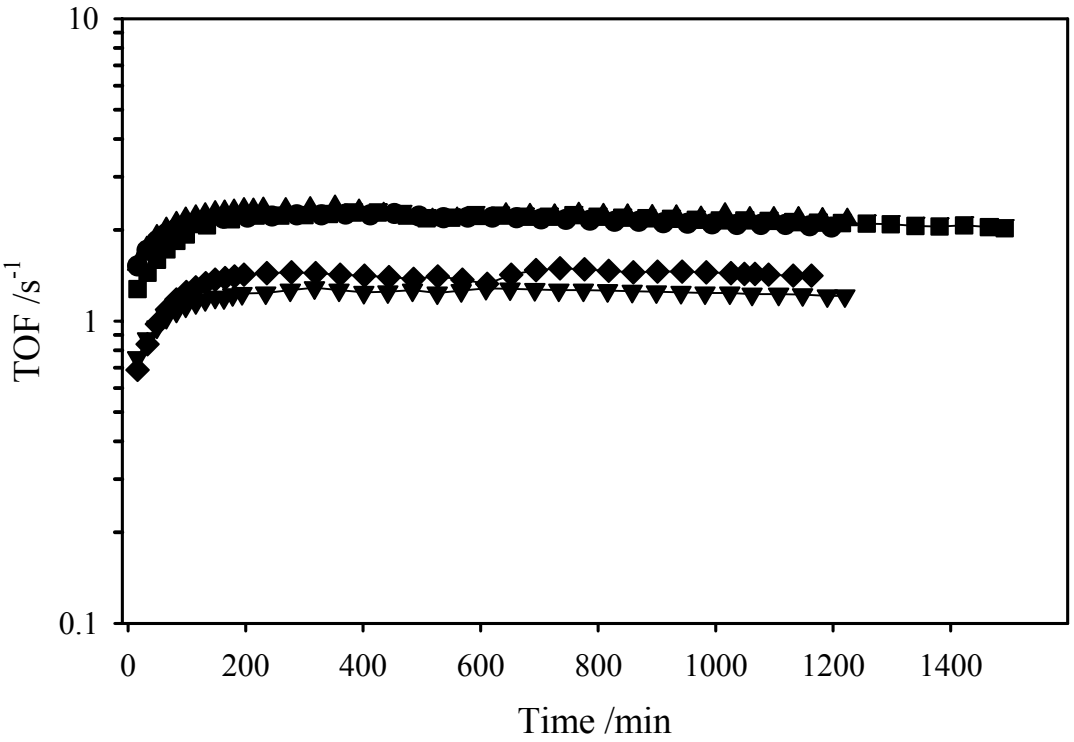

Figure 3.2-9: Long-term stability and deactivation of the Degussa catalysts (pretreatment: reductive conditioning at 200°C) during reaction in H_2-rich atmosphere (1 kPa CO, 1 kPa O_2, 75 kPa H_2, balance N_2). ●: Au/TiO_2(4), ■: Au/TiO_2(5), ▲: Au/TiO_2(6), ◆: Au/TiO_2(7), ▼: Au/TiO_2(8). For experimental conditions see Appendix B II.

Redox-conditioning was also applied by other groups [31,39,40]. The examples, however, are much more scarce than for calcination. In general, the reduction step was carried out at a higher temperature than the (subsequent) calcination step. Choudhary et al. reported only little deactivation during CO oxidation at high O_2-excess of (p_{O2}=2·p_{CO}= 36.7 mbar, reaction temperatures 40°C and 80°C) for a catalyst prepared via deposition precipitation of a Au-phosphine complex on Degussa P25 and subsequent conditioning via reduction at 500°C followed by calcination at 400°C [31]. The conversion in their experiments was at least 50%, the deactivation could even be decreased by redox regeneration cycles. Bollinger and Vannice studied the deactivation of a catalyst prepared via coprecipitation and subsequent conditioning via first reduction at 500°C in H_2 for one hour, followed by a calcination step at 400°C for one hour and finally low temperature reduction at 200°C for two hours. They reported a deactivation to 60% and 26% of the initial activity during CO oxidation within 3 hours in a H_2-free atmosphere with $p_{O2} = p_{CO} = 50$ mbar at reaction temperatures of 27°C and 0°C (differential conversions, particle size 4.5 nm, initial activity (TOFs) 0.076 s^{-1} at 27°C and 0.053 s^{-1} at 0°C), respectively [39]. Lin et al., who applied the same conditioning procedure for a catalyst prepared by the incipient wetness method, reported a deactivation to ~45 % of

the initial activity upon 1000 min CO oxidation at 40°C ($p_{O2} = p_{CO} = 50$ mbar and $p_{CO} = 2 \cdot p_{O2} = 9.3$ mbar, particle size ~30 nm, initial activity (TOF) at 87°C 0.24 s^{-1}) [40]. The deactivation behavior in [39] at 27°C is in the range of the results presented here, the catalysts in [31] and [40] show a better stability. However, the reaction rates in [39] and [40] (in [31] no reaction rates were reported) are lower than those presented here after redox-conditioning, even after a stronger deactivation.

The deactivation behavior of the reductively conditioned catalysts in H_2-rich atmosphere is displayed in fig. 3.2-9. In this case the general behavior differs strongly from that of the previous cases, showing an initial increase in activity during the first 300 min rather than the normal strong initial decrease. The initial TOF rates are smaller than after calcination and redox-conditioning. Following the initial activation phase the activity is very stable, comparable to the trend observed for the calcined samples in H_2-rich atmosphere. The absolute amount of the initial activation (increase of the reaction rate from 17 min to 300 min) is between 53 % and 109 %. On the other hand, even after the initial activation phase the absolute activity of the reductively conditioned catalysts is still slightly lower than that of the calcined catalysts. As mentioned above, the Sachtleben catalysts, which consisted of pure anatase support, did not show an activation period as it was observed for the Degussa catalysts. Hence, the activation must be related to the presence of rutile in the Degussa P25 support material.

Similar to the experiments on the redox-conditioned catalysts the agreement between the different catalysts is not as good as for the calcined catalysts. Again catalyst $Au/TiO_2(7)$ shows a worse performance than the other catalysts with the same loading, and similar to observations after redox-conditioning, it has the highest Au^{3+} amount of all samples. This points to an involvement of the Au^{3+} species in the lower activity of sample $AuTiO_2(7)$. A lower activity on Au^{3+} containing Au particles, i.e., not fully reduced particles, would also explain the initial activation phase. In that case the slight deactivation expected from comparison with the behavior of the calcined catalysts could be overcompensated by an increase of the reaction rate due to slow reduction of the Au^{3+} species during reaction. A reduction of Au^{n+} species to metallic gold by the reactive gas mixture was also reported by Dekkers et al. [138] on a Au/TiO_2 catalyst, Visco et al. [139] for Au/Fe_2O_3 and Guzman et al. [140] for a Au/MgO catalyst. Visco et al. [139] identified Au^{n+} to be the active species, since

they observed deactivation during reaction, which went along with an increase of the Au^0 content. Since they did not perform in-situ IR measurements, it can not be excluded, that the observed deactivation was caused by byproducts and not by the reduction of gold. By in-situ XANES and EXAFS measurements Guzman et al. [140] identified Au^+ to be the active species during CO oxidation catalyzed by Au/MgO. Equally to the study of Visco et al. [139], it can not be excluded, that the deactivation is caused by byproducts. Dekkers et al. [138] discarded the theory due to the fact, that they observed higher activity in the reduced samples. This corresponds with the above described activation of the Degussa catalysts after reductive conditioning. Finally the high loading catalyst $Au/TiO_2(8)$ is again less active than the other three low-loading catalysts, similar to the observations for the calcined samples.

In the only earlier study on the deactivation of a reductively conditioned catalyst Lin et al. reported a slight deactivation upon reaction at 40°C for a catalyst prepared via the incipient wetness method and subsequent reduction in H_2 for one hour at 500°C, in the presence of excess O_2 [40]. The deactivation was stronger, if the O_2 excess was reduced. When comparing this with the results presented here, it should be noted that their reduction temperature was 300°C higher than the one used here and that the reaction was carried out in a H_2-free atmosphere. The absence of an activation phase for higher reduction temperatures agrees with the above interpretation, that the initial activation of the low temperature (200°C) reduced catalyst during the initial stages of the reaction in a H_2-rich atmosphere is due to continuing reduction of the catalyst, until this is completely reduced.

3.2.2 Selectivity

The selectivity for CO oxidation is defined by the amount of O_2 consumed for CO oxidation, divided by the total amount of O_2 consumed. It is calculated from the balance between CO_2 formation and O_2 consumption [20] (see also experimental section). It should be noted that this is only correct as long as the H_2O and CO_2 levels are not affected by any other reaction such as the water gas shift (WGS) reaction ($CO+H_2O \leftrightarrows CO_2+H_2$) or the methanation reaction ($CO+3H_2 \leftrightarrows CH_4+H_2O$), which appears justified based on previous measurements of the forward WGS reaction on a Au/TiO_2 catalyst under comparable conditions by Sakurai et al. [95]).

3.2.2.1 Sachtleben catalysts

The selectivity of the Sachtleben samples during the activity measurements is illustrated in fig. 3.2-10. In contrast to the reaction rates the selectivity is well reproducible for these catalysts. The strong dependence of the selectivity on the partial pressures is illustrated in fig. 3.2-11a and b, respectively. For equal $p_{CO}=p_{O2}$ (fig. 3.2-11a and α^{λ}_{CO} plots in fig. 3.2-11b) the selectivity decreases from almost 70% for $p_{CO,O2}\geq 1$ kPa to a few percent at CO partial pressures <0.1 kPa. In order to elucidate, whether CO or O_2 partial pressures stronger influence the selectivity, the influence of p_{CO} and p_{O2} is separately illustrated in fig. 3.2-11b by the plots which are denoted α_{CO} and α_{O2}, respectively. Clearly, the selectivity decreases stronger with CO partial pressure than with O_2 partial pressure. Hence, the limiting factor for selectivity is the CO partial pressure, which questions the use of the Au/TiO_2 catalysts for the removal of CO from feed stream of PEM fuel cells. Concerning the temperature dependence of the selectivity, fig. 3.2-11a exhibits, that the selectivity decreases, if the temperature is increased from 40°C to 60°C. A further increase of the temperature does not lead to a decrease in selectivity.

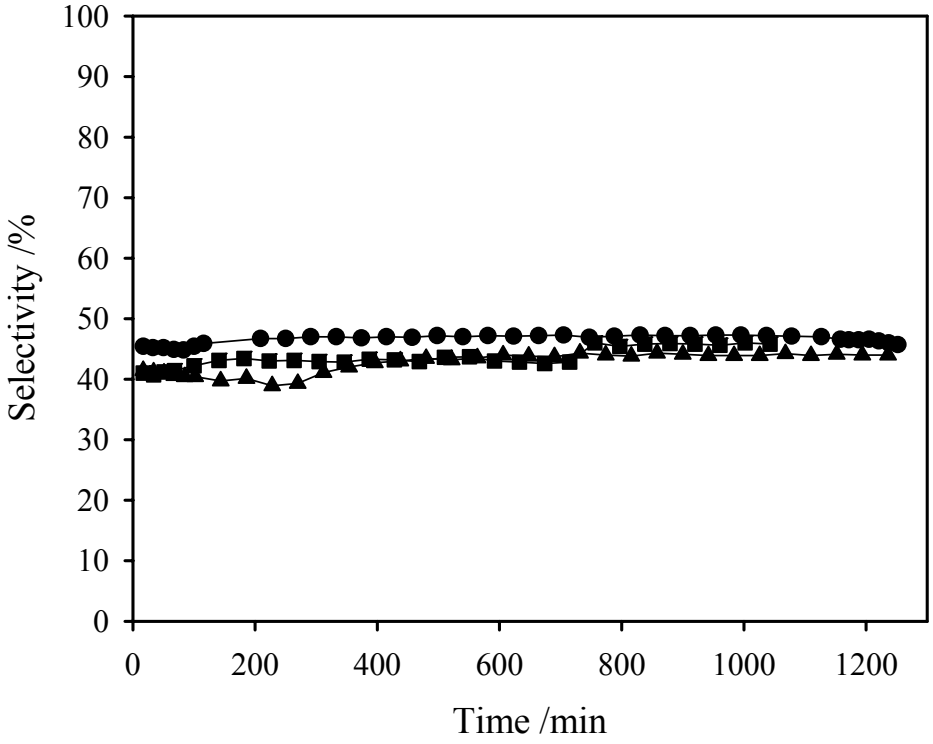

Figure 3.2-10: Selectivity during the activity measurements of fig. 3.2-3 at 80°C in H_2-rich atmosphere (1 kPa CO, 1 kPa O_2, 75 kPa H_2, balance N_2). ▲: Au/TiO_2(1), ■: Au/TiO_2(2) and ●: Au/TiO_2(3). For experimental conditions see Appendix B II.

The absolute values of the selectivity fit well to data reported by Choudhary et al. [31], who determined a selectivity of 73% during selective CO oxidation over Au/TiO_2 in a $CO:H_2:O_2$ mixture of 1:50:2, i.e, at $\lambda = 4$ and $p_{CO} \approx 2$ kPa at 80°C. A strong dependence of the selectivity on the CO partial pressure at constant λ was reported also for the PROX reaction over Au/Fe_2O_3 [16]. Interestingly, on Au/Fe_2O_3 [16] and Au/TiO_2 the pronounced changes in selectivity with CO partial pressure are mainly due to a change in CO oxidation activity, while the H_2 oxidation rate is little affected. These results lead to the conclusions that i) the reactive sites for H_2 adsorption are not or at least not to a significant extent blocked by the increasing CO coverage under the present conditions and that ii) the reactive oxygen species are not significantly depleted by the CO oxidation reaction.

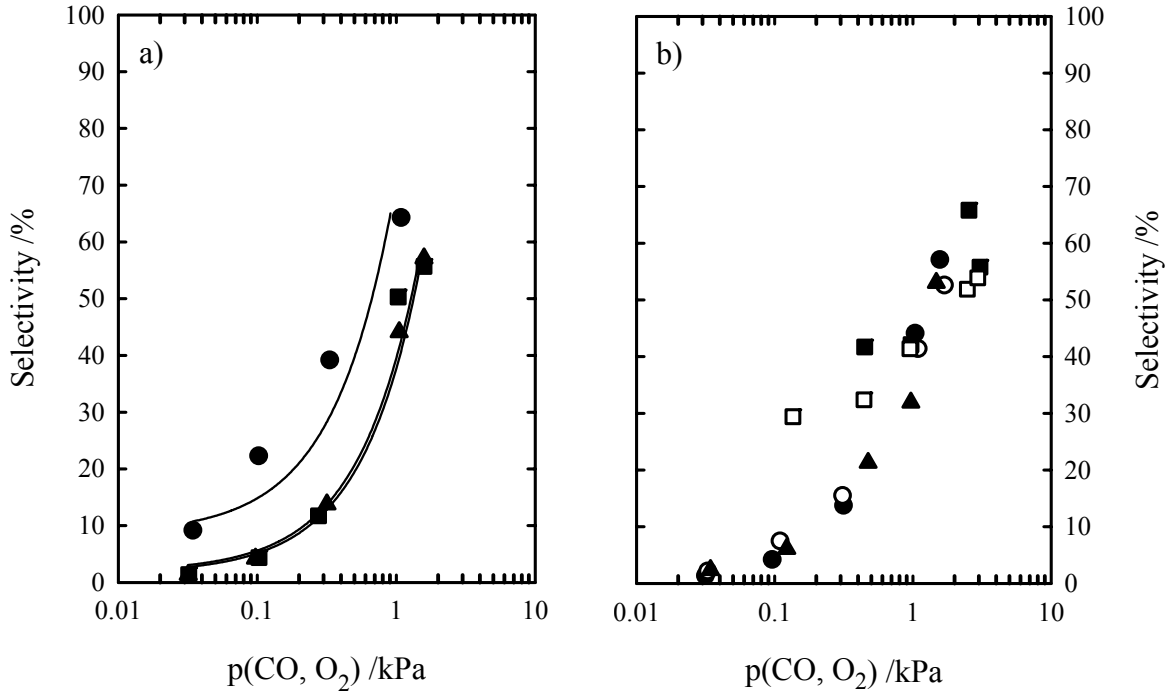

Figure 3.2-11: a) Selectivity for CO oxidation during the reaction in H_2-rich atmosphere for catalyst $Au/TiO_2(1)$ at different temperatures (40°C (●), 60°C (■), 80°C (▲), λ=2). b) Selectivity during the determination of the reaction orders (see section 3.3.1, figs. 3.3-1 to 3.3-3) in H_2-rich atmosphere for catalysts $Au/TiO_2(1)$ and $Au/TiO_2(3)$: $Au/TiO_2(1)$ α^{λ}_{CO} (●); $Au/TiO_2(3)$ α^{λ}_{CO} (○); $Au/TiO_2(1)$ α_{CO} (▲); $Au/TiO_2(1)$ α_{O2} (■); $Au/TiO_2(3)$ α_{O2} (□).

3.2.2.2 Degussa catalysts

Similar to the activity during reaction in the H_2-rich atmosphere (figs. 3.2-6 and 3.2-8) also the selectivity changes little with time (fig. 3.2-12). After calcination the selectivity is in the range between 40 % and 65 %, after reductive conditioning it is significantly lower, between 25 % and 45 %. Similar selectivities were also reported by Schubert et al. for a catalyst

pretreated by calcination at 400°C (80°C reaction temperature) [33]. The authors observed little temporal change in the selectivity for reaction in H_2-rich atmosphere.

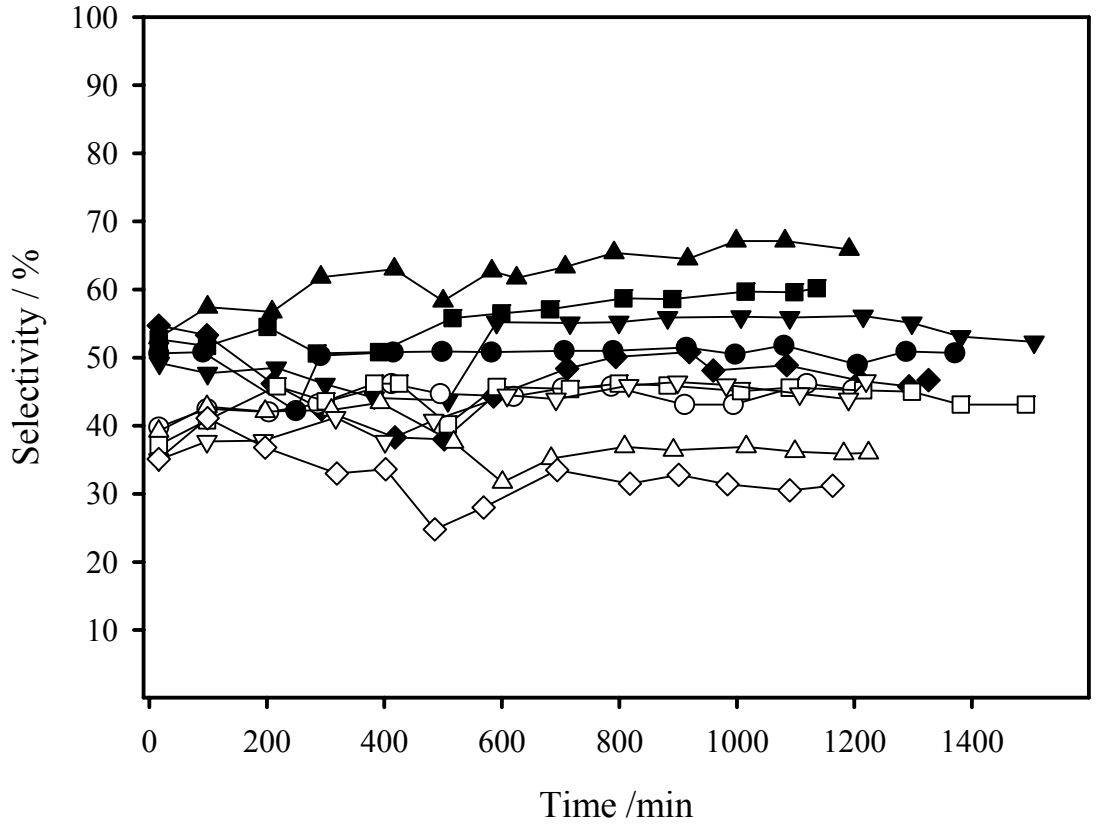

Figure 3.2-12: Selectivity of the calcined Degussa catalysts (filled symbols, measurements of fig. 3.2-6) and the reductively conditioned catalysts (empty symbols, measurements of fig. 3.2-8) in a H_2-rich atmosphere (1 kPa CO, 1 kPa O_2, 75 kPa H_2, blance N_2). ○: Au/TiO_2(4), □: Au/TiO_2(5), △: Au/TiO_2(6), ◇: Au/TiO_2(7), ▽: Au/TiO_2(8).

The stability of the signals in fig. 3.2-12 is worse than that for the CO oxidation rates, which originates in the fact that the columns of the GC were not freshly recovered by heating. Since the retention times of O_2 and N_2 deviate only ~20 s, the peaks of these two components were not completely separated. Hence, the integration of the O_2-peak beside the huge N_2-peak (the gas mixtures contained 25 kPa N_2 and 1 kPa O_2) resulted in a relative standard deviation of 1.06% for the O_2 peak area (for comparison, the standard deviation for the peak area of the well separated CO_2 peak was 0.2%). If the error propagation along Gauss is calculated, this results in an error of ±6% for the selectivity, which explains the fluctuations in fig. 3.2-12. The plots in fig. 3.2-12 do not, however, show any effect of the lower activity of catalyst Au/TiO_2(7) nor of the initial activation phase of the reductively conditioned catalysts. Therefore, whatever is responsible for these effects, does not affect the selectivity, or in another way, it equally affects the probability for CO oxidation and for H_2 oxidation. The

most plausible explanation for the lower activity of the respective catalysts – catalyst $Au/TiO_2(7)$ after redox-conditioning and reduction and the reductively conditioned catalysts before their initial activation phase - is therefore a reduced activity for O_2 activation (O-O bond breaking). This may be related to the presence of Au^{3+} species, but definite proof for that is missing.

The physical reason for the higher selectivity of the calcined catalysts is not clear. One may speculate that this is related to the larger Au particle sizes in these samples (see table 3.1-1) or to the presence of Au^{3+} on the reductively conditioned catalyst (see table 3.1-2). The latter explanation, however, would contradict the above tentative assumption that a change in Au^{3+} content does affect the activity, but not the selectivity.

Comparing the selectivity of the Sachtleben (fig. 3.2-10) and Degussa catalysts (fig. 3.2-12) after calcination at 400°C, no significant difference can be observed. Hence, the presence of rutile in the P25 support material does not influence the selectivity for CO oxidation in a H_2-rich atmosphere.

3.2.3 DRIFTS measurements

To gain more information on the origin of the deactivation process during reaction, we performed in-situ DRIFTS measurements in both H_2-free (1 kPa CO, 1 kPa O_2, balance N_2) and H_2-rich (1 kPa CO, 1 kPa O_2, 75 kPa H_2, balance N_2) atmospheres, at 80°C over calcined samples of catalysts $Au/TiO_2(1)$ and $Au/TiO_2(5)$, representatives of the Sachtleben and Degussa series, respectively. The deactivation process was studied on calcined samples, since especially the Degussa catalysts deactivated fewest in H_2-free atmosphere after this conditioning procedure. Therefore this conditioning procedure was used for the other studies presented in this dissertation. Figs. 3.2-13 and 3.2-14 show spectra recorded after 5 min, 90 min and 240 min reaction on the catalysts $Au/TiO_2(1)$ and $Au/TiO_2(5)$, respectively. The spectra in a) refer to the reaction in H_2-free and the spectra in b) to that in H_2-rich atmosphere. This subsection aims at a qualitative determination of possible reasons for deactivation. The exact temporal development of the detected species in H_2-free atmosphere will not be shown here, since it is discussed in detail in chapter 3.5.

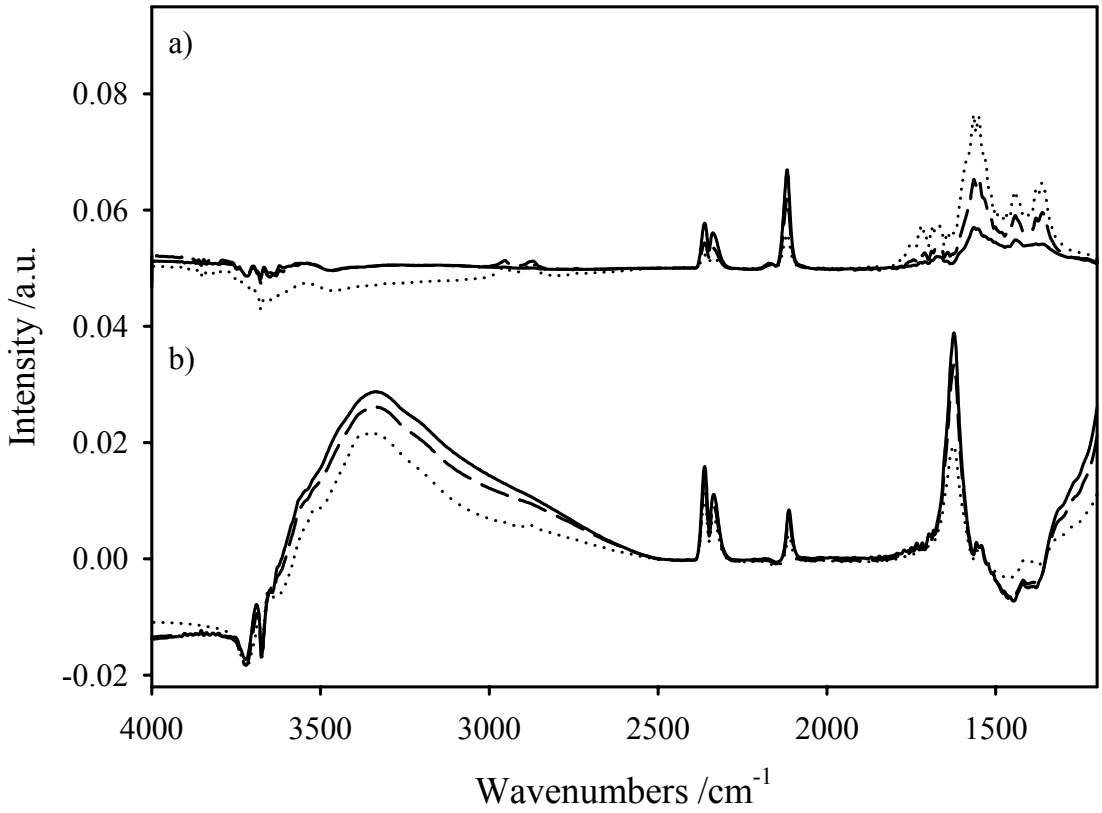

Figure 3.2-13: In-situ DRIFT spectra obtained during CO oxidation over $Au/TiO_2(1)$ in a) H_2-free and b) H_2-rich atmosphere, after 5 min (straight lines), 60 min (dashed lines), and 240 min (dotted lines).

For both samples characteristic differences between the spectra in the two gas mixtures are observable. The stretch vibration of linearly adsorbed CO (CO_{ad}) appears at 2112 cm^{-1} during CO oxidation in H_2-rich atmosphere on both samples and at 2219 cm^{-1} and at 2120 cm^{-1} on catalysts $Au/TiO_2(1)$ and $Au/TiO_2(5)$, respectively, in H_2-free atmosphere. Hence the presence of H_2 in the gas mixture leads to a weakening of the C-O bond, which goes along with a strengthening of the Au-CO bond. Different from metals such as Pd, CO adsorption on Au involves only the formation of a σ-bond between CO [141,142]. An even more pronounced peak shift in the presence of H_2 is observed for CO adsorption in the absence of O_2 in H_2-rich atmosphere (see subsection 3.3.2.2), which will be discussed in detail in that corresponding subsection.

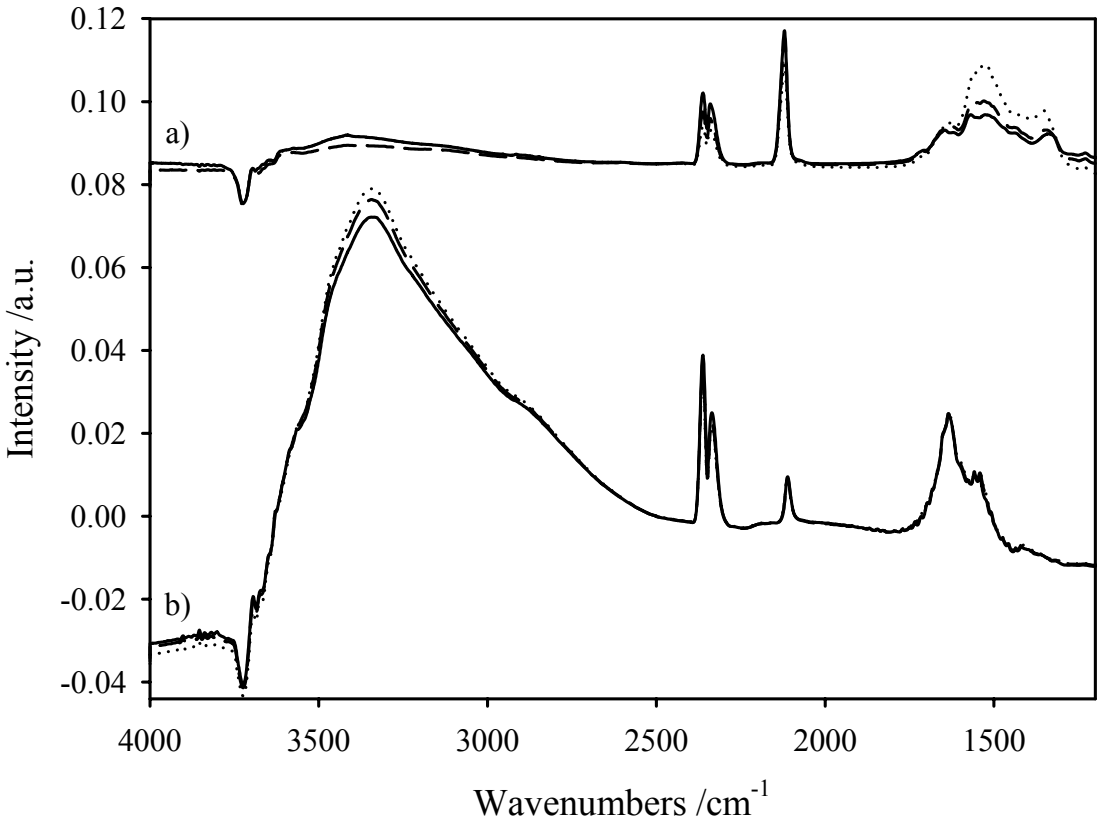

Figure 3.2-14: In-situ DRIFT spectra obtained during CO oxidation over $Au/TiO_2(5)$ in a) H_2-free and b) H_2-rich atmosphere, after 5 min (straight lines), 60 min (dashed lines), and 240 min (dotted lines).

In all spectra we found characteristic signals for CO_2 at 2362 cm^{-1} and 2335 cm^{-1}. For catalyst $Au/TiO_2(1)$ the CO_2 intensities decay significantly with time in both atmospheres. For catalyst $Au/TiO_2(5)$ a significant decrease appears only in H_2-free atmosphere, while it is minimal in H_2-rich atmosphere. This behavior goes along with the finding in the activity measurements, where catalyst $Au/TiO_2(1)$ deactivated in both atmospheres, while for catalyst $Au/TiO_2(5)$ significant deactivation occurs only in H_2-free atmosphere.

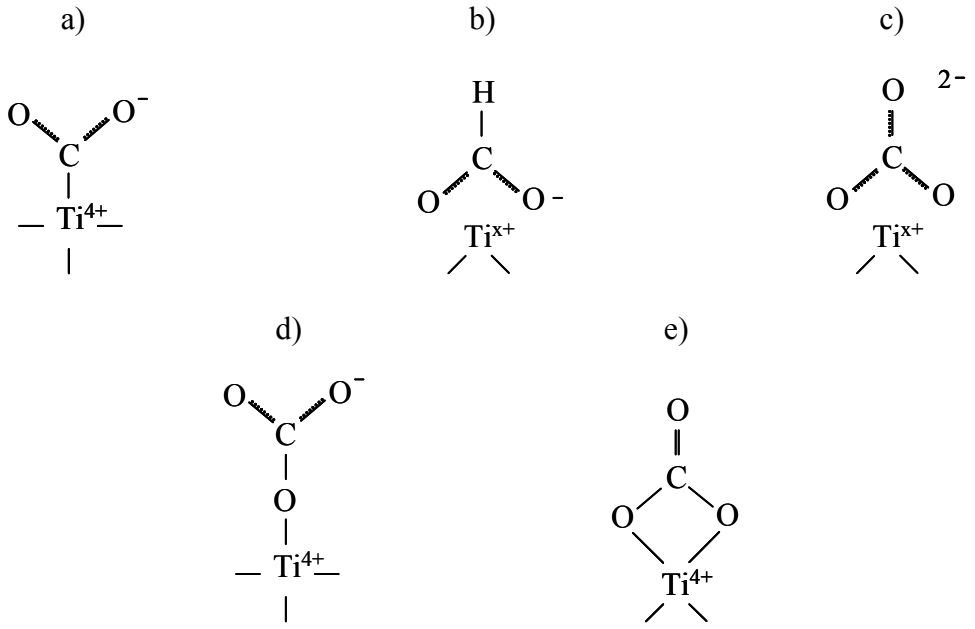

Figure 3.2-15: Structure of surface species identified with DRIFTS during CO oxidation (figs. 3.2-13 and 3.2-14). a) carboxylate, b) formate, c) bulk carbonate, d) monodentate carbonate and e) bidentate carbonate. The structure of the species and their assignment is in accordance to [143].

In those samples, which show significant deactivation, the amount of CO adsorbed in steady state decreases considerably during the reaction, which provides a plausible explanation for the decay in activity. The most likely reason for the decreasing CO_{ad} coverage in H_2-free atmosphere is found upon inspecting the spectral regions below 1700 cm^{-1}: Pronounced peaks evolve, which are attributed to adsorbed carbonate and formate/carboxylate species. In the spectra regarded on catalyst $Au/TiO_2(1)$ (see fig. 3.2-13a) the peaks at 1690 cm^{-1} and 1586 cm^{-1} are assigned to ν(C=O) of bidentate carbonate species with the bridging O atoms bonded on two Ti atom (fig. 3.2-15e), respectively [39,143,144], while ν_{as}(COO) of these species is located at 1253 cm^{-1}. The peak at 1586 cm^{-1} can be assigned to $\nu_{as}(COO^-)$ of carboxylate species (fig. 3.2-15a) [143]. This is supported by the doublet at 1381 cm^{-1} and 1374 cm^{-1}, which was attributed to formates (fig. 3.2-15b) in [39,145] and belongs to $\nu_s(COO^-)$ of carboxylate species (fig. 3.2-15a) and $\nu_s(COO^-)$ of monodentate carbonate (fig. 3.2-15d), respectively [143]. The peak at 1440 cm^{-1} is characteristic for monodentate carbonate (fig. 3.2-15d) or bulk carbonates (fig. 3.2-15c) [11,39,143]. Our interpretation of formate as carboxylate species (fig. 3.2-15b) is confirmed by the signals at 2953 cm^{-1} and 2881 cm^{-1}, which are attributed to C-H vibrations of formates [39]. During reaction on catalyst $Au/TiO_2(5)$ (see fig. 3.2-14a) the peaks appear at slightly different wave numbers.

Here ν(C=O) and ν_{as}(COO) of bidentate carbonate with both bridging O atom bonded on the same metal atom (fig. 2.1-15e) appear at 1531 cm^{-1} and 1230 cm^{-1} respectively. $\nu_s(COO^-)$ of monodentate carbonate (fig. 3.2-15d) appears at 1355 cm^{-1} while the $\nu_{as}(COO^-)$ vibration is hidden under the ν(C=O) peak of bidentate carbonate. The same holds true for the $\nu_{as}(COO^-)$ vibration of carboxylates (fig. 3.2-15a), whose $\nu_s(COO^-)$ peak appears at 1412 cm^{-1}. Formate formation can be ruled out here, since no peaks typical for C-H vibrations are visible. The small shoulders at 2847 cm^{-1} and 2914 cm^{-1} which show up after 240 min reaction time, are a relict of the background subtraction procedure - a comparison of the raw background and reaction spectra (see fig. 3.2-16) does not show any growth of the peaks at 2847 cm^{-1} and 2914 cm^{-1}.

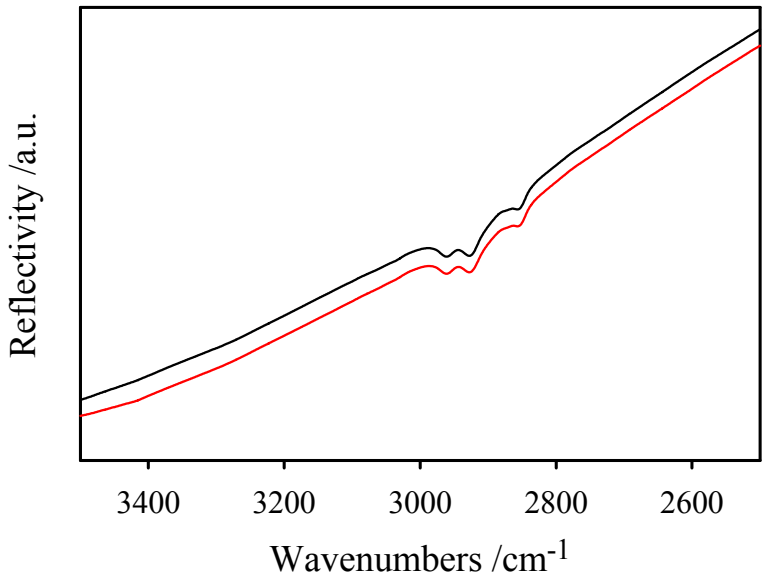

Figure 3.2-16: C-H vibration region of the raw spectra in the course of the DRIFTS measurement of the CO oxidation on catalyst $Au/TiO_2(5)$ in H_2-free atmosphere (1 kPa CO, 1 kPa O_2, balance N_2, see fig. 3.2-14a)) at 80°C. Black line: background spectrum in N_2 at 80°C after conditioning; red line: reaction spectrum after 240 min.

On both catalysts bidentate and monodentate carbonates species develop during CO oxidation in H_2-free atmosphere. The bond strengths differ slightly between the two samples, as indicated by the slight differences in peak positions. The carboxylate species are different in the two studied samples. On catalyst $Au/TiO_2(1)$ with pure anatase as support material, we can clearly identify formate formation, while on sample $Au/TiO_2(5)$ (support: Degussa P25, mixture of rutile and anatase) also carboxylate species are produced but formates can be discarded due to the absence of the C-H vibrations. The structural difference between these two species is, that in the formate a hydrogen atom is bound to the carbon atom (see

figs. 3.2-15a and b). If it is speculated that the formate is build-up from the carboxylate precursor, this reaction must be inhibited on sample Au/TiO_2(5). Since rutile is the additional component in catalyst Au/TiO_2(5), we can further speculate, that it inhibits the conversion from carboxylate to formate. An experimental prove, however, can not be given. In both samples the decay of the CO and CO_2 peaks during the reaction goes along with a significant growth of the formate/carboxylate and the carbonate-related peaks. Based on these data we conclude that the deactivation of the Au/TiO_2 catalysts during reaction in H_2-free atmosphere is mainly caused by the growth of carbonate and formate/carboxylate species, which increasingly cover the catalyst support and act as catalyst poison. Since CO adsorption on the Au particles is strongly affected, these species must partly overgrow the Au particle surface. This hypothesis is supported by the observation of a slight particle size 'reduction' of the Degussa catalyst Au/TiO_2(4) during CO oxidation over night in H_2-free atmosphere. The particle sizes were determined with TEM after conditioning and after reaction and decreased from 3.0±0.5 nm to 2.6±0.6 nm. For the anatase supported catalyst Au/TiO_2(2) this size 'reduction' was only marginal. It decreased from 2.6±0.8 nm to 2.4±0.5 nm. This observation corresponds to the much lower relative deactivation of the Sachtleben catalysts compared to the Degussa catalysts during CO oxidation in H_2-free atmosphere after calcination at 400°C, described in subsections 3.2.1.1 and 3.2.1.2.

The picture is completely different for reaction in H_2-rich atmosphere (see figs. 3.2-13b and 3.2-14b for samples Au/TiO_2(1) and Au/TiO_2(5) respectively). On both samples we detected only very small contributions from bidentate carbonates (ν(C=O)) [143], which occur at 1557 cm^{-1} and 1543 cm^{-1} for catalyst Au/TiO_2(1) and at 1557 cm^{-1} and 1539 cm^{-1} for catalyst Au/TiO_2(5). Instead, strong water signals at ~1630 cm^{-1} and 2500-3300 cm^{-1} are visible in both measurements. For catalyst Au/TiO_2(1), the intensity of these bands decrease parallel to the CO and CO_2 signals during reaction (see fig. 3.2-17a). Hence, the origin for the deactivation of this catalyst in H_2-rich gas mixture can not be deduced from the DRIFTS experiments. For catalyst Au/TiO_2(5) we observe a slight decrease of both the water signal in the range of 2500-3300 cm^{-1} and the CO_2 signal, while the peaks of CO_{ad}, H_2O_{ad} and of the carbonate-like species stay about constant (see fig. 3.2-17b). Hence, equally to the Sachtleben catalyst, the slight decrease in activity can not be correlated with an increase of a species observable with the DRIFTS technique.

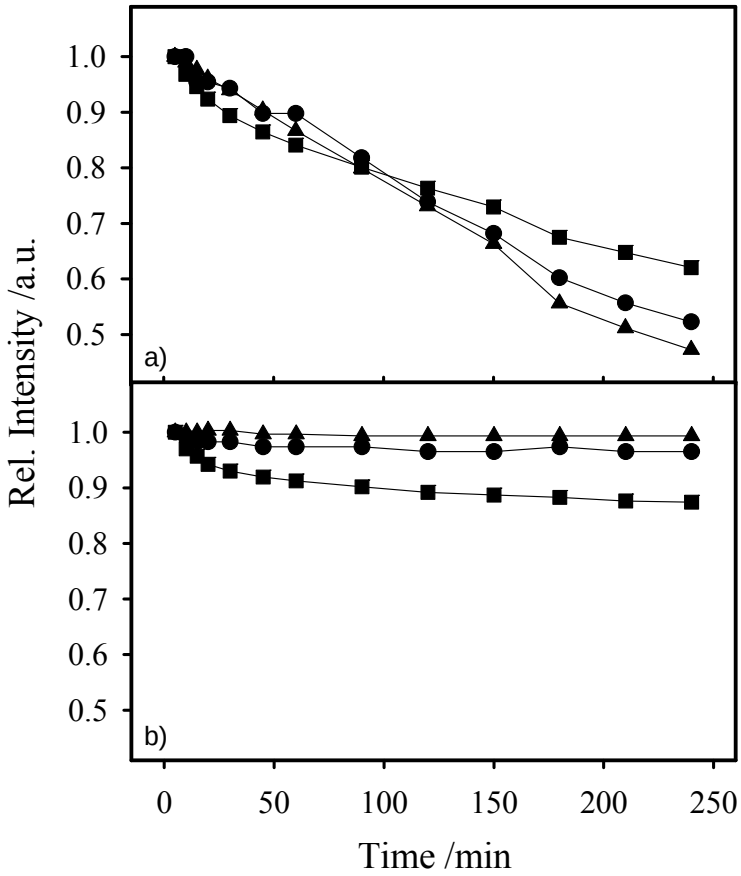

Figure 3.2-17: Temporal relative evolution of the CO_{ad} (●), CO_2 (■) and H_2O_{ad} (▲) peak intensities during CO oxidation in H_2-rich atmosphere on catalysts a) $Au/TiO_2(1)$ (spectra: fig. 3.2-13b) and b) $Au/TiO_2(4)$ (spectra: fig. 3.2-14b). The intensities were related to the value after 5 min of reaction.

As a summary, the long-term stability of the Sachtleben and Degussa catalysts was studied for CO oxidation in H_2-rich and H_2-free atmosphere after various conditioning procedures. Reaction rates and selectivity after calcination of both, Sachtleben and Degussa catalysts are comparable to high active catalysts presented in literature. Although the gold loading did not affect the gold particle sizes after the conditioning procedure, the higher loading Degussa catalysts revealed significantly lower surface normalized reaction rates after calcination in both atmospheres. The Sachtleben catalysts revealed higher reaction rates after reductive conditioning at 200°C than after calcination at 400°C. Since XPS did not show any differences in oxidation states, the origin of the higher reactivity was assigned to the smaller gold particles on the reduced samples. In contrast, the Degussa samples did not reveal higher reaction rates after reductive conditioning, than after calcination. The deactivation behavior of the Sachtleben catalysts was independent from the conditioning procedure and the reactive gas mixture, while on the Degussa catalysts it depended clearly on the reactive gas mixture: Independent from the conditioning procedure the samples deactivated significantly stronger in

H_2-free atmosphere. After reductive conditioning of the Degussa catalysts, activation could be observed within the first 300 min in H_2-rich atmosphere, similar to a Sachtleben catalyst, which was dried over night. In both cases the activation was assigned to a reduction of residual Au^{3+} to Au^0 during the reaction. Similar reaction rates for the low loading Degussa catalysts in both atmospheres, in particular after calcination, affirmed the high reproducibility of preparation and conditioning. Also the poor reproducibility in catalyst characterization of the Sachtleben samples could be approved by the activity measurements. DRFITS studies revealed that the deactivation in H_2-free atmosphere goes along with the growth of monodentate and bidentate carbonates for both the Sachtleben and Degussa samples. Additionally, carboxylates were detected for the Degussa and formates for the Sachtleben samples. Since carboxylate and formates are very similar species it was speculated, that the rutile in the Degussa P25 TiO_2 powder inhibits the conversion of the carboxylates to formates. Furthermore, it was assumed that the identified byproducts partly overgrow the Au particles, since the adsorption of CO on gold was strongly affected by the growth of these species and with TEM a slight decrease of the Au particle size during reaction could be observed. However, it could not be concluded from the results, which of the identified species caused the deactivation. Finally a potential source of deactivation in H_2-rich atmosphere could not be determined with DRIFTS, since the intensity of all detected species decreased during reaction.

3.3 The influence of CO and O_2

This chapter is focused on the influence of the CO and O_2 partial pressures on the CO oxidation: CO and O_2 reaction orders were determined in H_2-free and H_2-rich atmosphere (section 3.3.1). The interaction of CO with the catalyst in the two different atmospheres was studied by DRIFTS (section 3.3.2). Experiments with isotope labeled gases were performed in order to obtain information on the oxygen dissociation process and on the isotope exchange of $C^{18}O$ with the TiO_2 support. These results are presented in section 3.3.3. Additional experiments with isotope labeled gases are presented in section 3.5.

3.3.1 Reaction kinetics

The influence of CO/O_2 partial pressures at a constant ratio $p_{CO}=p_{O2}$, which is equivalent to an oxygen excess of $\lambda=2$, was studied after calcination at 400°C in 10% O_2/N_2 for 30 min. The variation of the normalized CO oxidation rate (normalized to 1 g of Au) is illustrated for two different catalysts ($Au/TiO_2(1)$ and $Au/TiO_2(3)$) in fig. 3.3-1. TOF numbers can be derived from these rates via the catalyst dispersion ($Au/TiO_2(1)$: 31.6% dispersion and $Au/TiO_2(3)$: 35.4% dispersion after calcination at 400°C, for details see section 3.1)); in the present case a rate of 10^{-3} mol·g_{Au}·s^{-1} corresponds to TOF numbers of 0.62 s^{-1} for catalyst $Au/TiO_2(1)$ and 0.56 s^{-1} for catalyst $Au/TiO_2(3)$, respectively. In both reaction atmospheres the reaction rates decay continuously with decreasing CO partial pressure. (Note that because of the constant λ in these measurements the O_2 partial pressure is reduced in the same way). As can be seen in the double logarithmic plot in fig. 3.3-1, the logarithmic reaction rates are proportional to the logarithmic CO partial pressure over the entire investigated pressure range (0.03–2 kPa), indicating a constant reaction order in a power law description of the reaction rates in this partial pressure range. In the present case, with constant λ, the slope of the resulting lines yields the overall reaction order α^{λ}_{CO}, which in this description is related to the reaction orders for CO and O_2, α_{CO} and α_{O2}, respectively, by $\alpha^{\lambda}_{CO}=\alpha_{CO}+\alpha_{O2}$ [20]. This correlation is deduced from the simple power-law functionality, by which the CO oxidation is described commonly:

$$\ln(r_{CO}) = \ln(k_{CO}) - \frac{E_A}{R \cdot T} + \alpha_{CO} \cdot \ln(p_{CO}) + \alpha_{O_2} \cdot \ln(p_{O_2})$$

for $p_{CO}=p_{O2}$, the slope of $\ln(r_{CO})$ versus $\ln(p_{CO})$ corresponds to:

$$\left(\frac{\partial \ln(r_{CO})}{\partial \ln(p_{CO})}\right)_{\lambda=\text{const}} = \alpha_{CO} + \alpha_{O_2} = \alpha^{\lambda}_{CO}$$

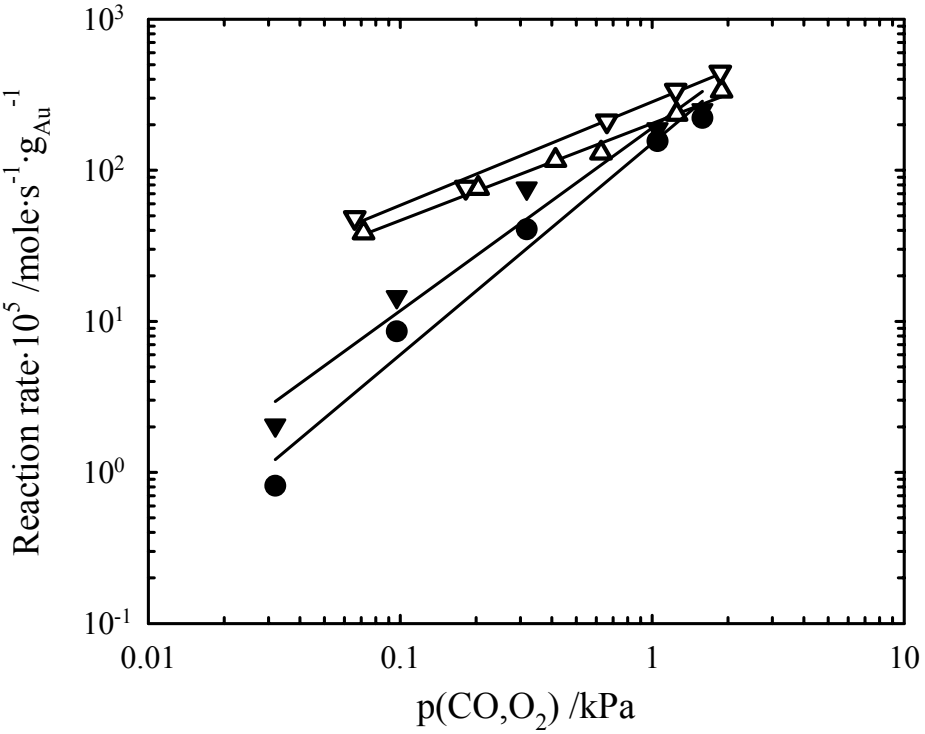

Figure 3.3-1: Determination of the overall reaction orders (α^{λ}_{CO}, λ=2, $p_{CO}=p_{O2}$=variable) for CO oxidation in a H_2-free (1 kPa CO, 1 kPa O_2, balance N_2) and in H_2-rich (1 kPa CO, 1 kPa O_2, 75 kPa H_2, balance N_2) atmosphere at 80°C after calcination at 400°C in 10% O_2/N_2 for 30 min. △: $Au/TiO_2(1)$ in H_2-free atmosphere measured from low to high (α^{λ}_{CO}=0.64) and ▽: from high to low partial pressures (α^{λ}_{CO}=0.69); ▼: $AuTiO_2(1)$ in H_2-rich atmosphere (α^{λ}_{CO}=1.21); ●: $Au/TiO_2(3)$ in H_2-rich atmosphere (α^{λ}_{CO}=1.40). The deactivation during reaction was corrected. For experimental conditions see Appendix B II.

For reaction in H_2-free atmosphere (open symbols) we show the two data sets, which were obtained on the same catalyst ($Au/TiO_2(1)$), but in a different sequence of measurements, one with increasing partial pressure (△), the other with decreasing partial pressures (▽). The data sets obtained in H_2-rich atmosphere (filled symbols) represent results obtained on two different catalysts, $Au/TiO_2(1)$ (▼) and $Au/TiO_2(3)$ (●).

Comparing the results obtained in the absence of H_2 (open symbols) with those measured in a H_2-rich atmosphere (filled symbols), it is obvious that the pressure dependence is much more pronounced for CO oxidation in the H_2-rich atmosphere, with a slope of α^{λ}_{CO}=1.21 (filled points) compared to α^{λ}_{CO}=0.66 in a H_2-free gas mixture (catalyst $Au/TiO_2(1)$). For $p_{CO} < 1$ kPa the CO oxidation rate is generally lower in the H_2-rich atmosphere than in the absence of H_2. The difference, however, decreases with increasing partial pressures.

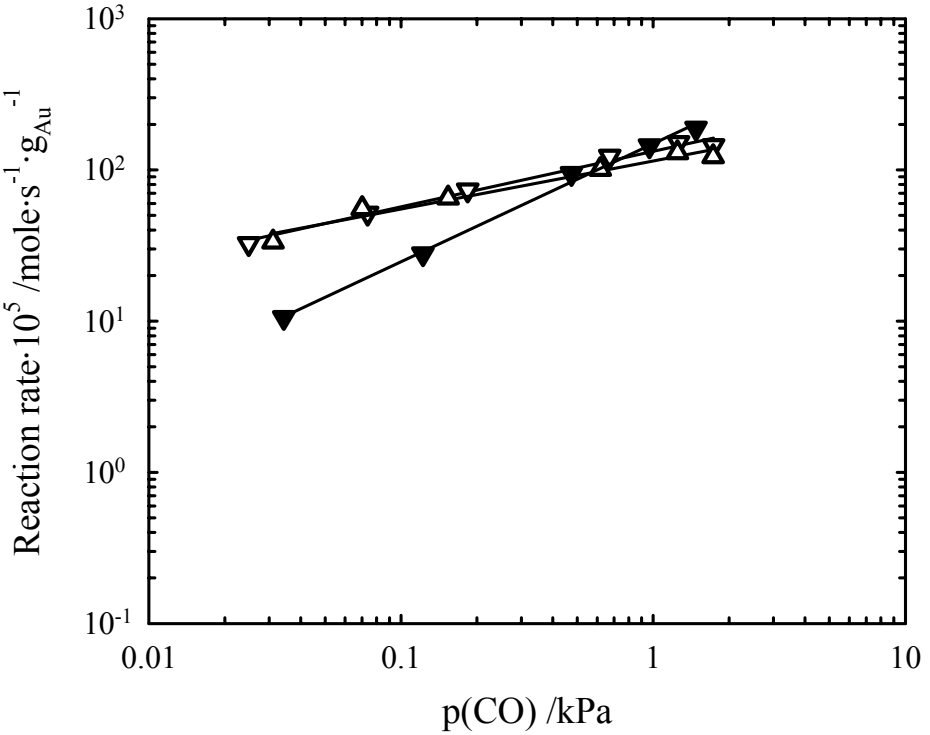

Figure 3.3-2: Determination of CO reaction orders (α_{CO}, p_{O2}=0.1 kPa, p_{CO} variable) for CO oxidation in a H_2-free (1 kPa CO, 1 kPa O_2, balance N_2) and a H_2-rich (1 kPa CO, 1 kPa O_2, 75 kPa H_2, balance N_2) atmosphere at 80°C after calcination at 400°C in 10% O_2/N_2 for 30 min. △: $Au/TiO_2(1)$ in H_2-free atmosphere measured from low to high (α_{CO}=0.32) and ▽: from high to low partial pressures (α_{CO}=0.37); ▼: $AuTiO_2(1)$ in H_2-rich atmosphere (α_{CO}=0.78) measured from high to low pressures. The deactivation during reaction was corrected. For experimental conditions see Appendix B II.

The CO reaction order, α_{CO}, was determined by keeping the O_2-partial pressure constant at 0.1 kPa and varying the partial pressure of CO between 0.025 and 2 kPa (fig. 3.3-2). Also in this case the data lie on a straight line, both for reaction in H_2-free (open symbols) and H_2-rich atmosphere (filled symbols). The slope is again considerably higher in the latter case, and the rates coincide at the highest pressures (1-2 kPa). The absolute values agree well with those in fig. 3.3-1 for comparable conditions (p_{CO}=p_{O2}=0.1 kPa).

The O_2 reaction order, α_{O2}, was determined by keeping the CO-partial pressure constant at 1 kPa and varying the partial pressure of O_2 between 0.01 and 3 kPa (fig. 3.3-3). Again the data fall on a straight line, both for reaction in a H_2-free (open symbols) and in a H_2-rich atmosphere (filled symbols). The absolute values agree well with those in fig. 3.3-1 for comparable conditions (p_{CO}=p_{O2}=1 kPa). In this case, however, the reaction order α_{O2} is not sensitive to the reaction atmosphere, with α_{O2}=0.32 in H_2-free atmosphere and α_{O2}=0.36 in H_2-rich atmosphere (catalyst $Au/TiO_2(1)$). In agreement with the findings for constant λ the

effect of the reaction atmosphere is rather small, though the rates are still higher in the absence of H_2 than in the presence of H_2.

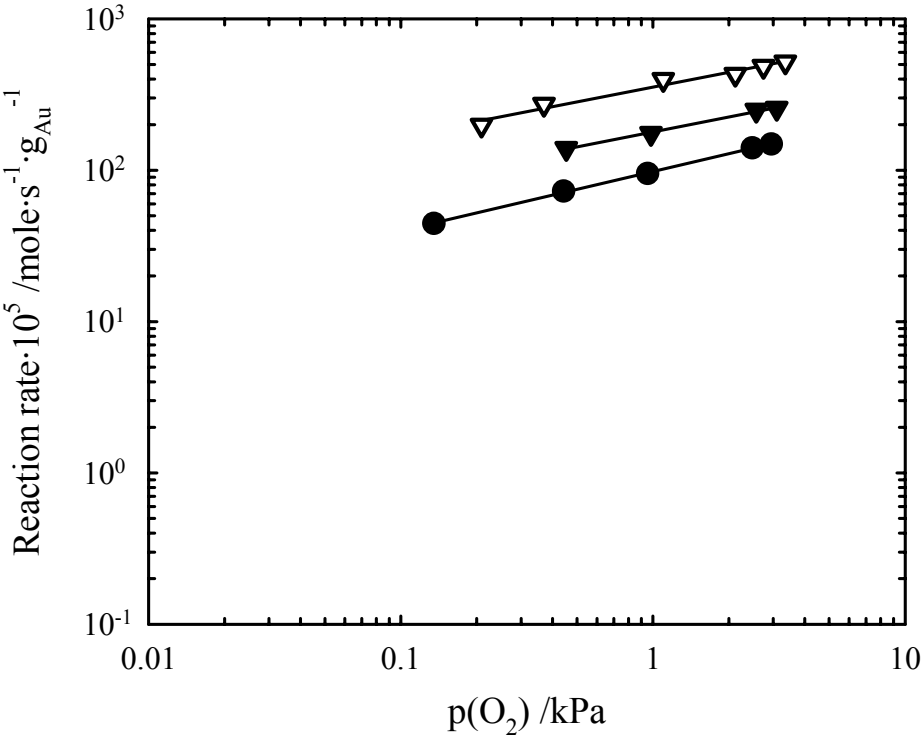

Figure 3.3-3: Determination of O_2 reaction orders (α_{O2}, p_{CO}=1 kPa, p_{O2} variable) for CO oxidation in a H_2-free (1 kPa CO, 1 kPa O_2, balance N_2) and a H_2-rich (1 kPa CO, 1 kPa O_2, 75 kPa H_2, balance N_2) atmosphere at 80°C after calcination at 400°C in 10% O_2/N_2 for 30 min. ▽: $Au/TiO_2(1)$ in H_2-free atmosphere (α_{O2}=0.32); ▼: $AuTiO_2(1)$ in H_2-rich atmosphere (α_{O2}=0.36); ●: $Au/TiO_2(3)$ in H_2-rich atmosphere (α_{O2}=0.39).The deactivation during reaction was corrected. For experimental conditions see Appendix B II.

Using the reaction orders α^{λ}_{CO} and α_{O2}, α_{CO} can also be determined via the relation $\alpha^{\lambda}_{CO}=\alpha_{CO}+\alpha_{O2}$. The resulting values for α_{CO} are very close to those determined directly from the data in fig. 3.3-2, at very different O_2 partial pressures. This indicates that there are no major changes in the reaction mechanism within the pressure range used in these experiments. The mean values of α_{CO} and α_{O2} of the two studied catalysts $Au/TiO_2(1)$ and $Au/TiO_2(3)$ in H_2-rich and H_2-free atmosphere are listed in table 3.3-1.

Table 3.3-1: Summary of reaction orders for CO oxidation over the catalysts $Au/TiO_2(1)$, $Au/TiO_2(3)$ and $Au/TiO_2(5)$ (see figs. 3.3-1 to 3.3.-4).

Catalyst	$Au/TiO_2(1)$		$Au/TiO_2(3)$	$Au/TiO_2(5)$
Reactive atmosphere	H_2-rich	H_2-free	H_2-rich	H_2-free
α_{CO}	0.82±0.16	0.34±0.07	1.01±0.15	0.72±0.22
α_{O2}	0.36±0.02	0.32±0.03	0.39±0.02	0.39±0.07

A completely different CO reaction order in H_2-free atmosphere can be observed for the Degussa catalyst Au/TiO_2(5) (see fig. 3.3-4 and table 3.3-1, the CO reaction order was calculated from the overall reaction order, α^{λ}_{CO}=1.11±0.15, and the oxygen reaction order, α_{O2}=0.39±0.07). With a value of α_{CO}=0.72±0.22 it is out of the range of the Sachtleben catalysts Au/TiO_2(1), also with consideration of the error bars. This difference can not originate in the gold particles, since for both catalysts the particle sizes were ~3 nm and gold was in metallic state. The differences between the two catalysts were i) the BET surface (50 and 56 m^2 for the Sachtleben and Degussa catalyst, respectively) and ii) the composition of the TiO_2 support (anatase for the Sachtleben and 25 % rutile, rest anatase for the Degussa catalyst, respectively). Hence, the significantly stronger dependence of the reaction rate on the CO partial pressure for the Degussa catalyst must originate either in the higher BET surface or in the rutile.

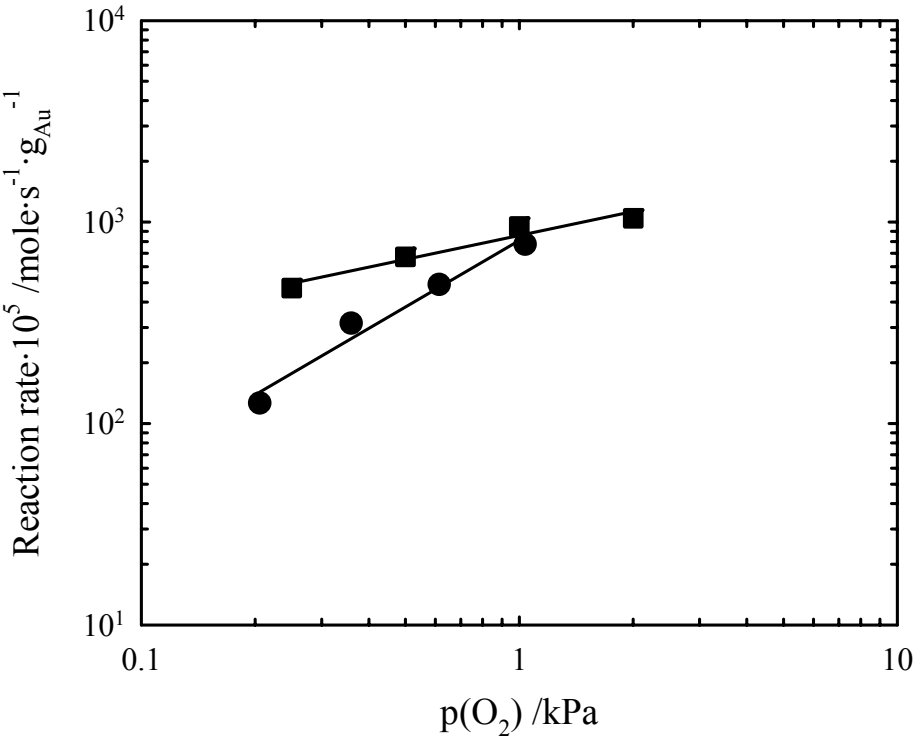

Figure 3.3-4: Determination of overall (●, p_{CO}=p_{O2}=0.2-1 kPa, α^{λ}_{CO}=1.11±0.15) and O_2 reaction orders (■, α_{O2}, p_{CO}=1 kPa, p_{O2}=0.25-2 kPa, α_{O2}=0.39±0.07) for CO oxidation in a H_2-free atmosphere on the Degussa catalyst Au/TiO_2(5). The deactivation during reaction was corrected. For experimental conditions see Appendix B II.

Table 3.3-2: Kinetic parameters for CO oxidation over supported Au/TiO_2 catalysts and relevant reaction parameters.

Cat.Load. wt%	**Prep.**	**Catal. Cond.**	**d_{Au}** nm	**α_{CO}**	**p_{CO};p_{O2}** kPa	**α_{O2}**	**p_{CO};p_{O2}** kPa	**T** K	**E^*** kJ/mol	**Ref.**
H_2-free atmosphere										
3.3	DP	C	3	0.05	0.5-20; 20	0.24	1; 0.7-20	273	34	[11]
2.3	IM	HTR/C/LTR	30	0.24[+]	2-25; 5	0.4[++]	5; 2-19	313-333	9.6	[40]
1	IM	HTR/C/LTR	30	~0.4[§]	n.r.; 5	~0[§]	5; n.r.	273-313	29	[39]
2	IM	HTR, C	30	0.45	0.5-2; 4	0.19	0.3-2, 4	320	32	[70]
1	IM	C		0.25	n.r.	0.41	n.r.	n.r.	16.3	[63]
1	IM			0.2	3.67-16.5; 3.67	0.46	3.67-17.0, 3.67	293	16.3	[31]
2.4	DP	LTR,C	2.7	0.34	0.02-2; 0.1	0.32	1; 0.2-3	353	--	Pres. work
3.4	DP	C	3.1	0.72	0.2-1;0.2-1	0.39	1;0.25-2	353		Pres. work
H_2-rich atmosphere										
2.4	DP	C	2.7	0.82	0.02-2; 0.1	0.36	1; 0.1-3	353	25	Pres. work

Abbreviations used in this table: DP: Deposition-Precipitation, IM: Impregnation, LTR: low temperature reduction, HTR: high temperature reduction, C: calcination;

[+] 0.6 at 353 K, 0.5 at 313 K and lower pressures;

[++] α_{O_2} may be somewhat lower at lower pressures;

[§] The difference in reaction orders between [40] and [39] was explained by these authors by changes in the 2.3% Au/TiO_2 catalyst due to stronger deactivation before the data were collected [39].

For comparison with previous studies we have collected the reaction orders determined in the present study and values reported in previous kinetic studies as well as the relevant reaction conditions in table 3.3-2. For reaction at 0°C on a 3.3 wt% Au/TiO_2 catalyst Haruta et al. derived a CO reaction order near zero (α_{CO}=0.05), an O_2 reaction order of α_{O2}=0.24 and an activation energy of 34 kJ/mol [11]. Vannice and coworkers reported reaction orders of α_{CO}=0.4 for reaction between 0°C and 20°C, which increased to α_{CO}=0.56 at 40°C, and an O_2 reaction order of α_{O2}=0 for reaction at 0-20°C ($\alpha_{O2}\approx$0.1 at 40°C) [39]. It should be noted that the catalysts used in the latter study, which were prepared via an impregnation procedure, exhibited much larger Au particles (particle size 30 nm) than the catalysts used by the Haruta group (2.5-5 nm, as visible on the TEM image in that paper), which were also prepared via a deposition precipitation procedure as was used for the catalysts presented here. For reaction on a 2% Au/TiO_2 catalyst prepared by an incipient wetness technique Cant and Ossipoff determined reaction orders of α_{CO}=0.45 and α_{O2}=0.19 under comparable conditions as well as an activation energy of 32 kJ/mol [112]. Using a different procedure for catalyst preparation, by grafting a Au-phosphine complex onto TiO_2 support material, Choudhary et al. derived reaction orders of α_{CO}=0.2 and α_{O2}=0.46 at 20°C for a 1 wt% Au/TiO_2 catalyst, and an activation energy of 16.3 kJ/mol [31]. Almost identical values were reported also by Liu et al. for a similar type catalyst [63].

The main results of this comparison are that (i) there is a considerable spread in the data and that (ii) in all studies both the CO and the O_2 reaction orders are slightly positive, between 0.05 and 0.46. The sum of the two reaction orders, which can be equated with α^{λ}_{CO}, if the mechanism does not change, increases with increasing temperature, which was also observed during measurements with the low-pressure micro-reactor (section 3.4). Furthermore, part of the spread in the data can be explained by the very different reaction conditions (CO:O_2 ratio, absolute partial pressures, reaction temperature), as, e.g., in the case of the data in ref. [11].

The results obtained in a H_2-rich atmosphere differ significantly from those obtained in the absence of H_2. Here the CO reaction order is more than twice as high as in the absence of H_2, while that for O_2 is little affected by the presence of H_2. An earlier study of the same reaction over Au/Fe_2O_3, which was performed under similar reaction conditions, gave a considerably lower value for the CO reaction order, α_{CO}=0.55, while the O_2 reaction order was of similar magnitude (α_{O2}=0.27) [16]. Hence, the presence of H_2 does not influence the dependence of

the reaction rates on the O_2 partial pressure. Additional kinetic data are rare and do not contain information on details such as reaction orders. Torres Sanchez et al. had shown, that CO can easily be oxidized over a Au/MnO_x catalyst in a H_2 feed streem (p_{CO}=p_{O2}=1 kPa, rest H_2) at temperatures of 50 – 100°C, but that the CO conversion decreases slightly at higher temperatures (120°C) [146]. This was attributed to increasing O_2 consumption by H_2 oxidation [146]. A reduction in the CO oxidation activity over Au/TiO_2 in the presence of H_2 by about one third, from 0.9 mmol/s·g_{Au} to 0.6 mmol/s·g_{Au}, can be calculated from the data in [31], which were obtained at not very different reaction conditions (80°C, p_{CO}≈2 kPa, p_{H2}≈48 kPa, λ=4) compared to ours. This reduction in reaction rate in the presence of hydrogen could not be observed in our activity measurements (see fig. 3.2-6). A comparison of the PROX activity of different metal oxide supported Au catalysts (Au/γ-Al_2O_3, Au/Co_3O_4, Au/CeO_2, Au/Fe_2O_3, Au/Ni_2O_3, $Au/Mg(OH)_2$, Au/TiO_2 etc.) at a single gas composition (p_{CO}=p_{O2}=1 kPa) by Schubert et al. [33] revealed a considerable variation in activity and selectivity. Likewise, Grisel et al. had reported that the presence of H_2 in the reactant flow has a slightly negative effect on the CO oxidation activity at room temperature over $Au/MnO_x/Al_2O_3$, but a considerable positive effect for $Au/MgO/Al_2O_3$ (p_{H2}:p_{CO}:p_{O2}=4:2:1, atmospheric pressure) [147].

3.3.2 CO adsorption (DRIFTS)

The kinetic studies revealed an increase in CO oxidation rate for higher CO partial pressures at constant λ. In order to deduce whether this increase of the rate is accompanied by a similar increase in CO_{ad} coverage or other changes in the adlayer, the adlayers resulting under different reaction conditions were investigated by in-situ DRIFTS. This was done in both H_2-free (various p_{CO}, balance N_2) and H_2-rich (various p_{CO}, 75 kPa H_2, balance N_2) dilute CO atmospheres, respectively. Prior to the DRIFTS measurements the catalysts were conditioned either via the reductive treatment or via calcination, as described in chapter 2.6, and then cooled down in a flow of N_2. It turned out, however, that the characteristic features and trends in the DRIFT spectra did not depend on the pretreatment, but increased the activity of the Sachtleben catalysts, as mentioned in subsection 3.2.1.1 (the reaction rates after reductive pretreatment were higher). The only exception was a weak peak in the carbonate region, at 1445 cm^{-1}, which appeared during CO adsorption in a H_2-rich atmosphere on a calcined catalyst, but not on a reductively pretreated Au/TiO_2 catalyst.

3.3.2.1 CO adsorption in H_2-free atmosphere

Spectra recorded in a dilute CO atmosphere, with different amounts of CO in N_2, are presented in fig. 3.3-5. As mentioned in the experimental section, due to an initial change of the reflectivity after the admission of CO (color changes due to partial reduction of the TiO_2 support) the background spectra did not fit perfectly to the CO adsorption spectra, when comparing over the entire spectral range. Therefore, the background subtraction was done separately for two different spectral regions, where these effects are negligible. Accordingly, differences between different background-corrected spectra are not caused by the initial modification of the TiO_2 support but reflect real changes in the adlayer.

The spectra obtained upon adsorption from CO/N_2 mixtures are dominated by the absorption peak of adsorbed CO (see fig. 3.3-5). As expected for CO adsorption on Au nanoparticles, i.e., in agreement with previous observations for CO adsorption on other supported Au catalysts [31,39,61,144,148] and on massive Au surfaces [141,149], only linearly adsorbed CO is observed. The vibrational frequency is almost independent of the CO partial pressure (fig. 3.3-5a, decreasing p_{CO} from bottom to top), with only a slight red shift from 2112 cm^{-1} at 0.05 kPa CO to 2108 cm^{-1} at 1.5 kPa CO partial pressure. The increase in intensity with increasing CO partial pressure and the frequency shift with increasing C-O absorption intensity are plotted in fig. 3.3-6.

A similar behavior of the C-O vibration, with a frequency shift from 2111 to 2104 cm^{-1} upon a CO partial pressure increase from 0.05 to 1.0 kPa, was observed also for CO adsorption on Au/Fe_2O_3 [148] and on massive Au, from 2129 cm^{-1} at $1.33 \cdot 10^{-4}$ kPa CO to 2106 cm^{-1} at atmospheric pressure [141]. In the latter case the peak shift was significantly more pronounced, since the CO partial pressure was varied over a broad range. This chemical shift, which is opposite to the behavior generally observed on transition and noble metal surfaces [150], had been explained by the lack of back donation from Au d-electrons into the $2\pi^*$ orbital of adsorbed CO, so that the Au-CO bond is dominated by electron donation from the 5σ orbital of the CO molecule, which is slightly anti-bonding for the C-O bond, to the metal [141]. With increasing CO coverage this effect becomes weaker, leading to a weakening of the C-O bond. This was the only peak in the C-O region. Additional peaks at 2071 cm^{-1}, as reported by Bollinger et al. during CO adsorption (p_{CO}=5 kPa) at room temperature [39], or of

a peak at 2183 cm^{-1} as reported by Haruta et al. [11], which was attributed to CO adsorption on Ti^{4+} sites at room temperature, can not be observed.

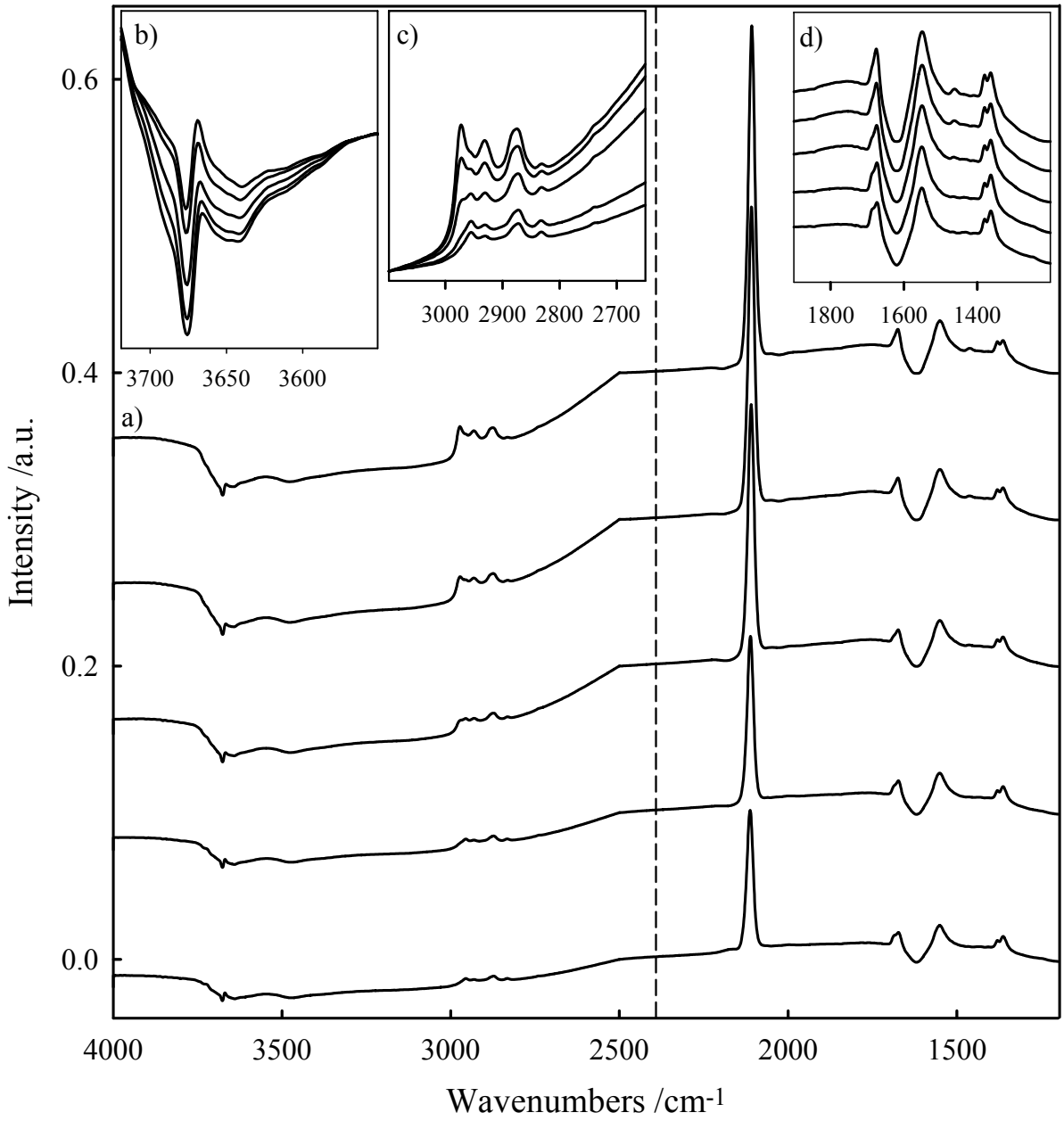

Figure 3.3-5: IR spectra recorded upon adsorption of CO from H_2-free gas mixtures containing increasing amounts of CO in N_2 on the catalyst $Au/TiO_2(1)$ (undiluted catalyst; reductive conditioning). a) Complete spectra, b) enlarged detail spectra of the spectral range characteristic for OH groups (on the support), c) enlarged detail spectra of the formate region, and d) enlarged detail spectra of the carbonate region. From bottom to top (fig. 3.3-5c top to bottom): 0.05 kPa CO, 0.1 kPa CO, 0.5 kPa CO, 1.0 kPa CO, 1.5 kPa CO.

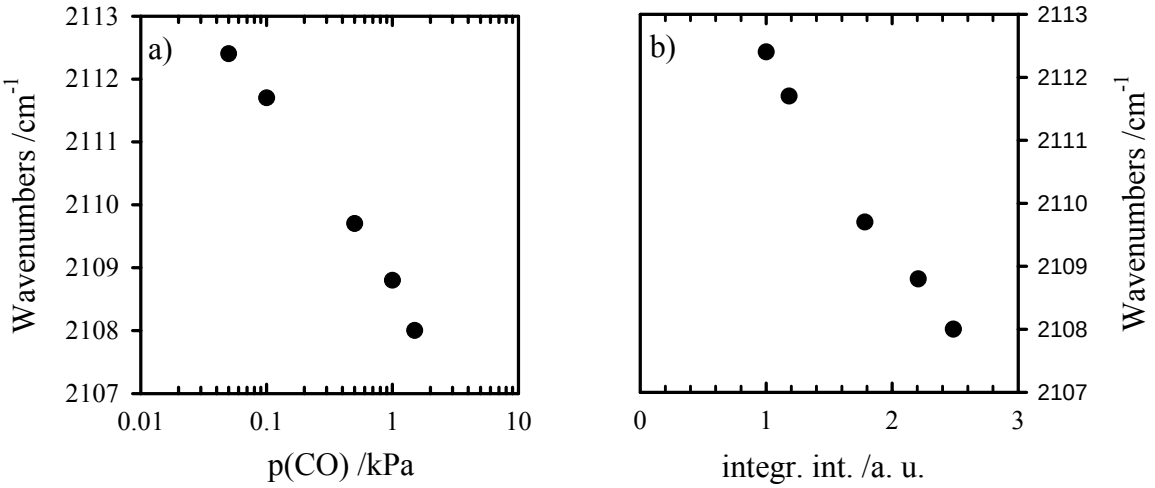

Figure 3.3-6: a) Frequency shift of the C-O stretch vibration with increasing CO partial pressure upon CO adsorption from H_2-free gas mixtures containing increasing amounts of CO in N_2 (see fig. 3.3-5). b) Frequency shift with increasing peak intensity (data from fig. 3.3-5a).

In addition to the C-O vibration signal the spectra exhibit weak, but characteristic absorption peaks also in the spectral ranges of 1350-1700 cm^{-1} (carbonate, carboxylate, and formate species), 2800-3000 cm^{-1} (C-H vibration of formates), and around 3630 cm^{-1} (O-H vibrations) [11,39,144,145]. In the 'carbonate/carboxylate region' (detail spectra see fig. 3.3-5d, for the structures see fig. 3.2-15), characteristic absorption lines are visible at 1672 cm^{-1}, 1552 cm^{-1}, 1381 cm^{-1} and 1363 cm^{-1}. (After oxidative pretreatment an additional weak peak at 1445 cm^{-1} appears at all CO partial pressures.) In previous studies peaks at 1690 cm^{-1} and 1585 cm^{-1} had been assigned to bidentate carbontes on the support [39,151]. Liao et al. distinguished between bridging carbonate (bound to two Ti ions) with frequencies around 1725 cm^{-1} on TiO_2 and bidentate carbonates (bound to a single Ti ion) with frequencies around 1560 cm^{-1} [152]. A peak at 1440 cm^{-1} was assigned to monodentate carbonate [144,152] or free carbonate, which is identical to bulk carbonate [39,152]. Vibrations between 1330 cm^{-1} and 1370 cm^{-1} were assigned to COO symmetric stretch frequencies of monodentate (1330 cm^{-1}) and bidentate (1370 cm^{-1}) carbonates as well as formates (1370 cm^{-1}) on the TiO_2 support [33,39,144,145,152,153]. Bond and Thompson had proposed that these species are formed by reaction of a CO molecule adsorbed on a Au particle ('Au^0-CO') with a hydroxyl group adsorbed either on a support cation or on a peripheral ionic Au species, e.g., a Au^{III} ion ('periphery mechanism') [5]. In their model, the hydroxyl group is recovered during CO oxidation when two carboxylate ions are oxidized by a superoxide ion. This explanation agrees with the observation that the intensity of the carbonate/carboxylate peaks does not

increase with CO partial pressure (0.05-1.5 kPa). It should be noted that adsorbed OH species are present on TiO_2 even after calcination at 500°C [126].

The proposed interaction of CO with OH_{ad} on peripheral sites agrees well with the evolution of the OH peak with increasing CO partial pressure (enlarged detail spectra see fig. 3.3-5b). The negative peak in the spectra of the O-H stretch frequency at 3677 cm^{-1} fits excellently to OH adsorbed on pure TiO_2, which was reported to have a characteristic absorption band at 3676 cm^{-1} [143,154]. The negative peak in the spectra indicates a decreasing amount of these species in a CO/N_2 atmosphere compared to that in pure N_2. A chemical interaction or even reaction with adsorbed CO changes the chemical state of the OH group and therefore also the frequency of the O-H stretch vibration, resulting in a positive peak at a somewhat different frequency. The red-shift of the new vibration points to a weakening of the O-H bond in the new OH_{ad} species due to interaction/reaction with CO_{ad}.

The intensity of the positive O-H peak does not change with the CO partial pressure in the gas mixture, which fits well to the constant intensity of the carboxylate species. In contrast, the intensity of the negative peak increases with higher CO concentrations, indicating that the consumption of the OH groups is caused not only by the formation of the carbonate/carboxylate species, but by additional reaction. This is confirmed in the detail spectra in fig. 3.3-5c, which show the continuous growth of characteristic peaks in the formate region, at 2833 cm^{-1}, 2873 cm^{-1}, 2931 cm^{-1} and 2955 cm^{-1} [39,145]. These peaks had been assigned to C-H stretch vibrations in formates adsorbed on the anatase support [39]. In addition, starting at partial pressures of 0.5 kPa a new peak appears at 2972 cm^{-1}, whose origin has not yet been clarified. This feature grows continuously with CO partial pressure (and adsorption time), in good agreement with the continuous consumption of OH species indicated by the behavior of the negative peak at 3677 cm^{-1}.

3.3.2.2 CO adsorption in H_2-rich atmosphere

For CO adsorption from a CO/H_2 atmosphere the results are very different. Since the DRIFT spectra showed slow modifications in their overall shape over a significant time span, spectra recorded at three different CO partial pressures after two minutes (fig. 3.3-7a) and the temporal evolution of spectra in 0.5 kPa CO in H_2/N_2 (fig. 3.3-7b) are presented. Equally to the CO adsorption in H_2-free atmosphere, background removal was performed in the two regions above and below 2800 cm^{-1} separately. The C-O stretch vibration is slightly

red-shifted compared to adsorption in H_2-free atmosphere, from about 2110 cm^{-1} to 2107 cm^{-1}. This peak increases in intensity, but does not shift with increasing CO partial pressure (fig. 3.3-7a). With increasing adsorption time at 0.5 kPa this peak decreases in intensity and is replaced by an asymmetric peak at 2032 cm^{-1}, which includes a shoulder at around 1985 cm^{-1} and possibly a second one at around 1930 cm^{-1} (fig. 3.3-7b). Bollinger et al. report a weak signal at 2062 cm^{-1} upon CO adsorption on a Au/TiO_2 catalyst pretreated by low temperature reduction as a last step, which disappears again upon O_2 addition [39]. Similar observations were reported by Boccuzzi et al., who observed a comparable peak at 2055 cm^{-1}, with a shoulder at 1990 cm^{-1}, for CO adsorption on a Au/TiO_2 sample that was reduced with H_2 at 255°C before adsorption, in addition to the 'normal' peak at 2100 cm^{-1} [110]. On the other hand, this new feature was not observed for CO adsorption from a similar H_2-rich atmosphere on Au/Fe_2O_3 [32]. Boccuzzi et al. explained their findings by a reduction of the support due to reaction with H_2 and a resulting transfer of negative charge to the gold particles, which leads to an increased back-donation and hence to a weakening of the C-O bond, in agreement with the observed peak shift. A charge transfer from TiO_2 to Au nano particles has indeed been reported by Jakob et al. [155] when exposing TiO_2 nano particles to UV-radiation and bringing the resulting, partly reduced, colored TiO_2 nano particles into contact with Au nano particles. They reduced Ti^{4+} by generating electron hole pairs via the UV radiation and trapping the holes. Since in our case also an electron surplus is generated at the Ti atoms, their findings could be applied to our observation. The detail spectra in the inset (fig. 3.3-7c) show a significant rise of the OH peak at 3775 cm^{-1} with increasing adsorption time, indicating that TiO_2 reduction takes place under present conditions. Other possible explanations for the shift in C-O frequency include interactions between H_{ad} and CO_{ad} species coadsorbed on the Au nano particles, or a H_{ad} induced decrease in the steady state CO coverage. In all three cases, however, one would expect a continuous shift in the C-O frequency and not a new peak at a fixed frequency, as it is observed experimentally. The latter fits better to a distinctly different new CO_{ad} species as expected, e.g., for a compound like a H-Au-CO adsorption complex, similar to reports for H_2/CO coadsorption on Ni(100) [156,157], or for a severe, H_2-induced restructuring of the Au nanoparticles. An experimental prove, however, can not be given for this theory. Finally it is noted that neither formates nor carbonate/carboxylate species are formed in the presence of H_2.

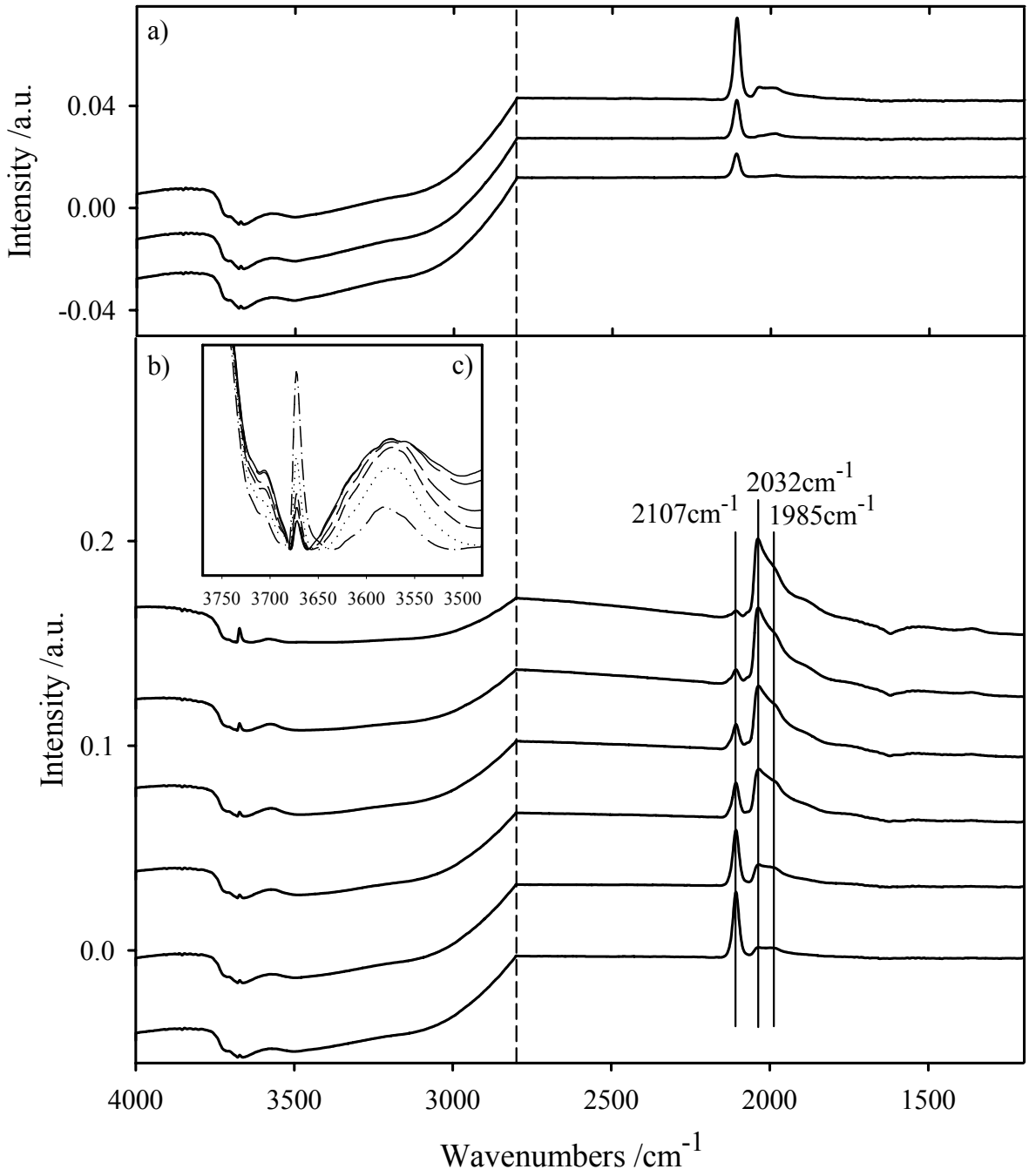

Figure 3.3-7: DRIFT spectra recorded upon adsorption of CO from H_2-rich gas mixtures containing different amounts of CO in 75 kPa H_2, balance N_2 (on the catalyst $Au/TiO_2(1)$ (undiluted catalyst; reductive conditioning). a) Pressure dependence (bottom to top): 0.05 kPa CO, 0.1 kPa CO, 0.5 kPa CO; spectra taken after 2 min. b) (complete spectra) and c) (detail spectra between 3770 cm^{-1} and 3480 cm^{-1}) show the temporal evolution of the spectra during adsorption from 0.5 kPa CO (from bottom to top in fig. 3.3-7b and in fig. 3.3-7c at 3675 cm^{-1}, from top to bottom at in fig. 5c at 3570 cm^{-1}: 2 min, 7 min, 30 min, 60 min, 120 min, and 240 min).

3.3.3 Isotope scrambling (IMR-MS)

In this section we describe experiments using isotope-labeled reactants. They were performed to get more information on the interaction of O_2 and CO with the catalyst. For all experiments the gas mixtures were passed to the bypass mode (flow through the bypass), before they were switched to the reactor mode (flow through reactor), in order to determine the inlet concentrations. In order to test whether the interaction of O_2 with the catalyst under reaction conditions results in isotope scrambling, i.e., if O_2 is dissociated without the presence of CO, a mixture of $^{16}O_2$ and $^{18}O_2$ was introduced to a dilute Au/TiO_2 catalyst (see fig. 3.3-8). The catalyst was calcined at 400°C before the experiments.

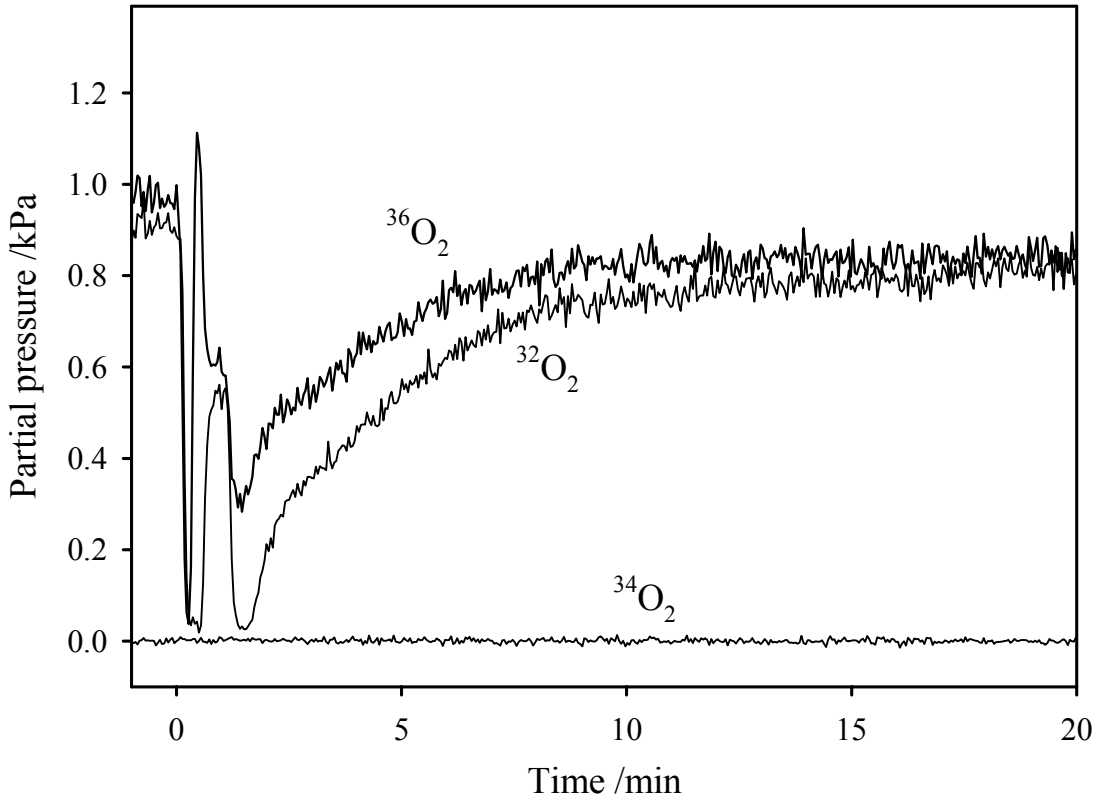

Figure 3.3-8: Introduction of 0.9 kPa $^{32}O_2$ and 1.0 kPa $^{36}O_2$ to the diluted Au/TiO_2(2) catalyst (diluted 1:15 with α-Al_2O_3, 100.7mg, flux: 40 Nml/min, 80°C). At t=0 min the gas mixture was introduced to the sample. At t<0 min the gas mixture passed the sample.

As shown in fig. 3.3-8, no $^{16}O^{18}O$ was formed, neither during the exposure to $^{16}O_2$ and $^{18}O_2$ under those conditions (fig. 3.3-8) nor during a subsequent desorption spectrum, when the sample was heated up to 300°C (fig. 3.3-9). This rules out reaction pathways involving dissociative adsorption and the formation of adsorbed O_{ad}, which could undergo recombinative desorption, on this catalyst. These findings agree fully with results from Iwasawa and coworkers [63,158], who studied the room temperature adsorption-desorption

behavior of a similar isotope labeled O_2 gas mixture on a Au/TiO_2 catalyst prepared from organic gold and titanium precursors and calcined at 400°C for 4 h, and from a study of the transient O_2 adsorption/desorption behavior by Olea et al. on the same catalyst [159]. Hence, the preparation of the Au/TiO_2 does not influence its interaction with O_2. It also agrees with observations in previous studies on Au/Fe_2O_3 catalysts, prepared by deposition precipitation or supporting $Au(PPh_3)(NO_3)$ on as-precipitated wet iron hydroxide, followed by calcination at 400°C, at 75°C and room temperature, respectively, where equally no isotope scrambling, i.e., no $^{16}O^{18}O$ formation, was observed [8,160].

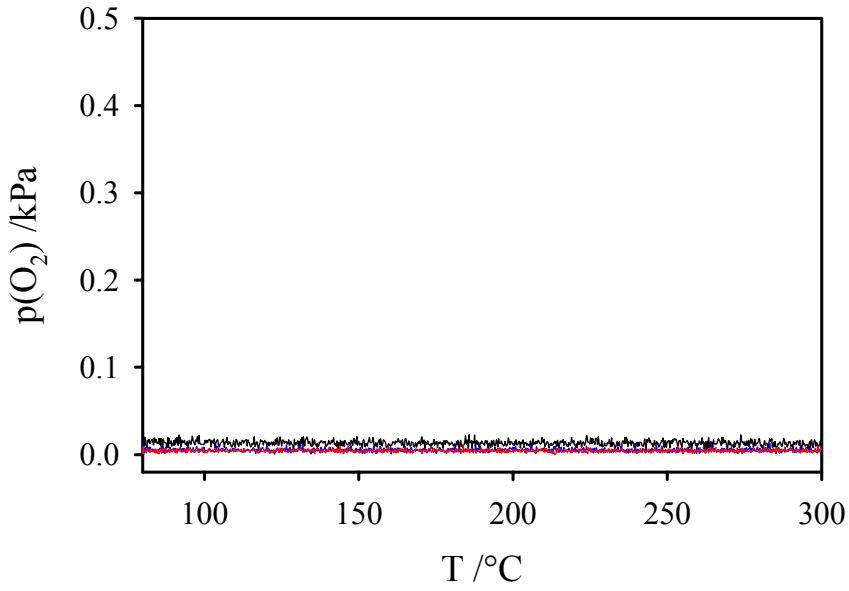

Figure 3.3-9: $^{32}O_2$ (black line), $^{34}O_2$ (red line) and $^{36}O_2$ (blue line) partial pressures during heating in 12 Nml/min N_2 (5°C/min) after exposing the sample to a $^{36}O_2$ and $^{32}O_2$ containing gas mixture (fig. 3.3-8)

The temporal evolution of the O_2 signals can not be analyzed here, since pressure surges occurred, when switching from the bypass mode to the reactor mode, which influenced the shape of the $^{36}O_2$ and $^{32}O_2$ curves in an unknown way.

Next is was tested whether the interaction of CO with the O-saturated Au/TiO_2 catalyst leads to oxygen exchange or reaction, by passing $C^{18}O$ over it (fig. 3.3-10). From the absence of any detectable amounts of $C^{16}O$ this can clearly be ruled out. Also CO_2 formation could not be observed. Hence significant contributions from a Mars-van-Krevelen type mechanism [161] can equally be ruled out under the present conditions. These results equals the behavior reported by Liu et al. [63]. The close similarity in the reaction behavior between their Au/TiO_2 catalyst and the Au/TiO_2 catalyst here, prepared via deposition precipitation, leads to

the conclusion, that there are no basic differences in the reaction mechanism on these rather differently prepared Au/TiO_2 catalysts.

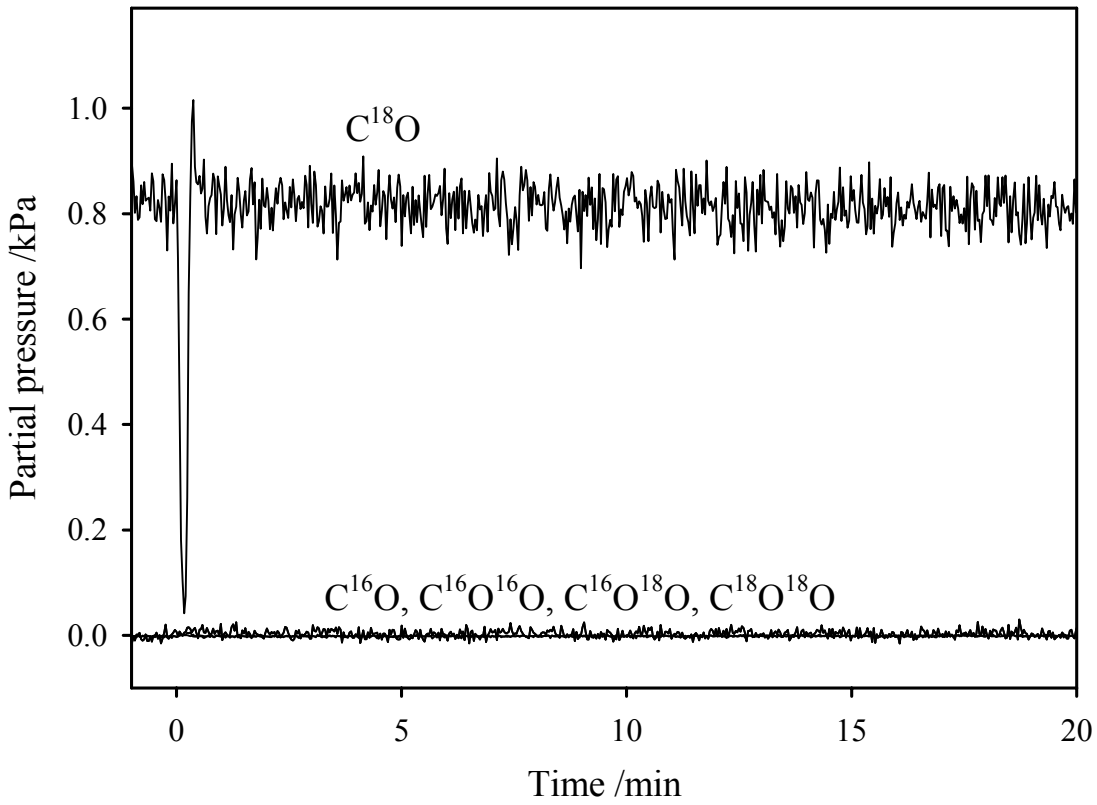

Figure 3.3-10: Introduction of $C^{18}O$ in N_2 to diluted catalyst Au/TiO_2(2) (1:5 with α-Al_2O_3, 74.6mg, flux: 40 Nml/min, 80°C). At t=0 min the gas mixture was introduced to the sample. At t<0 min the gas mixture passed the sample.

As a summary, of this chapter the following statements can be made. First, the presence of H_2 in the gas mixture leads to a significantly higher CO reaction order, while the reaction order for O_2 is not affected by the gas composition. Second, CO adsorption on Au/TiO_2 is also affected by H_2: In H_2-free atmosphere mainly linearly adsorbed CO is observable, beside small amounts of carbonate and carboxylate species, while in H_2-rich atmosphere a new CO_{ad} species developed, which could best be explained by H-Au-CO coadsorption. Third, neither for O_2 nor for CO, isotope scrambling could be observed upon interaction with Au/TiO_2. Additional experiments with isotope labeled gases are presented in section 3.5.

3.4 Reaction kinetics in the pressure gap

As mentioned in the introduction, CO oxidation on Au/TiO_2 model catalysts in the low partial pressure regime ($p_{CO}=10^{-7}$ - 10^{-6} mbar), was observed only with pre-adsorbed O_{ad} [54,57,58,81], while in the $p_{CO,O2}$=1-10 mbar range it could be observed during simultaneous introduction of gaseous CO and O_2 [35,82,83]. This is the same partial pressure range, in which CO oxidation on powder catalysts is performed [4-7]. Despite of the differences between model and powder catalysts, the reaction rates, determined in the 1-10 mbar region, were in the same range. Hence, the question arises, whether it is only an effect of the pressure gap, that for Au/TiO_2 model catalysts no oxidation of CO by gaseous O_2 was reported in the low pressure regime, or whether this reflects characteristic differences between the two materials. To verify this assumption, this chapter presents results of activity measurements on highly disperse Au/TiO_2 catalysts for CO and O_2 partial pressures <1-10 mbar.

The material gap reflects the differences between well ordered single crystal systems and in an experimental set-up laid out for these conditions on the one hand and non-ordered, highly dispersed powder samples on the other hand. The pressure gap originates from the different experimental conditions typically applied studies on these two kinds of material. Single crystal experiments are typically performed under ultra high vacuum conditions (UHV, $p \leq 10^{-9}$ mbar) [1], while measurements on powder samples are usually carried out at atmospheric pressure (10^3 mbar).

To bridge the material gap model catalysts are prepared with chemical and physical properties between those of single crystal, metal samples and powder catalysts [35,58,162-164]. There are different approaches to bridge the pressure gap: From the single crystal and model catalyst side measurements at elevated pressures are performed, e.g., by adding a separate high-pressure cell to standard UHV equipment, which can be closed off from the UHV system while operated at high pressure (see, e.g., [72-77]). Coming from the opposite side, from realistic high surface area catalysts operated at atmospheric pressure, attempts to move to significantly lower operating pressures have been scarce so far. The only exception were TAP (‘*temporal analysis of products*’) reactor studies, where a molecular beam is passed at variable effective pressure through the catalyst bed, while the surrounding atmosphere is held under vacuum conditions (typically <10^{-3} mbar) [78,79]. Another approach is the low pressure plug-flow micro-reactor, which was built by R. Leppelt within the experimental work of his

dissertation (see experimental section and [80]). With this set-up it is possible to carry out measurements in the pressure regime of 10^3-~10^{-1} mbar total pressure (p_{tot}). This reactor was used to determine kinetic data (reaction orders and activation energies) in the pressure gap range, which are presented and discussed in this chapter. Prior to the presentation of the results (section 3.4.2), a section with experimental information is inserted (section 3.4.1), in order to clearly demonstrate the implementation of the experiments and the appearing problems.

3.4.1 Experimental information

All measurements, reported in this chapter were carried out with constant contact times on catalyst Au/TiO_2(5), which was pretreated by calcination at 400°C for 30 min. The contact times were kept constant to avoid influences on the reaction rates, which are not caused by the variation of the partial pressures. As already mentioned in the introduction, the measurements were performed with two different set-ups. The reproducibility of measurements performed with the specific set-ups was as follows: With the initial set-up the maximal error was 22% and with the modified set-up 29%. Measurements performed with both set-ups were less comparable. The reaction rates deviated between 76% up to nearly one decade (538%). For both set-ups no systematic error is obvious, the measurements were performed under equal conditions (p_{tot}, T, gas mixtures). Changes in the performance of the catalyst are not expected, since the catalysts were stored in a deep freezer (see section 2.6). Therefore we used results determined with both set-ups. For a better overview it is marked in the text and in the plots, which set-up was used for the respective measurement.

For the determination of E_A and the overall reaction orders (α^{λ}_{CO}), measurements at fixed p_{tot} were carried out in the following sequence: 80°C-65°C-50°C-125°C-110°C-95°C-80°C. This allowed estimates on possible contribution from catalyst deactivation. Hence the determination of α^{λ}_{CO} was possible at six different temperatures. The second measurement at 80°C at the end of each cycle was done with the objective to check, whether the samples deactivated during the measurements. The corresponding reaction rates are shown as empty symbols in fig. 3.4-2c and fig. 3.4-5c. For each measurement, CO and O_2 were introduced with equal partial pressures (λ=2, 1 vol.-% of the total pressures, balance N_2), whereas in the entire measurement series, $p_{CO,O2}$ were varied from 10 mbar to $9 \cdot 10^{-4}$ mbar. The reaction rates were studied at the following total pressures (p_{tot}): $9 \cdot 10^{-2}$ mbar, $4 \cdot 10^{-1}$ mbar, 4 mbar, 20 mbar,

50 mbar, 10^2 mbar and 10^3 mbar. Except for $p_{tot}=10^2$ and 10^3 mbar, all measurements were carried out with both set-ups.

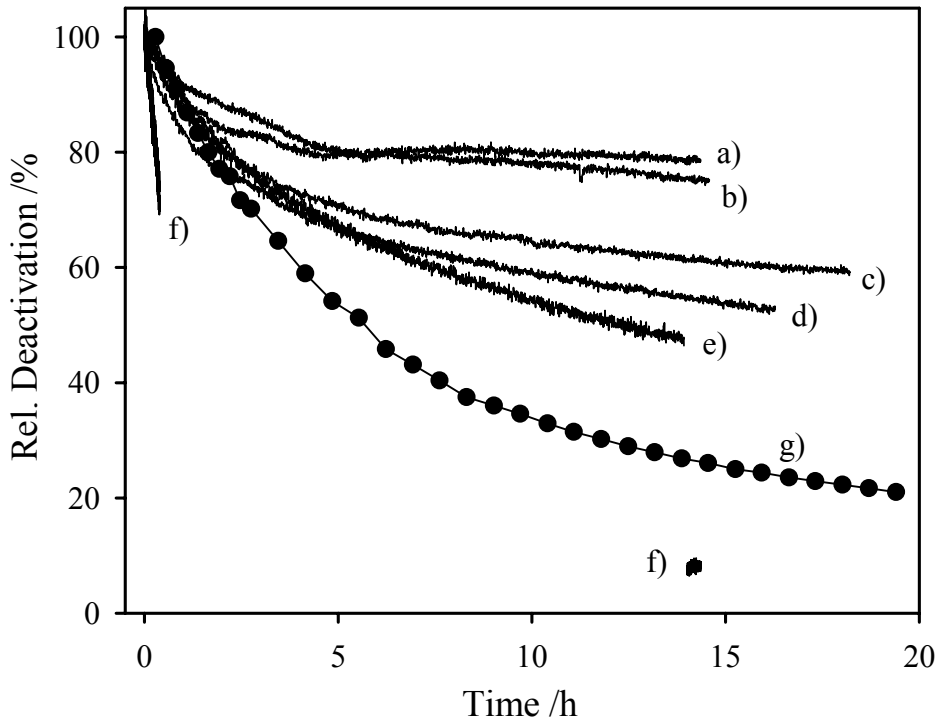

Figure 3.4-1: Relative deactivation of catalyst $Au/TiO_2(5)$ during CO Oxidation at 80°C and the following p_{tot}: a) 50mbar, b) 4mbar, c) 20mbar, d) 0.4mbar, e) 0.09mbar. The values of curve f) were determined in a 'conventional' plug-flow reactor at atmospheric pressure. Curve g) displays the relative deactivation of this catalyst during CO oxidation at atmospheric pressure in a gas flow of 60 Nml/min (data from fig. 3.2-7). All samples were calcined at 400°C in 10% O_2/N_2 for 30 min prior the experiments. The time was set to zero, when the data acquisition was started. The measurements in the low pressure reactor (a-e) were performed with the modified set-up. For experimental conditions see Appendix B II. For details about the two set-ups see experimental section.

Prior to the determination of the reaction rates, the samples were allowed to react over night at the given p_{tot} and 80°C to achieve a steady state situation. The deactivation behavior of the samples at different p_{tot} is shown in fig. 3.4-1. These measurements were carried out with the modified set-up, since the modifications enabled us to set the needed pressures within 1-2 hours (time not exactly equal for all measurements). In fig. 3.4-1 t is set to $t_0=0$ when the data acquisition was started, i.e., after 1-2 hours reaction under these conditions. As can be seen from fig. 3.4-1, the activity decreased to 46%-78% of the initial value during 14 h of CO oxidation (relative deactivation (RD), note that RD is the percentage of activity which was measured after the time t_1, related to the activity at the beginning of the detection, t_0, see equation 3.4-1). No clear dependence on p_{tot} is observable.

$$RD[\%] = 100 \cdot \frac{rate(t_1)}{rate(t_0)} \qquad (3.4\text{-}1)$$

t_1: Duration of reaction

t_0: Start of data acquisition

In order to estimate the deactivation during the first two hours, when the data acquisition could not yet be started because the system was not yet stable, we can use the behavior of the P25 catalysts during the activity measurements described in subsection 3.2.1.2. A comparison of the relative deactivation within in the first 14 h (t_0=0 h, t_1=14 h) and between 2 and 16 h (t_0=2 h, t_1=16 h), shows that the RD values in the first case are ~5% lower. Hence, if this value is subtracted from the relative deactivation observed in fig. 3.4-1, the activity decreased to 41%-73% of the initial values after 14 h of detection. This is a much less pronounced deactivation than observed during the activity measurement of catalyst Au/TiO_2(5) carried out with the GC equipment at a flow of 60 Nml/min (see fig. 3.2-6) and during an activity measurement with the 'conventional' plug-flow reactor connected to the IMR-MS at a flow of 92.7 Nml/min. In the first case the sample deactivated to 26.9% of the initial value and in the second case to 7.5% during 14 h of reaction. Data acquisition for the latter measurement was done during the first 20 min of the reaction and for another 20 min period after 14 h of reaction (the behavior during these two periods and the relative deactivation during the GC measurement is also added in fig. 3.4-1). Since the deactivation of the sample is much stronger under atmospheric conditions than at other p_{tot} values, a compartive measurement with the entire temperature sequence was performed also in the 'conventional' plug-flow reactor connected to the IMR-MS. From this measurement the extent of deactivation at the different temperatures was calculated (related to the activity at the beginning of the reaction). From this, correction factors for the deactivation were calculated and applied to the measurement performed at p_{tot}=1000 mbar in the low pressure reactor (note that these correction factors were not used for the measurements with lower total pressures). This procedure is justified, since the reaction in the low pressure reactor at 1000 mbar and in the 'conventional' plug flow reactor at atmospheric pressure led to similar reaction rates after reaction over night. In the first case the TOF was 0.21 s^{-1} and in the second case 0.17 s^{-1}.

Fig. 3.4-2 illustrates the determination of the overall reaction orders. Always both values for the measurement at p_{tot}=1000 mbar are plotted; the measured reaction rates, i.e., the rates in the deactivated state, with triangles pointing upwards and the corrected values with triangles

pointing downwards. A correction of the reaction rates at other p_{tot} was not made for the following two reasons: i) As can be seen in fig. 3.4-1, the deactivation is much weaker than in the 1000 mbar measurement, hence the error caused by this deactivation will be within the range caused by the 1000 mbar measurement (i.e., the error caused by the 'deactivated' and corrected rates in the slope for the overall reaction orders), and ii) there is no possibility to do comparative measurements like in the case of p_{tot}=1000 mbar and atmospheric pressure.

The use of the 'deactivated' reaction rates at 1000 mbar would cause a break and therefore require two separate fits in the regions for $p_{CO,O2}$ above and below 1 mbar (fig. 3.4-2). Since during the determination of the overall reaction order such a break was not observed (see fig. 3.3-4), the corrected values are used for the calculation of the overall reaction orders determined by the low-pressure micro-reactor (table 3.4-1). Additionally, the overall reaction orders without the 1000 mbar value are listed in table 3.4-1.

3.4.2 Results and discussion

The plots for the determination of the *overall reaction orders* α^{λ}_{CO} (λ=2, fig. 3.4-2) illustrate a strong dependence of the reaction rates on p_{tot}. Despite of the considerable error bars, a clear dependence on the temperature is obvious: From 50 to 95°C, the overall reaction order α^{λ}_{CO} increases from 0.76±0.14 to 0.94±0.15, while for higher temperatures it does not increase anymore (see table 3.4-1). A similar trend can be extracted from previous studies, if CO and O_2 reaction orders, reported for measurements under atmospheric conditions, are added up to obtain α^{λ}_{CO}: At 0°C Haruta et al. report a value of 0.29 [11], Bollinger and Vannice [39] found a value of 0.4 in the temperature range of 0-20°C and values >0.6 for temperatures ≥ 40°C. Similar results for temperatures ≥ 40°C have also been reported by other groups [40,63]. From our own measurements (section 3.3.1), we obtained an overall reaction order of 1.11±0.15 under atmospheric conditions at 80°C on the Degussa catalyst Au/TiO_2(5) (p_{tot}=1 atm, p_{CO}=p_{O2}=2-10 mbar, see fig. 3.3-4). Considering the error bars in these values, there is no significant difference between the overall reaction orders, determined with the low-pressure micro-reactor and those derived from measurements in the 'conventional' plug-flow reactor. Hence we conclude, that the total pressure does not influence the reaction mechanism in the pressure range studied.

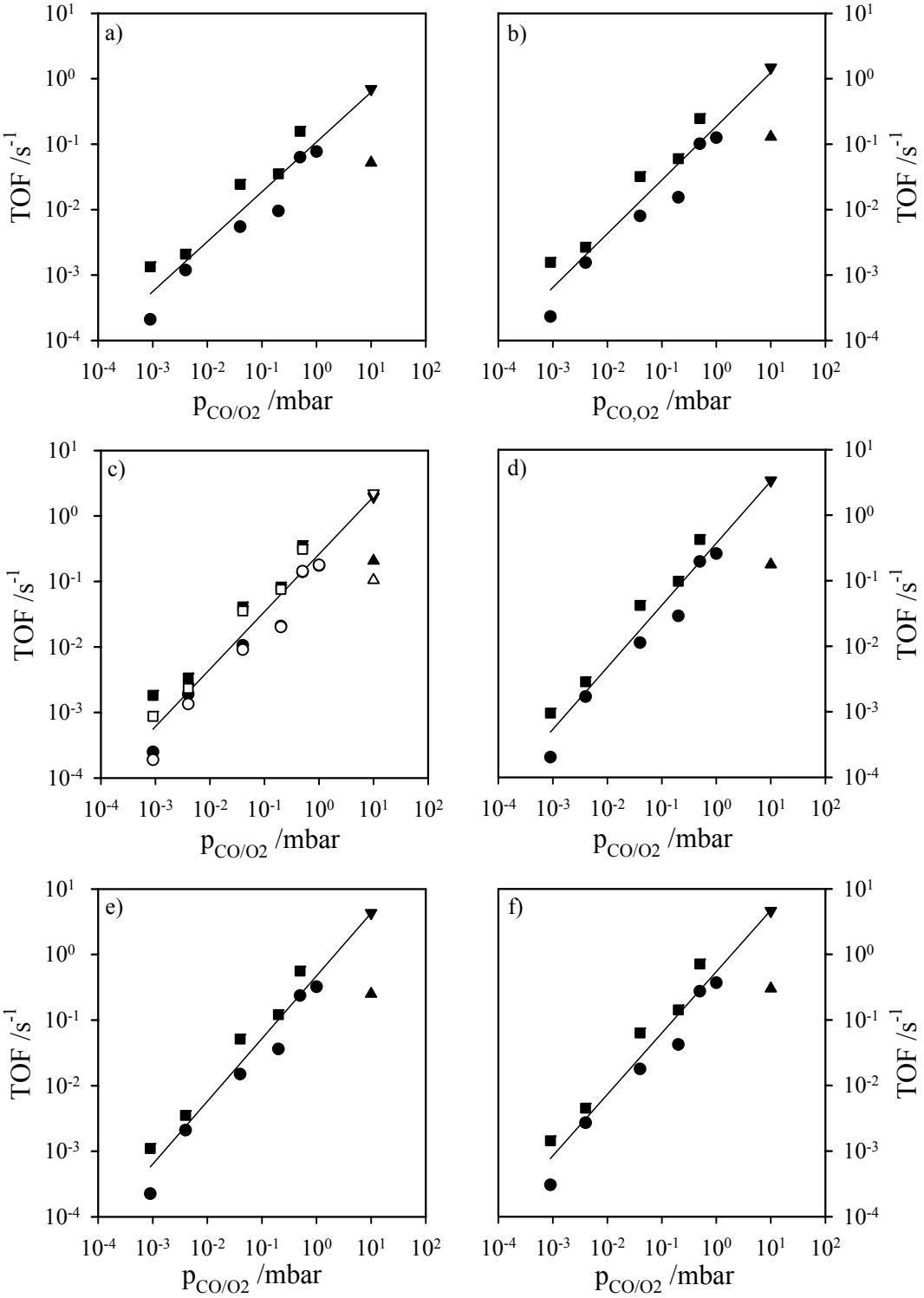

Figure 3.4-2: Overall reaction orders determined on catalyst $Au/TiO_2(5)$ after calcination at 400°C in the pressure gap with the low pressure micro-reactor for stationary measurements at a) 50°C, b) 65°C, c) 80°C, d) 95°C, e) 110°C and f) 125°C. For each p_{tot} value the measurements were carried out in the following temperature cycle: 80°C-65°C-50°C-125°C-110°C-95°C-80°C. Symbols for all graphs: ▼: deactivated sample at 1000 mbar; ▲: corrected sample at 1000 mbar; ●: data points with p_{tot}<1000bar measured with the initial set-up; ■: data points with p_{tot}<1000 mbar measured with the modified set-up. Empty symbols in graph c): measurement taken at the end of a measurements cycle. The contact time for all measurements was 0.06 s. For experimental conditions see Appendix B II. For details about the two set-ups see experimental section.

Table 3.4-1: Overall reaction orders (α^{λ}_{CO}) determined from the measurements in fig. 3.4-2 in the pressure range of 100 mbar to $9\cdot10^{-2}$ mbar total pressure (left column) and in the pressure range 1000 mbar to $9\cdot10^{-2}$ mbar (right column, for 1000 mbar the corrected values were used, due to the reasons mentioned in the experimental information of this chapter).

T /°C	α^{λ}_{CO}-100-$9\cdot10^{-2}$ mbar	α^{λ}_{CO}-1000-$9\cdot10^{-2}$ mbar
50°C	0.75±0.05	0.76±0.14
65°C	0.81±0.05	0.82±0.13
80°C	0.87±0.05	0.88±0.14
95°C	0.94±0.05	0.95±0.16
110°C	0.96±0.04	0.96±0.15
125°C	0.94±0.03	0.94±0.15

Measurements of the CO oxidation on a $Au/TiO_2/Ru(0001)$ model catalyst (0.2-0.4 ML Au) in our group [83] revealed an overall reaction order of 0.87±0.06 for p_{CO}=3.3-33.3 mbar (p_{CO}:p_{O2}=2:1) at 100°C, which fits excellently to our values. Hence, similar to the reaction rates, the different materials do not influence the reaction kinetics at high CO partial pressures.

Oxygen reaction orders (α_{O2}) were determined with the modified set-up at constant p_{CO} (1 vol.%) and variable p_{O2} (0.5-5 vol.%) for p_{tot}=20 mbar and 0.4 mbar (see figure 3.4-3) at 80°C. Under these conditions we obtained reaction orders of α_{O2}=0.40±0.02 and α_{O2}=0.19±0.03, respectively. Values reported for α_{O2} under atmospheric conditions [11,31,39,40,63,70] spread between 0 [39] and 0.46 [31] with no clear dependence neither on temperature nor on the concentration of CO or O_2. In our own measurements described in section 3.3.1 we derived an O_2 reaction order of α_{O2}=0.39±0.07 for reaction on the same catalyst at 80°C (p_{tot}=1 atm, p_{CO}=10 mbar, p_{O2}=2-20 mbar, see fig. 3.3-4). Hence, there is no significant difference between this value and the one obtained at p_{tot}=20 mbar in the low-pressure micro-reactor. The difference between the reaction orders at 20 mbar and 0.4 mbar, which has a value of 0.2, is more pronounced.

Two different overall reaction orders in the pressure ranges $p_{CO,O2}$ smaller and bigger than 1 mbar would result, if the 'deactivated' reaction rates were used (see fig. 3.4-2). If the 'corrected' reaction rates at $p_{CO,O2}$=10 mbar are used for the determination of the overall reaction orders, the results in the pressure ranges $p_{CO,O2}=9\cdot10^{-4}$-10 mbar and $p_{CO,O2}=9\cdot10^{-4}$-1 mbar are nearly identical (see table 3.4-1). Since the results with the use of the 'corrected' rates fit well with the overall reaction order, determined under atmospheric conditions with a 'conventional' plug-flow reactor, we conclude, that the overall reaction order does not change

in the partial pressure region $p_{CO,O2}$=1-10 mbar. For smaller pressure ranges, a variation in the reaction mechanism can not be excluded. This is concluded from the behavior of the oxygen reaction order, α_{O2}, which decreases with decreasing O_2 partial pressure. Since the overall reaction order, which is defined as the sum of the CO and O_2 reactions orders (see section 3.3.1), is constant in the entire pressure range studied, an increasing CO reaction order results from decreasing p_{tot}, which goes along with decreasing p_{CO}. Hence with decreasing partial pressures the influence of the CO partial pressure increases, while that of the O_2 partial pressure decreases.

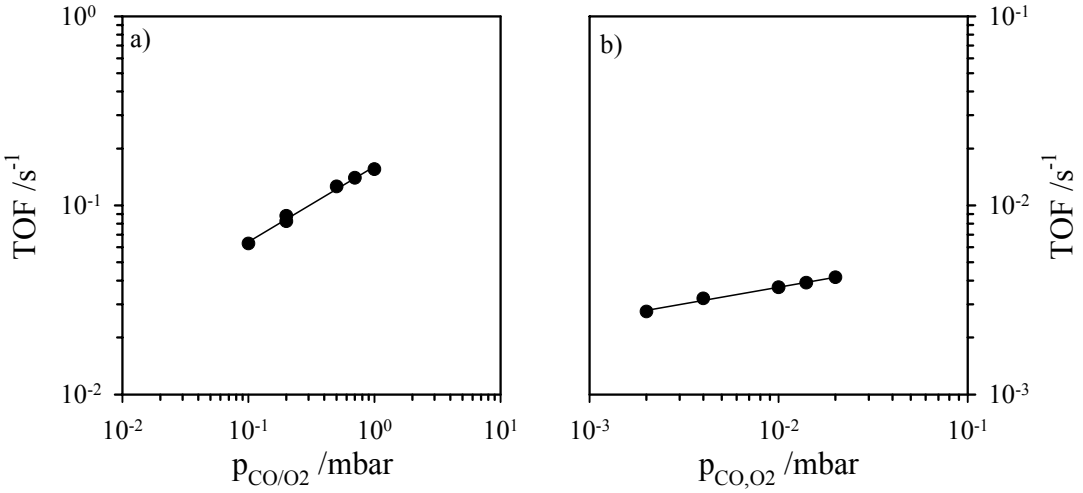

Figure 3.4-3: O_2 reaction orders determined on catalyst Au/TiO_2(5) after calcination at 400°C in the pressure gap with the low-pressure micro-reactor for stationary measurements at 80°C and a p_{tot} of a) 20 mbar and b) 0.4 mbar. The concentration of CO was constant (1 vol-%). p_{O2} was varied to scan λ values of 1-10 (0.5-5 vol-%) The contact time for both measurements was 0.06 s. Both measurements were carried out with the modified set-up. For experimental conditions see Appendix B II. For details about the two set-ups see experimental section.

As mentioned above, the motivation of this low-pressure study was that, i) the reaction rates on model catalysts and highly disperse catalysts are similar in the high pressure range ($p_{CO,O2}$=1-10 mbar) and ii) oxidation of CO with gaseous O_2 was not reported for lower CO and O_2 partial pressures. CO oxidation on Au/TiO_2 model catalysts in the low partial pressure regime (p_{CO}=10^{-7}-10^{-6} mbar) was observed only with pre-adsorbed O_{ad} [54,57,58,81]. Hence, the question arose, whether it is an effect of the pressure difference only, that for model catalysts no oxidation of CO by gaseous O_2 was reported in the low-pressure regime. To verify this question, the pressure dependence of the reaction probability is determined from our reaction rates and extrapolated to the low-pressure region.

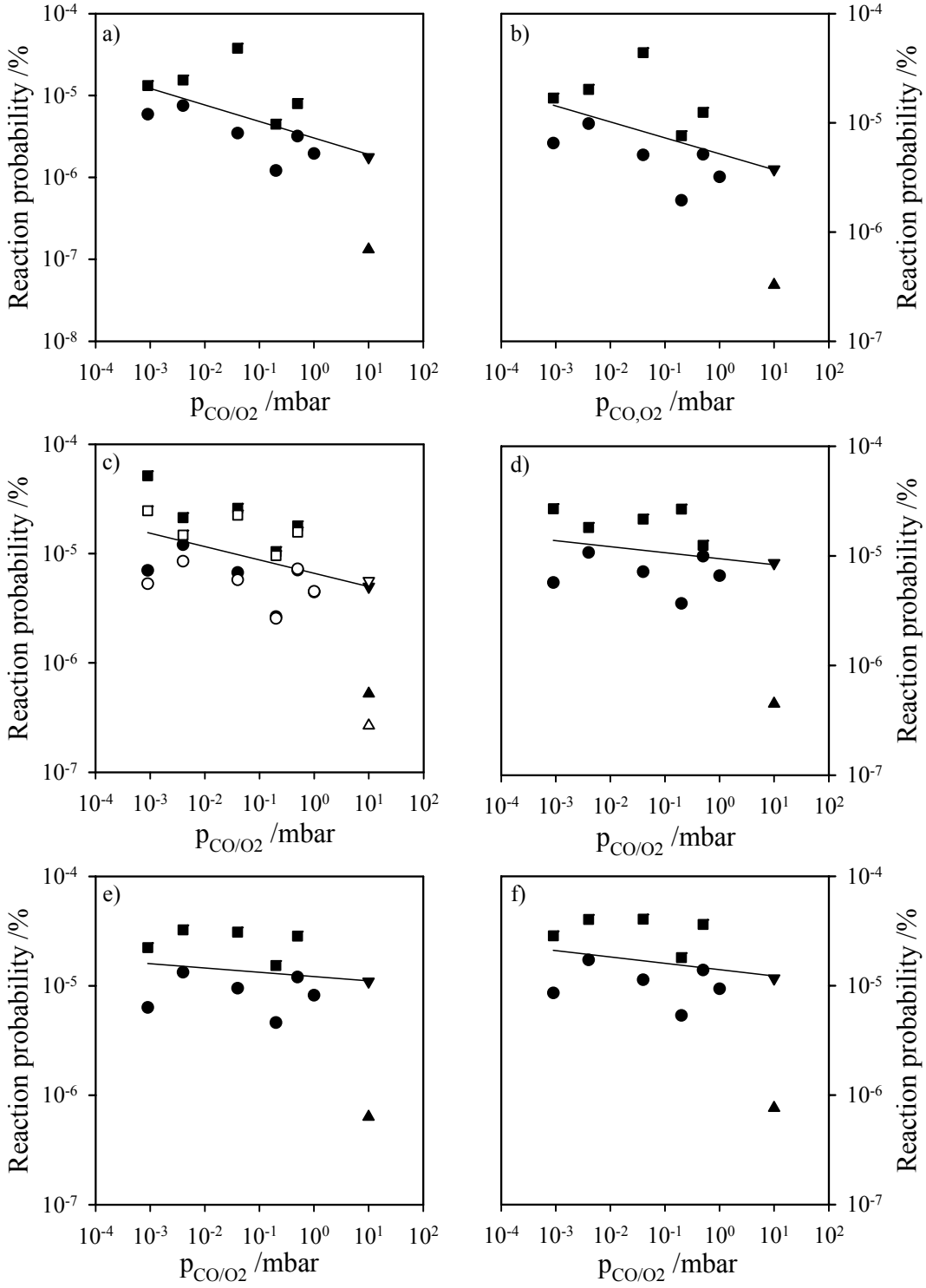

Figure 3.4-5: Dependence of the reaction probability on $p_{CO,O2}$ at a) 50°C, b) 65°C, c) 80°C, d) 95°C, e) 110°C and f) 125°C. For each p_{tot} value the measurements were carried out in the following temperature cycle: 80°C-65°C-50°C-125°C-110°C-95°C-80°C. Symbols for all graphs: ▼: deactivated sample at 1000 mbar; ▲: corrected sample at 1000 mbar; ●: data points with p_{tot}<1000bar measured with the initial set-up; ■: data points with p_{tot}<1000 mbar measured with the modified set-up. Empty symbols in graph c): measurement taken at the end of a measurements cycle. The contact time for all measurements was 0.06 s. The values are calculated from the reaction rates of fig. 3.4-2. For details about the two set-ups see experimental section.

The reaction probability (RP) for CO oxidation at a single collision with the catalyst surface at different p_{tot} can be determined by the quotient of the CO molecules converted into CO_2 per second and the impingement rate (F) of CO molecules on the catalyst surface at the given pressure (equation 3.4-5). For this the number of surface Au atoms (Au_{surf}) has to be calculated with equation 3.4-2. The amount of converted CO molecules (CO_{conv}) per cm^2 and s can be calculated from Au_{surf}, the TOF reaction rate and the BET surface along equation 3.4-3, while the impingement rate (F) is determined via equation 3.4-4 [1]. Note that the reaction probability, calculated along equations 3.4-2 to 3.4-5 is related to the impingement on the entire catalyst surface and not only for the gold particles.

$$Au_{surf}[\text{atoms}] = \frac{Au-\text{content}[\%]\cdot N_A[\text{atoms}\cdot\text{mole}^{-1}]\cdot D[\%]\cdot\text{weight}[g]\cdot 10^{-4}}{M[g\cdot\text{mole}^{-1}]\cdot\text{dilution}} \quad (3.4\text{-}2)$$

$$CO_{conv}[\text{molecules}\cdot\text{cm}^{-2}\cdot\text{s}^{-1}] = \frac{Au_{surf}[\text{atoms}]\cdot TOF[\text{s}^{-1}]\cdot\text{dilution}}{\text{weight}[g]\cdot BET\cdot 10^4[\text{cm}^2\cdot\text{g}^{-1}]} \quad (3.4\text{-}3)$$

$$F[\text{molecules}\cdot\text{cm}^{-2}\cdot\text{s}^{-1}] = 2.63\cdot 10^{22}\cdot\frac{p(\text{mbar})}{\sqrt{M\cdot T(K)}} \quad (3.4\text{-}4)$$

$$RP[\%] = \frac{CO_{conv}[\text{molecules}\cdot\text{cm}^{-2}\cdot\text{s}^{-1}]}{F[\text{molecules}\cdot\text{cm}^{-2}\cdot\text{s}^{-1}]}\cdot 10^2 \quad (3.4\text{-}5)$$

N_A: Avogadro's number ($6.022\cdot10^{23}$ molecules/mole)

D: Dispersion (fraction of surface Au atoms, 35.7%)

M: Molecular weight (Au: 197 g/mole; CO: 28 g/mol)

BET: BET surface ($56\cdot10^4$ cm^2/g)

The reaction probabilities calculated from the reaction rates in fig. 3.4-2 are shown in fig. 3.4-5. If the linear regression of the data points in the double logarithmic plots in fig. 3.4-5 are calculated (using the corrected values at p_{CO}=10 mbar), the slopes increase from -0.20±0.09 at 50°C to -0.06±0.07 at 95°C. For higher temperatures no further changes are observable. At the 'high' temperatures the absolute value of the error of the slope is bigger than the absolute value of the slope itself, hence it is denoted as zero. If the slope of the 50°C measurement is extrapolated to 10^{-7} mbar, the reaction probability is ~$8\cdot10^{-7}$. Calculating the converted CO molecules for a CO partial pressure of 10^{-7} mbar with the extrapolated reaction probabilities, this results in in rates the range of 10^6-10^7 molecules·s^{-1}·cm^{-2}. This is 3-4 orders of magnitude lower than the smallest rates determined in the present work (10^{10}-10^{11} molecules·s^{-1}·cm^{-2} were converted during CO oxidation at $p_{CO,O2}$=$9\cdot10^{-4}$ mbar) and clearly out of the detection

limit of the IMR-MS. Hence oxidation of CO by gaseous O_2 under UHV conditions is very hard to detect on Au/TiO_2 model catalysts. Furthermore, it is assumed, that the oxidation of CO with pre-adsorbed O_{ad} has a significantly higher reaction probability, since it was reported by several groups in the 10^{-6}-10^{-7} mbar range [54,57,58,165].

Finally, it has to be mentioned, that Meerson and Henry determined a reaction probability of 10-50% in a molecular beam experiment at 10^{-8}-10^{-7} mbar (molecular beam of CO in isotropic O_2 pressure) over Au/MgO(100) and Au/TiO_2(110) model catalysts at room temperature [165]. This is a significantly higher reaction probability, than estimated in this work. However, these results were not published so far, hence whether they could be reproduced. Furthermore, Yoon at al. reported CO oxidation with gaseous O_2 (molecular beam experiment) on Au_8 clusters deposited on defect-rich and defect-poor Mg(001) [166]. The partial pressures of O_2 and CO were not reported in the publication.

The *apparent activation energies (E_A)* at different p_{tot} were determined via the temperature cycle measurements described in section 3.4.1. Equally to the overall reaction orders, some values were determined with both set-ups. The Arrhenius plots are displayed in fig. 3.4-6. Measurements with the original set-up are plotted with filled symbols, those with the modified set-up with empty symbols. From fig. 3.4-6 the significant deviations in the reaction rates obtained from the measurements with the two different set-ups are clearly visible. Nevertheless, a significant difference for E_A between the two set-ups is only found at the lowest pressure ($9 \cdot 10^{-2}$ mbar), but the difference is still smaller than the error bars (fig. 4.3-4, the error bars were determined from the error in the linear regression of the Arrhenius plots). As illustrated, the mean value at this pressure is ~0 kJ/mole. The resulting apparent activation energies, E_A, decrease from 27 kJ/mole at p_{tot}=1000 mbar ($p_{CO,O2}$=10 mbar) to around 0 kJ/mole at p_{tot}=0.09 mbar ($p_{CO,O2}=9 \cdot 10^{-4}$ mbar, see fig. 4.3-4). The value at 1000 mbar is close to the ones reported in the literature, which were obtained via measurements at atmospheric pressure with $p_{CO,O2} \geq 10$ mbar [11,39,40].

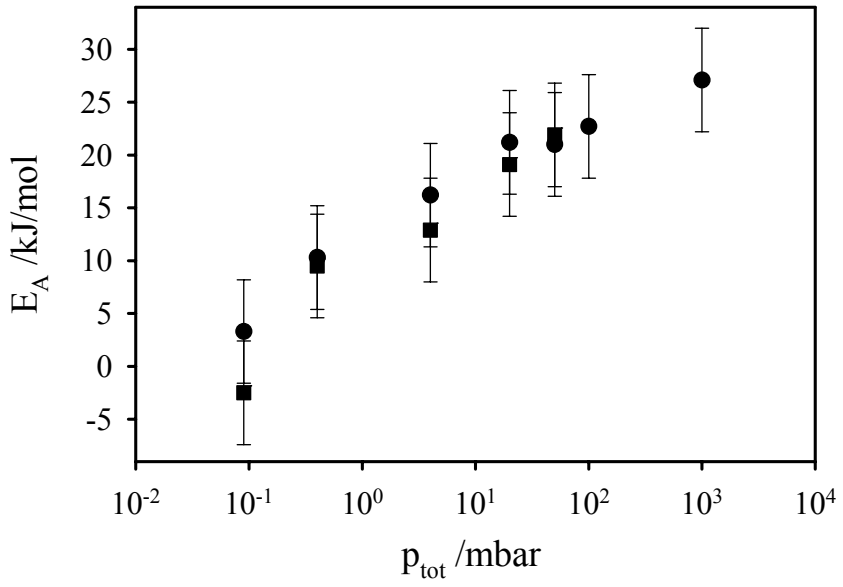

Figure 3.4-4: Dependence of the apparent activation energy (E_A) of the CO oxidation on catalyst $Au/TiO_2(5)$ on p_{tot}, determined from the reaction rates in fig. 3.4-2. The values plotted with circles were determined with the initial set-up, those with squares with the modified set-up. For details about the two set-ups see experimental section.

A dependence of E_A on the partial pressures of CO and O_2 was also found in the experimental work for my diploma thesis in H_2-rich atmosphere (75 kPa H_2). In that case, where the partial pressure decrease was attained by higher dilutions at atmospheric pressure, E_A decreased from 29 kJ/mol at $p_{CO,O2}$=15 mbar to 0 kJ/mole at $p_{CO,O2}$=0.3 mbar (the experiments were performed on catalyst $Au/TiO_2(1)$). In the measurements presented here, a CO partial pressure of 0.3 mbar corresponds to p_{tot}=30 mbar. According to fig. 4.3-4 an activation energy of ~20 kJ/mole is expected at this pressure. Hence, in H_2-rich atmosphere at atmospheric pressure, E_A decreased much faster than in the experiment presented here. Further reasons for the differences may be, the different supports of the catalysts, the different contact times during the experiments and the different pressure conditions, in which the experiments were performed. Although there is a discrepancy in the particular trends in the above mentioned experiments, a strong dependence of E_A on the partial pressures of the reactants is obvious. Such a dependence of E_A on the partial pressures has not yet been reported before. But it can be compared with the temperature dependence of the activation energy reported by Haruta [7], since both, different $p_{CO,O2}$ and different temperatures, cause changes in the steady state coverage. Haruta reported a decrease of E_A to 0 KJ/mol for reaction temperatures <-73°C and explained this finding with a model where the reaction takes place only on the gold surface (especially on steps, edge and corner sites), while the interface is covered with carbonates at

these temperatures. This suggestion can not explain the present results, since for lower p_{tot} carbonates are formed slower, while the decomposition rate is approximately constant, which leads to lower steady state coverage of carbonates.

A more reliable explanation for the decreasing apparent activation energy based on an increase of the adsorption enthalpie with decreasing CO coverage for decreasing CO partial pressures (see subsection 3.3.2.1). The dependence of the heats of adsorption ($-\Delta H_{ad}$) of CO on supported gold catalysts were studied by Meier and Goodman [167] and Derrouiche et al. [168]. Meier and Goodman [167] used a $Au/TiO_2/Mo(110)$ model catalyst with various gold loadings, where the particles consisted of bilayer islands with lateral diameters in the range of 1.8 to 3.1 nm, while Derrouiche et al. [168] used a disperse Au/TiO_2 powder catalyst with a gold loading of 1 wt.-% and an estimated Au particle size of 3-5 nm. Meier and Goodman [167] determined the isosteric adsorption enthalpy $-\Delta H_{ad}$ on the model catalyst via adsorption isotherms and found a strong dependence of $-\Delta H_{ad}$ on the gold loading. The model catalyst with the highest gold loading (0.5 ML, lateral diameter 3.1 nm,) correlates best to the sample used here. $-\Delta H_{ad}$ was constant up to a CO_{ad} coverage of ~33% with a value of 52.5 kJ/mole and then decreased to ~30 kJ/mole at a CO_{ad} coverage of 85% (100% CO_{ad} coverage was assumed at saturation of the IRAS signal). Derrouiche et al. [168] measured adsorption isobars and assumed a generalized expression of Temkin's adsorption model (100% CO coverage was set to the highest IR band area). The $-\Delta H_{ad}$ values were then determined by searching the values for the best theoretical fit of the experimental data. With this method they determined $-\Delta H_{ad}$ values of 74 kJ/mole and 47 kJ/mole for $\theta=0$ and 1, respectively. The $-\Delta H_{ad}$ values determined by the two groups differ by ~20 kJ/mole. The reason for this deviation is most likely, that the gold particles on the powder catalyst were hemispherical, while on the model catalysts the gold clusters consisted of bilayer particles.

The finding presented above, demonstrating an increase of the $-\Delta H_{ad}$ value with decreasing CO_{ad} coverage, leads to the assumption, that the variation of the apparent activation energy (decrease from 27 kJ/mole at $p_{CO}=10$ mbar to around 0 kJ/mole at $p_{CO}=9\cdot10^{-4}$ mbar in the temperature range 50-125°C) is caused by the higher adsorption enthalpies. Since at $p_{CO}=9\cdot10^{-4}$ mbar the apparent activation energy was ~0 kJ/mole, we suggest, that the heat of adsorption is as higher as the real activation energy. Our assumption is supported by a modelling approach to the preferential oxidation of CO (PROX) on Pt: Mhadeshwar and

Vlachos [90] calculated apparent activation energies (E_A) using the so called unity bind index quadratic exponential potential (UBI-QEP) method (the surface reaction mechanism was composed of three partial reactions: H_2-oxidation, CO oxidation and CO-H_2 coupling steps). They reported a dependence of E_A on the coverage of the involved species as well as on the temperature, where the former resulted from the known variation of the heats of adsorption with coverage.

A third explanation for the decreasing apparent activation energy is a transition to another pathway, which is negligible in the high pressure regime, but becomes dominant in the low pressure regime.

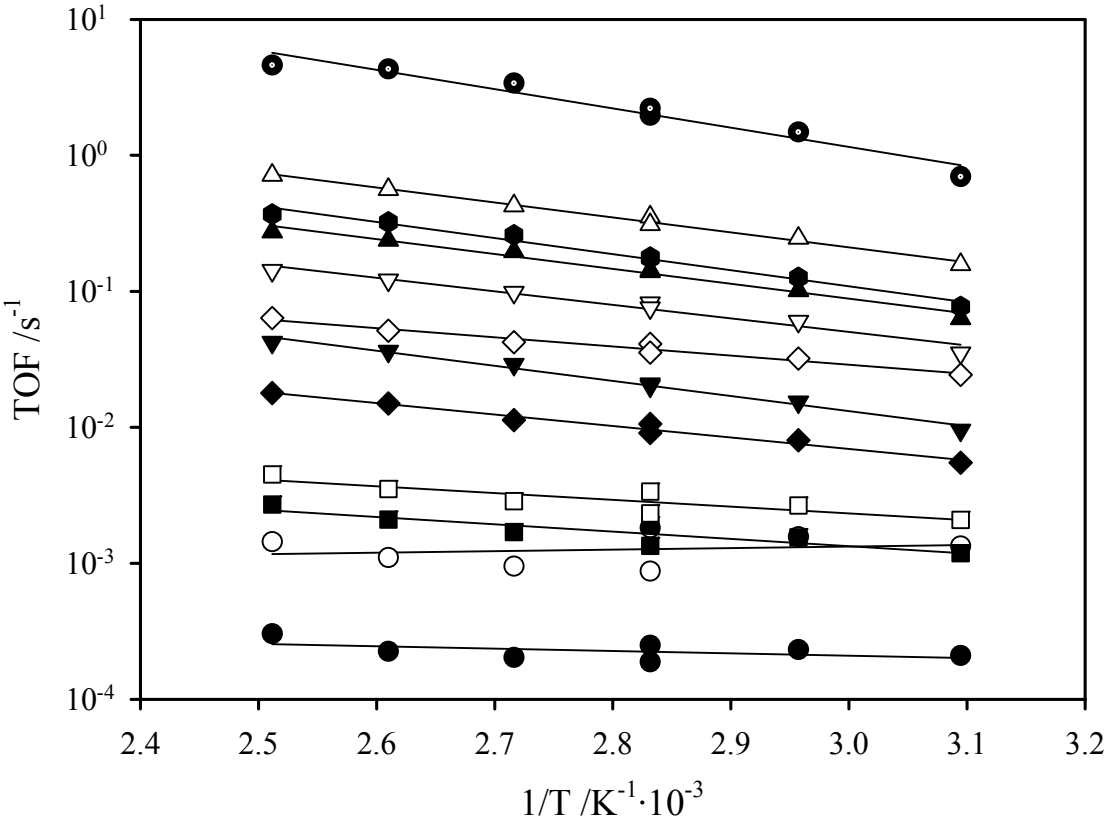

Figure 3.4-6: Arrhenius plots for the determination of the apparent activation energies (E_A) in at the following total pressures: ⭘: 1000 mbar, ⬢: 100 mbar, ▲: 50 mbar, ▼: 20 mbar, ◆: 4 mbar, ■: 0.4 mbar, ●: 0.09 mbar. Filled symbols: measurements with the original set-up, empty symbols: measurements with the modified set-up. Reaction rates from fig. 3.4-2. For details about the two set-ups see experimental section.

As a summary of this study of the reaction kinetics in the pressure gap (range of total pressure: 1000 mbar to $9 \cdot 10^{-2}$ mbar) the following results are highlighted. First, the overall reaction order increases slightly, if the temperature is increased from 50°C to 95°C, and is stable for higher temperatures (up to 125°C). Second, the overall reaction orders and the

reaction rates for p_{CO}=10 mbar on the powder catalyst are similar to those reported on a Au/TiO_2/Ru(0001) model catalyst, which leads to the conclusion, that the different materials do not cause significant modifications in the reaction kinetics. An estimation of the reaction probability for the p_{CO} range 10^{-6}-10^{-7} mbar results in 10^{6}-10^{7} molecules, which are produced per s and cm^2. This is below the detection limit of the IMR-MS used here. For this reason the CO oxidation with gaseous O_2 in the p_{CO}=10^{-6}-10^{-7} mbar range is extremely difficult to measure. Third, at 80°C the reaction order of O_2 decreases with decreasing total pressure, while the reaction order of CO increases. Fourth, the apparent activation energy decreases from 27 kJ/mole at 1000 mbar to ~0 kJ/mole at $9 \cdot 10^{-2}$ mbar, which can either be explained by a heat of adsorption in the low-pressure regime, that equals the real activation energy, or by change in reaction pathway, which is negligible in the high pressure regime and becomes dominant in the low pressure regime.

3.5 Transient measurements

In the preceding chapters information was obtained about (i) reaction kinetics at atmospheric pressure and in the pressure gap, (ii) surface species during the CO oxidation reaction and (iii) the deactivation behavior. Furthermore, first mechanistic questions concerning the role of O_2 and CO were answered. These measurements were carried out under steady state conditions. Hence, neither the beginning of the reaction nor the response to changes in the gas mixtures was considered. Since these two fields can provide useful information on the reaction mechanism, so called transient experiments were performed. The experiments were performed with the DRIFTS equipment and the 'conventional' plug-flow reactor connected to the IMR-MS. DRIFTS enables a qualitative observation of the surface species and the IMR-MS a quantification of produced and effluent gases.

To make the presentation of the results clearer, the term 'switch', which is used frequently in this chapter, has to be explained. By definition, a switch is a shift from one state to another, i.e., here from one gas mixture to another. Deviating from this definition, in this chapter the term 'switch' will not only be used for the act of changing the gas mixtures, but also for the entire period that follows the act of switching. For example, if the behavior in an O_2/N_2 atmosphere was studied first and then the gas mixture was changed to CO/N_2, the entire O_2/N_2 period will be denoted as switch 1 and the CO/N_2 period as switch 2.

The 'basic' switch experiment is shown in fig. 3.5-1 (modifications are presented in subsection 3.5.2). All experiments were performed with catalyst $Au/TiO_2(5)$ after calcination at 400°C at a reaction temperature of 80°C. Prior to the switches, CO oxidation was performed in order to reach steady state surface conditions. After the oxidation reaction, O_2- or CO-containing gas mixtures were introduced to the samples alternately. The flux was 40 Nml/min, both during the oxidation reaction and during the switches. The loss in gas flow, caused by the absence of one reactant, was compensated with N_2. With the IMR-MS equipment the changes of the gas mixture could be performed rapidly (duration ~1 s), since the gas mixtures could be changed, while the gas stream passed over the samples. Since this procedure led to pressure bursts, and would have destroyed the catalyst bed in the DRIFTS equipment, switching had to be modified for this measurement in the following way: Before the change of the gas mixture, the gas stream was set carefully from 'reaction' (flow through the sample) to 'bypass' mode (flow passes the sample), then the gas mixture was changed and

finally the gas stream was slowly set back from 'bypass' (flow passes the sample) to 'reaction' mode (flow through the sample). For this procedure about 30 sec were needed.

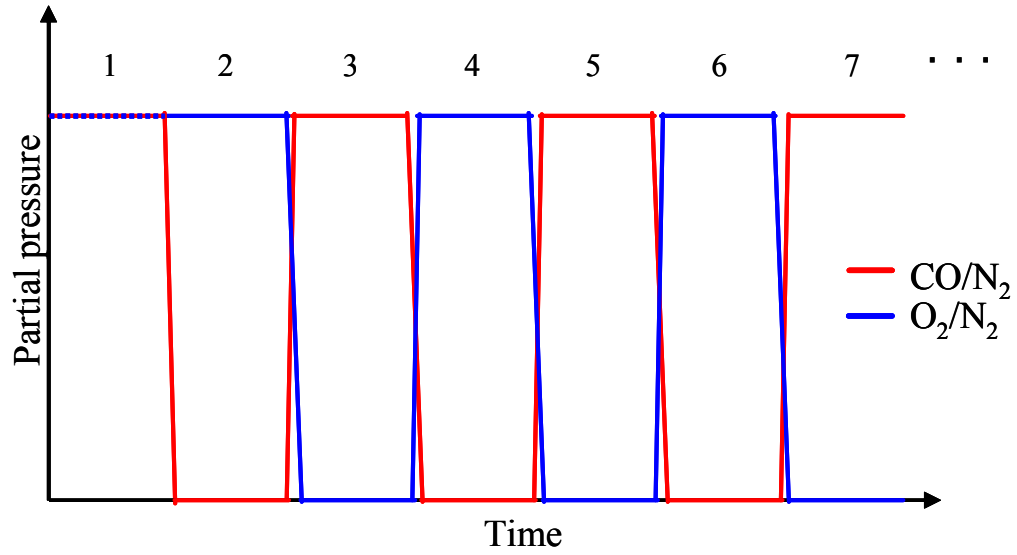

Figure 3.5-1: Schematic presentation of the basic switch experiment carried out with DRIFTS and the 'conventional' plug-flow reactor connected to the IMR-MS. With the IMR-MS two experiments were carried out: once the CO oxidation was performed with $^{32}O_2$ and $C^{16}O$ and once with $^{36}O_2$ and $C^{16}O$. In both cases the O_2/N_2 switches were done with $^{36}O_2/N_2$.

This chapter is divided into three sections. In the first two sections the results obtained with the DRIFTS and the IMR-MS equipment will be presented and discussed. For clarity these two sections are divided into subsections dealing with CO oxidation and O_2- or CO-containing switches. The results will be summarized in the third section.

3.5.1 DRIFTS measurements

3.5.1.1 CO oxidation

The spectra acquisition was started parallel to the introduction of the gas mixture (1 kPa CO, 1 kPa O_2, balance N_2, gas flow 40 Nml/min), in order to study the beginning of the reaction (the quasi steady state behavior was already discussed in section 3.2.3). Within the first five minutes, the period with the most significant changes in the spectra, 20 scans were added for one spectrum, equivalent to an acquisition time of 9 s per spectrum. Since additional 3 s were needed for data saving, spectra could be acquired in 12 s intervals. The evolution of the surface species during the CO oxidation reaction, starting form the introduction of the gas mixture up to a reaction time of 145 min, is shown in fig. 3.5-2. In the first spectrum (acquisition time 0-9 s.) we find primarily linearly adsorbed CO (CO_{ad}) on Au (2119 cm^{-1}) [11,14], and only little CO_2 (2389-2290 cm^{-1}) is produced. At ~1620cm^{-1} a small peak

resulting from adsorbed water H_2O_{ad} [144,169,170] can be observed and in the region of OH-groups (3800-3400 cm^{-1}) [170,171] no clear peak is visible. In the subsequent spectrum significant changes occur. The peak intensity of H_2O_{ad} has increased (i.e., H_2O is produced), OH-groups are consumed, which is obvious from a negative peak at 3723 cm^{-1}, the CO_2 production increased and the CO_{ad} peak decreased.

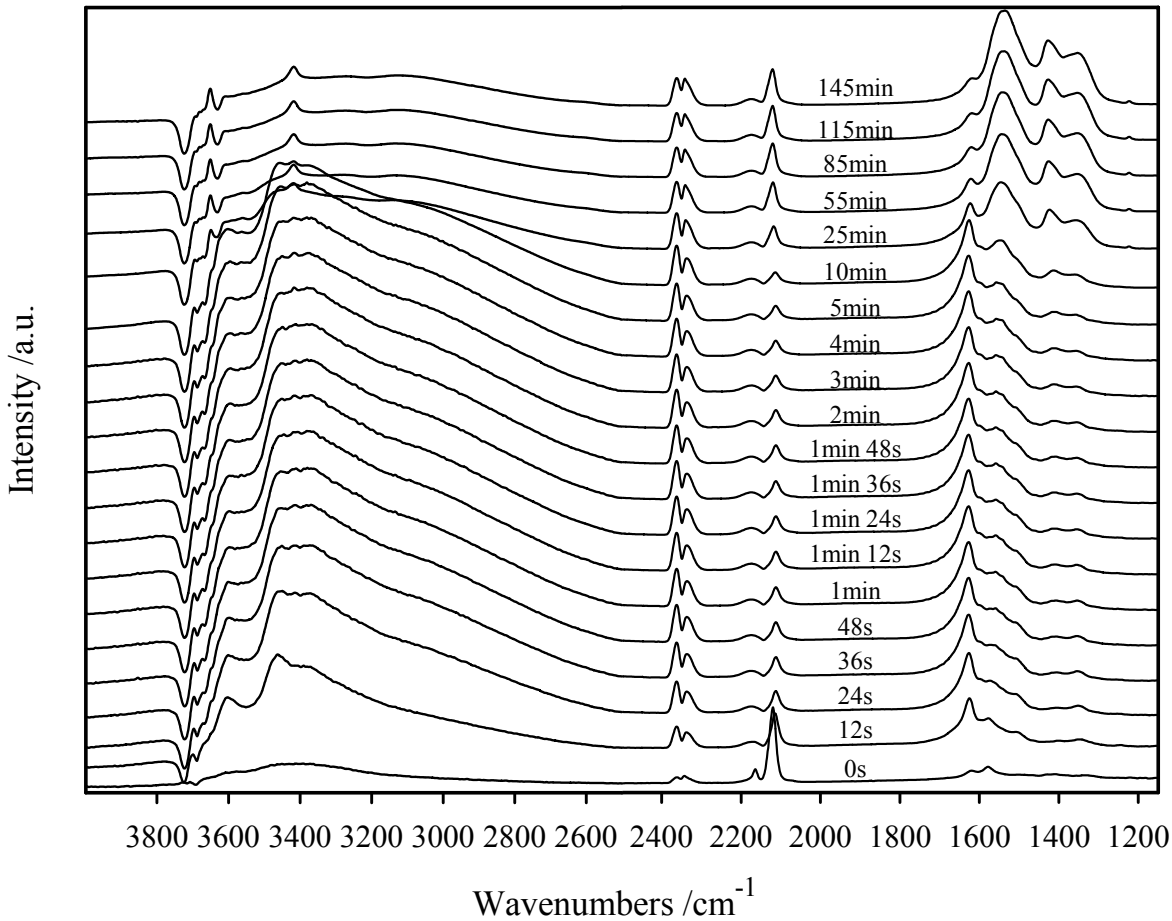

Figure 3.5-2: DRIFTS spectra taken during CO oxidation on catalyst $Au/TiO_2(5)$ at 80°C (undiluted catalyst, calcined at 400°C; 1 kPa CO, 1 kPa, O_2, rest N_2, gas flow 40 Nml/min). At the times given in the plot, the spectra acquisition was started. From 0 s to 5 min, 20 scans were added for one spectrum (acquisition time 9 s). For the spectra at 10 min, and higher times 600 scans were added for one spectrum (acquisition time 4 min 31 s).

The relation of CO_2 and CO is an indicator for the activity at a given time: It can be plotted as area ratio of CO_2 and CO_{ad} (CO_2/CO_{ad}), i.e., if CO_2/CO_{ad} is large, most of the adsorbed CO reacts to CO_2, and if it is small, less adsorbed CO reacts to CO_2. The correlation of the CO_2/CO_{ad} ratio with activity is justified, since the CO_{ad} peak decreased and increased during reaction (fig. 3.5-2), which would not occur, if $\theta(CO_{ad})$ depended on p_{CO} only (in that case it would increases and become stable, once steady state is reached). The enhancement of the CO_2/CO_{ad} ratio goes along with the consumption of OH-groups and the production of H_2O_{ad}

(fig. 3.5-2). A clear correlation between the CO_2/CO_{ad} ratio and the peak intensity of H_2O_{ad} is shown fig. 3.5-3, where the temporal development of these two variables is plotted, which is obviously parallel. Hence, a higher activity (larger CO_2/CO_{ad} ratio) goes along with a larger H_2O_{ad} peak and vice versa. This leads to the assumption, that the activity of the CO oxidation correlates with the formation of H_2O_{ad} and explains the higher stability of the Degussa Au/TiO_2 catalysts during CO oxidation in H_2-rich atmosphere than in H_2-free atmosphere (see chapter 3.2).

In recent reports, also higher activities for various catalyst systems were reported, if water was involved in the reaction [84-89]. Even first theoretic studies on the influence of the catalytic role of water in the CO oxidation reaction have been published [90,91]. Park et al. [86] found the qualitative enhancement of the reaction rates, if water moisture was added to the gas mixture for CO oxidation on Au/TiO_2. Haruta and his group studied this enhancing effect of water quantitatively [84,85] and found the maximum activity at a water content of 200 ppm (reaction temperature: 0°C, reactive gas mixture: 1 vol% CO in air) [84,85]. In a later publication they identified two roles of the moisture in the reaction mechanism [89]: First, the moisture is necessary for the activation of O_2 and, second, for the decomposition of carbonate species. The first explanation is in contrast to the model of the group of Kung and Costello [88,172], who also reported a higher stability of the CO oxidation reaction on Au/γ-Al_2O_3, if the gas mixture contained H_2O beside 1% CO, 2.5% O_2, balance He, at room temperature. A promoting effect of water on the CO oxidation was also observed on a Pt(111) single crystal by Bergald et al. [87] at temperatures of 180-230K. They proposed an autocatalytic role of OH groups, which are composed in the reaction of H_2O and O_2. According to the publication, the reaction of CO with the OH groups leads to desorbing CO_2 and a transient H atom, without the composition of an intermediate carboxylate. Inspired by the results of Bergald et al. [87], Mhadeshwar and Vlachos [90] studied the water promotion of the CO oxidation on Pt among other reactions, with a micro-kinetic model and confirmed that the direct reaction to the carboxylate intermediate is favored. For reaction at low temperatures (200 K) and on Pt(111), Gong and Hu [91] found via DFT calculations, that carboxylate is an intermediate product formed from CO and OH-groups and that its decomposition is catalyzed by water, which is a ‘bridge’ for H to react with a OH-group to H_2O ($COOH + H_2O + OH \leftrightarrows CO_2 + 2H_2O$, H_2O passes a H from COOH to a OH).

To elucidate the origin of the water in our experiment, an untreated spectrum of the sample after conditioning and cooling down to 80°C in a N_2-flux is shown in fig. 3.5-4. Both, isolated OH-groups with peaks at 3723 cm^{-1}, 3676 cm^{-1} and a shoulder at 3687 cm^{-1} [126,170,173,174], as well as adsorbed water, H_2O_{ad}, at around ~1620cm^{-1} can be identified. Hence, the conditioning procedure at 400°C does not cause their complete desorption. The presence of OH-groups on TiO_2 powder after treatment at elevated temperatures was also reported by Finnie et al. [170], who heated their samples up to 250°C, and by Martra [126], who reported OH-groups even after conditioning temperatures as high as 500°C.

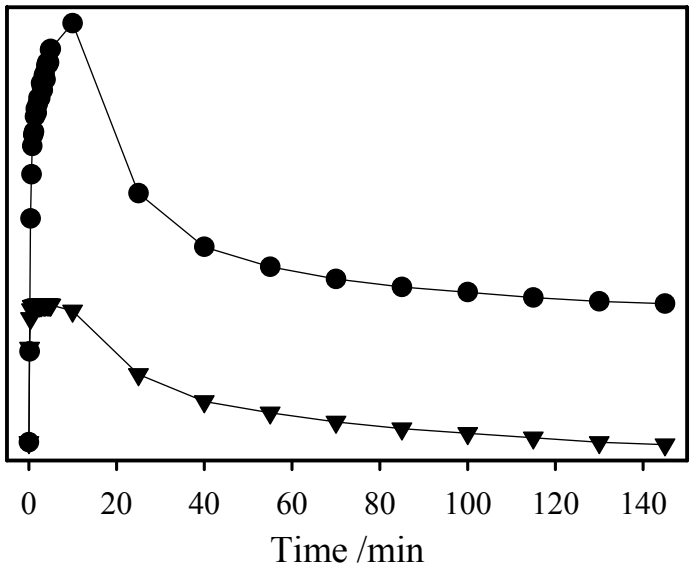

Figure 3.5-3: Relative behaviour of the H_2O_{ad} peak at ~1620 cm^{-1} (▼) and the ratio of the peak areas of CO_2:$CO_{ad,lin}$ (●) during CO oxidation (1 kPa CO, 1 kPa O_2, balance N_2, gas flow 40 Nml/min) in fig. 3.5-2. All values are correlated to the value of the spectrum taken from 0-9 s.

From the evaluation procedure of the DRIFTS spectra, which is described in the experimental section, the positive peaks for H_2O_{ad} in the reaction spectra of fig. 3.5-2 indicate an increase in the amount of water compared to the water present in the background spectrum, after the conditioning procedure in fig. 3.5-4. The negative peaks of the OH-groups indicate a decrease of their amount during reaction. Since the peaks of these two species behave contrary, we conclude, that H_2O_{ad} is formed from OH-groups. A direct formation of water via disproportionation of OH-groups ($OH_{ad} + OH_{ad} \rightarrow H_2O_g + O_{lattice} + V_O$ (V_O: oxygen vacancies)) was postulated by Kim and Barteau [173]. This conclusion was based on the observation of desorbing water during the decomposition of carboxylic acid on TiO_2 powder (anatase). The desorption temperature depended on the kind of carboxylic acid, which was introduced to the sample. The origin of the OH_{ad} groups, however, is not clear from the

article. According to Kim and Barteau they resulted from dissociative adsorption of carboxylic acids. Carboxylic acid as only source for the presence of the OH groups is unlikely, since prior to the experiments the samples were treated one hour in oxygen, followed by a purge with helium for one hour at 400°C. Based on the data in fig. 3.5-4 and the results presented by Martra [126], we assume that the samples were not completely dehydroxylated after this procedure. Henderson [175] also proposed a disproportionation of OH-groups on TiO_2(110) during the decomposition process of formic acid: $OH_{lattice}^-$ + $OH_{lattice}^-$ → H_2O +$O_{lattice}^{2-}$ + V_O (V_O: oxygen vacancies). In this case the $OH_{lattice}$-groups originated from the reaction of formic acid with lattice oxygen ($HCOOH + O^{2-}_{lattice} \rightarrow HCOO^-_{ad} + OH^-_{lattice}$). The desorption temperature of water decreased with higher HCOOH exposure, for a HCOOH exposure of $5.2 \cdot 10^{14}$ molecules/cm^{-2} the first desorption maximum was observed even at 205 K.

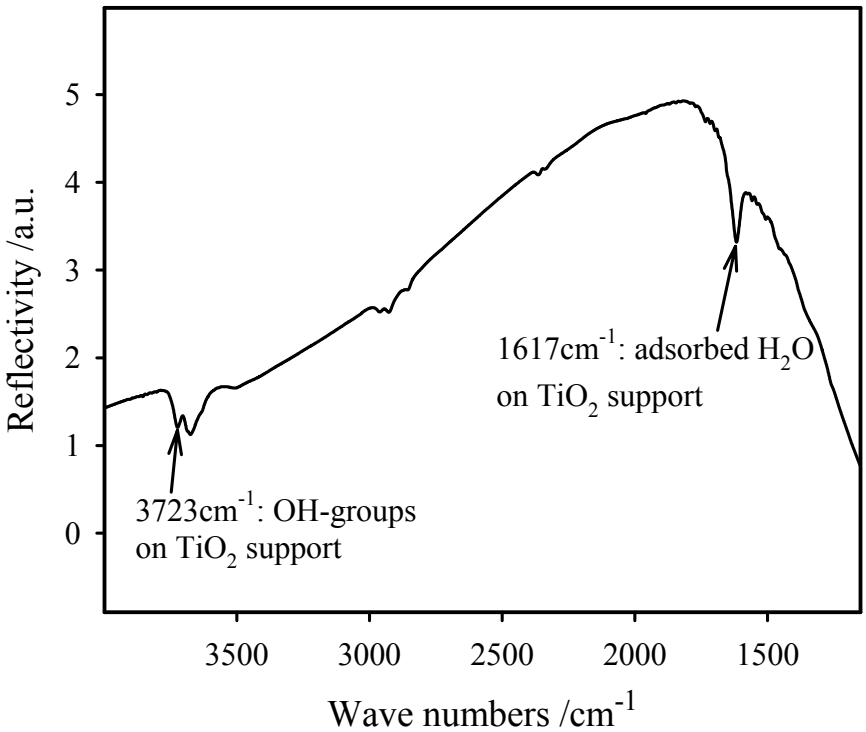

Figure 3.5-4: Raw spectrum of Au/TiO_2(5) after calcination in 10% O_2/N_2 at 400°C for 30 min and cooling down in N_2 to 80°C. The OH-groups and the peak of H_2O_{ad}, whose peak intensities change in during CO oxidation and the switches, are marked.

Considering (i) the possibility of a disproportion of OH-groups on TiO_2 powder and TiO_2(110) to H_2O and (ii) the presence of OH-groups and H_2O_{ad} (see fig. 3.5-4), we assume that on our sample OH-groups and H_2O_{ad} coexist in the subsequent equilibrium: $OH_{lattice}^-$

+ $OH_{lattice}^-$ ⇆ H_2O_{ad} +$O_{lattice}^{2-}$ + V_O (V_O oxygen vacancies), where water is adsorbed, since the reaction temperature is <100°C:

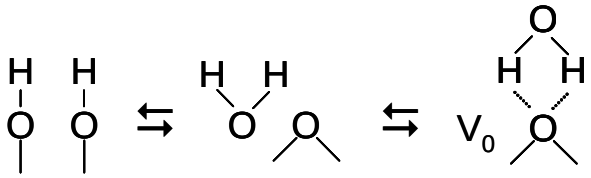

Nevertheless, we assume, that (i) the water diffuses on the surface and does not 'block' O_2 adsorption sides (according to the formulated equilibrium this would then decompose to two $OH_{lattice}^-$ groups again) and that (ii) part of the water desorbs and is removed from the reactor, since it has a high vapor pressure at the reaction temperature of 80°C (~470 mbar) and its desorption was already observed during CO oxidation in H_2-rich atmosphere (see section 3.2.3). An additional indication for the loss of water can be seen in fig. 3.5-5: The decrease of the H_2O_{ad} peak in the progress of the reaction does not go along with a significant increase of the OH-group peak. Hence, the water does not decompose back to OH-groups.

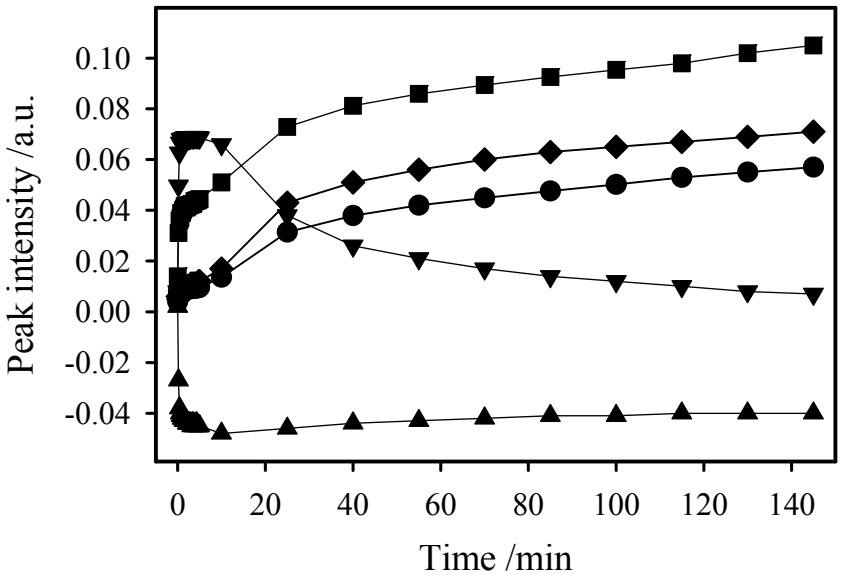

Figure 3.5-5: Temporal evolution of the peak intensities of H_2O_{ad} at ~1620 cm^{-1} (▼), OH groups on the support at 3723 cm^{-1} (▲), bidentate carbonate at ~1540-1570 cm^{-1} (■), monodentate carbonate at ~1330 cm^{-1} (●) and carboxylate at ~1420 cm^{-1} (♦) in the course of the CO oxidation (1 kPa CO, 1 kPa O_2, balance N_2, gas flow 40 Nml/min) in fig. 3.5-2.

Based on the behavior of the peak related to H_2O_{ad} (fig. 3.5-2), the postulated equilibrium between OH-groups and H_2O_{ad} shifts to the side of H_2O_{ad}, if the gas mixture is introduced to the sample. Since CO adsorption is only observed on the Au particles and not on oxygen vacancies of the TiO_2 support, this shift in equilibrium must be caused by the O_2 present in

the gas mixture. The concentration of the oxygen vacancies decreases by the adsorption of oxygen on the oxygen vacancies, which causes a shift of the above mentioned equilibrium to the right side. The possibility of oxygen adsorption and dissociation on oxygen vacancies has already been reported in [68]. More evidence for the influence of oxygen on the OH-H_2O_{ad} equilibrium will be given beneath, in the discussion of the O_2/N_2 and CO/N_2 switches.

Besides H_2O_{ad}, other peaks can be observed in the so called carbonate region (1700 cm^{-1} and 1200 cm^{-1}): At the beginning of the reaction the main peaks are located at 1576 cm^{-1}, 1506 cm^{-1}, 1401 cm^{-1}, ~1330 cm^{-1}, and a very small contribution is visible at 1242 cm^{-1}. The peaks at 1576 cm^{-1} and 1242 cm^{-1} are assigned to υ(C=O) and υ_{as}(COO) of bidentate carbonate, in which both bridging O atoms bind to the same metal atom [143]. The peaks at 1506 cm^{-1} and ~1330 cm^{-1} are assigned to $\upsilon_{as}(COO^-)$ and $\upsilon_s(COO^-)$ of monodentate carbonate [143]. Since the structures of the identified bidentate and monodentate carbonate are very similar, it is possible that they exist in equilibrium, which will be discussed in more detail below. The assignment agrees well with results of Liao et al. [152], who assigned a peak at 1579 cm^{-1}, which appeared during the introduction of CO_2 to TiO_2 powder (Degussa P25), to the carbonyl stretching vibration of bidentate carbonates. Busca et al. [145] assigned peaks in the regions 1600-1550 cm^{-1} and 1410-1350cm^{-1} to $\upsilon_{as}(COO^-)$, δ(CH) and $\upsilon_{as}(COO^-)$ of formate species. Since our spectra do not show C-H vibrations in the region of 2800 cm^{-1}-3000 cm^{-1} (see fig. 3.5-2), the presence of formates can be ruled out. Also the peak at 1401 cm^{-1} is assigned to $\upsilon_s(COO^-)$ of carboxylate species [143], formate species are excluded due to the lack of C-H vibration peaks. According to [143] the $\upsilon_{as}(COO^-)$ vibration of carboxylate species is situated in the region of 1560-1630 cm^{-1}. Here it is not visible aside the dominant peak of H_2O_{ad} and the $\nu_{as}(COO^-)$ peak of bidentate carbonates. The peak at 1620 cm^{-1} can not be assigned to this carboxylate vibration, since the temporal evolution of its peak intensity does not correlate with that of the symmetric vibration. The structures of the three identified species, carboxylate, monodentate and bidentate carbonate, are shown in fig. 3.5-6.

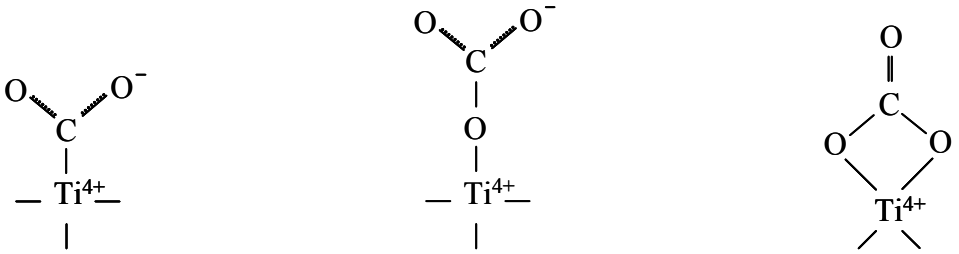

Figure 3.5-6: Structure of surface species identified with DRIFTS during CO oxidation and during O_2/N_2 and O_2/N_2 switches. From left to right: carboxylate, monodentate carbonate and bidentate carbonate. The structure of the species and their assignment is in accordance to [143].

During the reaction the peak intensities of the carboxylate and carbonate species increase significantly and the peaks are worse resolved than at the beginning of the reaction. Within 145 min of reaction their positions shift to 1536 cm^{-1}, 1428 cm^{-1}, 1353 cm^{-1} and 1221 cm^{-1}; additional peaks can be hidden due to the reduced resolution. According to [143] the peaks at 1536 cm^{-1} and 1221 cm^{-1} are assigned to the same bidentate carbonates as at the beginning of the reaction. The significant peak shifts to lower wave numbers result from weakening of the bonds (C=O and COO). This weakening goes along with an increase of thier coverage, as can be deduced from the increase of the peak intensities in figs. 3.5-2 and 3.5-5. The bidentate carbonate is bound to the Ti via two oxygen atoms (see fig. 3.5-6). Since the oxygen atoms are more electronegative than Ti, electrons are shifted from the Ti to the bidentate carbonate. The weakening of the bonds is either caused by a lowered electron density shifted to a binding orbital of the bidentate carbonate or by an enhanced electron density shifted to an anti-bonding orbital of the bidentate carbonate. The reason for the changes of electron density shifted to the bidentate carbonate, is not clear from the presented results. Monodentate carbonates are also still present after 145 min of reaction. The peak at 1353 cm^{-1} is assigned to the $\upsilon_s(COO^-)$ vibration, while the peak of $\upsilon_{as}(COO^-)$, which should appear at 1530-1470 cm^{-1}, is not visible in the spectrum. Due to the broad structure of the bidentate carbonate peak at 1535 cm^{-1} mentioned above, it is assumed that the missing monodentate carbonate peak is situated beneath this bidentate carbonate peak. The peak shift of the monodentate carbonate is of about the same magnitude as that of the bidentate carbonate, but in the opposite direction, which results from a strengthening of the bond. Parallel to this strengthening of the bond an increase of the peak intensity (coverage), can be observed (figs. 3.5-2 and 3.5-5). Hence, in contrast to the bidentate carbonate, either the electron density shift from the Ti into a bonding orbital of monodentate carbonate is enhanced or the shift to an anti-bonding orbital is

lowered. According to [143], the peak at 1428 cm^{-1} can either result from $\upsilon_{as}(CO_3^{2-})$ of uncoordinated carbonate species or from $\upsilon_s(COO^-)$ of carboxylate groups. In the latter case, the peak of the anti-symmetric vibration ($\upsilon_{as}(COO^-)$) should appear in the region of 1560 cm^{-1}–1630 cm^{-1}. Similar to the $\upsilon_{as}(COO^-)$ peak of monodentate carbonate, this peak can be hidden by the peaks of adsorbed water and bidentate carbonate. An assignment to uncoordinated carbonate species (CO_3^{2-}, see fig. 3.2-15c) can be discarded, since according to [143], the symmetric stretching vibration would occur in the region of 1090-1020 cm^{-1}. A comparison of the raw spectra (background and reaction spectra, data not shown here) does not show any change in reflectivity in this region. Equally to the monodentate carbonate, the peak of carboxylate species shift to higher wave numbers and the coverage increases (fig. 3.5-2).

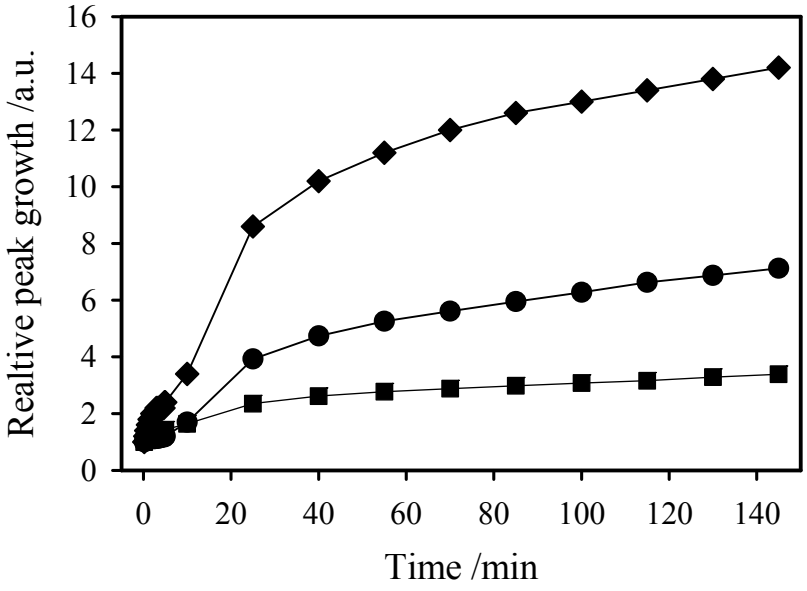

Figure 3.5-7: Relative temporal evolution of the peak intensities of bidentate carbonate at ~1540-1570cm^{-1} (■), monodentate carbonate at ~1330cm^{-1} (●) and carboxylate at ~1420cm^{-1} (♦) during CO oxidation (1 kPa CO , 1 kPa O_2, balance N_2, gas flow 40 Nml/min) in fig. 3.5-2. The peak intensities are normalized to those in the spectrum started at 12 s.

In the preceding paragraphs it was shown, that carboxylate, monodentate and bidentate carbonate are present on the surface during the entire reaction and that their coverage increases during reaction. Within the first 10 min of the reaction the peak of the bidentate carbonate increased stronger than that of the other two species, while starting from a reaction time of 20 min the development of their absolute peak intensities is parallel (see fig. 3.5-5). At this time the intensity of the H_2O_{ad} band has already passed its maximum and, according to fig. 3.5-3, the activity also starts to decrease. These correlations are a strong argument for the hypothesis, that at least one of the three species, bidentate and monodentate carbonate and

carboxylate, is responsible for the loss of activity. To identify the responsible species, the relative growth of the peak intensities is studied (fig. 3.5-7, the peak intensities are correlated to those in the spectrum taken from 12-21 s). Within the first 10 min, the peak of bidentate carbonate grows stronger than the peak of monodentate carbonate; afterwards the trend is the other way round. The carboxylate peak grows significantly stronger than the other two species, especially, when the activity for CO oxidation starts to decrease (compare figs. 3.5-3 and 3.5-7). The peak of bidentate carbonate shows the slightest increase during deactivation of the sample. From the relative behavior of the three species we assume that under the present conditions the growth of carboxylate, and to a smaller extent, of monodentate carbonate is one reason for the deactivation of the catalyst. Nevertheless, it can not be excluded that under different conditions (temperature, CO and O_2 partial pressure) their importance in the deactivation is different.

Carbonate-like species as a reason for deactivation have also been identified by Schubert et al. [32] for the selective CO oxidation in H_2-rich gases over Au/Fe_2O_3 and by Kung et al. [88] during CO oxidation over Au/Al_2O_3, respectively. For Au/TiO_2, however, carbonate-like species have been identified during CO oxidation in several publications [31,39,61,63], but they were not identified as source of deactivation. Lui et al. [63] and Bouccuzzi et al. [61] denoted them as species that do not participate in the reaction.

3.5.1.2 O_2/N_2 and CO/N_2 gas mixtures

The O_2/N_2 and CO/N_2 switches (1 kPa O_2 in N_2 and 1 kPa CO/N_2, respectively, gas flow 40 Nml/min) were started after the oxidation reaction (see fig. 3.5-1), to get knowledge about the influence of O_2 and CO on OH-groups, H_2O_{ad}, bidentate and monodentate carbonates and carboxylates. Immediately after the oxidation reaction (duration of CO oxidation: 145 min), the O_2/N_2 gas mixture was switched on and afterwards CO/N_2 and O_2/N_2 gas mixtures were introduced alternately. Figs. 3.5-8 and 3.5-9 display the spectra during a CO/N_2 switch (switch 5 in fig 3.5-1) and a O_2/N_2 switch (switch 6 in fig 3.5-1), respectively. The mode of spectra acquisition was similar to that during the oxidation reaction: During the first 5 min, spectra were recorded in 12 s intervals (20 scans per spectrum) and afterwards the acquisition mode was changed to 600 scans per spectrum (acquisition time 4 min 31 s per spectrum).

Except for a new peak at ~2055 cm^{-1} during the CO/N_2 switch, no additional peaks appeared in the spectra compared to the CO oxidation spectra (figs. 3.5-8 and 9). Hence, the assignment

of the peaks in subsection 3.5.1.1 shall be adopted and will not be discussed here, except from the new peak at ~2055 cm^{-1}. The first O_2/N_2 switch (switch 2 of fig 3.5-1) was used as transition from the 'steady state reaction mode' (CO oxidation) to 'transient mode' (CO/N_2 or O_2/N_2 gas mixture), since it followed the CO oxidation. In this switch the decomposition of the carboxylate and carbonate species was observed. Furthermore, the peak belonging to H_2O_{ad} increased and OH-groups were consumed (spectra not shown here). Since this behavior is slightly different from the other O_2/N_2 switches, and the differences originate from the preceding CO oxidation, this O_2/N_2 switch will not be considered and discussed further.

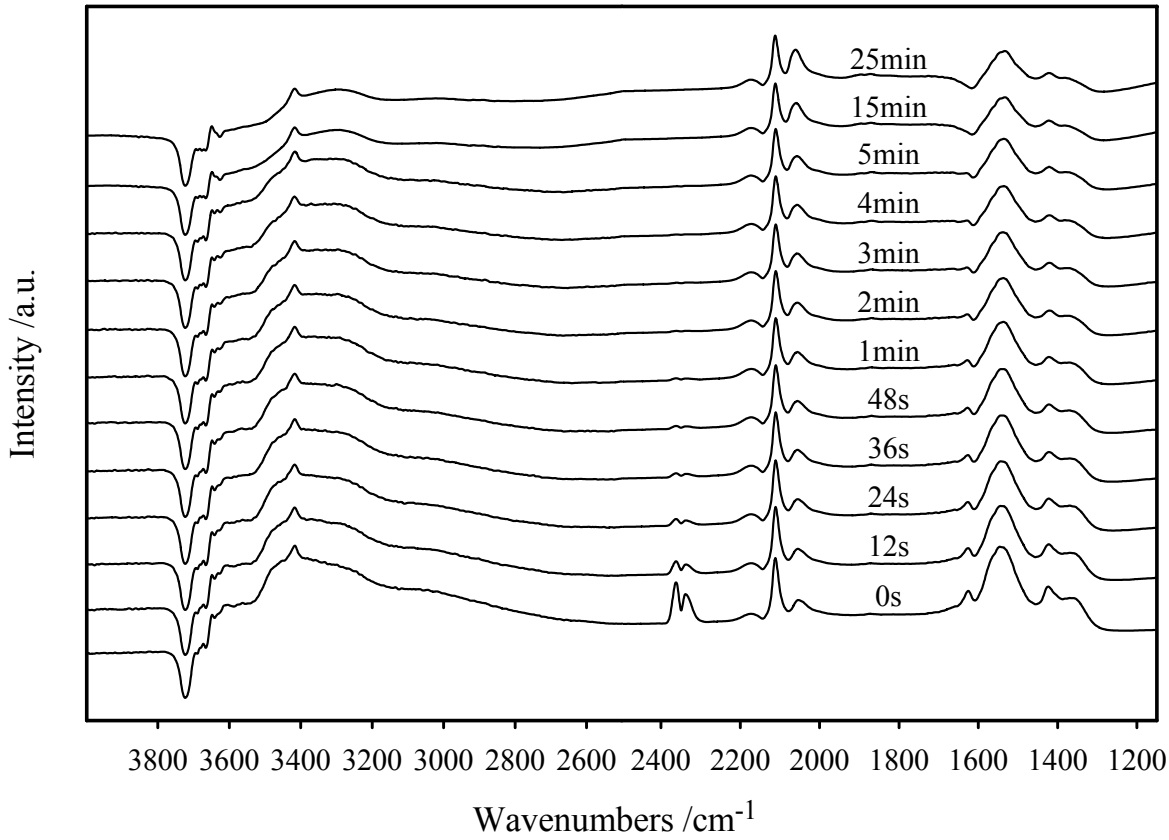

Figure 3.5-8: DRIFTS spectra recorded during a CO/N_2 switch (1 kPa CO in N_2, gas flow 40 Nml/min, switch 5 in fig. 3.5-1) at 80°C. At the times given in the plot, the spectra acquisition was started. From 0 s to 5 min, 20 scans were added for one spectrum (acquisition time 9 s). For the spectra taken at 15 and 25 min, 600 scans were added for one spectrum (acquisition time 4 min 31 s).

From the course of the other switches (switches 3-7 in fig. 3.5-1) the subsequent pattern can be deduced. During the CO/N_2 switches (for example see fig. 3.5-8 switch 5 in fig. 3.5-1), the peak intensities of H_2O_{ad} and the other peaks in the carbonate region decrease and the peak intensities of the OH-groups at 3723 cm^{-1} slightly increase, which means that these species are partly regenerated. During the O_2/N_2 switches (for example see fig. 3.5-9, switch 6 in fig. 3.5-1), the changes are more complex. The peak of H_2O_{ad} increases from the first to the second

spectrum, is consumed for some time and afterwards built up again. The other peaks in the carbonate region are built up from the first to the second spectrum and decomposed afterwards. CO_2 production can be observed during both kinds of switches. During the CO/N_2 switches, CO_2 was detected all time, while during the O_2/N_2 switches it was detectable during the initial 2 min. Nevertheless, since the gas mixtures flowed in the direction top → bottom of the catalyst bed, it can not be deduced from the latter observation, that at higher reaction times no CO_2 was produced. If only small amounts of CO_2 are produced, these are immediately flushed out of the DRIFTS cell (rather than into the IR dome) and can not be detected any more. Since DRIFTS is a qualitative technique, the amount of CO_2 produced during the switches can not be determined from the spectra. For this reason switch experiments with the IMR-MS as detection unit were carried out, which enables the calculation of eluted amounts (see section 3.5.2).

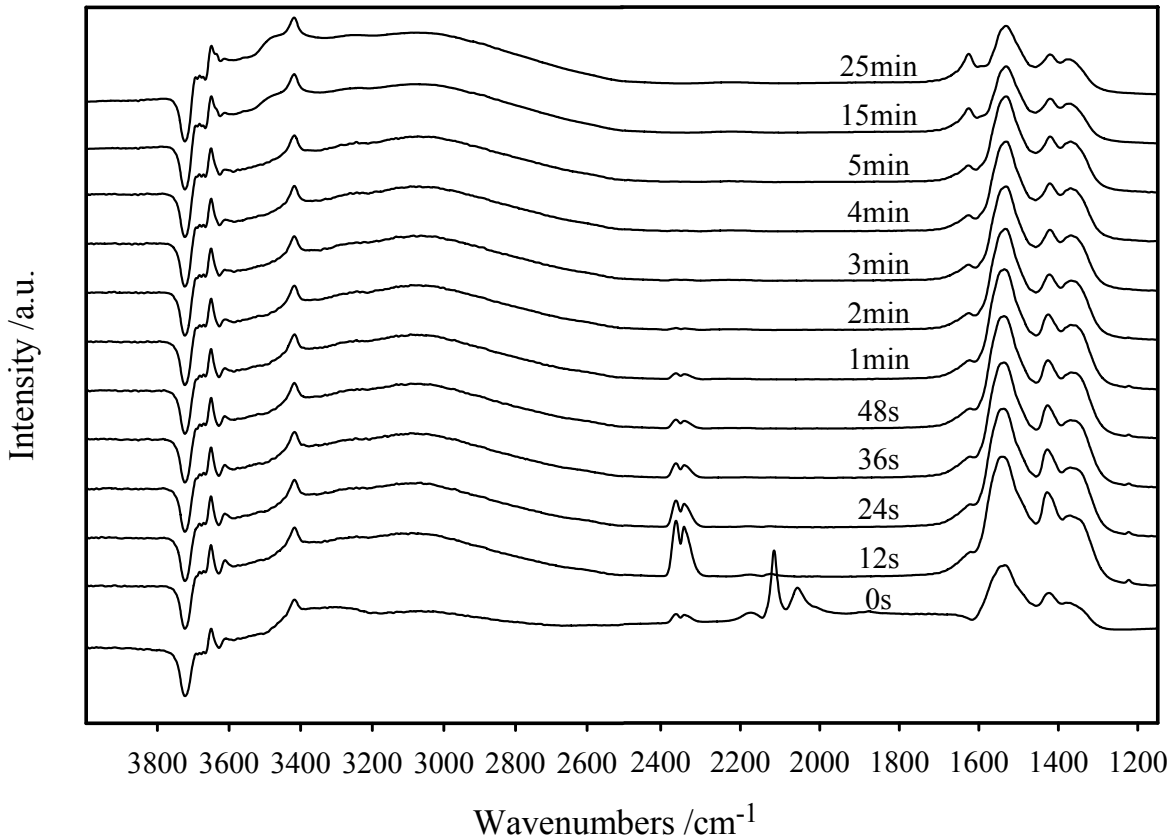

Figure 3.5-9: DRIFTS spectra recorded during an O_2/N_2 switch (1 kPa O_2 in N_2, gas flow 40 Nml/min switch 6 in fig. 3.5-1). At the times given in the plot, the spectra acquisition was started. From 0 s to 5 min, 20 scans were added for one spectrum (acquisition time 9 s). For the spectra taken at 15 and 25 min, 600 scans were added for one spectrum (acquisition time 4 min 31 s).

The behavior of the peak intensities of H_2O_{ad} and OH groups during the five switches is shown in detail in fig. 3.5-10. During the O_2/N_2 switches (4 and 6 in fig. 3.5-1), the peak

intensities of the OH groups at 3723 cm^{-1} decrease, i.e., they are consumed, while H_2O_{ad} is first consumed and afterwards produced (for both species squares and triangles down are used for the O_2/N_2 switches). From the first (acquired from 0-9 s of reaction) to the second (acquired from 12-21 s of reaction) spectrum, its peak intensity becomes positive and decays afterwards, as described above. In switch 4 more OH-groups are consumed than in switch 6, which goes along with higher peak intensities of H_2O_{ad} in the respective switches (the spectra for switch 6 are shown in fig. 3.5-9, the spectra of switch 4 are not shown, the temporal evolution of the peak intensities is summarized in fig. 3.5-10); in the first O_2/N_2 switch after the reaction (switch 2 in fig. 3.5-1, spectra not shown), the H_2O_{ad} peak intensity was even higher. Though the behavior of the OH-groups and H_2O_{ad} correlates during the O_2/N_2 switches, the decrease in peak intensity of H_2O_{ad} from switch 4 to switch 6 is not compensated entirely by an increase in OH-group peak intensity (fig. 3.5-10). This is evidence for the loss of H_2O and OH-groups during the experiment. Hence, the assumption, that water is not strongly adsorbed on the surface, but can desorb, is confirmed. Part of the desorbed water can be adsorbed again, which explains that the adsorption of water is not restricted to specific sites (see subsection 3.5.1.1).

During the CO/N_2 switches the OH groups regenerate slightly (fig. 3.5-10b), while the peak intensities of H_2O_{ad} decrease (fig. 3.5-10a). Note that the peak intensity of the OH groups increases switch by switch, which is in contrast to the behavior during the O_2/N_2 switches, where a loss of water and OH groups could be observed. A correlation of the development of the OH and H_2O_{ad} peak intensities, as it was found from switch 4 to switch 6 (O_2/N_2 switches), can not be observed during the CO/N_2 switches (switch 3→switch 5→switch 7). This can result from the integration of the negative H_2O_{ad} peak, since due to the large bidentate carbonate peak next to the negative H_2O_{ad} peak, a clear baseline could not be defined. Another possible explanation will be given beneath in the discussion of the additional CO_{ad} peak. Nevertheless, the consumption of OH-groups and production of H_2O_{ad} during the O_2/N_2 switches and the production of OH-groups and consumption of H_2O_{ad} duringthe CO/N_2 switches confirms the assumption made in subsection 3.5.1.1. There we had assumed that an equilibrium between OH-groups and H_2O_{ad} exists, which is influenced by O_2, in he following way: In the presence of O_2 the equilibrium is shifted to the side of H_2O_{ad}, while in the absence of O_2, i.e., during the CO/N_2 switches, it is shifted back to the side of the OH-groups.

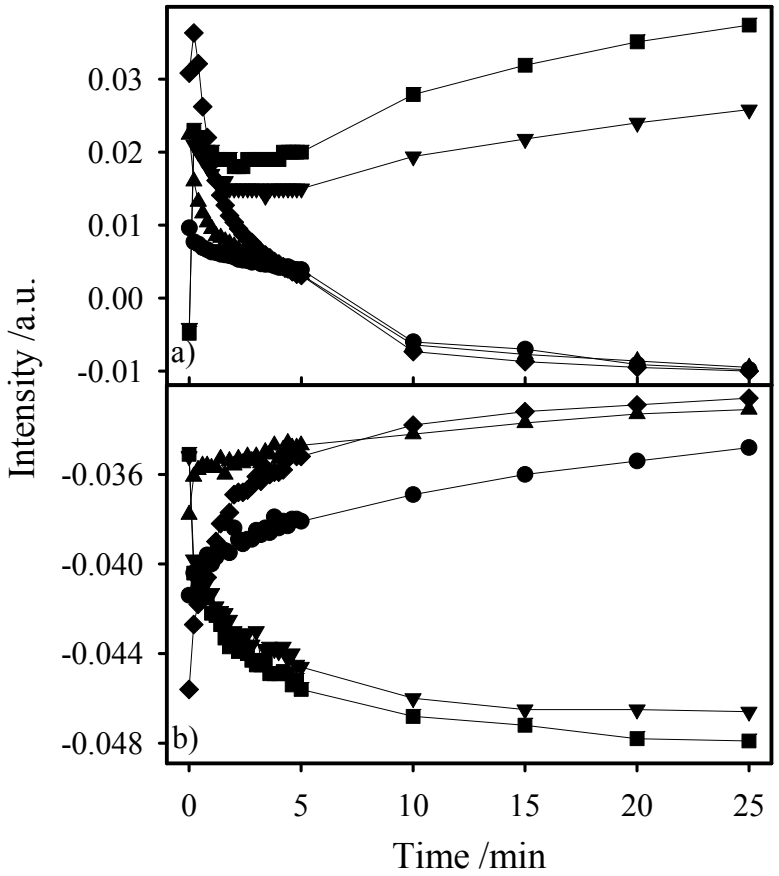

Figure 3.5-10: Temporal evolution of the peak intensities of a) H_2O_{ad} at ~1620 cm^{-1} and b) OH-groups at 3723 cm^{-1} in the following switches according to fig. 3.5-1. ●: switch 3 (CO/N_2), ■: switch 4 (O_2/N_2), ▲: switch 5 (CO/N_2), ▼: switch 6 (O_2/N_2), ♦: switch 7 (CO/N_2). CO/N_2 switches: 1 kPa CO in N_2; O_2/N_2 switches: 1 kPa O_2 in N_2; gas flow 40 Nml/min. The behaviour in the course of switch 2 (O_2/N_2) is not shown for reasons pointed out in the text.

Beside the OH-groups and H_2O_{ad} also the behavior of bidentate and monodentate carbonate and carboxylate peak intensity depends on the kind of switches that are performed (i.e. 1 kPa in O_2 in N_2 or 1 kPa CO in N_2, see fig. 3.5-11). At the beginning of the O_2/N_2 switches, all three species are produced, leading to a significant peak increase. Starting from the third acquired spectrum they are consumed, which continues during the CO/N_2 switches and leads to similar absolute intensities at the end of all three CO/N_2 switches. Furthermore, the peak intensities of all three species show similar trends, if the absolute intensities are considered, i.e., from fig. 3.5-11 it can not be deduced, whether one of those three species is favored during formation or decomposition. The parallel behavior of all three species in the progress of the measurements (fig. 3.5-11) leads to the assumption of the existence of an equilibrium. It was already mentioned in the discussion of the CO oxidation, that the monodentate and bidentate carbonate have very similar structures, which supports the hypothesis of a preceding equilibrium.

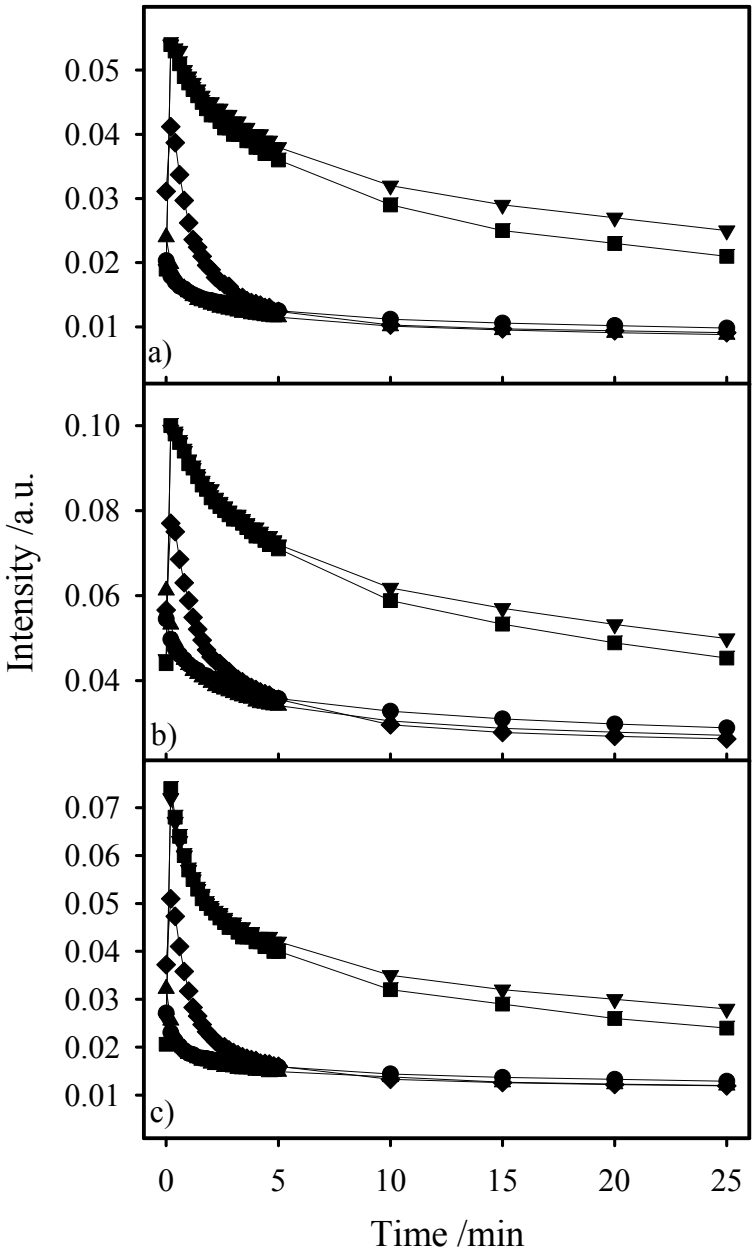

Figure 3.5-11: Temporal evolution of the peak intensities of a) monodentate carbonate at ~1330cm^{-1} b) bidentate carbonate at ~1540cm^{-1} and c) carboxylate at ~1420cm^{-1} in the following switches according to fig. 3.5-1: ●: switch 3 (CO/N_2), ■: switch 4 (O_2/N_2), ▲: switch 5 (CO/N_2), ▼: switch 6 (O_2/N_2), ♦: switch 7 (CO/N_2). CO/N_2 switches: 1 kPa CO in N_2; O_2/N_2 switches: 1 kPa O_2 in N_2; gas flow 40 Nml/min. The evolution during switch 2 (O_2/N_2) is not shown for reasons pointed out in the text.

The relative behavior of the peak intensities, normalized to the intensity in the first spectrum acquired in each switch, is plotted in fig. 3.5-12. Similar to the plots of the absolute intensities (fig. 3.5-11), the three species show the same trends, but the relative peak growth occurring during the O_2/N_2 switches is different. The carboxylate signals increase strongest, followed by the monodentate carbonates, while the bidentate carbonates have the lowest increase. This points to a build-up of these three species in the following order. First carboxylate is build-up,

which is converted to monodentate carbonate and then to bidentate carbonate. This assumption is confirmed by the peak decrease of the three species, relative to the peak maxima in the spectra taken from 12-21 s, which is listed in table 3.5-1 and behaves vice versa with respect to the peak increase. The decomposition of the carboxylate species is strongest, followed by the monodentate and then by the bidentate carbonate.

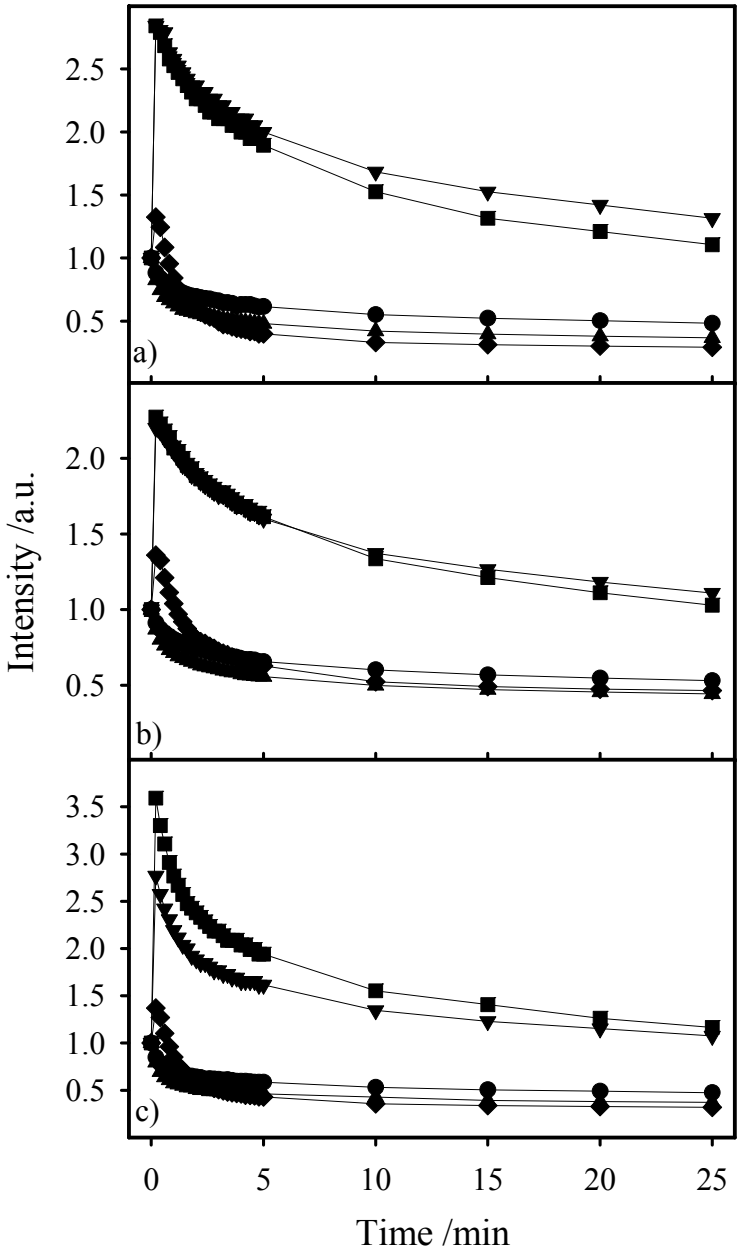

Figure 3.5-12: Temporal evolution of the peak intensities from fig. 3.5-11 normalized to the spectrum acquired from 0 to 9 s of a) monodentate carbonate at ~1330cm^{-1} b) bidentate carbonate at ~1540cm^{-1} and c) carboxylate at ~1420cm^{-1} in the following switches according to fig. 3.5-1: ●: switch 3 (CO/N_2), ■: switch 4 (O_2/N_2), ▲: switch 5 (CO/N_2), ▼: switch 6 (O_2/N_2), ♦: switch 7 (CO/N_2). CO/N_2 switches: 1 kPa CO in N_2; O_2/N_2 switches: 1 kPa O_2 in N_2; gas flow 40 Nml/min. The behaviour in the course of switch 2 (O_2/N_2) is not shown for reasons pointed out in the text.

The formation and decomposition behavior of the three species can be explained as follows: The three species exist in equilibrium and the carboxylate is formed first, which leads to a stronger peak increase (correlates with the amount produced), than for the monodentate and bidentate carbonates between the first and the second spectra of the O_2/N_2 switches. The carboxylate is converted to monodentate carbonate and afterwards to bidentate carbonate. The latter decomposes to CO_2, since it is thermally less stable than the other two species [176].

Bidentate carbonate as last intermediate product in the reaction mechanism before the production of CO_2 is in contrast to the proposal of the group of Kung and Costello [88,172], who proposed for a Au/γ-Al_2O_3 catalyst the transformation of a bicarbonate intermediate to inactive carbonate (byproduct, which does not poisen the catalyst) with the participation of OH-groups at the active sites. An inactive carbonate can be discarded here, since the decomposition of all three identified species, carboxylate, bidentate and monodentate carbonate, was observed after an initial increase at the beginning of the O_2/N_2 switches. The formation of carboxylate (formate) as initial step in the reaction mechanism was also proposed in a review article of Bond and Thompson [5]. As subsequent step they proposed the attack of one super oxide ion (O_2^-) at two carboxylates, which are transformed to CO_2, and the OH groups are retrieved. Furthermore, it was shown by Schubert et al. [32] and Boccuzzi et al. [61], that an enhanced composition of bidentate carbonate occurs during CO oxidation on Au/Fe_2O_3 and Au/TiO_2, respectively, if water was present in the gas mixture. These findings explain the evolution of the H_2O_{ad} peak. The introduction of O_2 to the sample leads to a shift of the OH-H_2O_{ad} equilibrium to the side of H_2O_{ad}, and therewith to the peak increase between the first and the second spectrum. We assume, that the water is involved in the conversion of monodentate to bidentate carbonates (a mechanism of this conversion can not be deduced from the spectra). Since the bidentate carbonate decomposes to CO_2, its loss is compensated by a continuous regeneration from monodentate species (which are built up from carboxylates). This explains the strongest decrease in the peak intensity of the carboxylate, followed by that of the monodentate species (table 3.5-1). Within the first ~2.5 min more water is involved in the process of monodentate to bidentate carbonate conversion than is produced by the OH-H_2O_{ad} equilibrium, which explains the decrease in peak intensity of H_2O_{ad} during this period. The peak intensity of H_2O_{ad} increases during the O_2/N_2 switches, when this relation is inverted due to the lack of CO in the gas mixture. When the residual CO from the previous switch is consumed, no new carboxylate is produced and the already

existing amount is decomposed. During the CO/N_2 switches the conversion to bidentate carbonates continues, but since no H_2O_{ad} is produced during the CO/N_2 switches, the carbonate like species are not decomposed completely (figs. 3.5-8 and 3.5-11).

Table 3.5-1: Relative peak decrease of the three species in the carbonate region during the O_2/N_2 switches, related to the peak maxima in the spectra acquired from 12-21 s. The values are calculated from the relative peak intensities in fig. 3.5-12. The switch numbers are related to the schematic presentation of the experiment in fig. 3.5-1.

Species	12 s → 5 min	12 s → 25 min	Switch number
Carboxylate	45.9%	67.6%	4
	41.7%	61.1%	6
Monodentate carbonate	33.3%	59.7%	4
	29.6%	53.7%	6
Bidentate Carbonate	27.5%	53.8%	4
	27.3%	49.6%	6

The peak intensity at the end of a switch is not exactly equal to the intensity at the beginning of the next switch (fig. 3.5-11), which is caused by the way the experiment is carried out: In order to avoid a spontaneous pressure increase, which would have destroyed the catalyst bed, the gas mixtures had to be turned to the 'bypass-mode' for the modification of the gas composition, and afterwards the gas mixture had to be switched back to the 'reaction mode'. During this modification procedure the 'old' gas mixture was still in contact to the catalyst and the reactions continued.

Finally, the behavior of the linearly adsorbed CO during the CO/N_2 switches shall be discussed. Beside the peak of normally linearly adsorbed CO at 2110-2120 cm^{-1}, an additional peak develops in the region of 2050-2060 cm^{-1}, whose intensity increases gradually (fig. 3.5-8). A peak shift for CO_{ad} to lower wave numbers is caused by a weakening of the C-O bond, which can originate from the following reasons: (i) A strengthening of the π-bond due to back donation from Au to CO and (ii) the weakening of the σ-bond from CO to Au. A peak shift of CO_{ad} similar to the one reported here has also been described by Bollinger and Vannice [39], when they switched off O_2 after CO oxidation over an Au/TiO_2 catalyst. The build-up of two peaks at 2175 cm^{-1} and 2055 cm^{-1} was observed, but the latter was not as pronounced as the one presented here. Hence, in both cases, the lack of O_2 in the gas mixture, i.e., the formation of a reductive atmosphere (reductive for the catalyst), resulted in the development of a new CO_{ad} species. Vannice and Bollinger assigned the peak at 2175 cm^{-1} to linearly adsorbed CO in rutile, anatase or Au/TiO_2, but the second peak was not assigned by

the authors. Boccuzzi et al. also reported about a peak at 2055 cm^{-1} with a shoulder at 1990 cm^{-1}, which appeared in addition to the 'normal' peak at 2100 cm^{-1} during CO adsorption on an Au/TiO_2 sample that was reduced with H_2 at 255°C before adsorption [110]. They explained their findings with a reduction of the support due to reaction with H_2 and a resulting transfer of negative charge to the gold particles, which causes an increased back-donation and hence a weakening of the C-O bond. A charge transfer from TiO_2 to Au nano-particles has indeed been reported by Jakob et al. [155], when exposing TiO_2 nano-particles to UV-radiation and bringing the resulting partly reduced and colored TiO_2 nano-particles into contact with Au nano particles. A peak shift of CO_{ad} was also observed during CO adsorption in H_2-rich atmosphere (see subsection 3.3.2.2). In this experiment (gas mixture: 5 mbar CO, 750 mbar H_2, balance N_2) the 'normal' peak at about 2110 cm^{-1} decreased with increasing adsorption time in favor of an asymmetric peak at 2032 cm^{-1}, which included a shoulder around 1985 cm^{-1} and possibly a second one around 1930 cm^{-1}. It was assigned to a distinctly different new CO_{ad} species, e.g., similar to reports for H_2/CO coadsorption on Ni(100) [156,157], or to a H_2-induced restructuring of the Au nanoparticles.

Since in the experiment presented there was no H_2 in the gas mixture, such H-Au-CO coadsorption can be excluded here. Nevertheless, a comparison of figs. 3.5-13 and 3.5-10b, where the first shows the behavior of the ratio of the newly developed CO_{ad} peak to the normal CO_{ad} peak and the latter the temporal development of the OH groups in the course of the switches, points to another interaction. The regeneration of the OH–groups during the three CO/N_2-switches (fig. 3.5-10b, circle, triangle up and diamond) increases from switch to switch (the intensity of the negative peak becomes smaller in each cycle). As described above, this is a discrepancy to the behavior of H_2O_{ad}, whose peak intensity does not show the corresponding dependence during these switches (see fig. 3.5-10a). The difference in the negative peak intensity of the OH-groups between the first two switches (3 and 5 in fig. 3.5-1) is bigger than between the second and the third switch (5 and 7 in fig. 3.5-1) (see fig. 3.5-10b), which is equal to the behavior of the intensity ratio of the new CO_{ad} peak (peak 2) to the normal CO_{ad} peak (peak 1) within these three CO/N_2 switches (fig. 3.5-13). This similarity points to an interaction between CO_{ad} and the OH groups, which weakens the C-O bond. An interaction of OH-groups with CO_{ad} on cationic Au^+ (in the neighborhood of metallic gold) at the gold-support interface has also been proposed by Costello et al. [172], who studied the CO oxidation on an $Au/\gamma\text{-}Al_2O_3$ catalyst. They suggested, that the interaction of CO with OH-

groups leads to the formation of carboxylate on the Au^+ cations, which reacts with O_{ad} to bidentate carbonate and is then decarboxylated. By this interaction of the OH-groups with CO_{ad} at the particle-support interface, the former are extracted from equilibrium between OH-groups and H_2O_{ad}, which leads to a stronger shift of the equilibrium to the OH-group side.

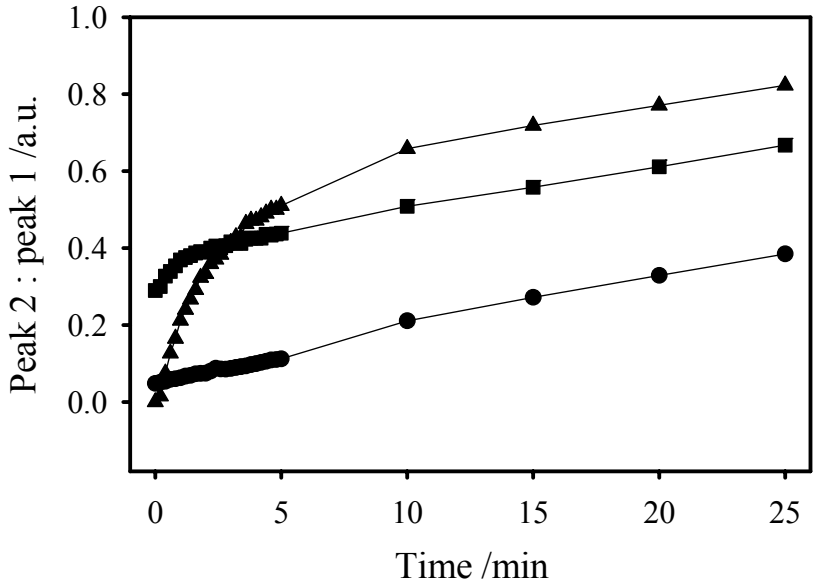

Figure 3.5-13: Ratio of peak intensities of CO_{ad} at 2050-2060cm^{-1} (denoted as peak 2) to $CO_{ad,lin}$ at 2110-2120cm^{-1} (denoted as peak 1) in the following CO/N_2 switches according to fig. 3.5-1: ●: switch 3, ■: switch 5, ▲: switch 7.

The above interaction of CO_{ad} and OH-groups is not observed during reaction, as is obvious from the absense of the shifted CO_{ad} peak in fig. 3.5-2. Due to the presence of O_2 they are converted immediately. The additional peak during the CO/N_2 switches supports the assumption, that carboxylate is the first intermediate product in a reaction mechanism including carboxylate, monodentate and bidentate carbonates, since the reaction of CO and OH results in carboxylates. This reaction path way gives a further explanation for the lack of OH-groups during CO-oxidation, which is plotted in fig. 3.5-5 (the decrease of H_2O_{ad} peak intensity does not go along with a corresponding peak increase of the OH-groups). Beside the desorption of water, these groups are consumed for the build-up of carboxylate. During the CO/N_2 switches, this reaction path ends at the stage of coadsorbed CO and OH due to the lack of O_2 in the gas mixture and results in the additional CO_{ad} peak.

3.5.2 IMR-MS measurements

From the switch experiments studied with DRIFTS, useful information was obtained on the involvement of OH-groups, H_2O, carboxylate and carbonate species in the reaction mechanism. It could not be elucidated, however, whether the proposed reaction mechanism is the only path for CO oxidation under the present conditions. Furthermore, at the beginning of the switches, CO_2 production could be detected (figs. 3.5-8 and 9), but the amount of eluted CO_2 could not be quantified. Due to this lack of information, similar switch experiments were carried out with a plug-flow reactor connected to the IMR-MS.

For the IMR-MS measurements, the information content was enhanced by the use of isotope labeled O_2, since information on the reaction mechanism is expected from the distribution of CO_2 isotopomers during the switches and the CO oxidation. The experiment along the scheme presented in fig. 3.5-1 was carried out twice, once with $^{36}O_2$ and $C^{16}O$ as reactants during CO oxidation (switch 1 in fig. 3.5-1) and once with $^{32}O_2$ and $C^{16}O$, in order to elucidate potential effects of the carboxylate and carbonate species on the distribution of CO_2 isotopomers. The subsequent switches were carried out with $^{36}O_2$ in both experiments in order to obtain information from the distribution of CO_2 isotopomer and for an experimental reason, which will be explained in the respective subsection.

3.5.2.1 CO Oxidation

This subsection deals with the distribution of CO_2 isotopomers during CO oxidation. The gas mixtures contained 1 kPa $C^{16}O$, 0.6 kPa $^{36}O_2$, balance N_2, flux 40 Nml/min. For experimental reasons the oxidation reaction could not be carried out in 1 kPa O_2, as it was done in the measurements described in section 3.5.1 and chapter 3.2 (the CO/N_2 gas contained 2% CO, the $^{36}O_2/N_2$ gas contained 1.25% $^{36}O_2$, which makes it impossible to create a gas mixture with 1 kPa $C^{16}O$ and 1 kPa $^{36}O_2$ in the existing set-up). CO oxidation was performed on a freshly conditioned catalyst and on a sample, which had catalyzed the oxidation of $C^{16}O$ with $^{32}O_2$ for 66 min prior to the oxidation with $^{36}O_2$ (figs. 3.5-14a and b, respectively). For both plots the time scale was set to zero at the beginning of the oxidation reaction. In plot 3.5-14a, which displays the CO oxidation on a freshly conditioned sample, the bypass concentrations are shown in the time scale from -0.5 min to 0 min, while in plot 3.5-14b, the oxidation reaction with $^{32}O_2$ can be observed in this time scale.

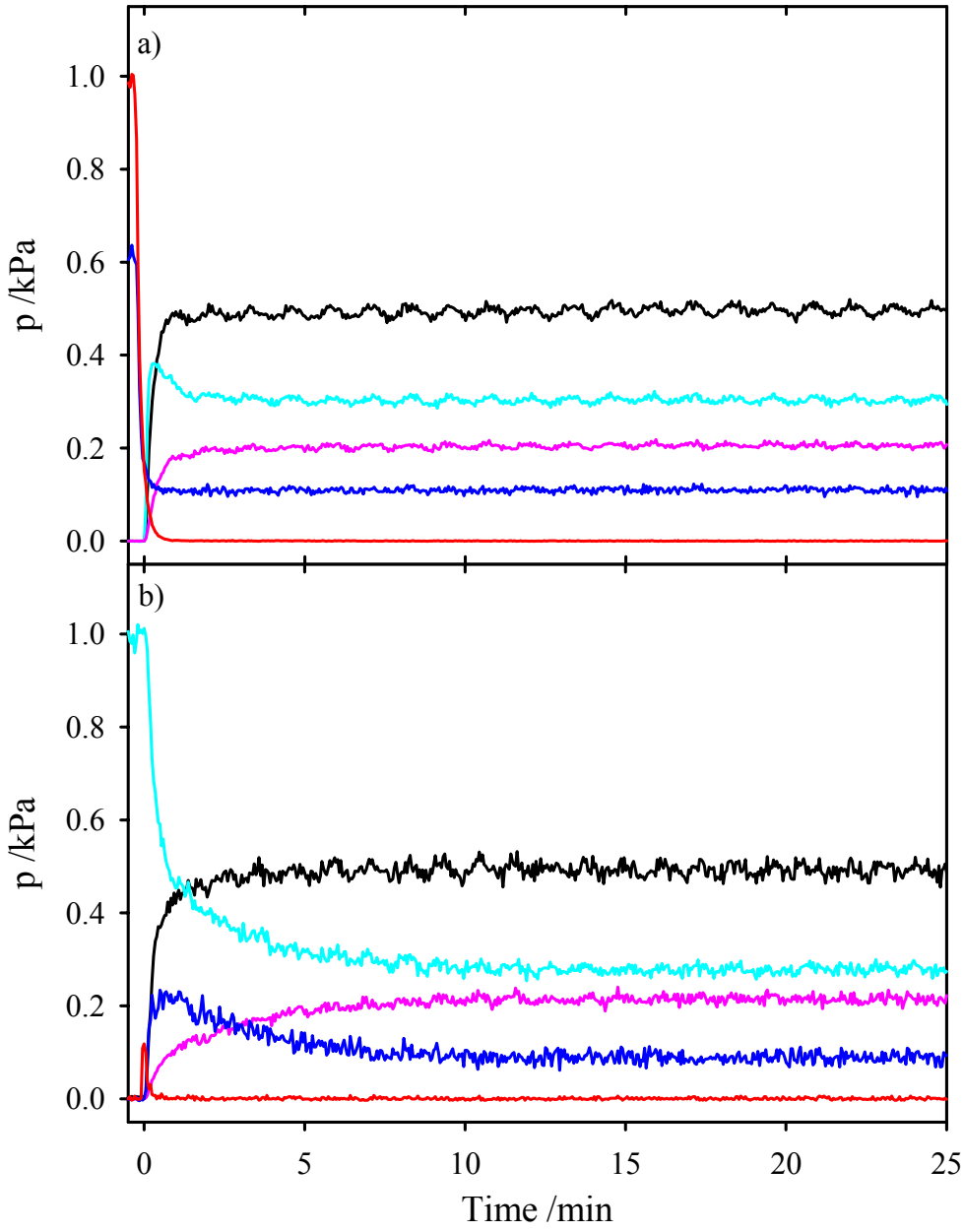

Figure 3.5-14: Distribution of CO_2 isotopomers during CO oxidation at 80°C of 1 kPa ^{28}CO, 0.6 kPa $^{36}O_2$, balance N_2, flow 40 Nml/min. a) Over a freshly conditioned, undiluted $Au/TiO_2(5)$ and b) over an undiluted sample of $Au/TiO_2(5)$ that had reacted in 1 kPa ^{28}CO 0.6 kPa $^{32}O_2$, balance N_2 (flow 40 Nml/min) for 66 min before switching to $^{36}O_2$. Legend for both plots: — $^{46}CO_2$, — $^{44}CO_2$, — $^{48}CO_2$, — $^{36}O_2$, — ^{28}CO. For both plots the time scale is shifted to t=0 min, when the oxidation with $^{36}O_2$ was started.

Under both conditions the oxidation reaction produces the three CO_2 isotopomers $C^{18}O^{16}O$, $C^{16}O^{16}O$ and $C^{18}O^{18}O$. Under steady state conditions, $C^{16}O^{18}O$ occurs with the highest partial pressure, followed by $C^{16}O^{16}O$ and by $C^{18}O^{18}O$. During CO oxidation on the freshly conditioned sample (fig. 3.5-14a) steady state is achieved after about 5 min reaction time (steady state partial pressures: $C^{16}O^{18}O$: 0.49 kPa, $C^{16}O^{16}O$: 0.30 kPa, $C^{18}O^{18}O$: 0.20 kPa). At the beginning of the reaction, the partial pressures of $C^{16}O^{16}O$ and $C^{16}O^{18}O$ increase nearly

simultaneously (for $C^{16}O^{16}O$ the slope is slightly higher), while the increase of $C^{18}O^{18}O$ partial pressure is much slower. After 26 s the partial pressure of $C^{16}O^{16}O$ reaches a maximum and is exceeded by the partial pressure of $C^{16}O^{18}O$. The partial pressure of $C^{16}O^{16}O$ decreases slightly and after about 5 min the partial pressures of all three CO_2 isotopomers become stable. In the sample, which underwent CO oxidation with $^{32}O_2$ prior to the CO oxidation with $^{36}O_2$ (fig. 3.5-14b), about 15 min were needed to achieve steady state conditions (steady state partial pressures: $C^{16}O^{18}O$: 0.49 kPa, $C^{16}O^{16}O$: 0.28 kPa, $C^{18}O^{18}O$: 0.21 kPa). Reasons for this longer time span can be i) residual $C^{16}O^{16}O$ from the first oxidation reaction, which had to be eluted and ii) residual carbonates, which were decomposed. Equally to the reaction on the freshly conditioned sample, the partial pressure of $C^{18}O^{18}O$ increased much slower than that of $C^{16}O^{18}O$.

Since $^{36}O_2$ was used for the oxidation of $C^{16}O$, the origin of the $C^{16}O^{16}O$ and $C^{18}O^{18}O$ has to be explained. Olea et al. reported, that CO_2 desorption is the rate determining step of the CO oxidation on Au/TiO_2 at a temperature of 100°C, which is close to the temperature used here (80°C) [158]. Furthermore, Liu et al. [63] as well as Boccuzzi and co workers [15,61,177] reported that CO_2 undergoes oxygen isotope exchange on Au/TiO_2. It can be deduced from the results of Liu et al. [63] that (i) oxygen from the TiO_2 support is involved in the exchange reaction and (ii) in the observed experiment only one oxygen isotope exchange occurred per CO_2 molecule, since the introduction of $C^{18}O^{18}O$ to the catalyst resulted in detectable amounts of $C^{16}O^{18}O$ and $C^{18}O^{18}O$ only. An estimation of the number of collisions of a CO_2 molecule in our experiments, gives an order of magnitude of 10^8, which leads to the question, whether only one isotope exchange reaction per CO_2 molecules is realistic. For this reason the two cases of (i) a single and (ii) a large number of oxygen isotope exchange reactions of CO_2 will be considered.

There are several possible models for a reaction mechanism of the CO oxidation. Three plausible will be studied here: (i) O_2 dissociates and reacts as atomic oxygen with adsorbed CO to CO_2 [4], (ii) reaction via a peroxide-like reaction intermediate, $CO{\cdot}O_2$, [178], or (iii) via a carbonate intermediate [4]. In the first two models only one O atom of the oxygen molecule gets in contact with the CO (beneath denoted as ‘model I’) and in the third model both atoms get in contact with the CO molecule and we assume, that all three C-O bonds have the same probability to be broken (beneath denoted as ‘model II’). In the above section we

identified the following mechanism as one reaction path: CO_{ad} reacts with OH-groups to carboxylate, is transformed to monodentate carbonate and afterwards to thermally instable bidentate carbonate. The transformation of carboxylate to monodentate carbonate can occur in two ways. First, CO is activated by the build-up of carboxylate and then reacts with an oxygen molecule (with regeneration of the OH-groups), which would follow 'model II' or second, O_2 gets dissociated on the catalyst and an oxygen atom reacts with the carboxylate to monodentate carbonate. In this case the reaction would follow 'model I'.

Above, it was pointed out that two limiting cases concerning the number of CO_2 oxygen isotope exchanges should be considered. First, we discuss the case of only one oxygen isotope exchange of CO_2. In 'model I', i.e., CO is in contact with only one O-atom of the O_2 and exclusively $C^{16}O^{18}O$ is produced in the reaction of $C^{16}O$ and $^{36}O_2$. In this case the other two isotopomers result exclusively from oxygen isotope exchange of CO_2. For this exchange the subsequent rules apply: i) If $C^{16}O^{18}O$ undergoes an exchange with ^{16}O, either $C^{16}O^{18}O$ or $C^{16}O^{16}O$ (equations 3.5-1 and 3.5-2) and ii) if $C^{16}O^{18}O$ exchanges with ^{18}O, either $C^{16}O^{18}O$ or $C^{18}O^{18}O$ can be produced (equations 3.5-3 and 3.5-4). Assuming that there are equal amounts of ^{16}O and ^{18}O, on the surface, which are active for oxygen isotope exchange of CO_2 (it will be shown beneath, that this is not the case), the resulting product distribution is $C^{16}O^{18}O$: 50%, $C^{16}O^{16}O$: 25% and $C^{18}O^{18}O$: 25%, (equation 3.5-5).

$$C^{16}O^{18}O + {}^{16}O \rightarrow C^{16}O{}^{16}O + {}^{18}O \qquad (3.5\text{-}1)$$

$$C^{16}O^{18}O + {}^{16}O \rightarrow C^{16}O{}^{18}O + {}^{16}O \qquad (3.5\text{-}2)$$

$$C^{16}O^{18}O + {}^{18}O \rightarrow C^{18}O{}^{18}O + {}^{16}O \qquad (3.5\text{-}3)$$

$$C^{16}O^{18}O + {}^{18}O \rightarrow C^{16}O{}^{18}O + {}^{18}O \qquad (3.5\text{-}4)$$

$$4C^{16}O^{18}O \rightarrow 2C^{16}O^{18}O + C^{16}O^{16}O + C^{18}O^{18}O \qquad (3.5\text{-}5)$$

'Model II' implies O_2 dissociation during the oxidation reaction (CO is in contact with the entire O_2 molecule), i.e., a $C^{16}O$-$^{36}O_2$ complex is built, which can dissociate ito all three different possible CO_2 combinations with the same probability. This leads to two $C^{16}O^{18}O$ and one $C^{18}O^{18}O$ molecules. The former undergoes the oxygen isotope exchanges shown in equations 3.5-1 to 3.5-4, and the latter the exchanges shown in equations 3.5-6 to 3.5-9. The balance with the assumption of equal amounts of active ^{16}O and ^{18}O is given in equation 3.5-10.

$$C^{18}O^{18}O + {}^{16}O \rightarrow C^{18}O{}^{16}O + {}^{18}O \qquad (3.5\text{-}6)$$

$$C^{18}O^{18}O + {}^{16}O \rightarrow C^{16}O{}^{18}O + {}^{18}O \qquad (3.5\text{-}7)$$

$$C^{18}O^{18}O + {}^{18}O \rightarrow C^{18}O^{18}O + {}^{18}O \quad (3.5\text{-}8)$$

$$C^{18}O^{18}O + {}^{18}O \rightarrow C^{18}O^{18}O + {}^{18}O \quad (3.5\text{-}9)$$

$$8C^{16}O^{18}O + 4C^{18}O^{18}O \rightarrow 6C^{16}O^{18}O + 2C^{16}O^{16}O + 4C^{18}O^{18}O \quad (3.5\text{-}10)$$

If there are equivalent amounts of ^{16}O and ^{18}O on the surface, that are active for oxygen isotope exchange with CO_2, then for both models the sum of all three CO_2 isotopomers is equal to the sum of the double amounts of $C^{16}O^{16}O$ and $C^{18}O^{18}O$ (equations 3.5-5 and 3.5-10, also, the sum of $C^{16}O^{16}O$ and $C^{18}O^{18}O$ equals the amount of $C^{16}O^{18}O$). For this reason the sum of the partial pressures of the CO_2 isotopomers from fig. 3.5-14 are plotted in fig. 3.5-15 with black lines and the sum of the doubled amounts of $C^{16}O^{16}O$ and $C^{18}O^{18}O$ with red lines. During oxidation on the freshly conditioned sample (fig. 3.5-15a), the red line is slightly higher than the black line within the first minute of reaction, which indicates that the sum of the doubled amounts of $C^{16}O^{16}O$ and $C^{18}O^{18}O$ is higher than the sum of all three CO_2 isotopomers. This slight difference must originate from the $C^{16}O^{16}O$ partial pressure, since the partial pressure of $C^{18}O^{18}O$ in this time regime is very low.

If the reaction is carried out after oxidation with $^{32}O_2$, the red line is also at a much higher level at the beginning of the reaction than the black one (fig. 3.5-15b), which results from $C^{16}O^{16}O$ produced in the foregoing CO oxidation with $^{32}O_2$. Hence, part of the $C^{16}O^{16}O$ does not result from the oxygen isotope exchange produced during the oxidation reaction with $^{36}O_2$ and therefore the sum of the double amounts of $C^{16}O^{16}O$ and $C^{18}O^{18}O$ is higher than the sum of the three isotopomers. In both plots of fig. 3.5-15 the red and the black lines are identical, when steady state of the reaction is reached, i.e., under these conditions the sum of all three CO_2 isotopomers is equal to the sum of the doubled amounts of $C^{16}O^{16}O$ and $C^{18}O^{18}O$.

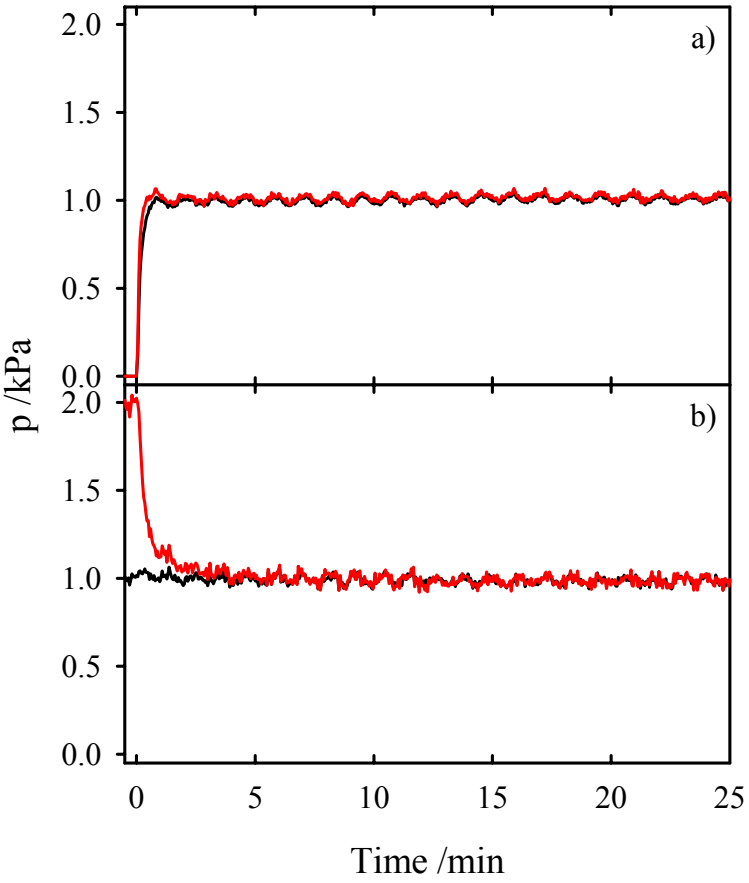

Figure 3.5-15: Comparison of the sum of the produced amounts of $C^{16}O^{18}O$, $C^{16}O^{16}O$ and $C^{18}O^{18}O$ (black lines) with the sum of the doubled amounts of $C^{16}O^{16}O$ and $C^{18}O^{18}O$ (red lines) during oxidation of $C^{16}O$ with $^{36}O_2$ at 80°C on a) a freshly conditioned sample and b) a sample that had catalyzed CO oxidation with $^{32}O_2$ prior the studied reaction. The values were calculated from the data in fig. 3.5-14.

To decide, which model is valid for the reaction, also the initial time evolution of $C^{18}O^{18}O$ is studied (fig. 3.5-14). In both experiments, the level of $C^{18}O^{18}O$ is below the level of $C^{16}O^{16}O$. On the freshly conditioned sample (fig. 3.5-14a), its partial pressure increases slower than that of the other two isotopomers, and after the oxidation reaction with $^{32}O_2$ (fig. 3.5-14b) it increases slower than $C^{16}O^{18}O$ (In the latter experiment the behavior of $C^{16}O^{16}O$ can not be taken into account at the beginning of the reaction, since there is still residual $C^{16}O^{16}O$ from the prior oxidation with $^{32}O_2$. Nevertheless, this $C^{16}O^{16}O$ can influence the amounts of $C^{16}O^{18}O$ and $C^{18}O^{18}O$). A certain time is necessary, until the TiO_2 support contains ^{18}O, which is active for the oxygen isotope exchange with CO_2, and more ^{16}O makes isotope exchange, when quasi steady state conditions are achieved. Hence, the two reaction models have to be calculated for ^{16}O:^{18}O ratios higher than 1. In that case the balances calculated for ^{16}O:^{18}O=1 are as follows: For ‘model I’ the reaction results in equal amounts of $C^{16}O^{16}O$ and

$C^{18}O^{18}O$ (see equation 3.5-5) and 'model II' results in an even higher amount of $C^{18}O^{18}O$ than $C^{16}O^{16}O$ (see equation 3.5-10). Hence, the reaction model has to be identified, which leads to the results of fig. 3.5-15, if the amounts of active ^{16}O and ^{18}O on the surface are not equal, but higher than 1 (^{16}O:$^{18}O \geq 1$). For 'model II', the equality of the sum of the three CO_2 isotopomers with the sum of doubled amounts of $C^{16}O^{16}O$ and $C^{18}O^{18}O$, which is laid down in fig. 3.5-15, is only fulfilled, if the amounts of active ^{16}O and ^{18}O are equal (table 3.5-2), hence this model can be discarded, if one isotope exchange occurs. For 'model I', the above mentioned equality is fulfilled for all ^{16}O:^{18}O ratios (table 3.5-2). Hence, for one oxygen isotope exchange of CO_2 'model I' is valid.

Table 3.5-2: Distribution of CO_2 isotopomers calculated from the two different reaction models at different ^{16}O:^{18}O ratios for one isotope exchange reaction.

	‚Model I'				‚Model II'			
^{16}O:^{18}O	1:1	2:1	3:1	4:1	1:1	2:1	3:1	4:1
$C^{16}O^{18}O$	2	3	4	5	6	10	14	18
$C^{16}O^{16}O$	1	2	3	4	2	4	6	8
$C^{18}O^{18}O$	1	1	1	1	4	4	4	4
$C^{16}O^{18}O + C^{16}O^{16}O + C^{18}O^{18}O$	4	6	8	10	12	18	24	30
$2 \cdot C^{16}O^{16}O + 2 \cdot C^{18}O^{18}O$	4	6	8	10	12	16	20	24

The assumption, that CO_2 undergoes only one oxygen isotope exchange, goes along with the results of Liu et al. [63], but as already mentioned above, it indicates a reaction probability of $\sim 10^{-8}$ for the exchange reaction. Therefore, also the case of a large number of exchange reactions has to be considered. In that case, dynamic equilibrium distributions would be expected. If the fractions of ^{16}O (beneath denoted as 'a') and ^{18}O (beneath denoted as 'b') on the surface, which do isotope exchange, were equal, the CO_2 distribution would be $C^{16}O^{18}O$: 50%, $C^{16}O^{16}O$: 25% and $C^{18}O^{18}O$: 25%. Since $p(C^{16}O^{16}O) \neq p(C^{18}O^{18}O)$ during reaction (fig. 3.5-14), the fractions of ^{16}O and ^{18}O are not equal on the TiO_2 support ($a \neq b$). In this case the distribution of the CO_2 isotopomers is as follows: $C^{16}O^{16}O : C^{16}O^{18}O : C^{18}O^{18}O$ is $a^2 : 2ab : b^2$. This distribution has to fulfill the requirement, that the sum of partial pressures of all three CO_2 isotopomers is equal to the sum of the doubled amounts of $C^{16}O^{16}O$ and $C^{18}O^{18}O$ (equation 3.5-11), which was found experimentally (fig. 3.5-15).

$$a^2 + 2ab + b^2 \overset{!}{=} 2a^2 + 2b^2 \quad \rightarrow \quad 2ab = a^2 + b^2 \qquad 3.5\text{-}11$$

This requirement is only fulfilled for a=b=0.5, which is not the case. To check whether this deviation could be detected in the presented measurements, the fractions of ^{16}O ('a') and ^{18}O

('b'), which undergo isotope exchange have to be calculated from the detected partial pressures of $C^{16}O^{16}O$ and $C^{18}O^{18}O$ during reaction (fig. 3.5-14). For this, the following assumptions are made: i) The sum of 'a' and 'b' is 1 (100% of the oxygen atoms, equation 3.5-12)and i) 'a' and 'b' are proportional to $\sqrt{p_{C^{16}O^{16}O}}$ and $\sqrt{p_{C^{18}O^{18}O}}$, respectively (equations 3.5-13 to 3.5-14, the probability for the formation of a $C^{16}O^{X}O$ is 'a', that for a $C^{16}O^{16}O$ is 'a^2', hence $p_{C^{16}O^{16}O} = \frac{1}{x} \cdot a^2$; the derivation for 'b' and $C^{18}O^{18}O$ is analogous). Solving the equation system 3.5-12 to 3.5-14, the results in equations 3.5-15 and 3.5-16 are obtained for 'a' and 'b' respectively.

$$a + b = 1 \tag{3.5-12}$$

$$a = x \cdot \sqrt{p_{C^{16}O^{16}O}} \tag{3.5-13}$$

$$b = x \cdot \sqrt{p_{C^{18}O^{18}O}} \tag{3.5-14}$$

$$a = \frac{\sqrt{p_{C^{16}O^{16}O}}}{\sqrt{p_{C^{16}O^{16}O}} + \sqrt{p_{C^{18}O^{18}O}}} \tag{3.5-15}$$

$$b = \frac{\sqrt{p_{C^{18}O^{18}O}}}{\sqrt{p_{C^{16}O^{16}O}} + \sqrt{p_{C^{18}O^{18}O}}} \tag{3.5-16}$$

Based on these equations, the fractions of ^{16}O ('a') and ^{18}O ('b'), which undergo isotope exchange are 0.551 and 0.449 on the freshly conditioned sample, and 0.536 and 0.464 on the sample, which had reacted with $^{32}O_2$ before, respectively. The difference of the $C^{16}O^{18}O$ partial pressures calculated for these values ($p_{C16O18O}$=2ab; 0.495 kPa and 0.497 kPa for the freshly conditioned sample and the one that had reacted in $^{32}O_2$ before, respectively) and those detected during the experiments (fig. 3.5-14) can not be detected due to the high noise.

In total, from the distribution of the CO_2 isotopomers in quasi steady state, it can not be concluded, how many oxygen isotope exchanges occur and which model is valid.

Next, the temporal development of the partial pressures of the three CO_2 isotopomers in the course of the two experiments is discussed (fig. 3.5-16, the behavior of $C^{16}O^{16}O$ after reaction of $C^{16}O$ and $^{32}O_2$ is excluded from this discussion, since its high initial partial pressures results form the preceding reaction). For $C^{16}O^{18}O$ and $C^{18}O^{18}O$, (i) the partial pressure of both isotopomers increases faster on the freshly conditioned sample than on the sample, which had catalyzed the CO oxidation with $^{32}O_2$ before, (ii) in both experiments the partial pressure of $C^{16}O^{18}O$ increases significantly faster than the one of $C^{18}O^{18}O$, and (iii) on the freshly

conditioned sample the $C^{16}O^{16}O$ partial pressure increases slightly faster than the one of $C^{16}O^{18}O$, reaches a maximum at 26 s and then decreases to its steady state value, as was already mentioned at the beginning of this subsection.

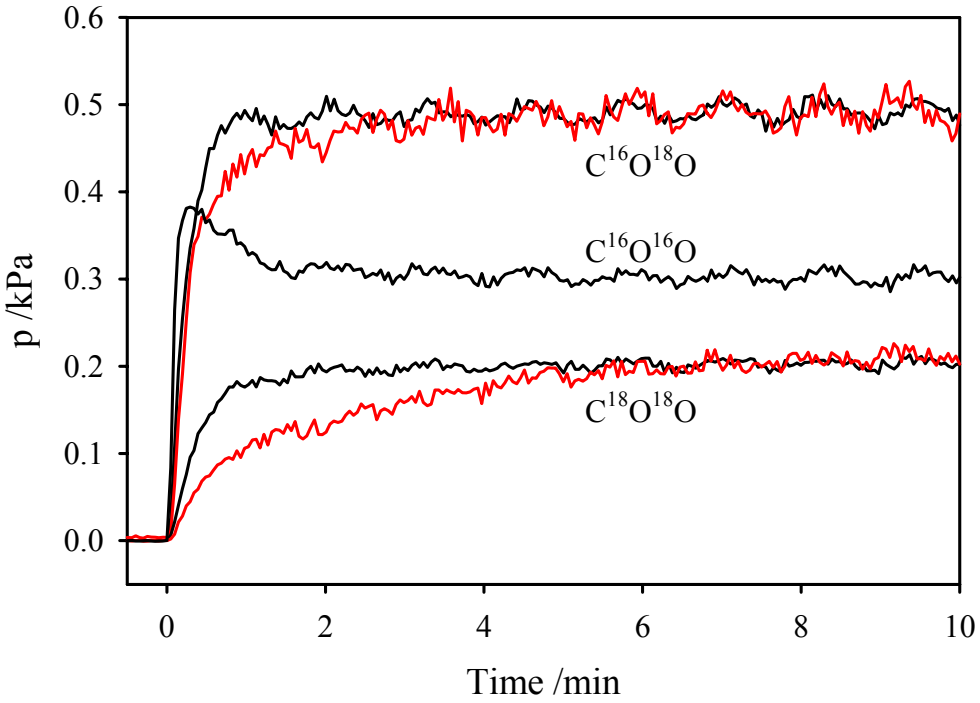

Figure 3.5-16: Comparison of partial pressures of $C^{16}O^{18}O$ and $C^{18}O^{18}O$ during CO oxidation of $C^{16}O$ with $^{36}O_2$ on the freshly conditioned sample (black lines) and the sample which underwent CO oxidation with $^{32}O_2$ before (red lines) in fig. 3.5-14.

The following conclusions can be drawn. First, the enrichment of the catalyst with ^{18}O active for the oxygen isotope exchange with CO_2 is a gradual process, which indicates its incorporation into the catalyst via the oxygen isotope exchange with ^{18}O-containing CO_2 produced in the CO oxidation. Dissociative adsorption of O_2, at least at measureable rates, was already ruled out in section 3.3.3. The enrichment of the TiO_2 support with ^{18}O from $^{36}O_2$, where only one ^{18}O atom reacts, can be excluded, since the excess $^{36}O_2$, which is stoichiometrically not needed for the CO oxidation, is eluted (fig. 3.5-14). Second, the presence of carboxylate and carbonate species on the surface (see DRIFTS experiments), resulting from the CO oxidation with $^{32}O_2$, delays the enrichment of the catalyst with ^{18}O, but once a steady state is achieved, they do not influence the ^{16}O:^{18}O ratio any more. Hence, CO oxidation with $^{32}O_2$ enhances the amount of ^{16}O on the sample and therefore a longer time scale is needed for reaching a quasi-steady state equilibrium concentration during CO oxidation with $^{36}O_2$, compared to the oxidation reaction on a freshly conditioned sample.

The steady state in both experiments with the reported concentrations ($C^{16}O^{16}O > C^{18}O^{18}O$) is unexpected, since more ^{16}O exits the samples than is introduced. This is apparent, if the values of 'a' (exchange probability for ^{16}O) and 'b' (exchange probability for ^{18}O), which where determined above for the reaction model with a large number of oxygen isotope exchanges, are compared. For both reactions 'a' (0.551 and 0.536) is higher than 'b' (0.449 and 0.464). The probability for an isotope exchange with ^{16}O on the TiO_2 surface is about 10% higher than for ^{18}O. Since half of the introduced $^{36}O_2$ leaves the reactor effectively 'unchanged' (fig. 3.5-14), effectively one ^{16}O from CO reacts with one ^{18}O from $^{36}O_2$ and the excess of ^{16}O must be provided by the TiO_2 support. From the mass balance both probabilities should develop towards 0.5. This discrepancy to the experiments in fig. 3.5-14 can be explained by the amounts of catalyst used for the experiments. In both cases the sample weight was 100 mg, which corresponds to $2.4 \cdot 10^{-3}$ mole oxygen atoms present in the sample, if stoichiometric TiO_2 is assumed. Since the catalyst was used undiluted, the conversion during reaction was 100%, hence $1.4 \cdot 10^{-5}$ mole CO_2 were produced per minute, calculated by the Ideal Gas Law ($V_{CO2}=0.4 \cdot 10^{-6}$ m^3, T=80°C). If all CO_2 produced exchanges oxygen, 2.2 h would be needed, until each support-oxygen was exchanged (for one exchange of oxygen CO_2). As shown above, the ^{16}O excess represents ~10% of ^{18}O, i.e., ~5 % of the total exchanges O is provided by the support, which enlarges the time scale to 44 h. Hence only a quasi steady state is achieved in fig. 3.5-14 and the approach of the equilibrium of ^{16}O:^{18}O=1 is too slowly and therefore too gradual to be observed in these experiments.

Finally, the role of the carboxylate-carbonate reaction pathway is studied, which was identified with DRIFTS in section 3.5.1. Therefore, the temporal evolution of $C^{16}O^{16}O$ at the beginning to the oxidation of $C^{16}O$ with $^{36}O_2$ is studied on the sample, which had reacted with $C^{16}O$ and $^{32}O_2$ before. If the pathway mentioned above was the primary reaction mechanism under the present conditions, the partial pressure level of $C^{16}O^{16}O$ from the oxidation reaction with $^{32}O_2$ should be constant at the beginning of the reaction with $^{36}O_2$, since at this stage the catalyst surface is covered with the carboxylate and carbonate species.

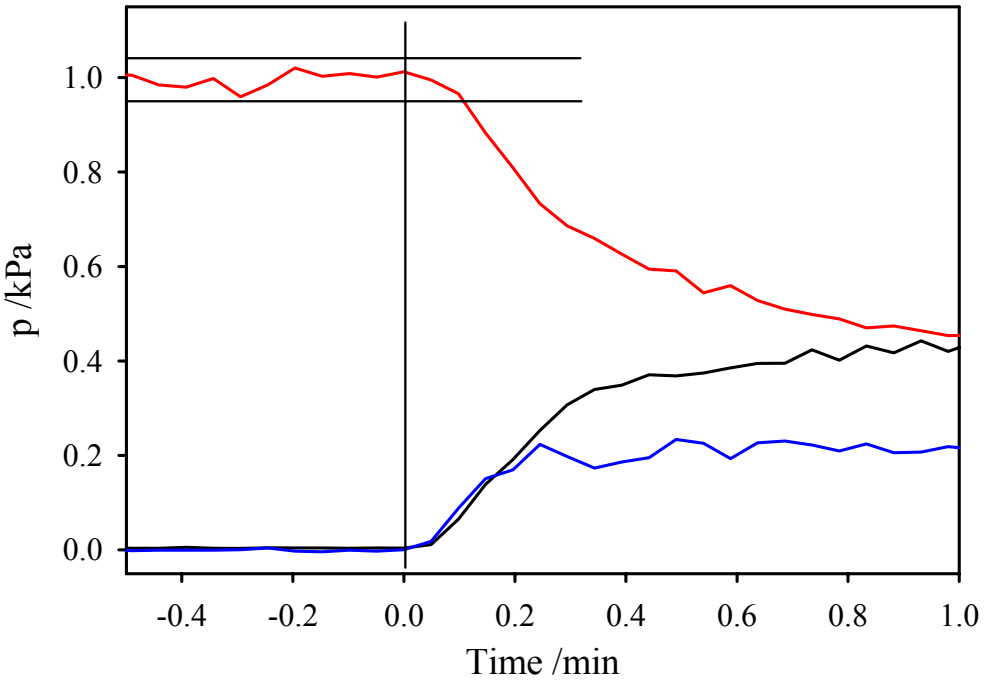

Figure 3.5-17: Temporal evolution of the partial pressures of the three CO_2 isotopomers (red line: $C^{16}O^{16}O$, black line: $C^{16}O^{18}O$, blue line: $C^{18}O^{18}O$) within the first minute after gas modification from $C^{16}O$ and $^{32}O_2$ to $C^{16}O$ and $^{36}O_2$ (reaction of fig. 3.5-14b). The horizontal lines frame the partial pressure range of $C^{16}O^{16}O$ during CO oxidation with $^{32}O_2$ and the vertical line marks the exchange of $^{32}O_2$ with $^{36}O_2$.

A detailed plot of the reaction right before and after the switch is shown in fig. 3.5-17. Due to the noise of the $C^{16}O^{16}O$ signal, the ranges of its partial pressure during the 6 min of reaction before the switch are included (horizontal lines). The signal of $C^{16}O^{16}O$ is inside the range marked by the two horizontal lines for about 6 s after the modification of the gas mixture (see fig. 3.5-17). Since the $C^{16}O^{16}O$ signal would drop immediately, if the carboxylate-carbonate mechanism is not dominant, it can be concluded, that this mechanism is the primary mechanism. This assumption is supported by the behavior of CO_2 partial pressure after a switch from the gas mixture 1 kPa CO, 1 kPa O_2, balance N_2 to 1 kPa O_2 in N_2, (fig. 3.5-18). Here the time is set to zero, when the O_2 partial pressure is out of its range during the oxidation reaction. The strong increase of O_2 partial pressure is an artifact of the gas modification procedure (the flow from the CO/N_2 line was replaced by a N_2 flow, which led to a temporary reduction of the flux and therefore an enhancement of the O_2 concentration, since the N_2-dilution was missing). Fig. 3.5-18 shows the same behavior of the CO_2 partial pressure as fig. 3.5-17; the level is constant for some seconds after the switch. However, it has to be stated at this place, that these findings can only be used as preliminary results and as an indication, that the carboxylate-carbonate mechanism is the dominant reaction pathway, since

the point of the gas exchange (vertical lines in figs. 3.5-17 and 3.5-18) could not be determined exactly (time resolution 2.9 s and 1.9 s for figs. 3.5-17 and 3.5-18, respectively). A definite decision requires experiments with a higher time resolution (for both gas dosing as well as product detection), such TAP (Temporal Analysis of Products) reactor measurements.

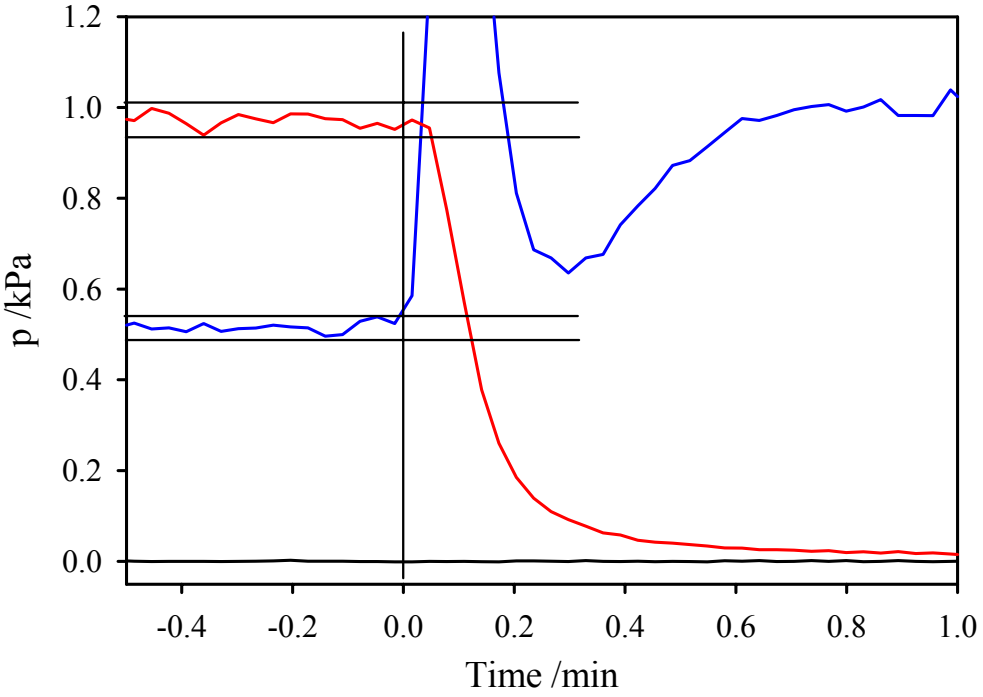

Figure 3.5-18: Development of partial pressures of CO_2 (red line), O_2 (blue line) and CO (black line), when the gas mixture is modified from 1 kPa $C^{16}O$, 1 kPa $^{32}O_2$, balance N_2 (flux 40 Nml/min, time scale in figure: -0.5 – 0 min) to 1 kPa $^{32}O_2$ in N_2 (flux 40 Nml/min, time scale in figure: 0 – 1 min) at 80°C on catalyst Au/TiO_2 (5). The horizontal lines frame the partial pressure ranges of CO_2 and O_2 during the CO oxidation reaction and the vertical line marks the modification of the gas mixture.

3.5.2.2 O_2/N_2 and CO/N_2 gas mixtures

Similar to the DRIFTS experiment, to fig. 3.5-1, a switch experiment with the IMR-MS as detection unit was carried out. In order to detect a potential influence of the carboxylate and of monodentate and bidentate carbonates, the oxidation step was carried out once with $^{32}O_2$ and $C^{16}O$ (in the following denoted as '$^{32}O_2$-experiment') and once with $^{36}O_2$ and $C^{16}O$ (in the following denoted as '$^{36}O_2$-experiment'). In both experiments the O_2/N_2 switches were performed with $^{36}O_2$ for the following two reasons: First, from the distributions of the isotopomers information concerning the reaction mechanism was expected. Second, as mentioned in the experimental section, $^{32}O_2$ is added undiluted and dosed by a MFC with a maximal flow of 5 Nml/min. Hence, the flow added to the gas mixture from this gas line was much smaller than the flow from the other lines (e.g., 0.4 Nml/min from the O_2 line and 20 Nml/min from the CO/N_2 line). During the switch experiments, the gases were flushed into

the exhaust, if they were not needed, and switched to 'reaction mode', if they were introduced to the sample. A pressure difference exists between the 'exhaust mode' and the 'reaction mode', since in the exhaust mode the MFCs have to work against atmospheric pressure only, while in the 'reaction mode' the base pressure is higher than atmospheric pressure, due to the resistence of the catalyst bed. This pressure difference has to be compensated by the MFCs, when the gas mixture in the respective line is switched from the 'exhaust mode' to the 'reaction mode'. This was done faster by the MFCs, if the gas flow was high, i.e., if diluted gas mixtures were used. Hence, the use of the diluted $^{36}O_2$ gas mixture for the O_2/N_2 switches led to sharper switch profiles and no difference appeared in the compensation of the pressure difference between 'exhaust mode' and 'reaction mode', compared to the gases added from the other lines. Beside the experiments according to fig. 3.5-1, experiments with slightly modified sequences were performed, which are illustrated schematically in fig. 3.5-19. Here, the objective was to test, whether CO_2 is also produced, if the preceding switch was carried out in pure N_2, i.e., if more carboxylates/carbonates can be decomposed.

The signals of the three CO_2 isotopomers during the '$^{36}O_2$-experiment' are shown in fig. 3.5-20 and those during the '$^{32}O_2$-experiment' in fig. 3.5-21. In the first case, the presentation was started with switch 3 and in the second case with switch 5 (for the denotation of the switches see fig. 3.5-1), since in the '$^{32}O_2$-experiment' a $^{32}O_2/N_2$ (switch 3) had to follow the oxidation with $^{32}O_2$ and the first switch with $^{36}O_2/N_2$ gas mixture was switch 5. The two most obvious results of these experiments are, first, the higher amount of eluted CO_2 caused by the switch combination $O_2/N_2 \rightarrow CO/N_2$ (left rows of figs. 3.5-20 and 3.5-21) compared to the combination $CO/N_2 \rightarrow O_2/N_2$ (right rows of figs. 3.5-20 and 3.5-21). Second, in both combinations $C^{16}O^{16}O$ is produced with the highest amount, followed by $C^{16}O^{18}O$ and, with the lowest amount, by $C^{18}O^{18}O$. This is an unexpected result, since $^{36}O_2$ was introduced to the samples and according to the results of subsection 3.5.2.1, the amount of $C^{16}O^{18}O$ should be higher than for $C^{16}O^{16}O$ (foregoing CO oxidation with $^{36}O_2$ in the '$^{36}O_2$-experiment' 28 min).

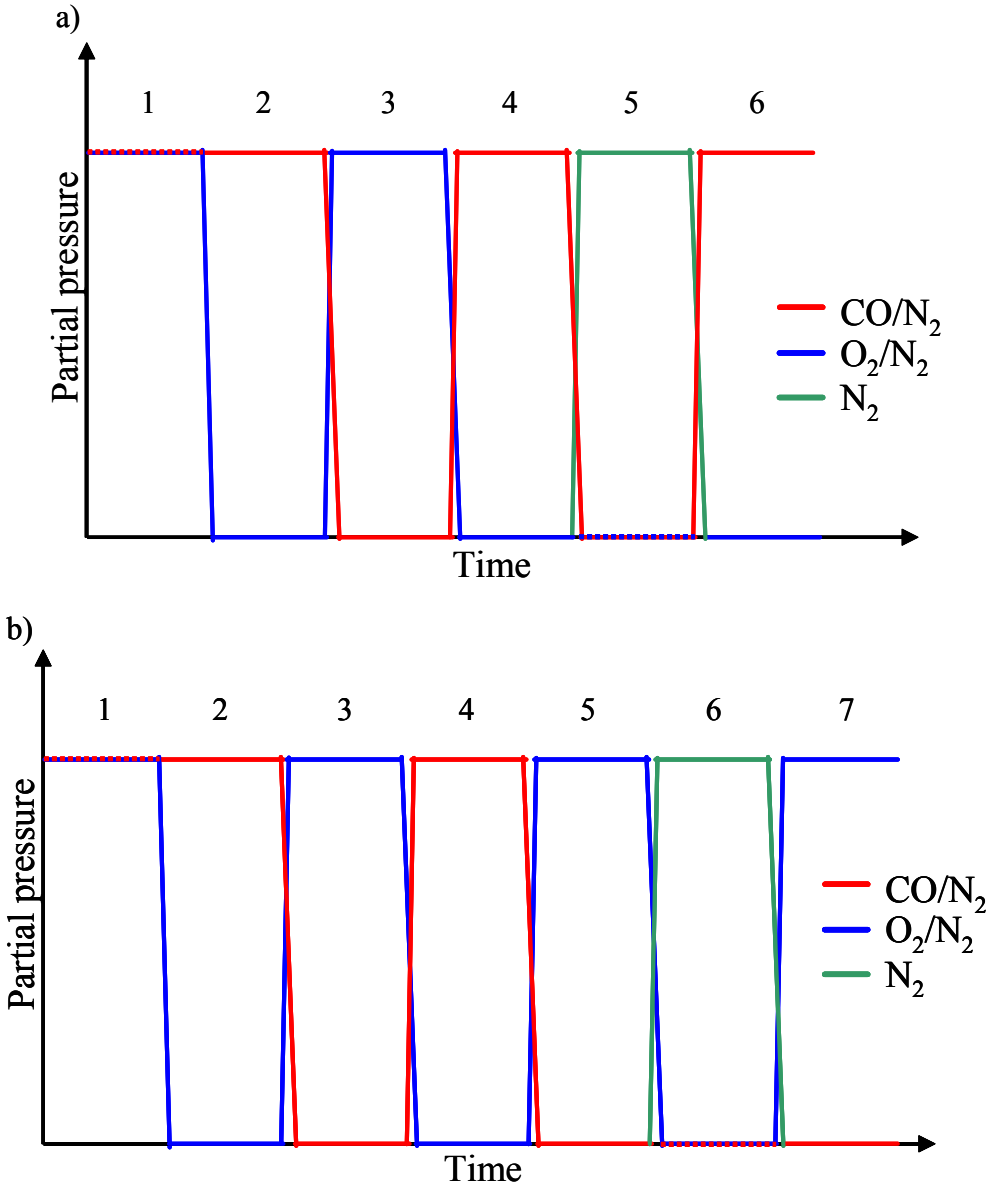

Figure 3.5-19: Schematic presentation of the modified switch experiments performed with a plug-flow reactor connected to an IMR-MS, in order to deduce, whether CO_2 production also occurs after N_2 switches. a) Including a CO/N_2-N_2-CO/N_2 combination. b) Including an O_2/N_2-N_2-O_2/N_2 combination.

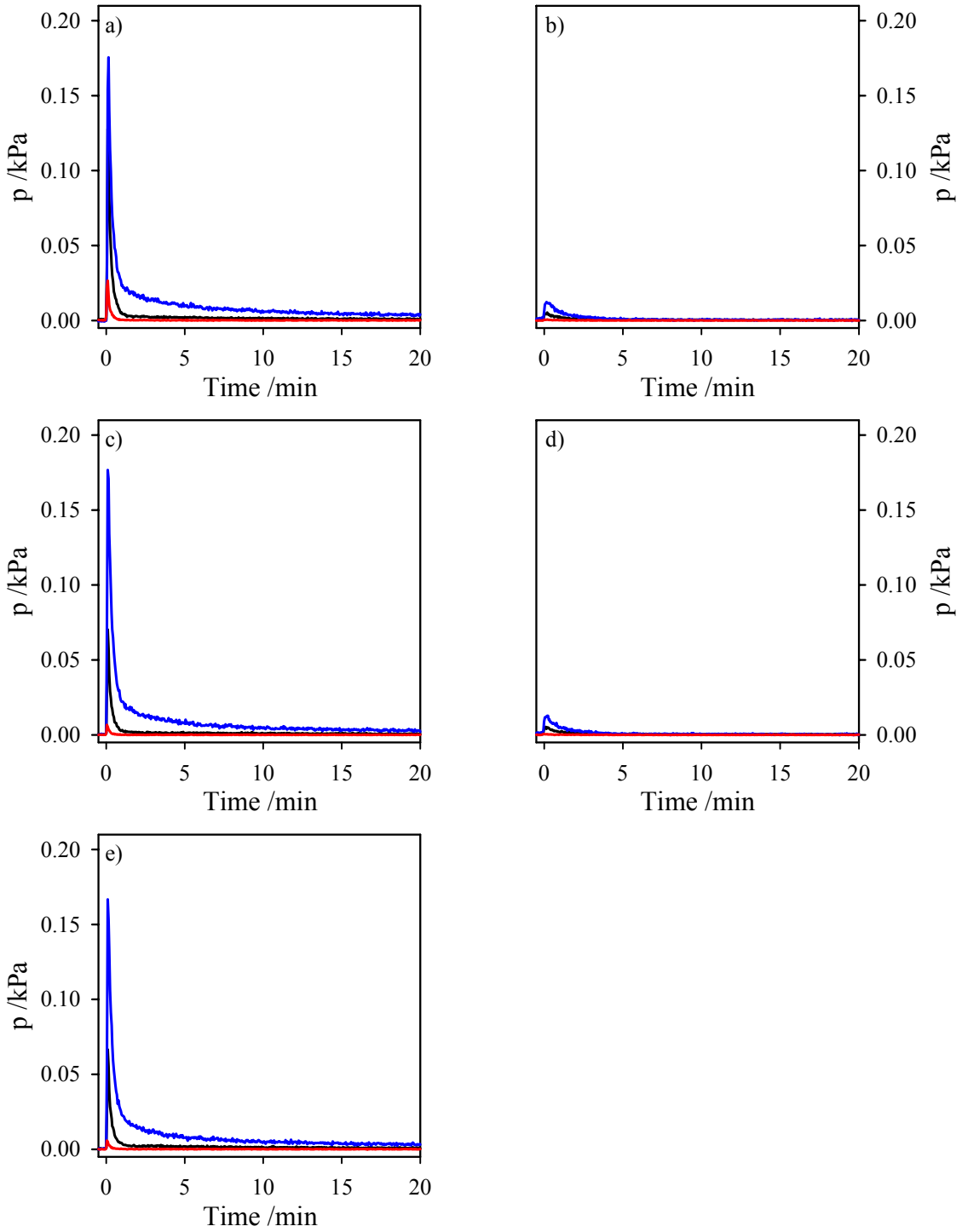

Figure 3.5-20: Evolution of the CO_2 isotopomers during the switches after CO oxidation carried out with 1 kPa ^{28}CO and 0.6 kPa $^{36}O_2$ (switch numbers referred to fig. 3.5-1): a) switch 3 ($^{28}CO/N_2$), b) switch 4 ($^{36}O_2/N_2$), c) switch 5 ($^{28}CO/N_2$), d) switch 6 ($^{36}O_2/N_2$) and e) switch 7 ($^{28}CO/N_2$). Legend for all plots: — $^{46}CO_2$, — $^{44}CO_2$, — $^{48}CO_2$. Time was set to zero, when the switch war started.

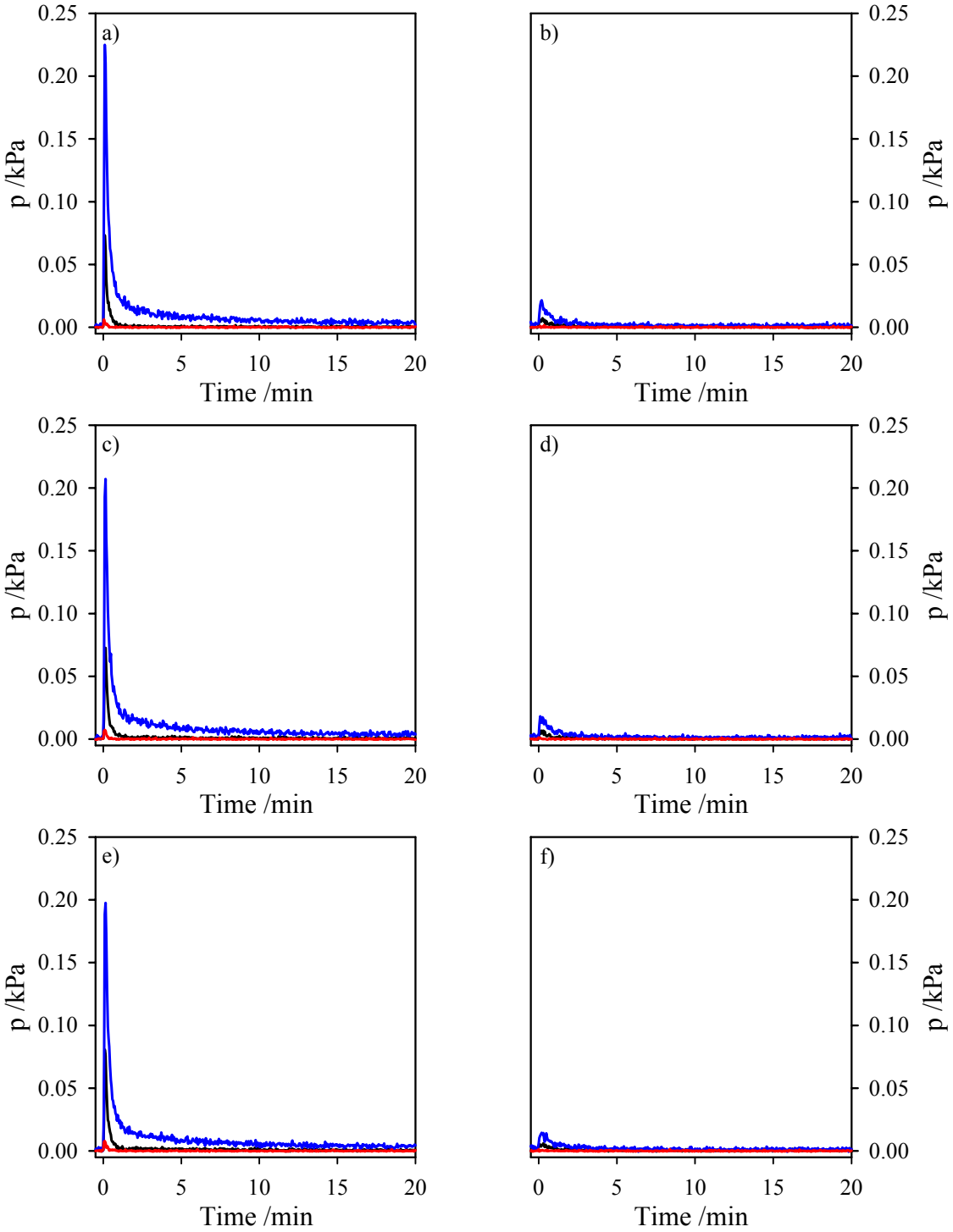

Figure 3.5-21: Evolution of the CO_2 isotopomers during the switches after CO oxidation carried out with 1 kPa ^{28}CO and 1 kPa $^{32}O_2$ and switch 2 and 3 were performed with $^{32}O_2/N_2$ and $^{28}CO/N_2$, respectively (switch numbers referred to fig. 3.5-1): a) switch 5 ($^{28}CO/N_2$), b) switch 6 ($^{36}O_2/N_2$), c) switch 7 ($^{28}CO/N_2$), d) switch 8 ($^{36}O_2/N_2$), e) switch 9 ($^{28}CO/N_2$) and f) switch 10 ($^{36}O_2/N_2$). Legend for all plots: — $^{46}CO_2$, — $^{44}CO_2$, — $^{48}CO_2$. Time set to zero, when the switch war started.

The phenomenon of an unexpectedly high amount of $C^{16}O^{16}O$ was also reported by Olea et al. [158], when they performed TAP experiments on Au/Ti(OH)*$_4$ with a single pulse, containing $C^{16}O$ and $^{36}O_2$. The population of the CO_2 product was about $C^{16}O^{16}O$: 60%, $C^{16}O^{18}O$: 24% and $C^{18}O^{18}O$: 16%. They explained the large amount of $C^{16}O^{16}O$ by $^{32}O_2$ impurities in the $^{36}O_2$ gas and, predominantly, by oxygen isotope exchange of CO_2 and TiO_2 (the TiO_2 support was not saturated with ^{18}O).

To clarify, what was responsible for the unexpected high amounts of $C^{16}O^{16}O$ in our experiments, the CO_2 peaks were integrated and the corresponding amounts were calculated according to equation 3.5-17 (the calculation of mole from Nml is based on the Ideal Gas Law).

$$n[\text{mole}] = \frac{\text{integrated area}[\%\cdot\text{min}]\cdot 0.01\cdot \text{flow}[\text{Nml}\cdot\text{min}^{-1}]}{22.4\cdot 10^3\,[\text{Nml}\cdot\text{mole}^{-1}]} \qquad (3.5\text{-}17)$$

A comparison of the eluted amount of CO_2 during the switches shows the comparability of the results received via the two methods shows. With DRIFTS, CO_2 could be detected during the O_2/N_2 switches for about 2 min, while during the CO/N_2 switches, traces of CO_2 were detected until the end of the switches. DRIFTS is a qualitative method and most of the produced CO_2 is eluted immediately and can not be detected, but from the described pattern in the different kind of switches, it can be deduced, that the amount of produced CO_2 during the O_2/N_2 switches is smaller than that in the CO/N_2 switches. The same was found during the IMR-MS experiments. Here the amount of eluted CO_2 during the CO/N_2 switches is 4-6 times as big as during the O_2/N_2 switches (table 3.5-3).

During the first $^{36}O_2/N_2 \rightarrow CO/N_2$ combination (switch 3) in the '$^{36}O_2$-experiment', the amount of eluted CO_2 (~5300 nmole) is significantly higher than the eluted amounts during all other $^{36}O_2/N_2 \rightarrow CO/N_2$ switches, which are in the range of 4200-4400 nmole (table 3.5-3). In particular, higher amounts of $C^{16}O^{18}O$ and $C^{18}O^{18}O$ can be observed. In the '$^{32}O_2$-experiment' such a significantly higher amount of eluted CO_2 during the first switch can not be observed. Since in this case the first switch with a $^{36}O_2/N_2 \rightarrow CO/N_2$ combination is switch 5, i.e., two additional switches have been made between the oxidation reaction and this switch, the reason for the higher amount in switch 3 of the '$^{36}O_2$-experiment' must be the decomposition of residual bidentate and monodentate carbonates and carboxylates, which where identified in section 3.5.1 (this was also observed after CO oxidation with $^{32}O_2$, see

fig. 3.5-14b). This hypothesis is supported by the fact that $C^{16}O^{16}O$ has a much lower share in this switch than in all other switches of both experiments. Since the carbonates and carboxylates in this experiment were built-up during CO oxidation with $^{36}O_2$, and hence these species consist of ^{18}O, their decomposition leads to higher amounts of $C^{16}O^{18}O$ and $C^{18}O^{18}O$.

Table 3.5-3: Integrated amounts of the CO_2 isotopomers eluted during the switch experiments, which are plotted in figs. 3.5-20 and 20.

Oxidation with $^{36}O_2$ and $C^{16}O$ (fig. 3.5-20)							
Switch	Amount /nmole			Sum	$C^{16}O^{16}O$: $C^{16}O^{18}O$	$C^{16}O^{16}O$: $C^{18}O^{18}O$	$C^{16}O^{18}O$: $C^{18}O^{18}O$
	$C^{16}O^{16}O$	$C^{16}O^{18}O$	$C^{18}O^{18}O$				
3 (a*)	3958.0	1194.8	143.9	5296.7	3.31	27.51	8.30
4 (b*)	453.5	230.05	20.2	703.8	1.97	22.43	11.38
5 (c*)	3478.1	719.6	40.3	4238.0	4.83	86.27	17.85
6 (d*)	413.5	233.0	18.8	665.2	1.77	22.04	12.42
7 (e*)	3527.6	839.0	52.7	4419.3	4.20	66.89	15.91
Oxidation with $^{32}O_2$ and ^{28}CO (fig. 3.5-21)							
Switch	Amount /nmole			Sum	$C^{16}O^{16}O$: $C^{16}O^{18}O$	$C^{16}O^{16}O$: $C^{18}O^{18}O$	$C^{16}O^{18}O$: $C^{18}O^{18}O$
	$C^{16}O^{16}O$	$C^{16}O^{18}O$	$C^{18}O^{18}O$				
5 (a**)	3734.9	453.0	16.1	4204.1	8.24	232.20	28.17
6 (b**)	814.1	216.9	4.2	1035.2	3.75	192.12	51.18
7 (c**)	3754.5	656.8	42.4	4453.7	5.72	88.60	15.50
8 (d**)	770.6	215.3	6.8	992.6	3.58	114.16	31.89
9 (e**)	3649.3	719.3	51.0	4419.6	5.07	71.51	14.09
10(f**)	727.0	221.0	16.6	964.6	3.29	43.79	13.31

* corresponding plot in fig. 3.5-20

** corresponding plot in fig. 3.5-21

If the eluted CO_2 amounts of the two experiments are studied starting from switch 5, the following observations can be made. During the $O_2/N_2 \rightarrow CO/N_2$ combinations (switches 5, 7 and 9), the amount of $C^{16}O^{16}O$ is about stable in both experiments, while the amounts of $C^{16}O^{18}O$ and $C^{18}O^{18}O$ are increasing during the experiments. The total amounts are about stable during the experiments. During the $CO/N_2 \rightarrow O_2/N_2$ combinations (switches 4, 6, 8, and 10) the sum of eluted CO_2 decreases switch by switch in both experiments. In the '$^{36}O_2$-experiment' this is caused by a decrease of $C^{16}O^{16}O$, while the amounts of the other isotopomers are about stable. In the '$^{32}O_2$-experiment', $C^{16}O^{16}O$ and $C^{16}O^{18}O$ have the same tendencies as in the '$^{36}O_2$-experiment', but $C^{18}O^{18}O$ behaves significantly different. Its eluted amount increases in the course of the experiment and approaches the values determined in the '$^{36}O_2$-experiment'. Its increase is overcompensated by the decrease of $C^{16}O^{16}O$. Except for switch 3 in the '$^{36}O_2$-experiment', whose exceptional behavior was discussed above, the

fraction of $C^{16}O^{16}O$ in the eluted CO_2 decreases in the course of both experiments, which shows the increasing enrichment of the support with active ^{18}O. This enrichment of ^{18}O in the surface is in contrast to the oxidation experiment, where an apparent quasi steady-state was achieved (see fig. 3.5-14). An increase of active ^{18}O was only observed at the beginning of the reaction. Hence, during the switches the samples must be in a state comparable to that in the beginning of the oxidation reaction in fig. 3.5-14. Furthermore, although the amount of active ^{18}O is enhanced during the CO oxidation performed prior to the switches, its level can not be retained in the course of the switches.

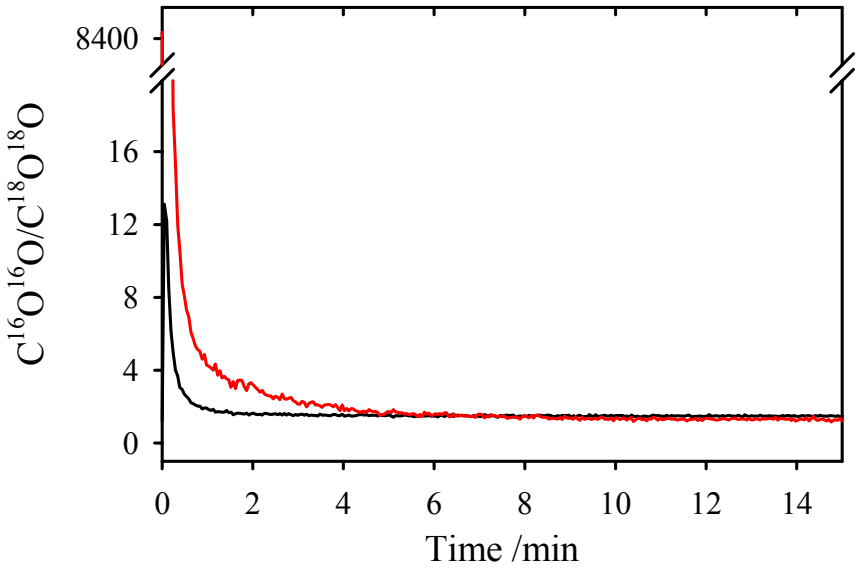

Figure 3.5-22: Comparison of the $C^{16}O^{16}O$:$C^{18}O^{18}O$ ratio during oxidation of $C^{16}O$ with $^{36}O_2$ at 80°C on a freshly conditioned sample (black line) and a sample that had catalyzed CO oxidation with $^{32}O_2$ prior the studied reaction (red line). The ratios were calculated from the data in fig. 3.5-14.

The unexpected high amount of $C^{16}O^{16}O$ is a further support of the assumption, that ^{18}O is placed on the samples only by the oxygen isotope exchange reaction of CO_2, and not by dissociative adsorption of O_2. For this argumentation the ^{18}O enrichment during the switches is compared with that during CO oxidation reactions in fig. 3.5.14. The $C^{16}O^{16}O$:$C^{18}O^{18}O$ ratios during the switch experiments are given in table 3.5-4 and those during the oxidation reaction are plotted in fig. 3.5-22. The $C^{16}O^{16}O$:$C^{18}O^{18}O$ level in the '$^{36}O_2$-experiment' is much higher than the highest point in the oxidation curve (on the freshly conditioned catalyst). If the $C^{16}O^{16}O$:$C^{18}O^{18}O$ ratios during the '$^{32}O_2$-experiment' are compared with that of the oxidation experiment, which included CO oxidation with $^{32}O_2$ prior to the oxidation with $^{36}O_2$, the level is of course higher at the beginning of the latter, since there was residual $C^{16}O^{16}O$ from the oxidation with $^{32}O_2$. The $C^{16}O^{16}O$:$C^{18}O^{18}O$ ratios during the switch

experiment are achieved after only ~6 s in the oxidation experiment. Since during the O_2/N_2 switches the partial pressure of $^{36}O_2$ is even higher than during the oxidation reactions, this should lead to higher ^{18}O fractions during the switches, if $C^{18}O^XO$ was produced by dissociative adsorption of $^{36}O_2$. In contrast to the O_2 partial pressures, the produced amount of CO_2 is much higher during the CO oxidation than during the switches, which goes along with the lower level of ^{18}O in the latter case.

Above, it was shown that CO_2 production occurs, if CO/N_2 and O_2/N_2 switches follow each other. To deduce whether at the end of these switches the maximum amount of carbonates and carboxylates are decomposed or if there are residual amounts, which are able to react, the experiments including a CO/N_2-N_2-CO/N_2 and a O_2/N_2-N_2-O_2/N_2 sequence (fig. 3.5-19), respectively, were performed (fig. 3.5-23). No more CO_2 is produced in both cases, hence the decomposition of the carbonates and carboxylates is completed during the switches and the residual carbonates and carboxylates (see figs. 3.5-8 and 3.5-9) can not be activated by flushing the sample with N_2. In contrast during the DRIFTS measurements residual carboxylate and carbonate species could be detected at the end of the switches, which supports the assumption, that under the used conditions (80°C, 40 Nml/min N_2) these can not be decomposed completely. We speculate, that the residual carboxylate and carbonate species can not be decomposed, since they are outside the capture zone of the goldparticles [132,137] or due to the loss of OH-groups and H_2O_{ad} (see section 3.5.1.2).

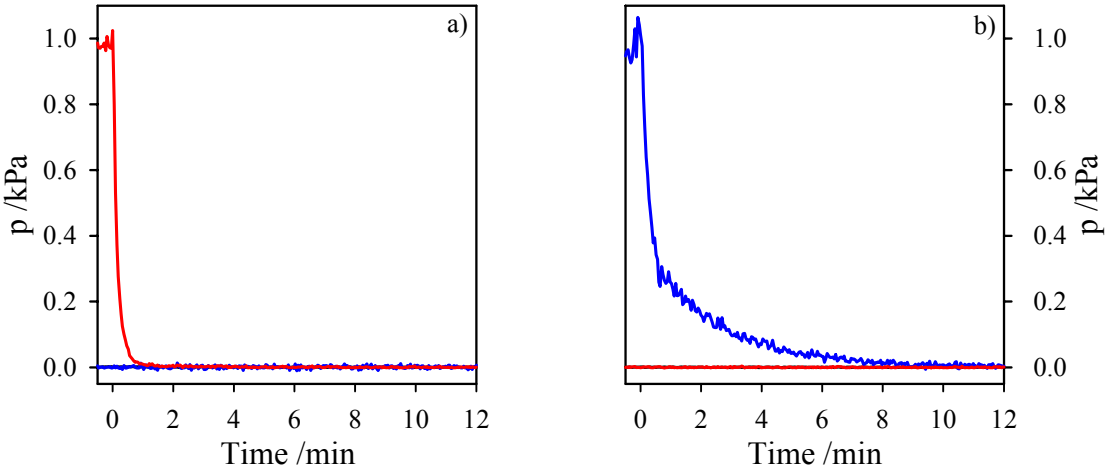

Figure 3.5-23: Evolution of CO, O_2 and CO_2 partial pressures during a) switch 5 of fig. 3.5-19a and b) switch 6 of fig. 3.5-19b. Legend for both plots: — CO_2, — CO, — O_2. Time was set to zero at the start of the switch.

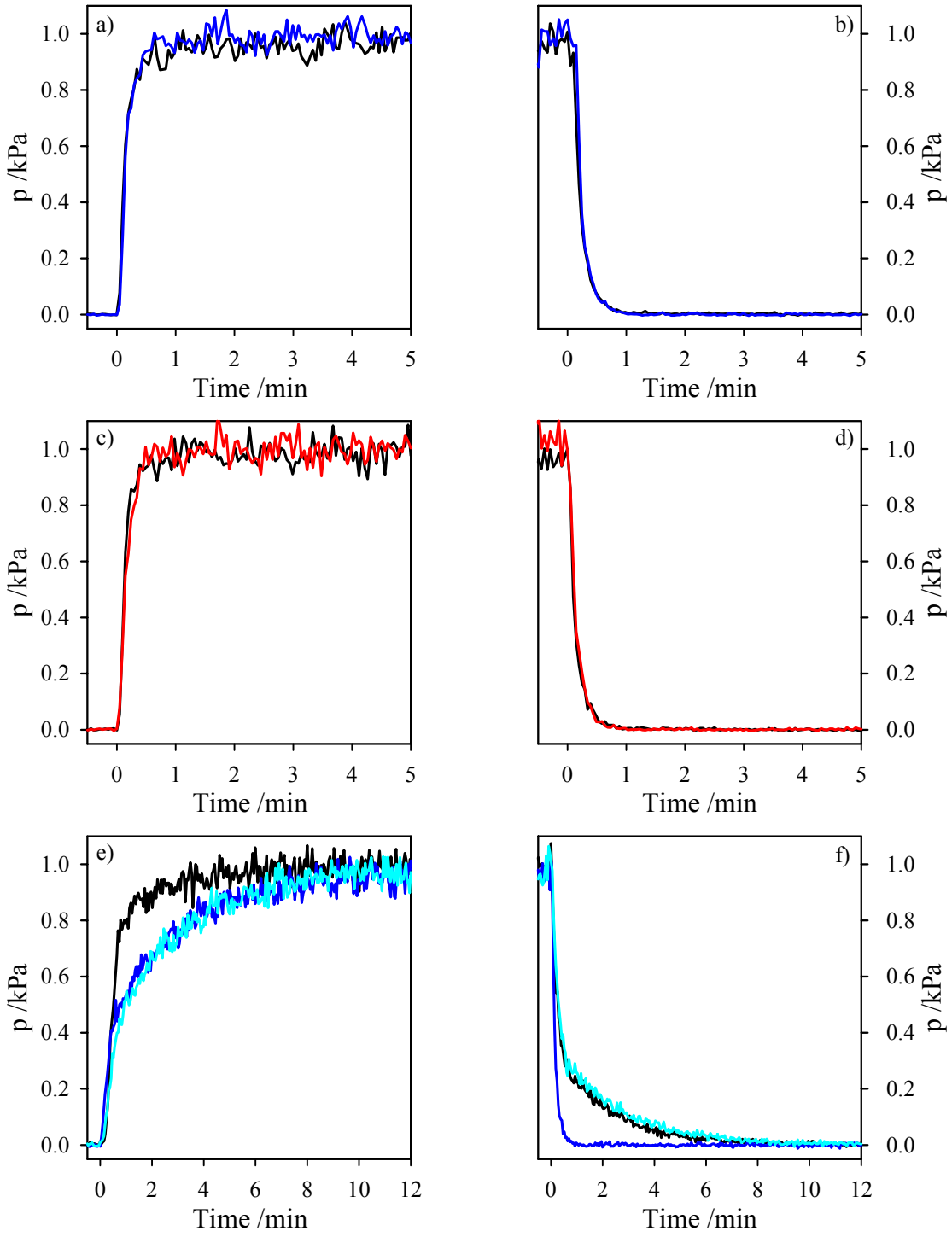

Figure 3.5-24: Comparison of increase and decrease profiles of $^{36}O_2$, ^{28}CO and $^{32}O_2$ during flow through an empty reactor (black lines) and through a reactor packed with 100 mg catalyst (colored lines) during the switches of fig. 3.5-1. a) Increase of $^{36}O_2$ (switch 6), b) decrease of $^{36}O_2$ (switch 9), c) increase of $C^{16}O$ (switch 5) and d) decrease of $C^{16}O$ (switch 6). e) and f) increase and decrease of $^{32}O_2$ respectively. In both plots the dark blue lines were recorded in connection with CO/N_2 switches and the light blue lines in connection with N_2 switches. The time was set to zero when the switches were started.

To deduce, how CO and O_2 are involved in the production of CO_2, the profiles of $^{36}O_2$, $^{32}O_2$ and CO during the switches are studied (fig. 3.5-24). The profiles recorded upon passing through an empty reactor, i.e., without the 'resistance' of the catalyst bed, are plotted with black lines and the profiles after passing a packed reactor, i.e., including the 'resistance' of the catalyst bed, in colored lines. Since the profile of $^{32}O_2$ is significantly influenced by the catalyst bed, also the switch combinations with N_2 and CO/N_2 are added (fig. 3.5-24e-f). The profiles of CO and $^{36}O_2$ are not significantly different after passing through an empty reactor and through a packed reactor (fig. 3.5-24a-d). For $^{32}O_2$ also no significant changes occur between the increase profiles of the switch combinations with N_2 and CO/N_2 (light and dark blue in fig. 3.5-24e, respectivley) and the decrease profiles with N_2 after passing through an empty and through a pakced reactor (black and light blue lines in fig. 3.5-24f, respectively). The faster decrease profile of the switch combination with CO/N_2 (dark blue line in fig. 3.5-24f) is caused by the consumption of the residual $^{32}O_2$ for the oxidation of the CO. Since for 36O2 and CO the profiles do not differ after passing a through an empty reactor and through a packed reactor, the adsorption of CO and O_2 is a continuous process during the switches and can not be detected with the IMR-MS. This continuous adsorption is confirmed by the continuous increase of the CO_{ad} and H_2O_{ad} peaks (the latter correlates with $O_{2,ad}$, as has been shown in section 3.5.1) during the observation of CO/N_2 and O_2/N_2 switches with DRIFTS respectively.

3.5.3 Summary

The study of the CO oxidation with DRIFTS unraveled the existence of an equilibrium between OH-groups and H_2O_{ad} present on the TiO_2 surface. It is shifted to the side of H_2O_{ad} in the presence of O_2 in the gas mixture. This shift was observed independent from the other components present in the gas mixture, i.e., the presence of a CO/N_2 mixture and in the presence of N_2 only. Furthermore, a direct correlation of the peak intensity of H_2O_{ad} and the activity for the CO oxidation reaction could be shown, which points to a participation of H_2O in the reaction mechanism and explains the higher stability of the Degussa Au/TiO_2 catalysts during the CO oxidation in H_2-rich atmosphere than in H_2-free atmosphere (see chapter 3.2).

Beside the equilibrium between OH-groups and H_2O_{ad}, an equilibrium between carboxylate, monodentate and bidentate carbonate was concluded from the study of these surface species with DRIFTS, in particular from their relative increase and decrease behavior during the

O_2/N_2 and CO/N_2 switches. The strongest relative increase for carboxylate, followed by monodentate carbonate and then by bidentate carbonate and an opposite order in the relative decomposition indicate, that carboxylate is the first species that is built-up in the reaction mechanism, and that it is afterwards transformed into monodentate carbonate and finally into bidentate carbonate. The latter is thermally instable and decomposes to CO_2. It was assumed that the transformation of monodentate carbonate to bidentate carbonate happens with the involvement of water. The data suggest that the carboxylate-carbonate mechanism is the primary reaction path under the present reaction conditions.

Beside their role as reaction intermediates, the carboxylate and carbonate species are also a source of deactivation during CO oxidation (their peak intensities increased, while the activity of the catalyst decreased). The strongest relative increase was observed for carboxylate. It was identified as main source of deactivation, followed by the monodentate carbonate, while the bidentate carbonate nearly achieved steady state. The influence of O_2 and CO on the three species is different. At the beginning of the O_2/N_2 switches additional carbonates, monodentate and bidentate carbonates are produced and subsequently decomposed, while during the CO/N_2 switches this decomposition was even enhanced. The amount of eluted CO_2 was higher during the CO/N_2 switches than during the O_2/N_2 switches. During a O_2/N_2-N_2-O_2/N_2 sequence CO_2 could be detected neither during the N_2 switch nor in the second O_2/N_2 switch. A similar result was also obtained for a CO/N_2-N_2-CO/N_2 sequence. With DRIFTS in both cases (O_2/N_2 as well as CO/N_2 switches) residual carboxylates, monodentate and bidentate carbonates could be detected at the end of the first switch. Additionally, the amount of H_2O_{ad} decreased continuously with each switch. This loss was not compensated by a recovery of the OH-groups. Hence, we assume that under the present conditions carboxylate and carbonate species can not be decomposed completely due to the loss of H_2O_{ad} and OH-groups. The loss of water and OH-groups can be considered as aging. But taking the definition of a catalyst, which requires a similar state before and after a reaction turnover [2], it is concluded that the Au/TiO_2 system is not a catalyst, if the loss of water is not compensated, as it is done for example, if water moisture if added to the reaction gas or the reaction is performed in H_2-rich atmosphere. This is supported by the stability of the Degussa catalyst in H_2-rich atmosphere (section 3.2).

From the distribution of the CO_2 isotopomers during the CO oxidation reaction no conclusions can be drawn on the reaction mechanism and the exact amount of oxygen isotope exchange reactions of CO_2. ^{18}O active for the oxygen isotope exchange reaction is deposited on the sample by ^{18}O-containing CO_2 molecules and not by dissociative adsorption of O_2. The adsorption of CO and O_2 during the switches is a continuous process and does not occur only at the beginning of the switches.

4 Summary

In the previous chapters I presented results on the CO oxidation on highly disperse Au/TiO_2 catalysts in H_2-free and H_2-rich atmosphere. The catalysts were prepared via a modified deposition precipitation with either pure anatase or a mixture of rutile and anatase as support. The catalysts with the rutile/anatase support showed a better reproducibility with respect to the activity. The activity of all Au/TiO_2 samples was comparable to 'good' catalysts reported in literature. Calcination at 400°C led to particle sizes of ~3 nm and a complete reduction of gold to Au^0, while reduction at 200°C and redox-conditioning at 200°C and 300°C resulted in particles sizes of ~2 nm and in the presence of Au^{3+} species beside the main component Au^0.

The relative deactivation was similar in both atmospheres for the anatase supported catalysts, while the rutile/anatase supported catalysts deactivated much stronger in H_2-free atmosphere. For both kinds of catalysts mainly water was observed as side product during CO oxidation in H_2-rich atmosphere, while in H_2-free atmosphere carboxylates/formates, monodentate and bidentate carbonates were identified as side products. Carboxylates were identified as main source of deactivation, followed by monodentate carbonates. The build-up of carboxylates from adsorbed CO and OH-groups, its transformation to monodentate carbonate and afterwards to the thermally instable bidentate carbonate was found to be a reaction path and first preliminary results indicate, that this is the primary reaction mechanism. An equilibrium of OH groups and adsorbed water, which is shifted to the side of water in the presence of oxygen, was identified and it could be shown, that the amount of adsorbed water correlates with the activity of the catalyst. Since a loss of water and therefore OH-groups from the catalytic system was detected in H_2-free atmosphere, the stronger deactivation under these conditions can be explained by the lack of water, which is essential for the decomposition of the intermediates carboxylate and/or monodentate carbonate.

CO adsorption was observed exclusively on the gold particles in both atmospheres. In H_2-rich atmosphere the development of a new species, denoted as H-Au-CO coadsorption complex, was observed. The CO reaction order was also influenced by the presence of H_2 – it was significantly higher than in H_2-free atmosphere. The reaction order of oxygen on the other side was not influenced by hydrogen, but in the pressure gap it decreased with decreasing total pressure. The CO reaction order, in contrast, increased with decreasing total pressure. A significant influence of the material differences on reaction rates and reaction kinetic was not

found. An estimation of the reaction probability in the 10^{-6}-10^{-7} mbar range showed, that the amounts of produced CO_2 are beneath the detection limit.

Experiments with isotope labeled gases revealed that (i) oxygen does not dissociate on the catalyst surface and (ii) CO neither makes isotope exchange with the TiO_2 support, nor reacts with the support oxygen, which excludes a Mars-van Krevelen mechanism under the present conditions. CO_2 on the other hand undergoes oxygen isotope exchange with the support. From the distribution of the CO_2 isotopomers during oxidation of $C^{16}O$ with $^{36}O_2$ no conclusions can be drawn on the reaction mechanism, since the distribution found here is valid for several models.

5 References

[1] G.A.Somorjai, 'Introduction to Surface Science and Catalysis', John Wiley and Sons, New York (1994)

[2] J.M.Thomas and W.J.Thomas, 'Principles and Practice of Heterogeneous Catalysis', VCH, Weinheim (1997)

[3] J.R.McNeil, 'Blue Planet', Campus Verlag, Frankfurt/New York (2000)

[4] M.Haruta, *Catal.Surv.Jap.* **1,** 61 (1997).

[5] G.C.Bond and D.T.Thompson, *Gold Bull.* **33,** 41 (2000).

[6] G.C.Bond, *Catal.Rev.Sci.Eng.* **41,** 319 (1999).

[7] M.Haruta, *CATECH* **6,** 102 (2002).

[8] M.M.Schubert, S.Hackenberg, A.C.van Veen, M.Muhler, V.Plzak, and R.J.Behm, *J.Catal.* **197,** 113 (2001).

[9] F.Boccuzzi and A.Chiorino, *J.Phys.Chem.B* **104,** 5414 (2000).

[10] G.R.Bamwenda, S.Tsubota, T.Nakamura, and M.Haruta, *Catal.Lett.* **44,** 83 (1997).

[11] M.Haruta, S.Tsubota, T.Kobayashi, H.Kageyama, M.J.Genet, and B.Delmon, *J.Catal.* **144,** 175 (1993).

[12] Y.Iizuka, H.Fujiki, N.Yamauchi, T.Chijiiwa, S.Arai, S.Tsubota, and M.Haruta, *Catal.Today* **36,** 115 (1997).

[13] A.I.Kozlov, A.P.Kozlova, H.Liu, and Y.Iwasawa, *Appl.Catal.A* **182,** 9 (1999).

[14] J.-D.Grunwaldt and A.Baiker, *J.Phys.Chem.B* **103,** 1002 (1999).

[15] F.Boccuzzi, A.Chiorini, M.Manzoli, P.Lu, T.Akita, S.Ichikawa, and M.Haruta, *J.Catal.* **202,** 256 (2001).

[16] M.J.Kahlich, H.A.Gasteiger, and R.J.Behm, *J.Catal.* **182,** 430 (1999).

[17] M.J.Kahlich, ‚CO-Feinreinigung H_2-reicher Reformergase durch selektive Oxidation an geträgerten Edelmetallkatalysatoren: Kinetische Untersuchungen und Reaktoredesign-Berechnungen', Dissertation, Universität Ulm (2000).

[18] M.M.Schubert, 'Mechanistic Insights into the Preferential CO Oxidation in H_2-rich Gas (PROX) over Supported Noble Metal Catalysts', Dissertation, Universität Ulm, (2000).

[19] Y.-F.Han, M.J.Kahlich, M.Kinne, and R.J.Behm, *Appl.Catal.B* **50,** 209 (2004).

[20] M.J.Kahlich, H.A.Gasteiger, and R.J.Behm, *J.Catal.* **171,** 93 (1997).

[21] A.Wootsch, C.Descorme, and D.Duprez, *J.Catal.* **225,** 259 (2004).

[22] C.Özdemir, A.N.Akin, and R.Yildrim, *Appl.Catal., A* **258,** 145 (2004).

[23] J.Yan, J.Ma, P.Cao, and P.Li, *Catal.Lett.* **93,** 55 (2004).

[24] F.Garcia, W.Li, and E.E.Wolf, *Catal.Lett.* **91,** 235 (2003).

[25] K.-I.Tanaka, Y.Moro-Oka, K.Ishigure, T.Yajima, Y.Okabe, Y.Kato, H.Hamano, S.i.Sekiya, H.Tanaka, Y.Matsumoto, H.Koinuma, H.He, C.Zhang, and Q.Feng, *Catal.Lett.* **92,** 115 (2004).

[26] M.M.Schubert, M.J.Kahlich, G.Feldmeyer, M.Hüttner, S.Hackenberg, H.A.Gasteiger, and R.J.Behm, *Phys.Chem.Chem.Phys.* **3,** 1123 (2001).

[27] S.-I.Ito, H.Tanaka, Y.Minemura, S.Kameoka, K.Tomishige, and K.Kunimori, *Appl.Catal.A* **273,** 302 (2004).

[28] M.Echigo and T.Tabata, *Appl.Catal.A* **251,** 157 (2003).

[29] Y.-F.Han, M.Kinne, and R.J.Behm, *Appl.Catal.B* **52,** 123 (2004).

[30] G.Avgouropoulos, T.Ioannides, Ch.Papadopoulou, J.Batista, S.Hocevar, and H.K.Matralis, *Catal.Today* **75,** 157 (2002).

[31] T.V.Choudhary, C.Sivadinarayana, C.C.Chusuei, A.K.Darye, J.P.Fackler, and D.W.Goodman, *J.Catal.* **207,** 247 (2002).

[32] M.M.Schubert, A.Venugopal, M.J.Kahlich, V.Plzak, and R.J.Behm, *J.Catal.* **222,** 32 (2004).

[33] M.M.Schubert, V.Plzak, J.Garche, and R.J.Behm, *Catal.Lett.* **76,** 143 (2001).

[34] J.-D.Grunwaldt, C.Kiener, C.Wögerbauer, and A.Baiker, *J.Catal.* **181,** 223 (1999).

[35] M.Valden, S.Pak, X.Lai, and D.W.Goodman, *Catal.Lett.* **56,** 7 (1998).

[36] M.Valden, D.Lai, and D.W.Goodman, *Science* **281,** 1647 (1998).

[37] M.Okumura, S.Nakamura, S.Tsubota, T.Nakamura, M.Azuma, and M.Haruta, *Catal.Lett.* **51,** 53 (1998).

[38] S.Tsubota, T.Nakamura, K.Tanaka, and M.Haruta, *Catal.Lett.* **56,** 131 (1998).

[39] M.A.Bollinger and M.A.Vannice, *Appl.Catal.B* **8,** 417 (1996).

[40] S.D.Lin, M.A.Bollinger, and M.A.Vannice, *Catal.Lett.* **17,** 245 (1993).

[41] A.Sanchez, S.Abbet, U.Heiz, W.-D.Schneider, H.Häkkinen, R.N.Barnett, and U.Landman, *J.Phys.Chem.A* **103,** 9573 (1999).

[42] F.Boccuzzi, G.Cerrato, F.Pinna, and G.Strukul, *J.Phys.Chem.B* **102,** 5733 (1998).

[43] M.Ruff, S.Frey, B.Gleich, and R.J.Behm, *Appl.Phys.A* **66,** S513 (1998).

[44] M.Mavrikakis, P.Stoltze, and J.K.Nørskov, *Catal.Lett.* **64,** 101 (200).

[45] S.Giorgio, C.R.Henry, B.Pauwels, and G.Van Tendeloo, *Mater.Sci.Eng., A* **A297,** 197 (2000).

[46] R.Meyer, C.Lemire, S.K.Shaikhutdinov, and H.-J.Freund, *Gold Bull.* **37,** 72 (2004).

[47] M.S.Chen and D.W.Goodman, *Science* **306,** 252 (2004).

[48] J.M.Gottfried, K.J.Schmidt, S.L.M.Schröder, and K.Christmann, *Surf.Sci.* **511,** 65 (2002).

[49] J.M.Gottfried and K.Christmann, *Surf.Sci* **566-568,** 1112 (2003).

[50] J.M.Gottfried, K.J.Schmidt, S.L.M.Schroeder, and K.Christmann, *Surf.Sci.* **536,** 206 (2003).

[51] J.M.Gottfried, K.J.Schmidt, S.L.M.Schroeder, and K.Christmann, *Surf.Sci.* **525,** 184 (2003).

[52] J.M.Gottfried, K.J.Schmidt, S.L.M.Schroeder, and K.Christmann, *Surf.Sci.* **525,** 197 (2003).

[53] J.D.Stiehl, T.S.Kim, S.M.McClure, and C.B.Mullins, *J.Am.Chem.Soc.* **126,** 1606 (2004).

[54] J.D.Stiehl, T.S.Kim, S.M.McClure, and C.B.Mullins, *J.Am.Chem.Soc.* **126,** 13574 (2004).

[55] J.D.Stiehl, T.S.Kim, S.M.McClure, and C.B.Mullins, *J.Phys.Chem.B* **109,** 6316 (2005).

[56] X.Lai, T.P.St.Clair, M.Valden, and D.W.Goodmann, *Prog.Surf.Sci.* **59,** 25 (1998).

[57] T.S.Kim, J.D.Stiehl, C.T.Reeves, R.J.Meyer, and C.B.Mullins, *J.Am.Chem.Soc.* **125,** 2018 (2003).

[58] J.D.Stiehl, T.S.Kim, C.T.Reeves, R.J.Meyer, and C.B.Mullins, *J.Phys.Chem.B* **108,** 7917 (2004).

[59] M.Manzoli, A.Chiorino, and F.Boccuzzi, *Surf.Sci.* **532-535,** 377 (2003).

[60] F.Boccuzzi, A.Chiorino, and M.Manzoli, *Surf.Sci.* **502-503,** 513 (2002).

[61] F.Boccuzzi, A.Chiorino, S.Tsubota, and M.Haruta, *J.Phys.Chem.* **100,** 3625 (1996).

[62] M.Maciejewski, P.Fabrizioli, J.-D.Grunwaldt, O.S.Becker, and A.Baiker, *Phys.Chem.Chem.Phys.* **3,** 3846 (2001).

[63] H.Liu, A.I.Kozlov, A.P.Kozlova, T.Shido, K.Asakura, and Y.Iwasawa, *J.Catal.* **185,** 252 (1999).

[64] M.Okumura, J.M.Coronado, J.Soria, M.Haruta, and J.Conesa, *J.Catal.* **203,** 168 (2001).

[65] Y.Iizuka, T.Tode, T.Takao, K.Yatsu, T.Takeuchi, S.Tsubota, and M.Haruta, *J.Catal.* **187,** 50 (1999).

[66] E.Wahlström, N.Lopez, R.Schaub, P.Thostrup, A.Ronnau, C.Africh, E.Laegsgaard, J.K.Nørskov, and F.Besenbacher, *Phys.Rev.Lett.* **90,** 261011 (2003).

[67] N.Lopez, J.K.Nørskov, T.V.W.Janssens, A.Carlsson, A.Puig-Molina, B.S.Clausen, and J.-D.Grunwaldt, *J.Catal.* **225,** 86 (2004).

[68] U.Diebold, *Surf.Sci.Rept.* **48,** 53 (2003).

[69] Y.Xu and M.Mavrikakis, *J.Phys.Chem.B* **107,** 9298 (2003).

[70] N.W.Cant and N.J.Ossipoff, *Catal.Today* **36,** 125 (1997).

[71] M.Haruta, *Gold Bull.* **37,** 27 (2004).

[72] D.W.Blakely, E.I.Kozak, B.A.Sexton, and G.A.Somorjai, *J.Vac.Sci.Technol.* **13,** 1091 (1976).

[73] J.T.Yates, 'Experimental Innovations in Surface Science - A Guide to Practical Laboratory Methods and Instruments', Springer-Verlag, New York (1998)

[74] W.Reichl, G.Rosina, G.Rupprechter, C.Zimmermann, and K.Hayek, *Rev.Sci.Instrum.* **71,** 1495 (2000).

[75] D.W.Goodman, *J.Vac.Sci.Technol.* **20,** 522 (1982).

[76] C.T.Campbell and M.T.Paffett, *Surf.Sci.* **139,** 396 (1984).

[77] G.Rupprechter, T.Dellwig, H.Unterhalt, and H.-J.Freund, *Topics in Catalysis* **15,** 19 (2001).

[78] J.T.Gleaves, J.R.Ebner, and T.C.Kuechler, *Catal.Rev.Sci.Eng.* **30,** 49 (1988).

[79] J.T.Gleaves, G.S.Yablonskii, P.Phanawadee, and Y.Schuurman, *Appl.Catal.A* **160,** 55 (1997).

[80] R.Leppelt, B.Schumacher, T.Häring, M.Kinne, and R.J.Behm, *Rev.Sci.Instrum.* **76,** 024102-1 (2005).

[81] V.A.Bondzie, S.C.Parker, and C.T.Campbell, *Catal.Lett.* **63,** 143 (1999).

[82] S.Kielbassa, 'Investigation of Au/TiO_2 model catalysts - Advanced catalyst preparation routine and the task to measure very low absolute CO conversion', Seminar Abt. Oberflächenchemie und Katalyse, Universität Ulm (2005).

[83] Z.Zhao and T.Diemant, 'CO Oxidation on Au/TiO_2 model catalysts - Sample preparation, high pressure cell, kinetic and PM-IRAS measurements', Seminar Abt. Oberflächenchemie und Katalyse, Universität Ulm (2005).

[84] M.Daté, Y.Ichihashi, A.Chiorino, F.Boccuzzi, and M.Haruta, *Catal.Today* **72,** 89 (2002).

[85] M.Daté and M.Haruta, *J.Catal.* **201,** 221 (2001).

[86] E.D.Park and J.S.Lee, *J.Catal.* **186,** 1 (1999).

[87] J.Bergeld, B.Kasemo, and D.V.Chakarov, *Surf.Sci.* **495,** L815 (2001).

[88] H.H.Kung, M.C.Kung, and C.K.Costello, *J.Catal.* **216,** 425 (2003).

[89] M.Daté, M.Okumura, S.Tsubota, and M.Haruta, *Angew.Chem.* **116,** 2181 (2004).

[90] A.B.Mhadeshwar and D.G.Vlachos, *J.Phy.Chem.B* **108,** 15246 (2004).

[91] X.-Q.Gong and P.Hu, *J.Chem.Phys.* **119,** 6324 (2003).

[92] A.Wolf and F.Schüth, *Appl.Catal.* **226,** 1 (2002).

[93] O.Levenspiel, 'Chemical Reaction Engineering', Wiley & Sons, New York (1972)

[94] M.Boudart, *Chem.Rev.* **95,** 666 (1995).

[95] H.Sakurai, A.Ueda, T.Kobayashi, and M.Haruta, *Chem.Commun.*271 (1998).

[96] P.B.Weisz, *Chem.Engin.Progr.Symp.Ser.* **55,** 29 (1992).

[97] M.Kahlich, ‚Untersuchungen zur selektiven CO-Oxidation an geträgerten Edelmetallkatalysatoren in einem Gasphasenreaktorsystem mit on-line Analytik', Diplomarbeit, Universität Ulm (1996).

[98] K.Giles, N.G.Adams, and D.Smith, *J.Phys.B: At.Mol.Opt.Phys.* **22,** 873 (1989).

[99] S.Hackenberg, ‚Untersuchungen zum Einfluß von Kalium und Cadmium auf die Formierung und katalytische Aktivität SiO_2 geträgerter Palladiumkatalysatoren bei der Totaloxidation von Ethylen', Dissertation, Universität Ulm (2002).

[100] I.M.Hamadeh and P.R.Griffiths, *Appl.Spec.* **41,** 682 (1987).

[101] F.Kießlich, P.M.Prechtl, H.Gerhard, M.A.Liauw, H.Popovska, and G.Emig, *CIT* **75,** 349 (2003).

[102] R.F.Berg, *Rev.Sci.Instrum.* **75,** 772 (2004).

[103] J.W.Niemantsverdriet, 'Spectroscopy in Catalysis - An Introduction -', VCH, Weinheim (1993)

[104] D.A.Shirley, *Phys.Rev.B* **5,** 4709 (1972).

[105] D.Briggs and M.P.Seah, 'Practical Surface Analysis - Auger and X-Ray Photoelectron Spectroscopy', 2nd Ed., John Wiley & Sons, Chichester (1990)

[106] S.Hackenberg, ‚Einflußgrößen in der Anwendung der Ionen-Molekül Reaktions Massenspektrometrie (IMR-MS) zur Untersuchung der Reaktionskinetik am Modellsystem der Ethylenoxidation', Diplomarbeit, Universität Ulm (1996).

[107] H.S.Oh, J.H.Yang, C.K.Costello, Y.M.Wang, S.R.Bare, H.H.Kung, and M.C.Kung, *J.Catal.* **210,** 375 (2002).

[108] T.Ohno, K.Sarukawa, K.Tokieda, and M.Matsumura, *J.Catal.* **203,** 82 (2001).

[109] The measurements were performed and evaluated by Dr.V.Plzak at the Center for Solar Energy and Hydrogen Research (ZWS) and kindly provided by him for presentation in this work (2004).

[110] F.Boccuzzi, A.Chiorino, and M.Manzoli, *Surf.Sci.* **454-456,** 942 (2000).

[111] R.Zanella, S.Giorgio, C.-H.Shin, C.R.Henry, and C.Louis, *J.Catal.* **222,** 357 (2004).

[112] N.J.Ossipoff and N.W.Cant, *Topics in Catalysis* **8,** 161 (1999).

[113] S.Kielbassa, M.Kinne, and R.J.Behm, *J.Phys.Chem.B* **108,** 19184 (2004).

[114] S.Schimpf, M.Lucas, C.Mohr, U.Rodemerck, A.Brueckner, J.Radnik, H.Hofmeister, and P.Claus, *Catal.Today* **72,** 63 (2002).

[115] J.F.Moulder, W.F.Stickle, P.E.Sobol, and K.D.Bomben, 'Handbook of X-ray Photoelectron Spectroscopy', Perkin Elmer Corp., Eden Prairie/USA (1992)

[116] D.Gonbeau, C.Guimon, G.Pfister-Guillouzo, A.Levasseur, G.Meunier, and R.Dormoy, *Surf.Sci.* **254,** 81 (1991).

[117] A.M.Linsebigler, G.Lu, and J.T.Yates Jr, *Chem.Rev.* **95,** 735 (1995).

[118] M.A.Fox and M.T.Dulay, *Chem.Rev.* **93,** 341 (1993).

[119] M.A.Hoffmann, S.T.Martin, W.Choi, and D.W.Bahnemann, *Chem.Rev.* **95,** 431 (1995).

[120] C.R.Aita and N.C.Tran, *Sci.Technol.* **A9,** 1498 (1991).

[121] H.-G.Boyen, G.Kästle, F.Weigl, B.Koslowski, C.Dietrich, P.Ziemann, J.P.Spatz, S.Riethmüller, C.Hartmann, M.Möller, G.Schmid, M.G.Garnier, and P.Oelhafen, *Science* **297,** 1533 (2002).

[122] J.M.C.Soares, P.Morrall, A.Crossley, P.Harris, and M.Bowker, *J.Catal.* **219,** 17 (2003).

[123] R.Holm and S.Storp, *Appl.Phys.* **9,** 217 (2003).

[124] T.Dickinson, A.F.Povey, and P.M.A.Sherwood, *J.Chem.Soc.Faraday Trans.* **71,** 298 (1974).

[125] J.-C.Dupin, D.Gonbeau, P.Vinatier, and A.Levasseur, *Phys.Chem.Chem.Phys.* **2,** 1319 (2000).

[126] G.Martra, *Appl.Catal.A* **200,** 275 (2000).

[127] A.B.Christie, J.Lee, I.Sutherland, and J.M.Walls, *Appl.Surf.Sci.* **15,** 237 (1983).

[128] W.J.Landis and J.R.Martin, *J.Vac.Sci.Technol.A* **2,** 1108 (1984).

[129] H.Tsai, E.Hu, K.Perng, M.Chen, J.-C.Wu, and Y.-S.Chang, *Surf.Sci.* **537,** L447 (2003).

[130] J.-J.Pireaux, M.Liehr, P.A.Thiry, J.P.Delrue, and R.Caudano, *Surf.Sci.* **141,** 221 (1984).

[131] S.Srinivas, A.Dhingra, H.Im, and E.Gulari, *Appl.Catal.A* **274,** 285 (2004).

[132] R.J.Behm, D.Rosenthal, K.Christmann, E.A.Willneff, N.Weiher, S.L.M.Schröder, S.Kielbassa, B.Schumacher, and Z.Zhao, 'Low-temperature CO Oxidation on metal oxide supported Gold Catalysts', EUROCAT IV, Insbruck, Berichtssymposium SPP 1091 (2003).

[133] R.J.Behm, K.Christmann, R.Schlögl, and S.L.M.Schröder, ‚Brückenschläge zwischen idealen und realen Systemen in der heterogenen Katalyse - Mechanismus der Tieftemperatur-CO-Oxidation an metalloxidgeträgerten Au-Katalysatoren', Fortsetzungsantrag SPP 1091 (2004).

[134] P.Konova, A.Naydenov, Cv.Venkov, D.Mehandjiev, D.Andreeva, and T.Tabakova, *J.Mol.Catal.A* **213,** 235 (2004).

[135] S.Arrii, F.Morfin, A.J.Renouprez, and J.-L.Rousset, *J.Am.Chem.Soc.* **126,** 1199 (2004).

[136] K.Mallick and M.S.Scurrell, *Appl.Catal., A* **253,** 527 (2003).

[137] R.J.Behm, U.Heiz, and M.M.Kappes, ‚Katalytse Funktionen metallischer Nanostrukturen und nanostrukturierter Materialien', Antrag Kompetenznetz ‚Funktionelle Nanostrukturen' - Teilprojekt C6 (2005).

[138] M.A.P.Dekkers, M.J.Lippits, and B.E.Nieuwenhuys, *Catal.Lett.* **56,** 195 (1998).

[139] A.M.Visco, F.Neri, G.Neri, A.Donato, C.Milone, and S.Galvagno, *Phys.Chem.Chem.Phys.* **1,** 2869 (1999).

[140] J.Guzman and B.C.Gates, *J.Am.Chem.Soc.* **126,** 2672 (2004).

[141] J.France and P.Hollins, *J.Electron Spectros.Rel.Phenom.* **64/65,** 251 (1993).

[142] A.Ortega, F.M.Hoffmann, and A.M.Bradshaw, *Surf.Sci.* **119,** 79 (1982).

[143] A.A.Davydov, 'Infrared spectroscopy of adsorbed species on the surface of transition metal oxides', John Wiley & Sons Ltd., Chichester, UK (1984)

[144] J.-D.Grunwaldt, M.Maciejewski, O.S.Becker, P.Fabrizioli, and A.Baiker, *J.Catal.* **186,** 458 (1999).

[145] G.Busca, J.Lamotte, J.-C.Lavalley, and V.Lorenzelli, *J.Am.Chem.Soc.* **109,** 5197 (1987).

[146] R.M.Torres Sanchez, A.Ueda, K.Tanaka, and M.Haruta, *J.Catal.* **168,** 125 (1996).

[147] R.J.H.Grisel, K.-J.Weststrate, A.Goossens, M.W.J.Craje, A.M.van der Kraan, and B.Nieuwenhuys, *Catal.Today* **72,** 123 (2002).

[148] M.M.Schubert, M.J.Kahlich, H.A.Gasteiger, and R.J.Behm, *J.Power Sources* **84,** 175 (1999).

[149] C.Ruggiero and P.Hollins, *J.Chem.Soc.Faraday Trans.* **92,** 4829 (1997).

[150] P.Hollins, *Surf.Sci.Rept.* **16,** 51 (1992).

[151] F.Boccuzzi, S.Tsubota, and M.Haruta, *J.Electr.Spectr.Rel.Phenom.* **64-65,** 241 (1993).

[152] L.-F.Liao, D.-L.Lien, D.-L.Shieh, M.-T.Chen, and J.-L.Lin, *J.Phys.Chem.B* **106,** 11240 (2002).

[153] C.-C.Chuang, W.-C.Wu, M.-C.Huang, I.-C.Huang, and J.-L.Lin, *J.Catal.* **185,** 423 (1999).

[154] M.I.Zaki, G.Kunzmann, B.C.Gates, and H.Knözinger, *J.Phys.Chem.* **91,** 1486 (1987).

[155] M.Jakob, H.Levanon, and P.V.Kamat, *Nano Lett.* **3,** 353 (2003).

[156] B.E.Koel, D.E.Peebles, and J.M.White, *Surf.Sci.* **125,** 709 (1983).

[157] B.E.Koel, D.E.Peebles, and J.M.White, *Surf.Sci.* **125,** 739 (1983).

[158] M.Olea, M.Kunitake, T.Shido, and Y.Iwasawa, *Phys.Chem.Chem.Phys.* **3,** 627 (2001).

[159] M.Olea, M.Kunitake, T.Shido, K.Asakura, and Y.Iwasawa, *Bull.Chem.Soc.Jpn.* **74,** 255 (2001).

[160] H.Liu, A.I.Kozlov, A.P.Kozlova, T.Shido, and Y.Iwasawa, *Phys.Chem.Chem.Phys.* **1,** 2851 (1999).

[161] P.Mars and D.W.van Krevelen, *Chem.Eng.Sci.* **3,** 41 (1954).

[162] S.Kielbassa, M.Kinne, and R.J.Behm, *Langmuir* **20,** 6644 (2004).

[163] Z.M.Liu and M.A.Vannice, *Catal.Lett.* **43,** 51 (1997).

[164] S.K.Shaikhutdinov, R.Meyer, M.Naschitzki, M.Bäumer, and H.-J.Freund, *Catal.Lett.* **86,** 211 (2003).

[165] O.Meerson and C.R.Henry, E-mail communication (2004).

[166] B.Yoon, H.Häkkinen, U.Landman, A.S.Wörz, M.Antonietti, S.Abbet, K.Judai, and U.Heiz, *Science* **307,** 403 (2005).

[167] D.C.Meier and D.W.Goodman, *J.Am.Chem.Soc.* **126,** 1892 (2004).

[168] S.Derrouiche, P.Gravejat, and C.L.Bianchi, *J.Am.Chem.Soc.* **126,** 13010 (2004).

[169] L.-F.Liao, W.-C.Wu, C.-Y.Chen, and J.-L.Lin, *J.Phys.Chem.B* **105,** 7685 (2001).

[170] K.S.Finnie, T.J.Cassidy, J.R.Bartlett, and J.L.Woolfrey, *Langmuir* **17,** 816 (2001).

[171] C.Morterra, *J.Chem.Soc.Faraday Trans.* **84,** 1617 (1988).

[172] C.K.Costello, M.C.Kung, H.-S.Oh, Y.Wang, and H.H.Kung, *Appl.Catal.* **232,** 159 (2002).

[173] K.S.Kim and M.A.Barteau, *Langmuir* **4,** 945 (1988).

[174] M.I.Zaki and H.Knözinger, *Mat.Chem.Phys.* **17,** 201 (2003).

[175] M.A.Henderson, *J.Phys.Chem.B* **101,** 221 (1997).

[176] Y.Fu, L.Kraus, M.I.Zaki, C.Kappenstein, B.Tesche, and H.Knözinger, *J.Mol.Catal.* **44,** 295 (1988).

[177] F.Boccuzzi and A.Chiorini, *Stud.Surf.Sci.Catal.* **140,** 77 (2001).

[178] L.M.Molina and B.Hammer, *Phys.Rev.Lett.* **90,** 206102-1 (2003).

APPENDIX

A) Deutsche Zusammenfassung (German summary)

In der vorliegenden Arbeit wurden Ergebnisse bezüglich der CO Oxidation in H_2-reicher und H_2-freier Atmosphäre an hochdispersen Au/TiO_2 Katalysatoren präsentiert. Die Katalysatoren wurden mittels modifizierter ‚deposition precipitation', sowohl mit reinem Anatas als auch mit einem Rutil/Anatas Gemisch als Träger, synthetisiert, wobei die letzteren Proben eine deutlich höhere Reproduzierbarkeit bezüglich der Aktivität aufwiesen. Alle Au/TiO_2 Katalysatoren zeigten eine Aktivität vergleichbar mit ‚guten' Katalysatoren in der Literatur. Kalzinierung bei 400°C führte zu Goldpartikelgrößen von ~3 nm und einer vollständigen Reduktion des Goldes zu Au^0, wohingegen nach Reduktion bei 200°C und Redoxkonditionierung bei 200°C und 300°C Partikelgrößen von ~2 nm vorlagen und neben der Hauptkomponente Au^0 auch Au^{3+} Spezies detektiert werden konnte.

Die relative Deaktivierung war bei den Proben mit Anatas als Träger in beiden Atmosphären ähnlich, während die Rutil/Anatas geträgerten Katalysatoren in H_2-freier Atmosphäre deutlich stärker deaktivierten. Bei allen Proben wurde in H_2-reicher Atmosphäre Wasser als Nebenprodukt beobachtet, in H_2-freier Atmosphäre dagegen Karboxylate/Formiate sowie monodendate und bidendate Karbonate. Karboxylate wurden als Hauptursache der Deaktivierung identifiziert, gefolgt von den monodentaten Karbonaten, welche einen weniger starken Beitrag leisten. Der Aufbau von Karboxylaten aus adsorbierten CO und OH-Gruppen, ihr Umbau zu monodentaten und dann zu den thermisch instabilen bidentaten Karbonaten wurde als Reaktionsmechanismus identifiziert und erste vorläufige Ergebnisse deuten darauf hin, dass es sich hierbei um den einzigen Reaktionsweg handelt. Des Weiteren wurde ein Gleichgewicht zwischen OH-Gruppen und adsorbiertem Wasser gefunden, welches in Anwesenheit von Sauerstoff auf die Seite der Wassers verschoben wird. Es konnte gezeigt werden, dass die Menge an adsorbiertem Wasser mit der Aktivität korreliert und dass im Laufe der Reaktion in H_2-freier Atmosphäre Wasser und damit auch OH-Gruppen desorbieren. Damit kann die stärkere Deaktivierung unter diesen Bedingungen mit dem Verlust von Wasser erklärt werden, welches eine essentielle Rolle im Abbau der Zwischenprodukte Karboxylate und monodentate Karbonate spielt.

CO Adsorption wurde in beiden Atmosphären nur auf den Goldpartikeln beobachtet, wobei in H_2-reicher Atmosphäre die Entstehung einer zusätzlichen Spezies, welche als H-Au-CO

Koadsorption bezeichnet wurde, beobachtet werden konnte. Auch die CO Reaktionsordnung wurde von der Anwesenheit von H_2 beeinflusst – sie war signifikant größer als in H_2-freier Atmosphäre. Die Reaktionsordnung von Sauerstoff dagegen wurde von H_2 nicht beeinflusst, aber in ‚pressure gap' nahm sie mit abnehmendem Gesamtdruck ab. Im Gegensatz dazu nahm die CO Reaktionsordnung mit abnehmendem Druck zu. Ein signifikanter Einfluss der unterschiedlichen Materialen auf Reaktionsraten und Reaktionskinetik wurde nicht gefunden. Eine Abschätzung der Reaktionswahrscheinlichkeit im 10^{-6}-10^{-7} mbar Bereich zeigte, dass die dabei produzierten CO_2 Mengen unter dem Detektionslimit liegen.

Experimente mit isotopenmarkierten Gasen zeigten, dass (i) Sauerstoff auf der Katalysatoroberfläche nicht dissoziiert, und (ii) CO weder Sauerstoff mit dem TiO_2-Träger austauscht, noch mit Trägersauerstoff zu CO_2 reagiert, wodurch ein Mars van Krevelen Mechanismus unter den gegebenen Bedingungen ausgeschlossen werden kann. Andererseits tauscht CO_2 mit dem Träger Sauerstoff aus. Aus der Verteilung der CO_2 Isotopomere während der Oxidation von $C^{16}O$ mit $^{36}O_2$ kann nicht auf den Reaktionsmechanismus geschlossen werden, da die gefundene Verteilung für mehrere Modelle gültig ist.

B Additional figures and experimental information

I Deconvolution of the Au 4f peaks after different conditioning procedures (fig. 3.1-7)

See subsection 3.1.2.2, fig. 3.1-7).

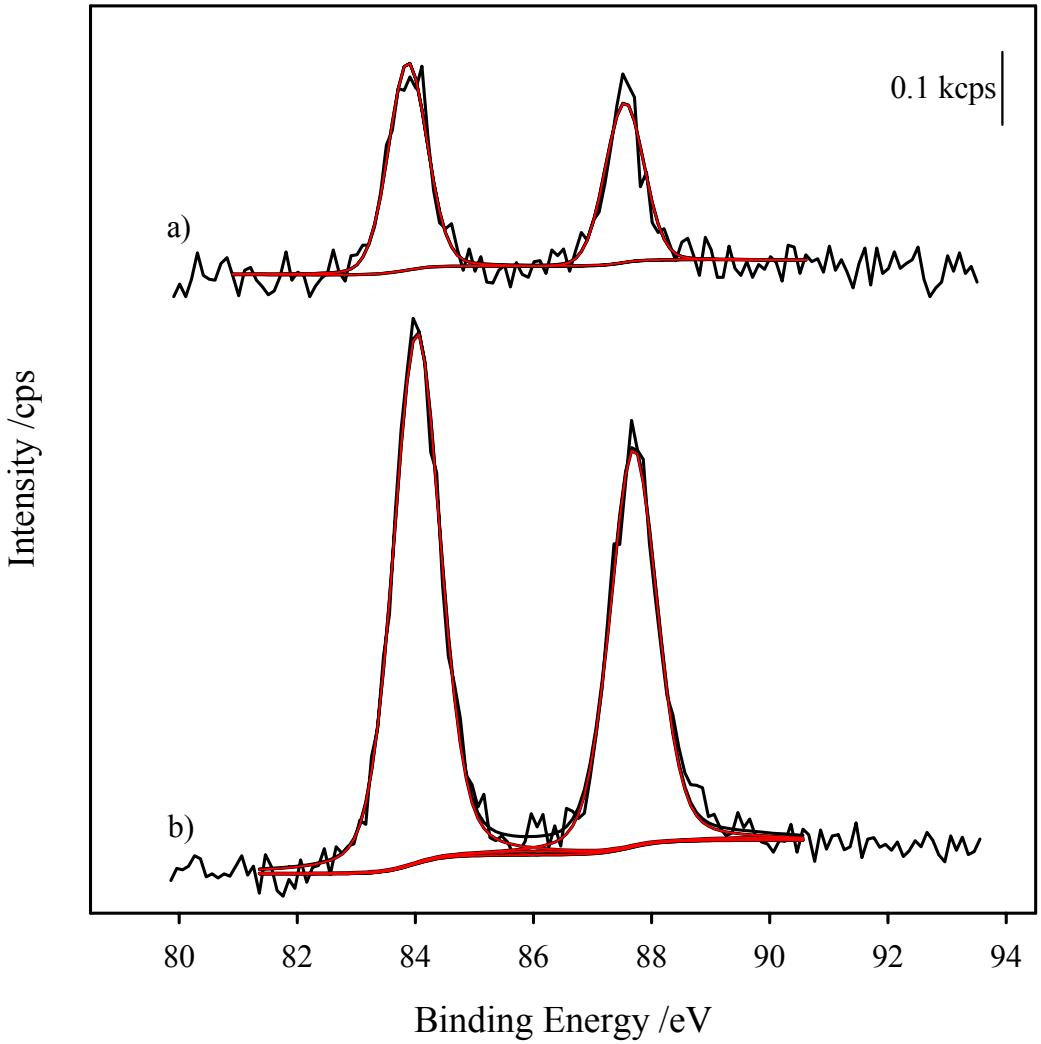

Figure B.I-1: Au 4f peak of a a) calcined and b) reduced sample of catalyst $Au/Ti_2(1)$ and the fits for Au^0 and Au^{3+} (red lines). For the calcined sample only Au^0 could be fitted, the reduced sample consisted also of a contribution of Au^{3+} with a BE shift of 1.9 eV. The peak areas were calibrated according to table 3.1-2. Pass energy: 11.75 eV; scanning time: 6.67 min.

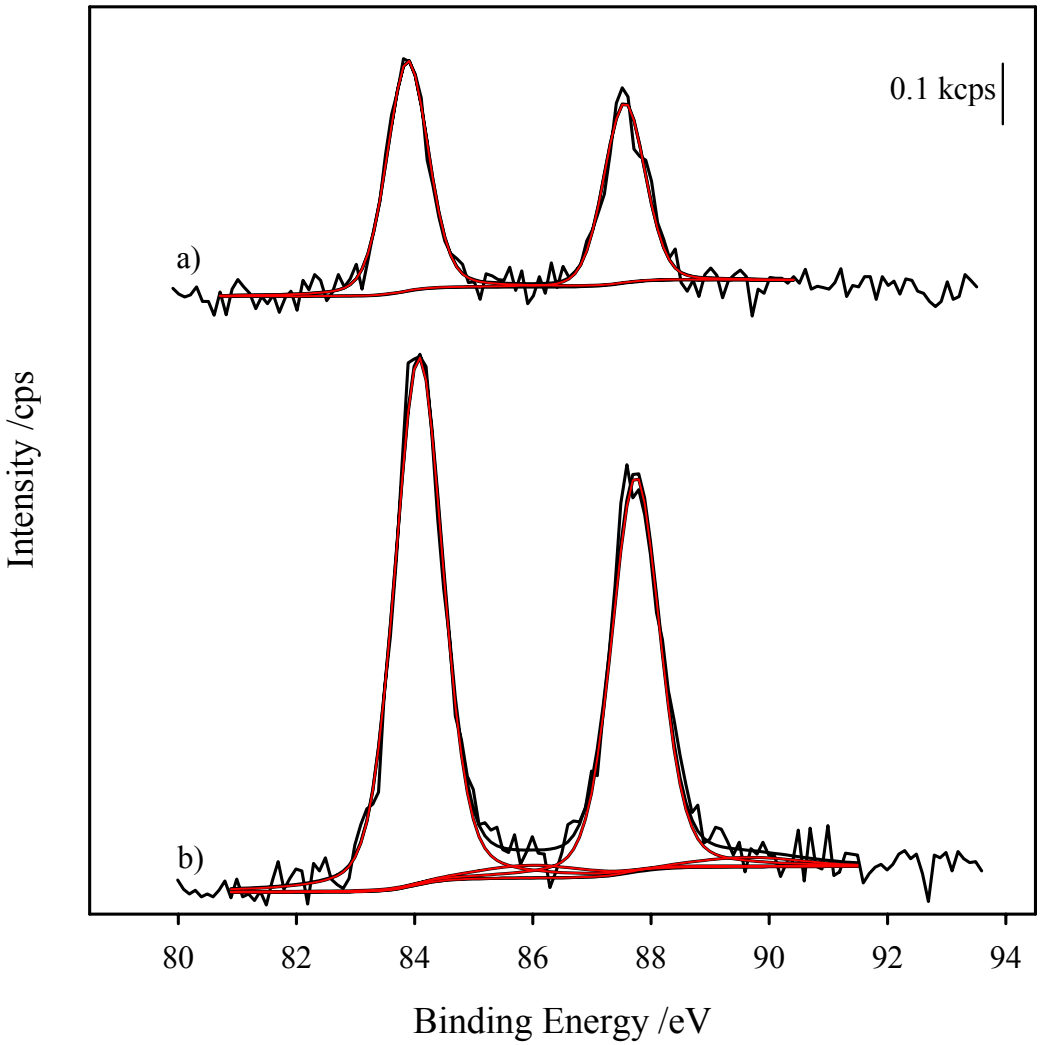

Figure B.I-2: Au 4f peak of a a) calcined and b) reduced sample of catalyst Au/Ti_2(2) and the fits for Au^0 and Au^{3+} (red lines). For the calcined sample only Au^0 could be fitted, the reduced sample consisted also of a contribution of Au^{3+} with a BE shift of 1.9 eV. The peak areas were calibrated according to table 3.1-2. Pass energy: 11.75 eV; scanning time: 6.67 min.

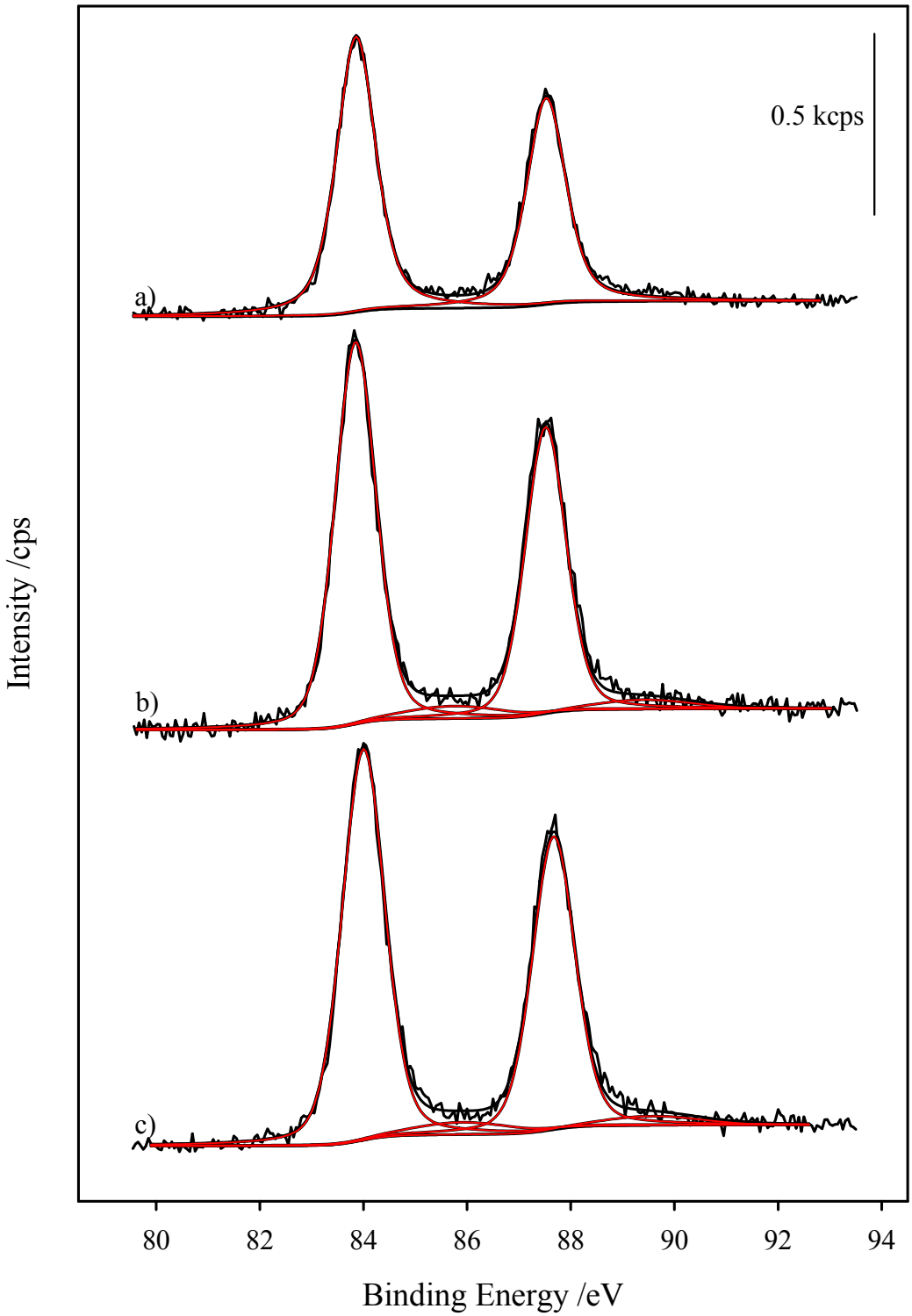

Figure B.I-3: Au 4f peak of a a) calcined, b) redox-conditioned and c) reduced sample of catalyst $Au/Ti_2(5)$ and the fits for Au^0 and Au^{3+} (red lines). For the calcined sample only Au^0 could be fitted, the redox-conditioned and reduced samples consisted also of a contribution of Au^{3+} with a BE shift of 1.9 eV. The peak areas were calibrated according to table 3.1-2. Pass energy: 11.75 eV; scanning time: 25 min.

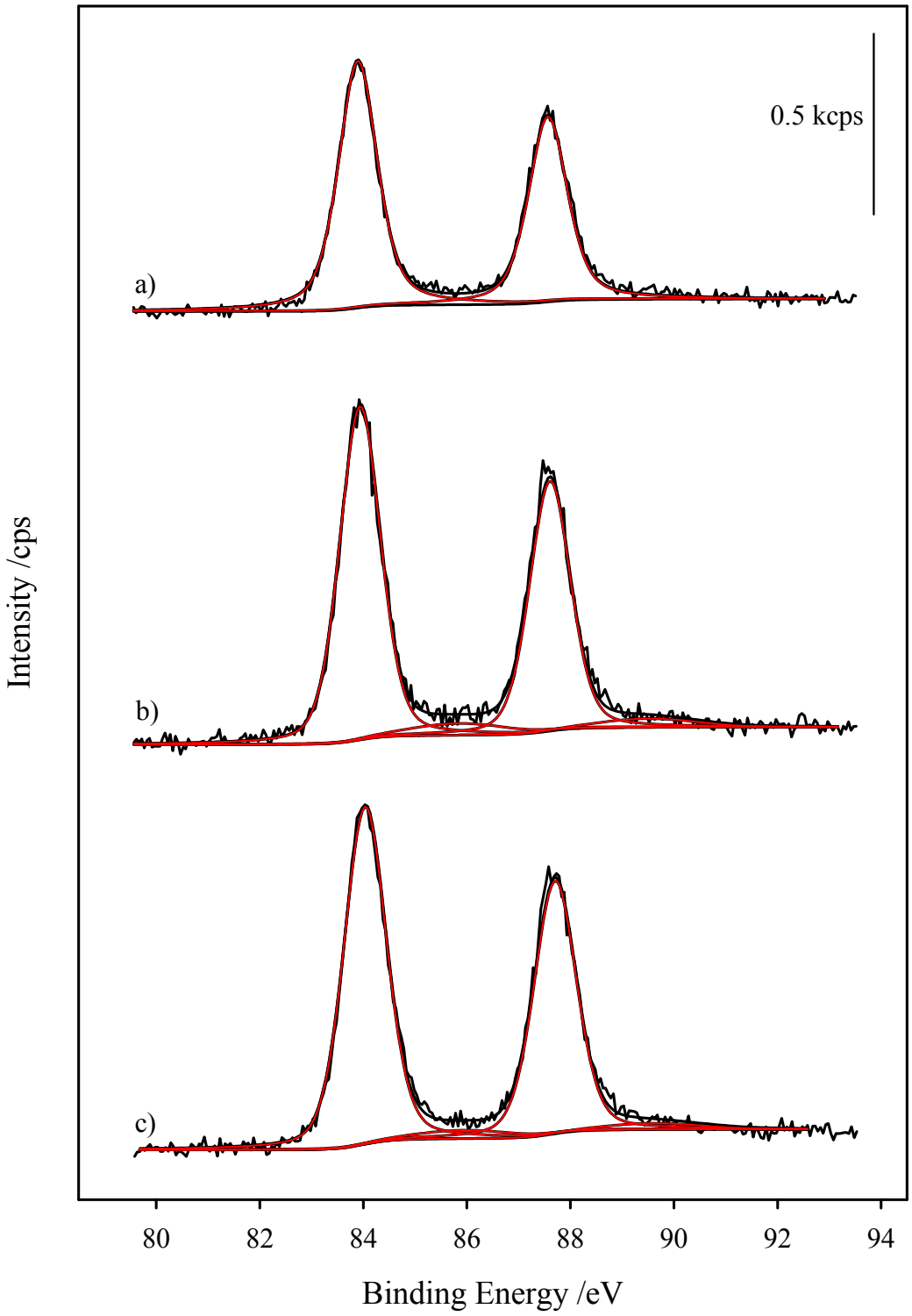

Figure B.I-4: Au 4f peak of a a) calcined, b) redox-conditioned and c) reduced sample of catalyst $Au/Ti_2(6)$ and the fits for Au^0 and Au^{3+} (red lines). For the calcined sample only Au^0 could be fitted, the redox-conditioned and reduced samples consisted also of a contribution of Au^{3+} with a BE shift of 1.9 eV. The peak areas were calibrated according to table 3.1-2. Pass energy: 11.75 eV; scanning time: 25 min.

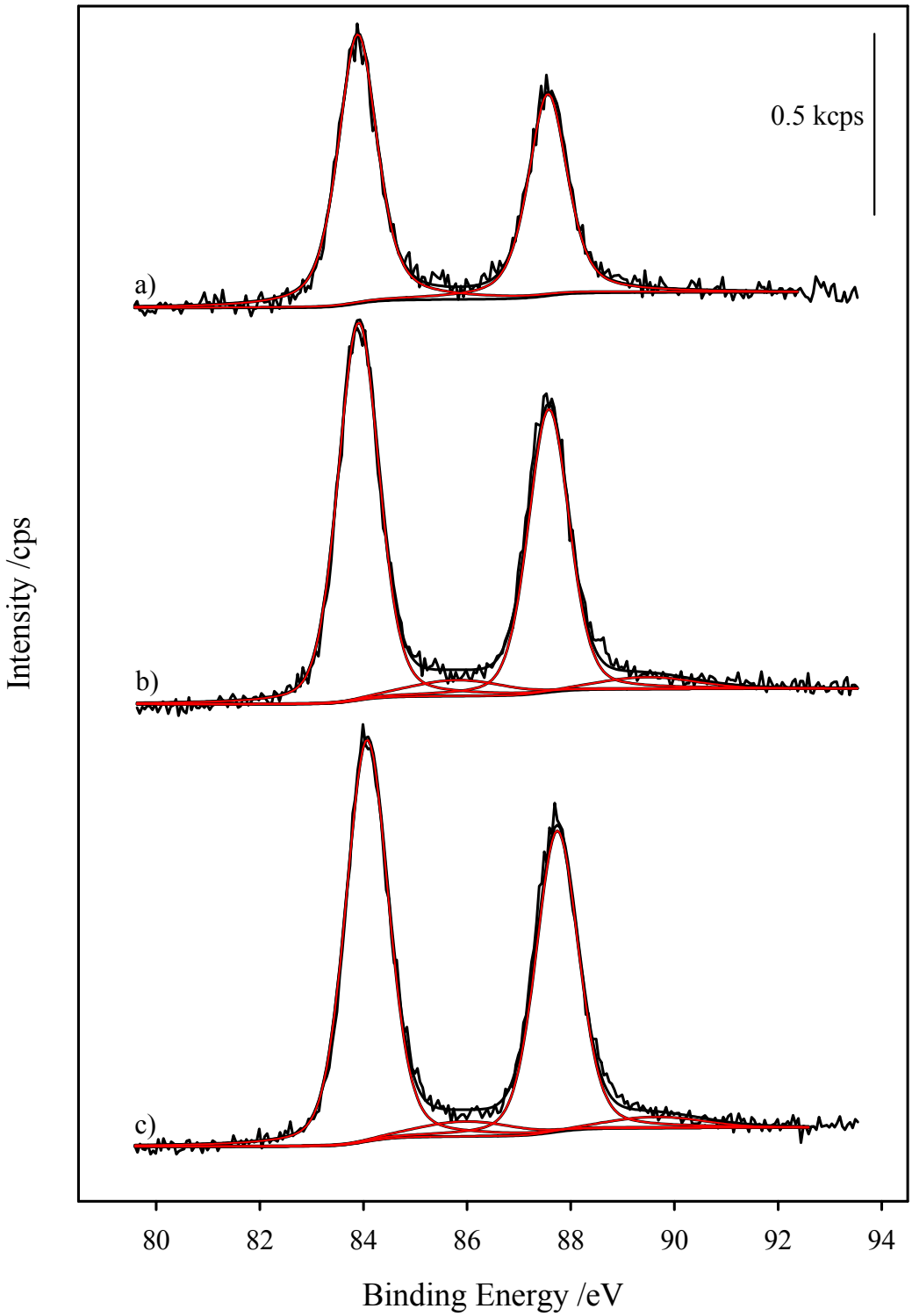

Figure B.I-5: Au 4f peak of a a) calcined, b) redox-conditioned and c) reduced sample of catalyst $Au/Ti_2(7)$ and the fits for Au^0 and Au^{3+} (red lines). For the calcined sample only Au^0 could be fitted, the redox-conditioned and reduced samples consisted also of a contribution of Au^{3+} with a BE shift of 1.9 eV. The peak areas were calibrated according to table 3.1-2. Pass energy: 11.75 eV; scanning time: 25 min.

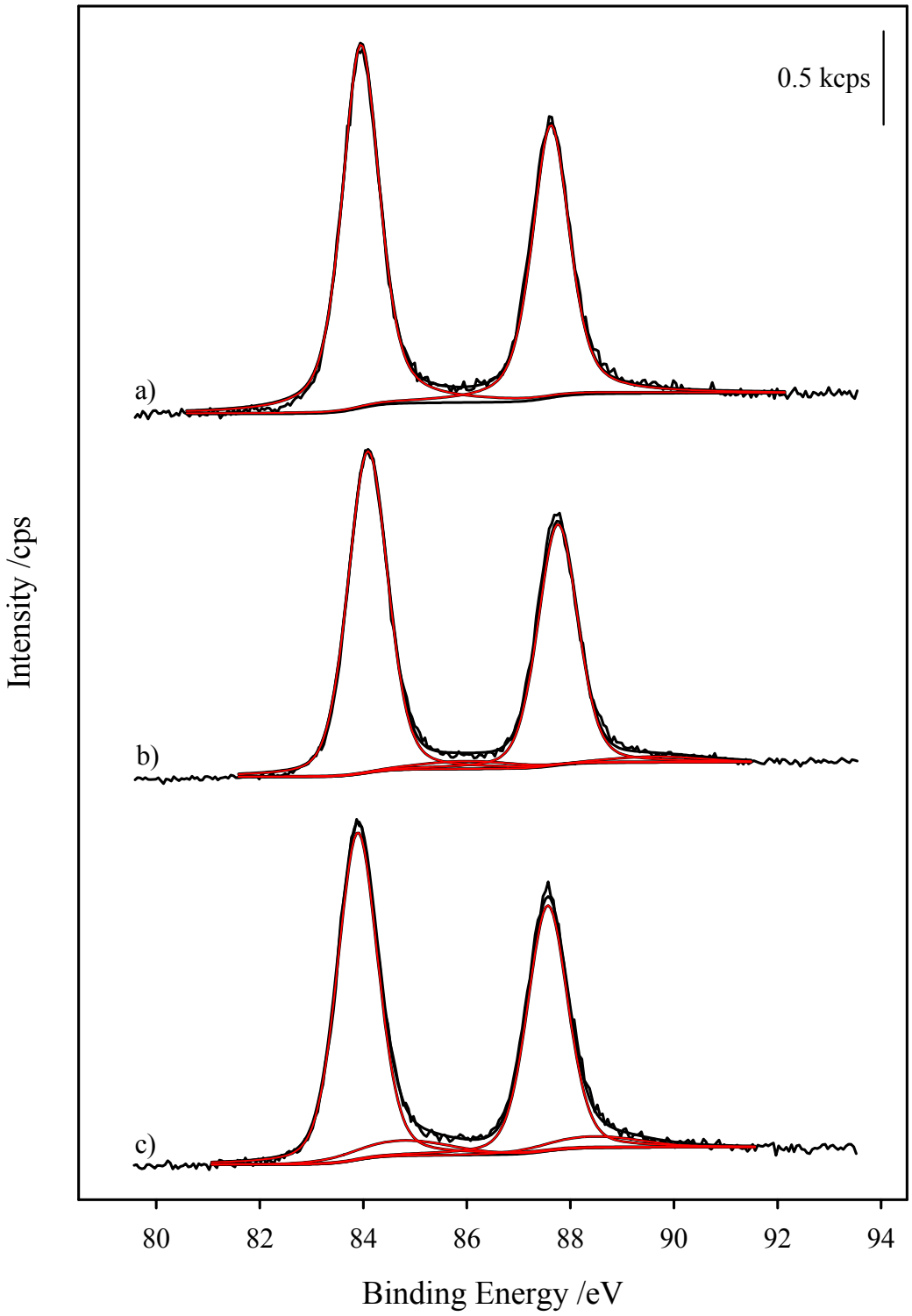

Figure B.I-6: Au 4f peak of a a) calcined, b) redox-conditioned and c) reduced sample of catalyst $Au/Ti_2(8)$ and the fits for Au^0 and Au^{3+} (red lines). For the calcined sample only Au^0 could be fitted, the redox-conditioned and reduced samples consisted also of a contribution of Au^{3+} with a BE shift of 1.9 eV. The peak areas were calibrated according to table 3.1-2. Pass energy: 11.75 eV; scanning time: 25 min.

II Experimental conditions during activity measurements

Figure	Measurement	Catalyst:Dilution	Sample Weight (in mg)	Conversion (in %)
3.2-1	a)	1:50	50.2	8.8-12.2
	b)	1:100	61.5	17.6-19.9
	c)	1:50	49.8	1.6-8.0
3.2-2	●	1:50	49.8	1.6-8.0
	▲	1:50	49.8	4.5-7.6
3.2-3	▼	1:50	50.7	36.7-55.1
	▲	1:20	60.3	22.3-34.8
	■	1:20	53.5	40.3-63.9
	●	1:20	60.1	23.2-35.5
3.2-4	a)	1:50	50.2	8.8-12.2
	b)	1:80	50.6	26.3-31.0
	c)	1:50	49.8	19.4-24.3
3.2-5	Calcined H_2-free	1:200	62.5	3.7-11.6
	Calcined H_2-rich	1:200	64.4	13.3-18.5
	Reduced H_2-free	1:200	84.2	5.4-15.1
	Reduced H_2-rich	1:200	64.2	9.8-14.5
	Redox H_2-free	1:200	84.9	6.3-26.1
	Redox H_2-rich	1:200	61.8	10.4-16.6
3.2-6 **3.2-7**	●	1:200	64.4	13.3-18.5
	■	1:200	63.0	15.2-20.7
	▲	1:200	63.0	11.8-16.5
	◆	1:200	62.3	11.2-16.8
	▼	1:200	65.6	13.7-18.1
	○	1:200	62.5	3.7-11.6
	□	1:200	63.9	2.8-14.8
	△	1:200	63.0	2.4-12.4
	◇	1:200	64.5	2.3-15.3
	▽	1:200	62.0	1.2-12.2
3.2-8	○	1:200	84.9	6.3-26.1
	□	1:200	77.3	6.3-24.8
	△	1:200	75.4	7.5-26.9
	◇	1:200	86.2	8.5-32.9
	▽	1:200	64.2	1.5-20.8
3.2-9	●	1:200	64.2	9.8-14.2
	■	1:200	64.7	9.4-16.6
	▲	1:200	66.7	10.9-16.9
	◆	1:200	66.0	5.2-11.3
	▼	1:200	65.0	8.9-15.1
3.2-10	▲	1:20	60.3	22.3-34.8
	■	1:20	53.5	40.3-63.9
	●	1:20	60.1	23.2-35.5
3.3-1	△: $p_{CO,O2}$=1.8 kPa	1:50	50.3	12.1
	△: $p_{CO,O2}$=1.2 kPa	1:50	50.3	13.5
	△: $p_{CO,O2}$=0.7 kPa	1:50	50.3	15.2
	△: $p_{CO,O2}$=0.4 kPa	1:50	50.3	13.1

	△: $p_{CO,O2}$=0.2 kPa	1:50	50.3	19.1
	△: $p_{CO,O2}$=0.07 kPa	1:50	50.3	33.3
	▽: $p_{CO,O2}$=1.9 kPa	1:50	51.1	7.7
	▽: $p_{CO,O2}$=1.2 kPa	1:50	51.1	8.5
	▽: $p_{CO,O2}$=0.6 kPa	1:50	51.1	13.4
	▽: $p_{CO,O2}$=0.2 kPa	1:50	51.1	18.6
	▽: $p_{CO,O2}$=0.07 kPa	1:50	51.1	27.5
	▼: $p_{CO,O2}$=1.6 kPa	1:50	50.2	8.3
	▼: $p_{CO,O2}$=1.0 kPa	1:50	50.2	8.9
	▼: $p_{CO,O2}$=0.3 kPa	1:50	50.2	11.4
	▼: $p_{CO,O2}$=0.1 kPa	1:50	50.2	7.0
	▼: $p_{CO,O2}$=0.03 kPa	1:50	50.2	3.1
	●: $p_{CO,O2}$=1.6 kPa	1:50	49.8	17.8
	●: $p_{CO,O2}$=1.0 kPa	1:50	49.8	19.4
	●: $p_{CO,O2}$=0.3 kPa	1:50	49.8	17.8
	●: $p_{CO,O2}$=0.1 kPa	1:50	49.8	10.6
	●: $p_{CO,O2}$=0.03 kPa	1:50	49.8	3.4
3.3-2	△:p_{CO}=1.7 kPa	1:50	50.8	3.2
	△: p_{CO}=1.2 kPa	1:50	50.8	4.8
	△: p_{CO}=0.6 kPa	1:50	50.8	7.6
	△: p_{CO}=0.15 kPa	1:50	50.8	20.3
	△: p_{CO}=0.07 kPa	1:50	50.8	40.5
	△: p_{CO}=0.03 kPa	1:50	50.8	56.2
	▽: p_{CO}=1.7 kPa	1:50	51.9	4.5
	▽: p_{CO}=1.2 kPa	1:50	51.9	5.8
	▽: p_{CO}=0.7 kPa	1:50	51.9	8.7
	▽: p_{CO}=0.2 kPa	1:50	51.9	18.9
	▽: p_{CO}=0.07 kPa	1:50	51.9	32.4
	▽: p_{CO}=0.02 kPa	1:50	51.9	59.1
	▼: p_{CO}=1.5 kPa	1:50	53.0	6.2
	▼: p_{CO}=1.0 kPa	1:50	53.0	7.5
	▼: p_{CO}=0.5 kPa	1:50	53.0	10.1
	▼: p_{CO}=0.1 kPa	1:50	53.0	12.1
	▼: p_{CO}=0.03 kPa	1:50	53.0	16.9
3.3-3	▽: p_{O2}=3.3 kPa	1:50	50.9	19.2
	▽: p_{O2}=2.7 kPa	1:50	50.9	18.4
	▽: p_{O2}=2.1 kPa	1:50	50.9	16.6
	▽: p_{O2}=1.1 kPa	1:50	50.9	15.6
	▽: p_{O2}=0.4 kPa	1:50	50.9	11.1
	▽: p_{O2}=0.2 kPa	1:50	50.9	8.5
	▼: p_{O2}=3.1 kPa	1:50	50.0	13.8
	▼: p_{O2}=2.5 kPa	1:50	50.0	13.2
	▼: p_{O2}=1.6 kPa	1:50	50.0	6.0
	▼: p_{O2}=0.4 kPa	1:50	50.0	7.2
	●: p_{O2}=2.9 kPa	1:50	51.0	15.6
	●: p_{O2}=2.4 kPa	1:50	51.0	14.4
	●: p_{O2}=0.9 kPa	1:50	51.0	9.7
	●: p_{O2}=0.4 kPa	1:50	51.0	7.4
	●: p_{O2}=0.1 kPa	1:50	51.0	4.5

3.3-4	●: 1 kPa	1:300	81.4	6.8
	●: 0.6 kPa	1:300	81.4	7.2
	●: 0.4 kPa	1:300	81.4	7.8
	●: 0.2 kPa	1:300	81.4	5.4
	■: 2 kPa	1:300	80.0	9.4
	■: 1 kPa	1:300	80.0	9.6
	■: 0.5 kPa	1:300	80.0	6.4
	■: 0.25 kPa	1:300	80.0	4.3
3.4-1	a)	1:270	79.9	19.6-25.1
	b)	1:400	80.0	19.9-26.5
	c)	1:300	81.1	15.9-24.2
	d)	1:500	81.6	13.5-25.7
	e)	1:1100	82.0	16.1-35.2
	f)	1:60	75.4	1.9-22.0
	g)	1:200	63.9	2.8-14.8
3.4-2a	$p_{CO,O2}=9\cdot10^{-4}$ mbar, ●	1:510	80.7	4.2
	$p_{CO,O2}=9\cdot10^{-4}$ mbar, ■	1:1100	82.0	9.8
	$p_{CO,O2}=4\cdot10^{-3}$ mbar, ●	1:510	80.7	3.3
	$p_{CO,O2}=4\cdot10^{-3}$ mbar, ■	1:500	81.9	7.6
	$p_{CO,O2}=4\cdot10^{-2}$ mbar, ●	1:170	78.7	5.6
	$p_{CO,O2}=4\cdot10^{-2}$ mbar, ■	1:400	80.0	10.8
	$p_{CO,O2}=2\cdot10^{-1}$ mbar, ●	1:170	78.7	2.0
	$p_{CO,O2}=2\cdot10^{-1}$ mbar, ■	1:300	80.6	4.2
	$p_{CO,O2}=5\cdot10^{-1}$ mbar, ●	1:130	78.0	6.7
	$p_{CO,O2}=5\cdot10^{-1}$ mbar, ■	1:270	79.9	8.26
	$p_{CO,O2}=10^{0}$ mbar, ●	1:130	78.0	4.1
	$p_{CO,O2}=10^{1}$ mbar, ▲	1:60	75.4	0.3
3.4-2b	$p_{CO,O2}=9\cdot10^{-4}$ mbar, ●	1:510	80.7	5.4
	$p_{CO,O2}=9\cdot10^{-4}$ mbar, ■	1:1100	82.0	11.5
	$p_{CO,O2}=4\cdot10^{-3}$ mbar, ●	1:510	80.7	3.6
	$p_{CO,O2}=4\cdot10^{-3}$ mbar, ■	1:500	81.9	9.7
	$p_{CO,O2}=4\cdot10^{-2}$ mbar, ●	1:170	78.7	8.2
	$p_{CO,O2}=4\cdot10^{-2}$ mbar, ■	1:400	80.0	14.5
	$p_{CO,O2}=2\cdot10^{-1}$ mbar, ●	1:170	78.7	3.2
	$p_{CO,O2}=2\cdot10^{-1}$ mbar, ■	1:300	80.6	7.2
	$p_{CO,O2}=5\cdot10^{-1}$ mbar, ●	1:130	78.0	10.8
	$p_{CO,O2}=5\cdot10^{-1}$ mbar, ■	1:270	79.9	12.9
	$p_{CO,O2}=10^{0}$ mbar, ●	1:130	78.0	6.7
	$p_{CO,O2}=10^{1}$ mbar, ▲	1:60	75.4	1.0
3.4-2c	$p_{CO,O2}=9\cdot10^{-4}$ mbar, ●	1:510	80.7	6.7
	$p_{CO,O2}=9\cdot10^{-4}$ mbar, ■	1:1100	82.0	13.4
	$p_{CO,O2}=9\cdot10^{-4}$ mbar, ○	1:510	80.7	4.7
	$p_{CO,O2}=9\cdot10^{-4}$ mbar, □	1:1100	82.0	6.43
	$p_{CO,O2}=4\cdot10^{-3}$ mbar, ●	1:510	80.7	3.9
	$p_{CO,O2}=4\cdot10^{-3}$ mbar, ■	1:500	81.9	12.3
	$p_{CO,O2}=4\cdot10^{-3}$ mbar, ○	1:510	80.7	2.9
	$p_{CO,O2}=4\cdot10^{-3}$ mbar, □	1:500	81.9	8.5
	$p_{CO,O2}=4\cdot10^{-2}$ mbar, ●	1:170	78.7	10.9
	$p_{CO,O2}=4\cdot10^{-2}$ mbar, ■	1:400	80.0	18.2

	$p_{CO,O2}=4\cdot10^{-2}$ mbar, ○	1:170	78.7	9.3
	$p_{CO,O2}=4\cdot10^{-2}$ mbar, □	1:400	80.0	15.7
	$p_{CO,O2}=2\cdot10^{-1}$ mbar, ●	1:170	78.7	4.3
	$p_{CO,O2}=2\cdot10^{-1}$ mbar, ■	1:300	80.6	9.8
	$p_{CO,O2}=2\cdot10^{-1}$ mbar, ○	1:170	78.7	4.1
	$p_{CO,O2}=2\cdot10^{-1}$ mbar, □	1:300	80.6	9.0
	$p_{CO,O2}=5\cdot10^{-1}$ mbar, ●	1:130	78.0	14.9
	$p_{CO,O2}=5\cdot10^{-1}$ mbar, ■	1:270	79.9	18.5
	$p_{CO,O2}=5\cdot10^{-1}$ mbar, ○	1:130	78.0	15.2
	$p_{CO,O2}=5\cdot10^{-1}$ mbar, □	1:270	79.9	16.3
	$p_{CO,O2}=10^{0}$ mbar, ●	1:130	78.0	9.3
	$p_{CO,O2}=10^{0}$ mbar, ○	1:130	78.0	9.5
	$p_{CO,O2}=10^{1}$ mbar, ▲	1:60	75.4	1.9
	$p_{CO,O2}=10^{1}$ mbar, △	1:60	75.4	0.9
3.4-2d	$p_{CO,O2}=9\cdot10^{-4}$ mbar, ●	1:510	80.7	6.0
	$p_{CO,O2}=9\cdot10^{-4}$ mbar, ■	1:1100	82.0	7.0
	$p_{CO,O2}=4\cdot10^{-3}$ mbar, ●	1:510	80.7	3.2
	$p_{CO,O2}=4\cdot10^{-3}$ mbar, ■	1:500	81.9	10.4
	$p_{CO,O2}=4\cdot10^{-2}$ mbar, ●	1:170	78.7	11.6
	$p_{CO,O2}=4\cdot10^{-2}$ mbar, ■	1:400	80.0	18.7
	$p_{CO,O2}=2\cdot10^{-1}$ mbar, ●	1:170	78.7	6.0
	$p_{CO,O2}=2\cdot10^{-1}$ mbar, ■	1:300	80.6	11.7
	$p_{CO,O2}=5\cdot10^{-1}$ mbar, ●	1:130	78.0	20.8
	$p_{CO,O2}=5\cdot10^{-1}$ mbar, ■	1:270	79.9	22.4
	$p_{CO,O2}=10^{0}$ mbar, ●	1:130	78.0	13.8
	$p_{CO,O2}=10^{1}$ mbar, ▲	1:60	75.4	1.4
3.4-2e	$p_{CO,O2}=9\cdot10^{-4}$ mbar, ●	1:510	80.7	7.4
	$p_{CO,O2}=9\cdot10^{-4}$ mbar, ■	1:1100	82.0	8.1
	$p_{CO,O2}=4\cdot10^{-3}$ mbar, ●	1:510	80.7	3.5
	$p_{CO,O2}=4\cdot10^{-3}$ mbar, ■	1:500	81.9	12.8
	$p_{CO,O2}=4\cdot10^{-2}$ mbar, ●	1:170	78.7	15.4
	$p_{CO,O2}=4\cdot10^{-2}$ mbar, ■	1:400	80.0	22.7
	$p_{CO,O2}=2\cdot10^{-1}$ mbar, ●	1:170	78.7	7.5
	$p_{CO,O2}=2\cdot10^{-1}$ mbar, ■	1:300	80.6	14.4
	$p_{CO,O2}=5\cdot10^{-1}$ mbar, ●	1:130	78.0	25.2
	$p_{CO,O2}=5\cdot10^{-1}$ mbar, ■	1:270	79.9	29.4
	$p_{CO,O2}=10^{0}$ mbar, ●	1:130	78.0	17.2
	$p_{CO,O2}=10^{1}$ mbar, ▲	1:60	75.4	2.3
3.4-2f	$p_{CO,O2}=9\cdot10^{-4}$ mbar, ●	1:510	80.7	9.5
	$p_{CO,O2}=9\cdot10^{-4}$ mbar, ■	1:1100	82.0	10.6
	$p_{CO,O2}=4\cdot10^{-3}$ mbar, ●	1:510	80.7	4.7
	$p_{CO,O2}=4\cdot10^{-3}$ mbar, ■	1:500	81.9	16.4
	$p_{CO,O2}=4\cdot10^{-2}$ mbar, ●	1:170	78.7	18.3
	$p_{CO,O2}=4\cdot10^{-2}$ mbar, ■	1:400	80.0	28.2
	$p_{CO,O2}=2\cdot10^{-1}$ mbar, ●	1:170	78.7	8.7
	$p_{CO,O2}=2\cdot10^{-1}$ mbar, ■	1:300	80.6	17.0
	$p_{CO,O2}=5\cdot10^{-1}$ mbar, ●	1:130	78.0	29.2
	$p_{CO,O2}=5\cdot10^{-1}$ mbar, ■	1:270	79.9	37.5
	$p_{CO,O2}=10^{0}$ mbar, ●	1:130	78.0	19.6

	$p_{CO,O2}=10^{1}$ mbar, ▲	1:60	75.4	3.2
3.4-3a	$p_{O2}=1\cdot10^{-1}$ mbar	1:300	81.1	7.5
	$p_{O2}=2\cdot10^{-1}$ mbar	1:300	81.1	10.6
	$p_{O2}=2\cdot10^{-1}$ mbar	1:300	81.1	9.9
	$p_{O2}=5\cdot10^{-1}$ mbar	1:300	81.1	15.1
	$p_{O2}=7\cdot10^{-1}$ mbar	1:300	81.1	16.7
	$p_{O2}=10^{0}$ mbar	1:300	81.1	18.6
3.4-3b	$p_{O2}=2\cdot10^{-3}$ mbar	1:500	81.6	9.9
	$p_{O2}=4\cdot10^{-3}$ mbar	1:500	81.6	11.6
	$p_{O2}=1\cdot10^{-2}$ mbar	1:500	81.6	13.3
	$p_{O2}=1.4\cdot10^{-2}$ mbar	1:500	81.6	14.1
	$p_{O2}=2\cdot10^{-2}$ mbar	1:500	81.6	15.1

C Danksagung (Acknowledgement)

An dieser Stelle möchte ich mich bei all denen bedanken, die zum Gelingen dieser Arbeit beigetragen haben.

- Mein spezieller Dank gilt Herrn **Prof. Dr. Rolf Jürgen Behm** für die Bereitstellung des anspruchsvollen und interessanten Themas und die Möglichkeit zur Durchführung dieser Doktorarbeit in seiner Abteilung.
- **Herrn Prof. Dr. Werner Tillmetz** danke ich für seine Bereitschaft, diese Arbeit zu lesen und das Zweitgutachten zu erstellen.
- **Dr. Markus Kinne** danke ich für die Betreuung eines Teils meiner Doktorarbeit.
- **Thomas Häring** and **Gerd Bräth** möchte ich für die breite technische Unterstützung danken.
- **Danielle Hansgen** and **Xin Zhang** danke ich für die Beteiligung an den Messungen am Niederdruckreaktor.
- **Prof. Florian Banhart** danke ich für die Messung der TEM Bilder.
- **Dr. Jun Cai** danke ich für die Messung der XPS Spektren.
- **Dr. Voitech Plzak** danke ich für die Präparation der Katalysatoren, für die Bereitstellung der XRD and TGA Messungen und für die fruchtbare Kooperation.
- Ganz besonderer Dank an **Dipl.-Chem. Rainer Leppelt** für die unglaublichen Mengen an Spaß in Labor und Büro, für die geduldigen Lehrstunden in Sachen Computer und für die Weltverbesserungsdiskussionen.
- Allen Mitgliedern der ÅOK danke ich für das freundschaftliche Miteinander und besonders den Rauchern für die Zigarettenpausen auch in klirrender Kälte.

Schließlich möchte ich mich noch bei zwei besonderen Personen bedanken: **VERENA**, dass sie eine Freundin ist und meinem Mann **ALEX**, ohne den mein Leben Schwarz-Weiß wäre.

D Publications and Conference Contributions

Publications:

- B. Schumacher, V. Plzak, M. Kinne, and R.J. Behm, *'Highly active Au/TiO_2 catalysts for low-temperature CO oxidation: preparation, conditioning and stability'*, Cat. Lett. **89**, 109 (2003)
- B. Schumacher, Y. Denkwitz, V. Plzak, M. Kinne, and R.J. Behm, *'Kinetics, mechanism, and the influence of H_2 on the CO oxidation reaction on a Au/TiO_2 catalyst'*, J. Catal. **224**, 449 (2004)
- B. Schumacher, V. Plzak, J. Cai, and R.J. Behm, *'Reproducibility of highly active Au/TiO_2 catalyst preparation and conditioning'*, Cat. Lett., **101**, 215 (2005)
- R. Leppelt, B. Schumacher, T. Häring, M. Kinne, and R.J. Behm, *'A low-pressure micro-reactor system for kinetic studies on high surface area catalysts in the pressure gap'*, Rev. Sci. Instrum., **76**, 024102 (2005)

Conference Contributions:

- XXXV. Jahrestreffen Deutscher Katalytiker, 20.-22. März 2002, Weimar

  B. Schumacher, V. Plzak, M. Kinne, R.J. Behm, *'Der Einfluss von H_2 auf die CO Oxidation an geträgerten Au/TiO_2 Katalysatoren'*
- XXXVI. Jahrestreffen Deutscher Katalytiker, 19.-21. März 2003, Weimar

  B. Schumacher, V. Plzak, M. Kinne, R.J. Behm, *'CO Oxidation an geträgerten Katalysatoren'*
- XXXVII. Jahrestreffen Deutscher Katalytiker, 17.-19. März 2004, Weimar

  B. Schumacher, V. Plzak, M. Kinne, R.J. Behm, *'Untersuchung zur Reproduzierbarkeit der Sythese von Au/TiO_2 Katalysatoren: CO-Oxidation und Charakterisierung'*

  B. Schumacher, M. Kinne, R.J. Behm, *'Au/TiO_2: CO, O_2 Adsorption und Reaktion und nichtstationären Bedingungen'*
- XXXVIII. Jahrestreffen Deutscher Katalytiker, 16.-18. März 2005, Weimar

  B. Schumacher, R. Leppelt, D. Hansgen, R.J. Behm, *'CO Oxidation an Au/TiO_2 Katalysatoren in der Drucklücke'*

  B. Schumacher, R.J. Behm, *'Zum Mechanismus der CO Oxidation an Au/TiO_2 Katalysatoren'*

F Erklärung

Hiermit bestätige ich, diese Arbeit selbstständig angefertigt zu haben und keine weiteren, außer den angegebenen Hilfsmitteln verwendet zu haben.

Ulm, den

Birgit Schumacher